Mechanical behaviour of tools for shearing Ultra High-Strength Steels: influence of the microstructure on fracture and fatigue micro-mechanisms of tool steels and evaluation of micro-mechanical damage in tools

Ingrid Picas

Supervisors: Dr. Daniel Casellas Padró
Prof. José Manuel Prado Pozuelo

A Thesis submitted for the degree of Doctor in the Universitat Politècnica de Catalunya, Fundació CTM Centre Tecnològic.

Manresa, September 2012

3. RESULTS

3.1 Tool steels microstructure

3.1.1 Primary alloy carbides

3.1.1.1 Structure, percentage in the microstructure and chemical composition

In Figure 3.1.1 the microstructure of the four steels studied in this work can be observed. The microstructure of 1.2379 (Figure 3.1.1 a)) is markedly anisotropic, with large carbide stringers forming bands in the metallic matrix. K360 (Figure 3.1.1 b)) shows a more homogeneous carbide distribution in the matrix than 1.2379. UNIVERSAL (Figure 3.1.1 c)) in turn, has the most homogeneous microstructure amongst 1.2379 and K360, even though it still shows preferential carbide alignment following the forging direction. HWS presents a typical PM tool steel microstructure (Figure 3.1.1 d)) with very small spherical carbides distributed in the matrix with no preferred orientation.

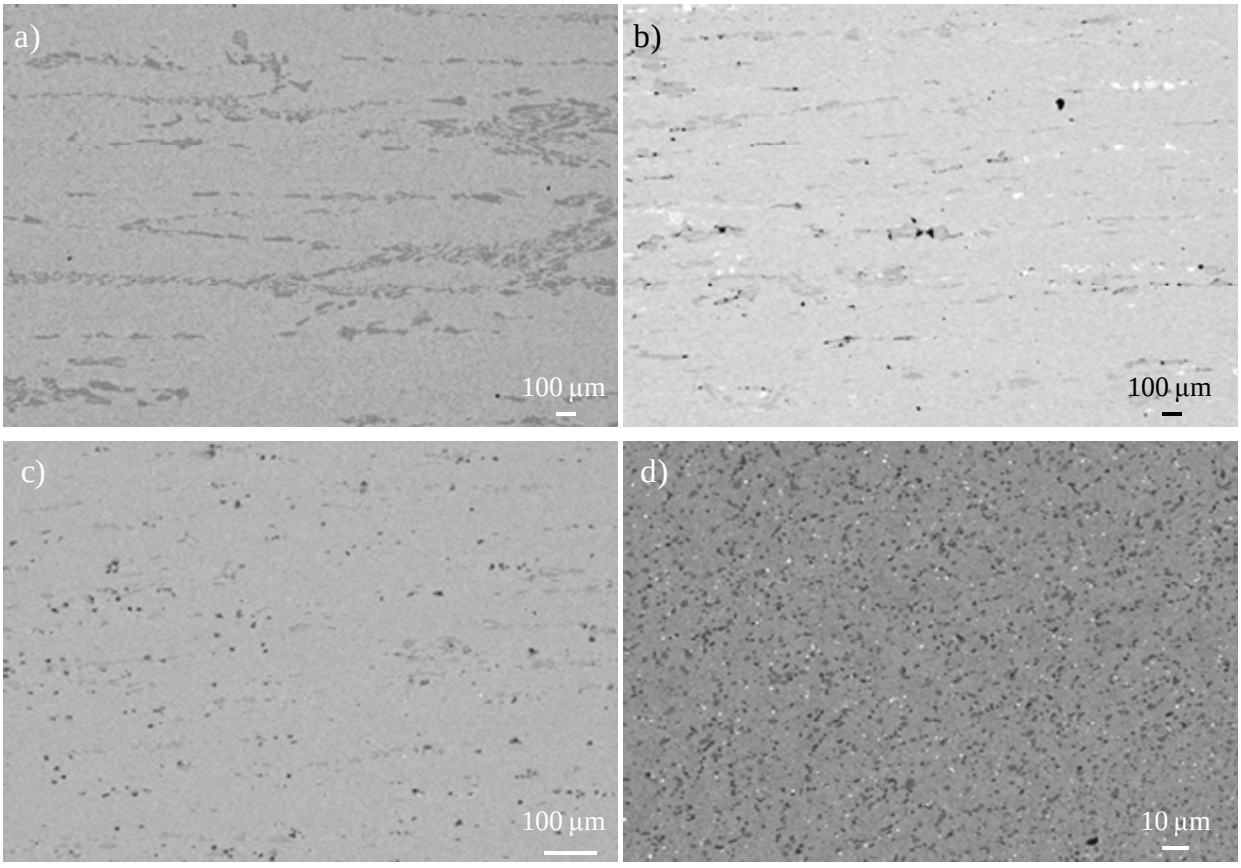

Figure 3.1.1 Microstructures of the four studied tool steels: a) 1.2379, b) K360, c) UNIVERSAL and d) HWS

Crystallographic structures, chemical compositions and amounts of primary alloy carbides embedded in 1.2379, K360, UNIVERSAL and HWS are presented in Table 3.1.1. In 1.2379 there is only one type of

primary carbide, M_7C_3-type (Figure 3.1.2 a)), rich in Fe and Cr and with an amount in the microstructure of 11,20 %. In K360 there is a total percentage of 7,9 % primary carbides of the following types: 6,10 % are M_7C_3, 0,80 % are MC and 1,00 % are M_6C (Figure 3.1.2 b)). The chemical composition of the M_7C_3 is very similar to that of the 1.2379, with some V and Mo replacing Cr and Fe. The MC are mainly Nb carbides and the M_6C show high amounts of Mo and Fe. In UNIVERSAL there is a lower quantity of primary carbides, 5,66 %, and it corresponds to 2,09 % of M_7C_3 and 3,57 % of MC (Figure 3.1.2 c)). M_7C_3 carbides are also similar to those of 1.2379, except for some Cr which is replaced by V and W. MC carbides are mainly formed by V although the composition of these is rather heterogeneous (as shown by the backscatter SEM image of Figure 3.1.2 c)).

In case of HWS the amount of carbides in the microstructure is 8,16 % and it is shared between three different types: 3,70 % M_7C_3, 4,40 % MC and 0,06 % M_6C (Figure 3.1.2 d)). No accurate data of the chemical composition of HWS carbides could be obtained by EDX due to their small sizes. However, as HWS presents the same nominal composition as UNIVERSAL, it was assumed that their primary carbides had similar chemical compositions. M_6C carbides were found in HWS in a very low percentage but they were not identified in UNIVERSAL, hence they were assumed to be mainly formed by Mo and/or W according to the light colour observed in the backscatter images.

The amount of primary carbides in UNIVERSAL and HWS was expected to coincide since they both showed the same initial quantity of carbon in their composition. However, results revealed that the quantity of primary carbides in UNIVERSAL is markedly lower than in HWS. The reason for this difference was attributed to the fact that in HWS, image analysis was performed at higher magnifications than UNIVERSAL and hence, in HWS even the smallest carbides were measured.

Table 3.1.1 Structure, amount in the microstructure and chemical composition (in wt %) of the primary alloy carbides in 1.2379, K360, UNIVERSAL and HWS

Tool Steel	Carbide	Amount, %	Chemical composition (wt %)							
			V	Cr	Fe	Mo	W	Nb	Ti	Si
1.2379	M_7C_3	11,20 [(1)]	3,46	42,18	44,17	2,12	-	-	-	-
K360	M_7C_3	6,10 [(1)]	6,31	38,54	39,92	6,87	-	-	-	-
K360	MC	0,80 [(1)]	6,52	-	-	-	-	75,44	1,53	-
K360	M_6C	1,00 [(1)]	3,35	6,06	33,74	50,07	-	-	-	3,44
UNIVERSAL	M_7C_3	2,09 [(1)]	7,66	38,44	40,03	3,28	2,17	-	-	-
UNIVERSAL	MC	3,57 [(1)]	61,32	10,81	1,95	3,84	3,99	-	-	-
HWS	M_7C_3 [(2)]	3,70	*7,66*	*38,44*	*40,03*	*3,28*	*2,17*	-	-	-
HWS	MC [(2)]	4,40	*61,32*	*10,81*	*1,95*	*3,84*	*3,99*	-	-	-
HWS	M_6C [(3)]	0,06	*	*	*	**	**	-	-	-

[(1)] Amount of carbides with an *ECD* > 5 μm

[(2)] The chemical composition of carbides is assumed as the same as the UNIVERSAL

[(3)] The structure and the chemical composition could not be determined accurately using EDX

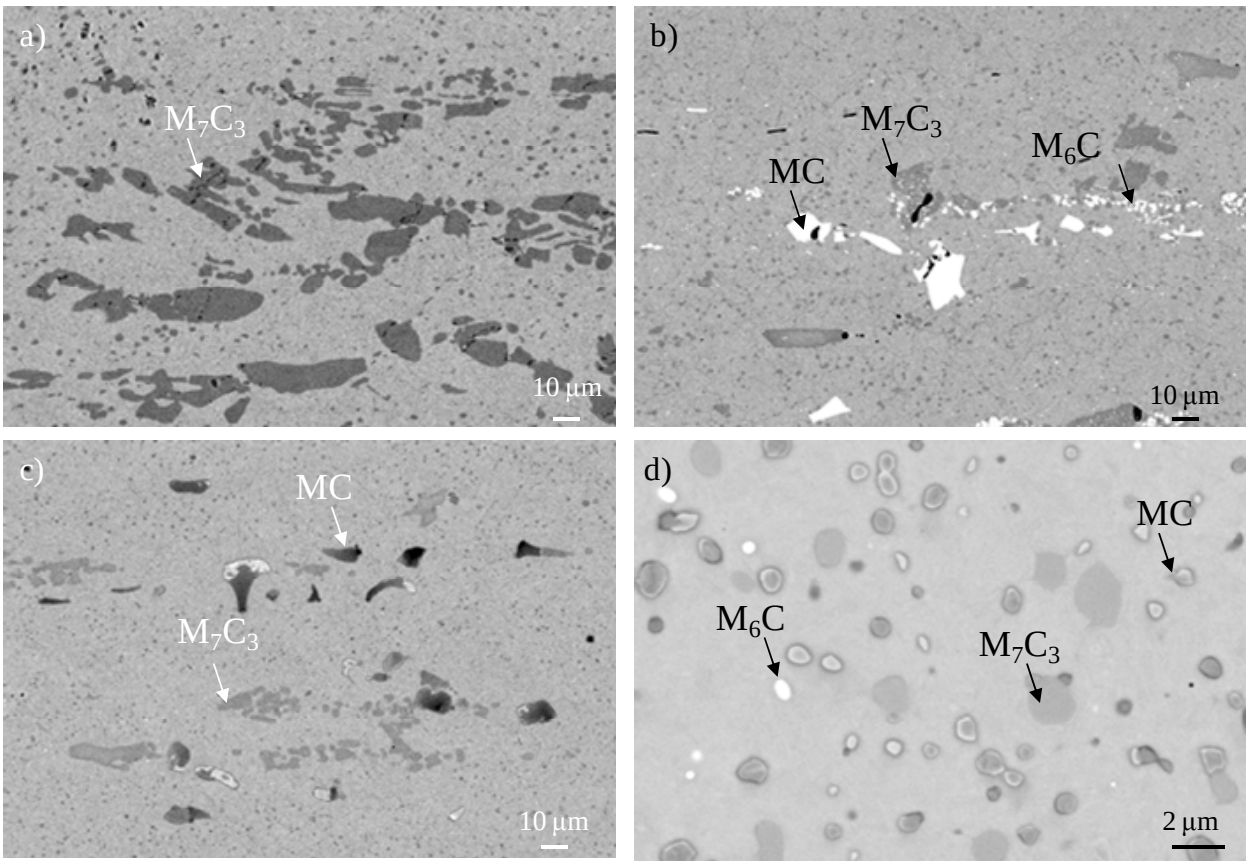

Figure 3.1.2 Backscatter Diffraction images showing the carbides identified at the microstructure of a) 1.2379; b) K360; c) UNIVERSAL and d) HWS

It is noteworthy to observe that the estimation of carbide percentage shows a good correlation with respect to the C content in the nominal composition of the steels; i.e. in 1.2379 the highest carbon content and carbide percentage are found, followed by K360 and UNIVERSAL.

3.1.1.2 Distributions of size and morphology

The size of primary carbides was determined in terms of the equivalent diameter, *ECD*, minimum diameter, D_{min} and maximum diameter, D_{max}. The morphology was assessed by means of the aspect ratio, *AR*, sphericity, ψ, and shape factor, *SF*. In Table 3.1.2 the mean carbide sizes and morphologies are shown for M_7C_3 carbides of 1.2379, M_7C_3, MC and M_6C of K360, M_7C_3 and MC of UNIVERSAL and M_7C_3, MC and M_6C of HWS.

Although these values provide useful information about the mean size and morphology of each type of carbide, a statistic approach was required to take into account their distribution in the microstructure. The carbide size and morphology distributions can be observed in Figures 3.1.3 and 3.1.4 respectively, in terms of the cumulative number of carbides with size or morphology parameters higher than a certain

value of the same parameters. Statistical interpretation of the size and morphology of primary carbides will be helpful to rationalise the mechanical properties and behaviour of tools.

Table 3.1.2 Mean carbides size and geometry in terms of *ECD*, D_{min}, D_{max}, *AR*, ψ and *SF* in 1.2379, K360, UNIVERSAL and HWS

Tool Steel	Carbide	*ECD*, µm	D_{min}, µm	D_{max}, µm	*AR*	ψ	*SF*
1.2379	M_7C_3	10,6 ± 5,7	9,4 ± 6,0	22,5 ± 15,1	2,9 ± 1,5	0,2 ± 0,2	0,3 ± 0,1
K360	M_7C_3	11,2 ± 0,7	10,3 ± 6,6	21,6 ± 13,0	2,5 ± 1,2	0,2 ± 0,2	0,3 ± 0,2
K360	MC	7,8 ± 2,8	7,3 ± 3,1	13,7 ± 4,9	2,2 ± 1,1	0,3 ± 0,2	0,3 ± 0,2
K360	M_6C	1,0 ± 0,7	0,8 ± 0,7	1,3 ± 1,3	1,7 ± 0,7	0,4 ± 0,3	0,9 ± 0,3
UNIVERSAL	M_7C_3	8,4 ± 3,1	7,5 ± 3,2	16,3 ± 7,7	2,5 ± 0,1	0,2 ± 0,2	0,2 ± 0,2
UNIVERSAL	MC	9,2 ± 3,1	8,7 ± 4,9	14,4 ± 5,8	2,0 ± 0,9	0,3 ± 0,2	0,4 ± 0,2
HWS	M_7C_3	1,3 ± 0,4	1,1 ± 0,4	1,6 ± 0,5	1,4 ± 0,3	0,6 ± 0,2	0,8 ± 0,1
HWS	MC	0,6 ± 0,2	0,5 ± 0,2	0,7 ± 0,3	1,3 ± 0,3	0,6 ± 0,2	0,8 ± 0,1
HWS	M_6C	0,3 ± 0,1	0,3 ± 0,1	0,4 ± 0,2	1,2 ± 0,2	0,7 ± 0,2	0,8 ± 0,1

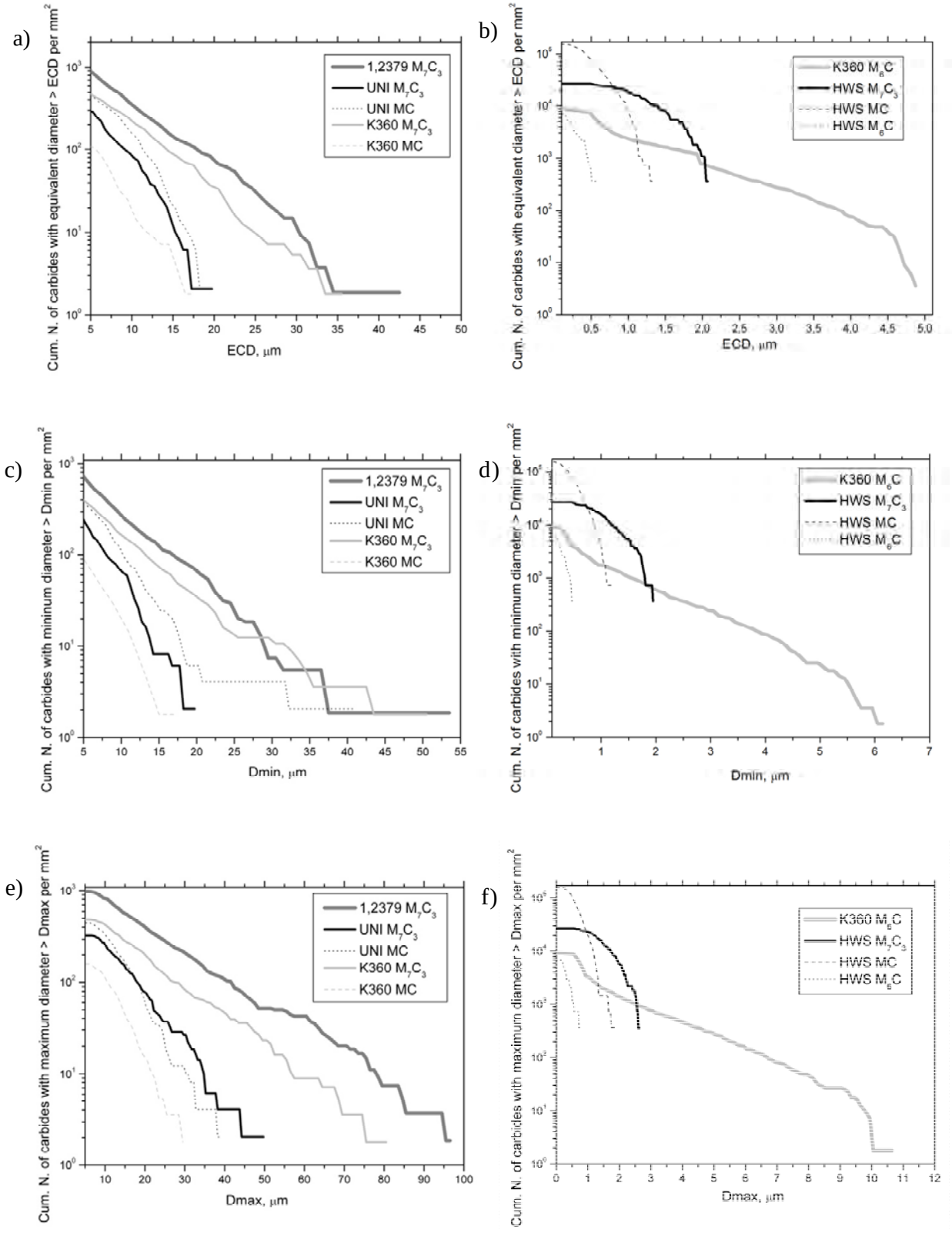

Figure 3.1.3 Size distribution of primary carbides in terms of the cumulative number of carbides with equivalent diameter, minimum diameter and maximum diameter larger than a certain: a) - b) *ECD*, c) - d) D_{min} and e) - f) D_{max}, plotted vs *ECD*, D_{min} and D_{max} respectively. a), c) and e) M_7C_3 carbides of 1.2379, M_7C_3 and MC carbides of UNIVERSAL and M_7C_3 and MC of K360; b), d) and f) M_6C carbides of K360 and M_7C_3, MC and M_6C carbides of HWS

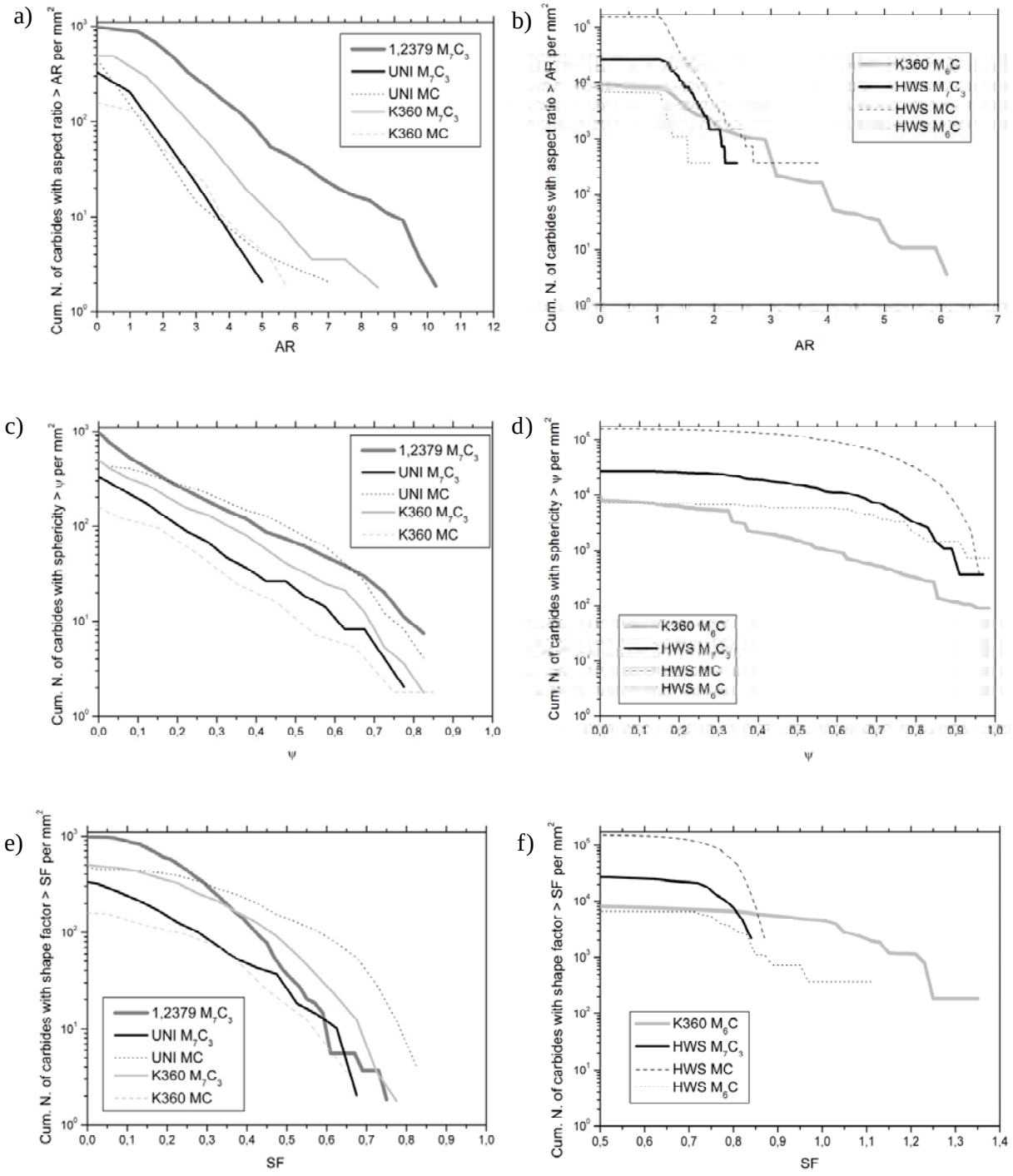

Figure 3.1.4 Geometry distribution of primary carbides in terms of the cumulative number of carbides with aspect ratio, sphericity and shape factor larger than a certain a) – b) *AR*, c) – d) *ψ* and e) – f) *SF*, plotted vs *AR*, *ψ* and *SF* respectively. a), c) and e) M_7C_3 carbides of 1.2379, M_7C_3 and MC carbides of UNIVERSAL and M_7C_3 and MC of K360; b), d) and f) M_6C carbides of K360 and M_7C_3, MC and M_6C carbides of HWS

1.2379 shows the largest carbide sizes while HWS presents the smallest carbides amongst the studied steels. M_7C_3 carbides in K360 are very close in terms of size to those of 1.2379, while those of UNIVERSAL are smaller than these two. However, MC carbides of UNIVERSAL have larger sizes than the MC of K360. M_6C carbides of K360 are markedly smaller than the M_7C_3 and MC which are also embedded in this steel. Carbides in HWS show very small sizes (from 0,5 to 2 μm) and the M_7C_3 are the largest, followed by the MC and finally, the M_6C.

The distribution of morphology parameters suggests that carbides embedded in 1.2379 have the most irregular and elongated shapes. M_7C_3 carbides of K360 show similar morphology distributions to these, while M_7C_3 carbides of UNIVERSAL are more regular and rounded than the previous ones. MC carbides of UNIVERSAL are the most spherical amongst the ingot cast steels and they have also the highest sphericity values. M_6C of K360 are quite round compared to the other two in this steel. Finally, carbides of HWS are almost like perfect spheres.

3.1.2 Metallic matrix

The metallic matrix of tool steels generally consists of a tempered martensitic microstructure with a very fine dispersion of secondary carbides, precipitated as a result of secondary hardening heat treatment. An in-depth characterization of the secondary carbides in the UNIVERSAL steel was performed by CTM and UPC within the frame of the FORMA0 project using TEM and EBSD. The results of this investigation are summarized in this section in order to have more knowledge about the microstructural features of this steel for further comprehension of its micromechanical response.

The microstructure was found to be 100 % martensitic with a BCC crystal lattice. Four different types of secondary carbides could be mainly identified using TEM and classified attending to their average chemical composition, as detailed in Table 3.1.3.

- Type A (Fe-Cr): it corresponded to the most encountered carbide in the steel and although their chemical composition was rather broad. These carbides showed the common characteristic that Fe was the main forming element but always with the presence of some Cr. In Figure 3.1.5 a) it can be observed that these carbides had an irregular morphology with a broad distribution of sizes. In spite of their chemical composition, they seemed to better agree with typical crystal lattices observed in chromiun carbides (hexagonal or cubic) than in cementite-type iron carbides. Then, some carbides were found to be accurately described by FCC lattices, with a $Cr_{23}C_6$ pattern and an interatomic distance, *a*, of 10,65 Å. Other carbides were better described by hexagonal lattices, $(Cr,Fe)_7C_3$ where $a = b = 13{,}98$ Å and c is 4,52 Å.
- Type B (Cr): in this carbides Cr was clearly the main forming element, even though V was present in small percentages. Type B was observed in rounded shapes with diameters varying between 200

and 800 nm (Figure 3.1.5 b)). The crystal lattice was well described as orthorhombical and compatible with Cr_7C_3 where a = 7,01 Å, b = 12,14 Å and c = 4,52 Å.

- Type C (V): these carbides were particularly rich in V even though Cr and small quantities of Mo and W were also found in the chemical composition. Many of them showed diameters higher than 500 nm (Figure 3.1.5 c)), but some others were larger than 1 μm. They were associated to MC structures with FCC lattices.

- Type D (W): in this group W was the main forming carbide element but some of them also showed important contents of Mo. The size of these carbides was about 500 nm (Figure 3.1.5 d)) and they were described by M_6C structures, but no references could be found to identify their space group.

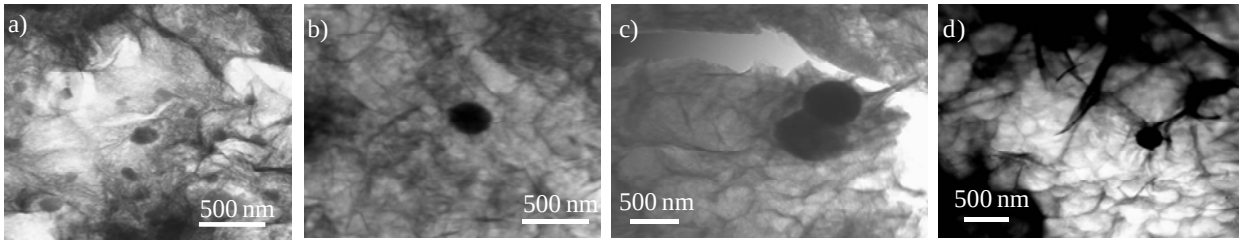

Figure 3.1.5 TEM micrographies of the identified secondary carbides in the UNIVERSAL steel matrix: a) type A (Fe-Cr); b) type B (Cr); c) type C (V) and d) type D (W)

Table 3.1.3 Classification of secondary carbides in UNIVERSAL steel

Type	Chemical composition (at. %)	Space group	Structure type	Reference
A (Fe-Cr)	Fe: 90 ± 10 Cr: 10 ± 15	$Fm\bar{3}m$	$Cr_{23}C_6$	[BOW72]
	Fe: 95 ± 10 Cr: 3 ± 5 W: 2 ± 0	$P6_3mC$	$(Cr,Fe)_7C_3$	[BAU81]
B (Cr)	Cr: 80 ± 5 V: 18 ± 4 Fe: 3 ± 3	$Pnma$	Cr_7C_3	[KAY96]
C (V)	V: 83 ± 2 Cr: 13 ± 2 Mo: 2 ± 0 W: 2 ± 1	$Fm\bar{3}m$	VC	[NOW47]
D (W-Mo)	W: 83 ± 13 Mo: 12 ± 9 Cr: 6 ± 2 V: 4 ± 1	-	M_6C	-

A local quantification of the secondary carbides identified in the UNIVERSAL steel matrix was carried out using EBSD. In this case only two different carbides could be identified: a first type was softer and stayed at the same plane of the matrix while the other was harder and slightly stood out. They could be associated to the Cr_7C_3 (B type (Cr)) and VC (C type (V)) respectively, as listed before. The study was performed locally and a 82,3 % total indexation was obtained, with 74,66 % of martensite (in red in Figure 3.1.6), 0,85 % Cr_7C_3 (in blue in Figure 3.1.6) and 2,11 % to VC (in yellow in Figure 3.1.6).

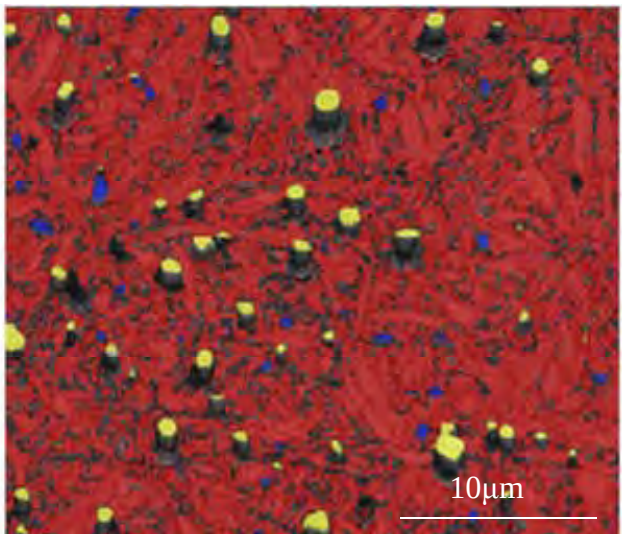

Figure 3.1.6 Results of the EBSD local indexation of the UNIVERSAL steel matrix

The chemical composition of the metallic matrix is presented in Table 3.1.4 for 1.2379, K360, UNIVERSAL and HWS. In all cases, the main alloying element detected at the matrix is Cr with a percentage of 6,5 % in K360, 6,8 % in UNIVERSAL, 6,9 % in HWS and 7,5 % in 1.2379. UNIVERSAL and HWS show very similar compositions, as expected since their initial chemical compositions are the same (see Table 2.1.1). UNIVERSAL and HWS show slightly higher percentages of V and Si than 1.2379 and K360, but K360 has the highest Mo and Al contents.

Table 3.1.4 Chemical composition (in wt %) of the matrix in 1.2379, K360, UNIVERSAL and HWS

Tool Steel	Chemical composition (wt %)					
	Al	Si	V	Cr	Fe	Mo
1.2379	0,07	0,41	0,20	7,57	91,08	0,68
K360	0,89	1,09	0,51	6,55	88,86	2,10
UNIVERSAL	0,17	1,57	0,84	6,96	89,05	1,42
HWS	0,20	1,75	0,75	6,79	89,04	1,45

3.2 Influence of the microstructure on the macro- and micro-mechanical properties of tool steels

3.2.1 Macro-mechanical properties

3.2.1.1 Fracture strength, σ^R

Figure 3.2.1 shows the average σ^R of 1.2379, UNIVERSAL and HWS D1, D2 and D3, and K360 D1 and D2 (no D3 samples could be tested). σ^R of 1.2379, UNIVERSAL and K360 D2 is significantly higher than D1 and D3, while HWS shows very similar fracture behaviours in all three configurations. These results are in agreement with the microstructures that have been observed in these steels. As described in section 3.1.1.1, ingot cast steels are rather anisotropic due to their marked carbide fibre orientation while PM steels are more isotropic, as expected after its very fine and homogeneous carbide distribution. HWS shows the highest σ^R results amongst the studied materials (σ^R is around 4400 MPa). UNIVERSAL has higher σ^R values than K360 and 1.2379, and in addition UNIVERSAL D1, D2 and D3 show less difference than K360 and 1.2379 D1, D2 and D3. 1.2379 in turn, has the lowest and the most anisotropic fracture results.

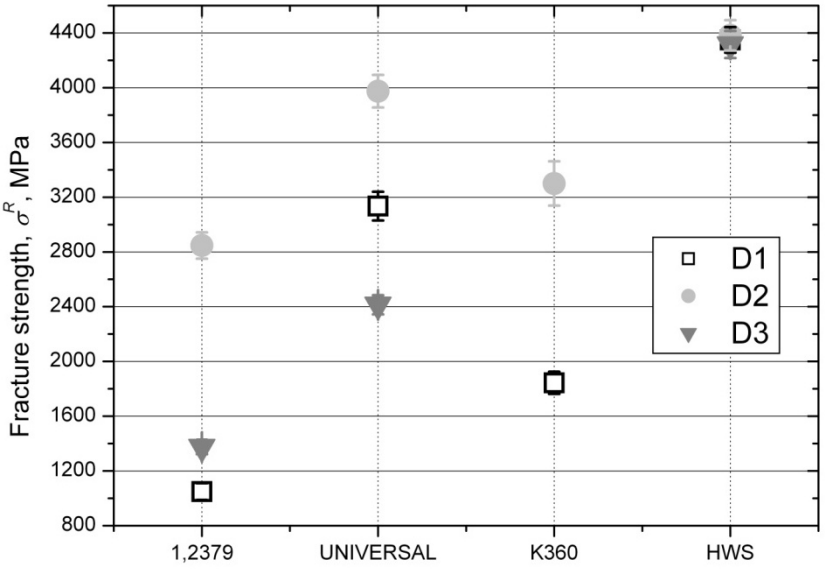

Figure 3.2.1 Fracture strength, σ^R, of 1.2379, UNIVERSAL and HWS in D1, D2 and D3, and K360 D1 and D2

Weibull statistics was used to evaluate fracture strength results by means of the following equation:

$$P = 1 - e^{-\left(\frac{\sigma}{\sigma_0}\right)^m} \tag{3.2.1}$$

where P is the probability of failure at a given stress level, σ, and m and σ_0 are respectively the Weibull modulus and the reference strength. P was estimated through the ratio $n/(N+1)$, where n is the position of

a given experimental result in a classification of strengths (ordered from the lowest to the highest), and N and is the total number of tested specimens. For each sample, *Ln(1/(1-P))* was calculated and plotted versus the correspondent σ value, as shown in Figure 3.2.2. By linear regression of the probability distribution, m and σ_0 were estimated for each material and configuration and they are listed in Table 3.2.1.

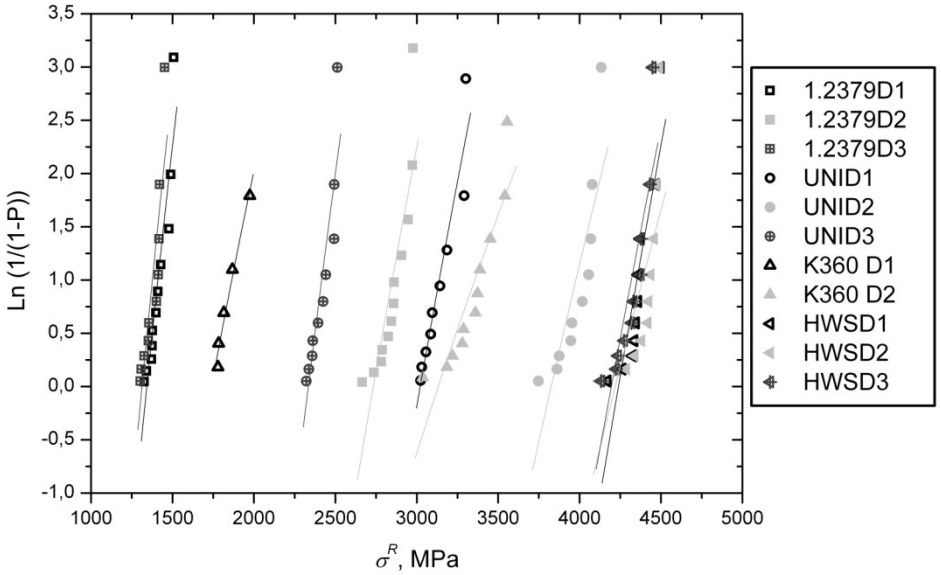

Figure 3.2.2 Weibull probability of failure, *P*, expressed in terms of *Ln((1/1-P))* vs σ^R

Table 3.2.1 Weibull parameters, *m* and σ_0

	D1		D2		D3	
	m	σ_0	m	σ_0	m	σ_0
1.2379	27	1437	36	2889	30	1399
UNIVERSAL	33	3187	40	4027	40	2446
K360	18	1932	21	3410	-	-
HWS	55	4392	46	4433	52	4359

The Weibull modulus, m, indicates the nature, severity and dispersion of flaws in a material. 1.2379, UNIVERSAL, K360 and HWS show high m values (what is typical for hardened steels) meaning that there is a small variability in the measured strength of the tested specimens. Hence, σ^R results are a good description of the sample-to-sample performance.

For most metals m is over 20 while for ceramics it is usually less than 10. Despite consisting in a composite of ceramic (carbide particles) in a metallic matrix, these small brittle phases do not influence sufficiently the variability of σ^R in tool steels since their m values are typical for metals. The highest m values are obtained in HWS, followed by UNIVERSAL and 1.2379. The fact that K360 shows the lowest m values may be due to the lower number of samples of this material that were available for testing. As the distribution of fracture strength is rather narrow, σ_0 values are very close to the average σ^R presented in Figure 3.2.1.

Fracture initiation sites of D1 and D3 samples could not be clearly identified because the fracture took place in such brittle-like manner (by coalescence of cracks initiated in multiple sites) that a single propagation path could not be observed. However, in D2 samples fracture origins were easily distinguished in the surface and they started from primary carbides, or agglomerates of them, as shown in Figure 3.2.3 a) 1.2379, b) UNIVERSAL and c) K360. However and despite the halos indicating the site for failure origin in HWS samples (Figure 3.2.3 d)), no specific nucleation site could be detected. Likely the presence of carbide agglomerates in the initiation sites could have explained the nucleation of cracks, as well as the presence of inclusion particles.

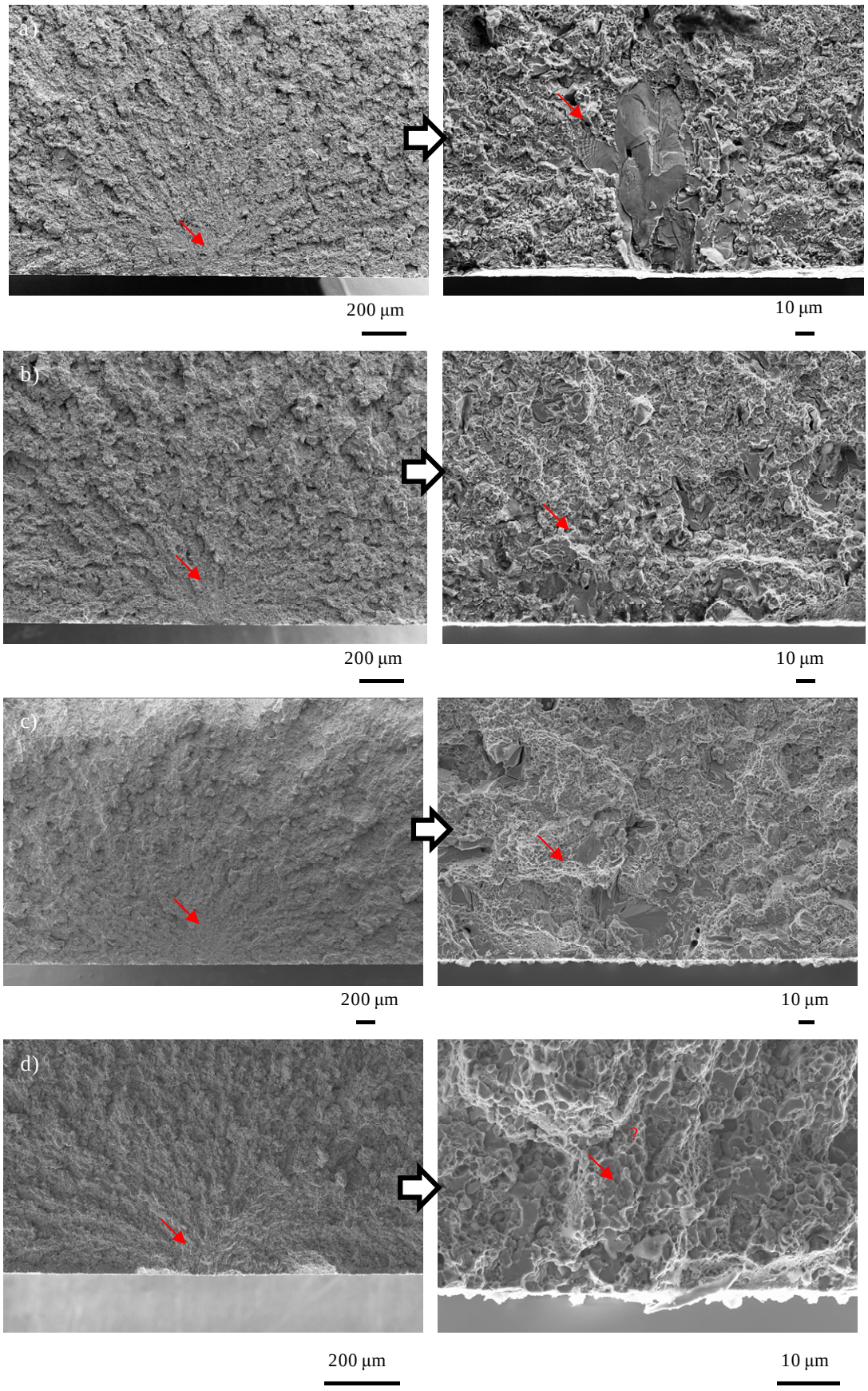

Figure 3.2.3 Fracture initiation sites in D2 samples of a) 1.2379; b) UNIVERSAL; c) K360 and d) HWS. Red arrows indicate the presence of primary carbides at failure origins

3.2.1.2 Fatigue limit, $\Delta\sigma^{fat}$

Figure 3.2.4 shows the fatigue limit, $\Delta\sigma^{fat}$, of 1.2379, UNIVERSAL and HWS D1, D2 and D3, and K360 D1 and D2. HWS presents the highest $\Delta\sigma^{fat}$ but it also shows high scattering of results. 1.2379, UNIVERSAL and K360 D2 show similar $\Delta\sigma^{fat}$ values, even though UNIVERSAL D1 and D3 are much higher than 1.2379 and K360 D1 and D3. Once again UNIVERSAL D1, D2 and D3 show less difference than 1.2379 and K360 D1, D2 and D3.

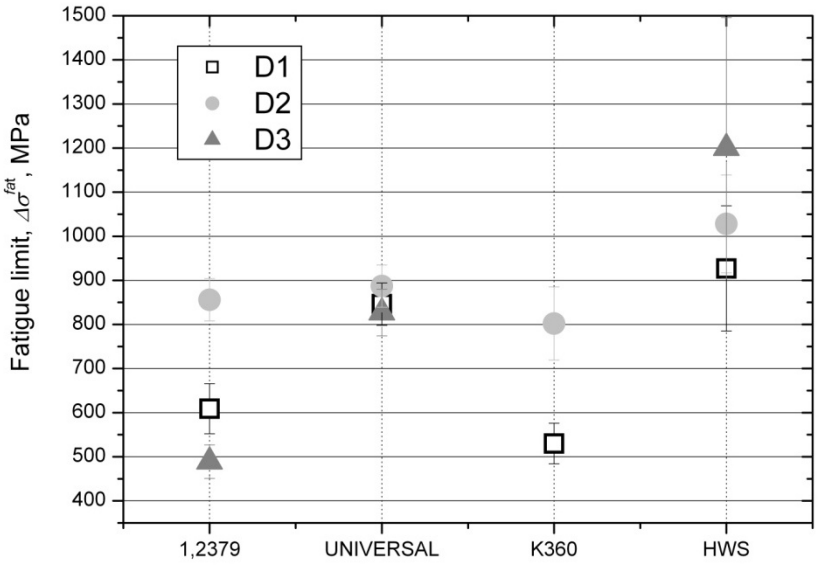

Figure 3.2.4 Fatigue limit, $\Delta\sigma^{fat}$, of 1.2379, UNIVERSAL and HWS in D1, D2 and D3, and K360 D1 and D2

Although these four materials show rather different fracture behaviours (see Figure 3.2.1), in fatigue these differences are reduced. Hence, it makes sense to talk about the fatigue sensitivity of these steels. The notion of fatigue sensitivity refers to the loss of strength with the increase of the number of cycles and in case of ceramics, it is typically very low. In contrast, fatigue sensitivity of metals is rather high, especially if they are very ductile. The ratio $\Delta\sigma^{fat}/\sigma^{R}$ is a common measure of fatigue sensitivity: if $\Delta\sigma^{fat}/\sigma^{R} = 1$ there is no fatigue sensitivity, but if $0 < \Delta\sigma^{fat}/\sigma^{R} < 1$ then the strength of the material is certainly reduced with the number of cycles (i.e. the material shows fatigue sensitivity). Table 3.2.2 shows the ratio $\Delta\sigma^{fat}/\sigma^{R}$ for 1.2379, UNIVERSAL, K360 and HWS and it can be observed that, generally speaking, ingot cast steels have superior $\Delta\sigma^{fat}/\sigma^{R}$ ratios than HWS and therefore, they present lower fatigue sensitivities.

Table 3.2.2 Fatigue sensitivity expressed in terms of the ratio between $\Delta\sigma^{fat}/\sigma^{R}$

$\Delta\sigma^{fat}/\sigma^{R}$	D1	D2	D3
1.2379	0,48	0,33	0,39
UNIVERSAL	0,27	0,22	0,34
K360	0,29	0,24	-
HWS	0,21	0,23	0,25

In this case, fracture initiation sites are clearly distinguished in D1, D2 and D3 configurations since a smooth zone at the fracture surface is created as a consequence of the stable crack propagation before failure. Primary carbides are identified at the failure initiation sites of 1.2379, UNIVERSAL and K360 samples (Figure 3.2.5). In some cases these carbides present defects, such as pores or shrinkages, which would trigger their fracture. Only M_7C_3 carbides are observed to have triggered fracture of UNIVERSAL samples, while in K360 even though M_7C_3 carbides are mainly observed, some MC carbide (as that shown in Figure 3.2.5 c)) is also identified.

Failure initiation sites of HWS are related to the presence of inclusion particles with large sizes compared to the primary carbides embedded in the microstructure (Figure 3.2.5 d)), as PM steels typically show crack origins at inclusion particles. Some of these inclusions are round, but some others are more irregular or elongated. Fracture is caused either by surface or internal inclusions, but under no circumstances primary carbides are detected at the failure origins. The EDX analysis of these inclusions revealed that they consist in silicon and aluminium oxides. Very likely the presence of inclusions can explain the wide scattering of fatigue results observed in Figure 3.2.4. The resistance to fatigue of HWS samples depended on the probability that one inclusion was located at the most stressed region (and on if it had the required shape and size so as to nucleate a crack at the applied stress level).

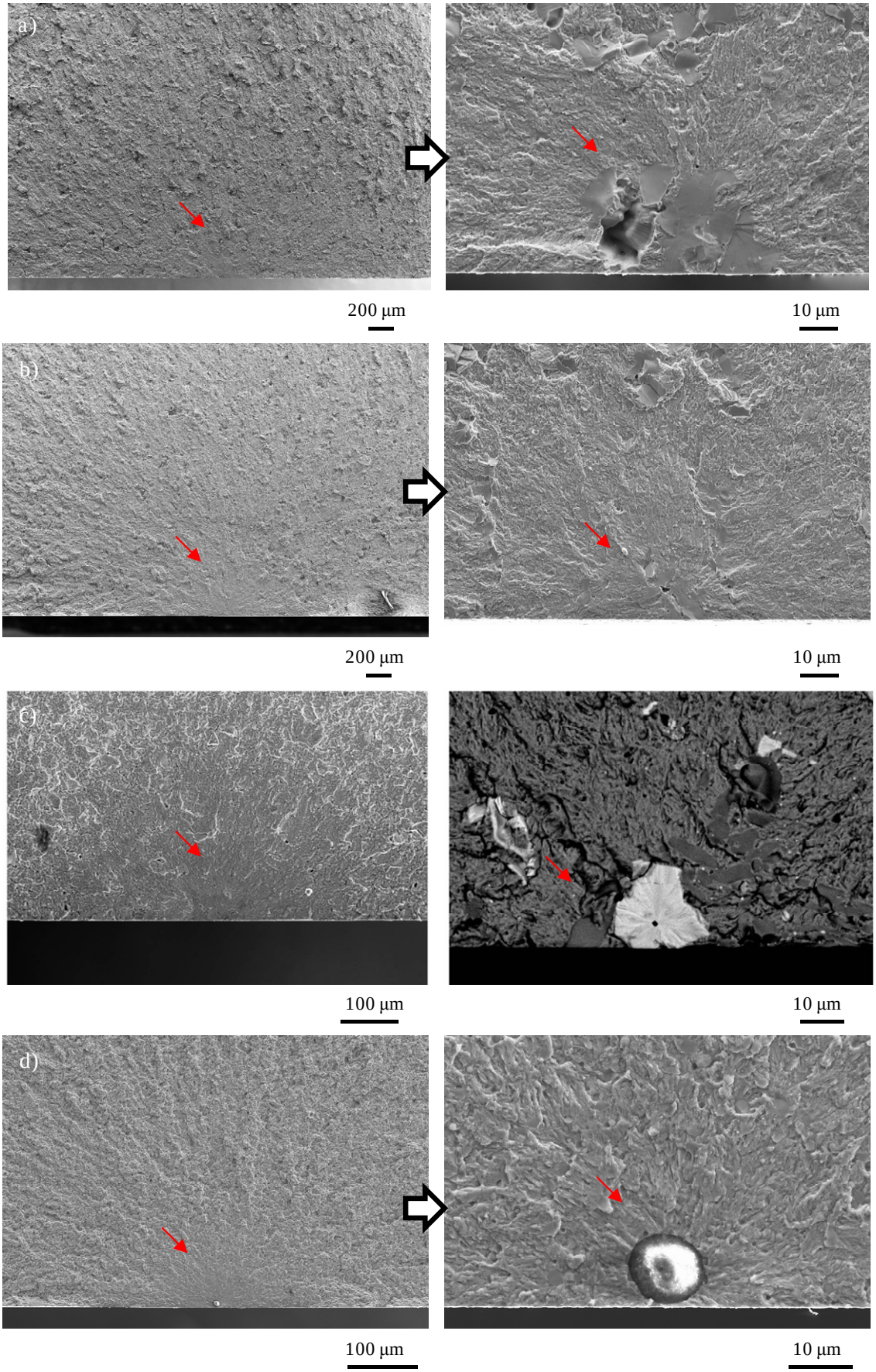

Figure 3.2.5 Fatigue initiation sites in D2 samples of a) 1.2379; b) UNIVERSAL; c) K360 and d) HWS. Red arrows indicate the presence of primary carbides and inclusions at failure origins

In ingot cast steels, failure both under monotonic and cyclic conditions is initiated from breakage of primary carbides, or agglomerates of these. They are heterogeneously dispersed in the metallic matrix forming bands and the failubre initiation sites are in carbide rich-layers where the metallic matrix has locally low volume fractions. As primary carbides are hard ceramic particles, in principle, they are assumed to not loose strength in fatigue. Therefore, they may be expected to fail in fatigue at the same stress ranges as in fracture. On the contrary and although the presence of inclusions in HWS is rather random, inclusions trigger the failure under cyclic conditions since they introduce discontinuities in terms of stress and strain distributions in the matrix. Under repetitive loading, these discontinuities may have such a detrimental effect that the matrix is damaged at much lower applied stresses than under monotonic loads.

As it follows from the explanation above, if failure in ingot cast steels is dictated by primary carbides (ceramic-like phases) while in HWS it is governed by damage in the matrix near inclusions, then it is plausible to understand that the fatigue sensitivity in terms of $\Delta\sigma^{fat}/\sigma^{R}$ of ingot cast steels compared to HWS is closer to 1.

Similar arguments account for the behaviour of D1, D2 and D3 configurations of ingot cast steels. The dispersion of carbides in D1 and D3 with respect to the load axis triggers a rapid coalescence and growth of cracks through carbide bands. But in D2, once carbides (or carbides agglomerates) have failed, cracks have to propagate through the matrix bands before attaining the critical size for fracture. That explains why in D2, σ^{R} is the highest (as cracks have to grow through the tougher metallic matrix before attaining the critical size for failure), but it also accounts for the loss of strength with the number of cycles (since the metallic counterpart in D2 is further involved in the fracture mechanism than in D1 or D3). Then it is reasonable that the lowest $\Delta\sigma^{fat}/\sigma^{R}$ ratios in 1.2379, UNIVERSAL and K360 are observed in D2, and that UNIVERSAL D1, D2 and D3 ratios show less difference than 1.2379 and K360 D1, D2 and D3 since the microstructure of UNIVERSAL is more homogeneous in all directions than 1.2379 or K360.
While in all the fractured specimens of 1.2379 and UNIVERSAL failure initiation sites are located at the surface, in K360 some surface and subsurface crack origins were identified, as shown in Figure 3.2.6. (Note: this figure plots the results of the staircase method in terms of stress vs number of cycles for a better interpretation of the results, but under no circumstances these diagrams can be used as real S-N curves of these materials. The black straight lines are only indicative of the S-N behaviour even though they fit with rather good accuracy to the results of the staircase).

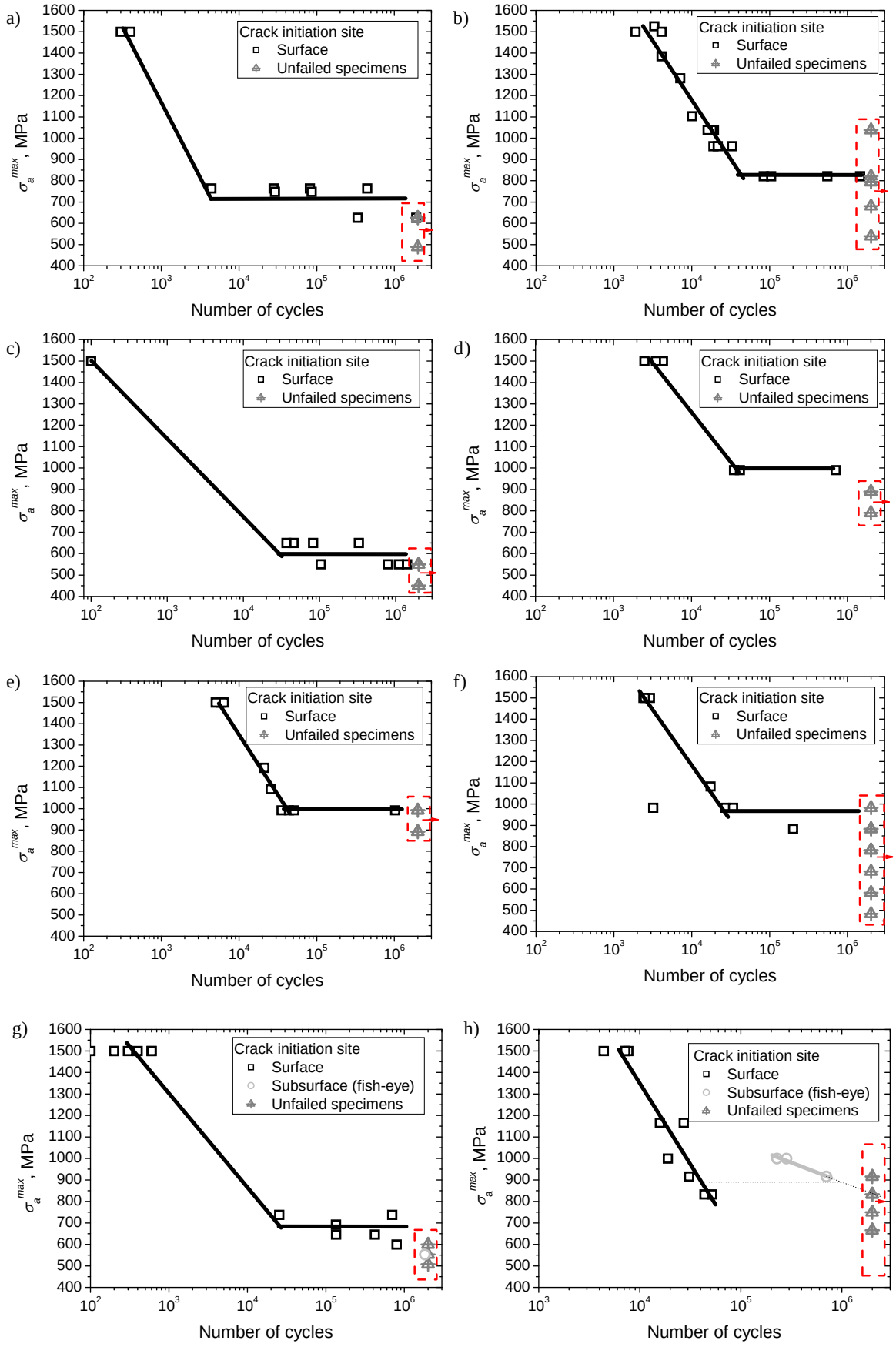

Figure 3.2.6 Maximum applied stress, σ_a^{max}, vs the number of cycles for the specimens tested in the staircase method to determine $\Delta\sigma^{fat}$: a) 1.2379 D1; b) 1.2379 D2; c) 1.2379 D3; d) UNIVERSAL D1; e) UNIVERSAL D2; f) UNIVERSAL D3; g) K360 D1 and h) K360 D2

At the high cycle fatigue regime of $2 \cdot 10^6$ cycles, 1.2379 and UNIVERSAL show governing surface crack mode. But as shown by Sohar et al. [SOH08], subsurface crack mode in 1.2379 appears beyond the 10^6-10^7 cycles. Alternatively, at the same regime of $2 \cdot 10^6$ cycles K360 D2 (Figure 3.2.6 h)) shows a "duplex S-N curve" similar to that reported in the work of Shiozawa et al. at VHCF regimes [SHI01]. These authors attributed these two different behaviours to different fracture modes: the first one occurring at high stress amplitude level and low number of cycles, is governed by surface fractures as a result of the surface crack initiation and growth; the second appears at high number of cycles and is governed by internal crack initiation and growth.

In K360, primary carbides are always found at the failure initiation sites of surface crack origins (as shown in Figure 3.2.7 a)) while fish-eye patterns around primary carbides are identified in case of subsurface crack origins (Figure 3.2.7 b)).

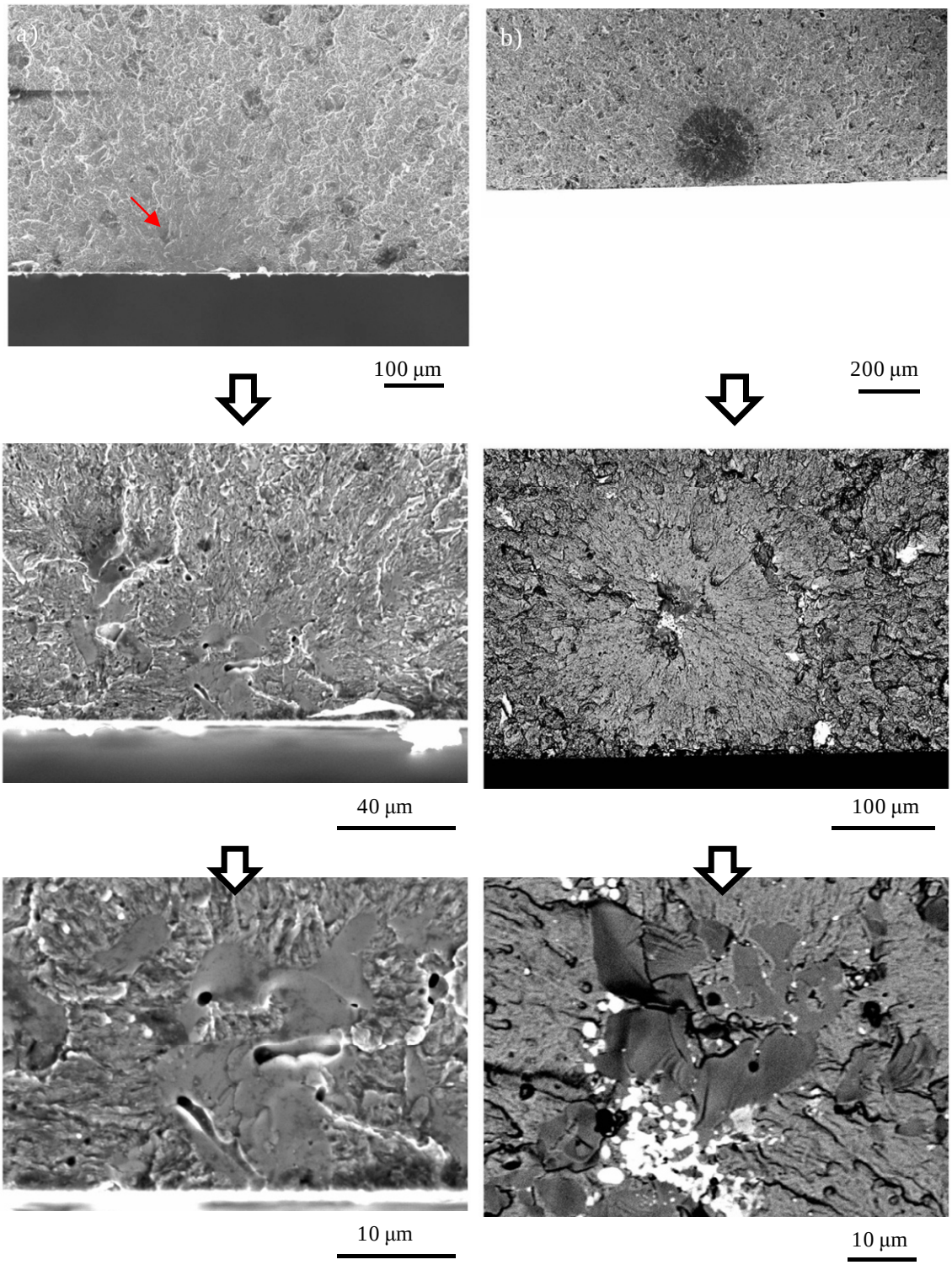

Figure 3.2.7 SEM observations of the fracture initiation sites in K360 D2: a) surface crack initiation at low number of cycles and b) internal crack initiation forming fish-eye at higher number of cycles

Interestingly, it seems that at the regime of $2 \cdot 10^6$ cycles K360 presents a duality of stress and number of cycles caused by two competing occurrences of surface and subsurface fatigue failure modes which practically overlap. It is typically reported that the fracture mechanism shifts from surface to subsurface decreasing the applied stress level or consequently, when the number of cycles increases. The reason for this modification of the failure mode has been linked to factors including environment, residual stresses, hardened layers and surface roughness, loading types and inclusion or carbide sizes [SHI02].

Roughness profiles in the fish-eye of subsurface mode cracked specimens were measured using confocal microscopy, as shown in Figure 3.2.8. Roughness variations in the fracture surface are observed in all samples and could be attributed to different mechanisms related both to the microstructure of the material and the propagation rate. Cracks initiated at the carbide cluster (Figure 3.2.9) propagated outside this area forming a smooth fracture surface in the fish-eye region, to finally turn to a rough surface prior to final fracture.

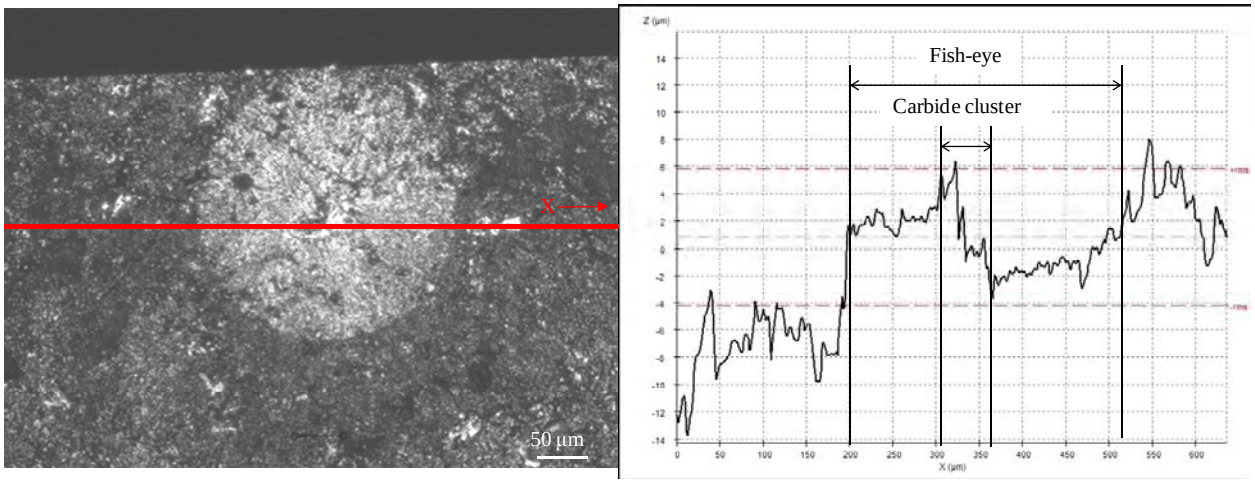

Figure 3.2.8 Surface roughness along the red line on the fracture surface of a specimen showing subsurface failure mode

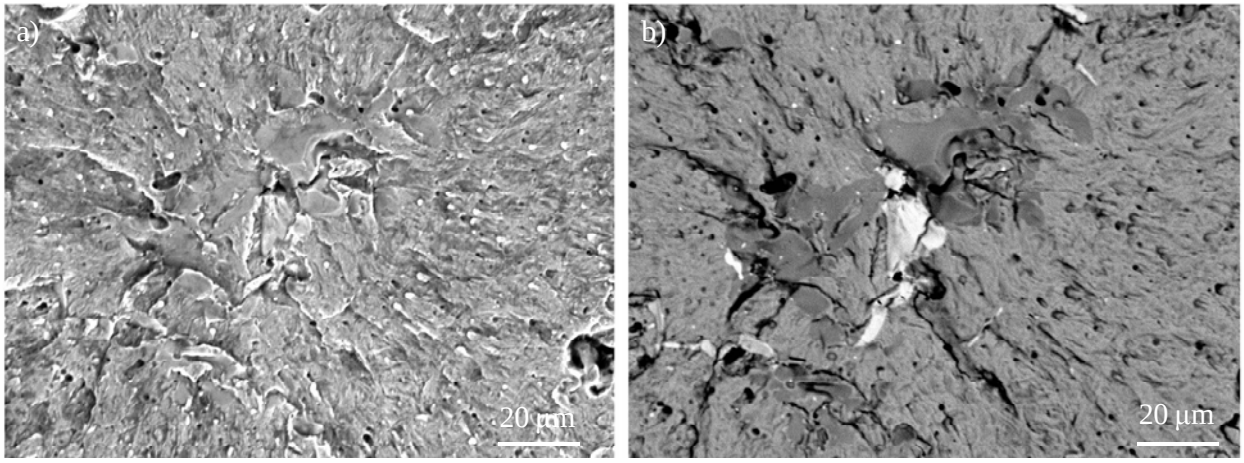

Figure 3.2.9 SEM observations of the crack initiation site at the centre of the fish-eye: a) secondary electron and b) back scatter images

3.2.1.3 Fracture toughness, K_{IC}

Fracture toughness, K_{IC}, of 1.2379, UNIVERSAL and HWS D1, D2 and D3, as well as K6360 D2, are presented in Figure 3.2.10. As it can be observed, ingot cast steels have a higher K_{IC} than HWS, as it was expected according to the work of Horton and Child [HOR83]. 1.2379, UNIVERSAL and K360 show K_{IC} values comprised between 20 and 30 MPa·m$^{1/2}$ depending on the sample configuration, while HWS has a K_{IC} around 20 MPa·m$^{1/2}$. Horton and Child attributed such differences to the less mean free path between carbides in PM than in ingot cast steels. After the work of these authors, in PM steels microcracks nucleated in carbides link up with a minimum of plastic deformation of the matrix, owing to the smaller ligament sizes compared to ingot cast steels.

K_{IC} of HWS has almost the same value in D1, D2 and D3 while 1.2379 and UNIVERSAL D2 show markedly higher results than D1 and D3. K_{IC} is higher in D2 because in this configuration cracks run perpendicular to the carbide fibre and thus, they must propagate across matrix bands. On the contrary, in D3 cracks easily run along a carbide band and K_{IC} is the lowest. Although only D2 specimens of K360 could be tested, similar K_{IC} values to 1.2379 are expected for D1 and D3 configurations of this steel.

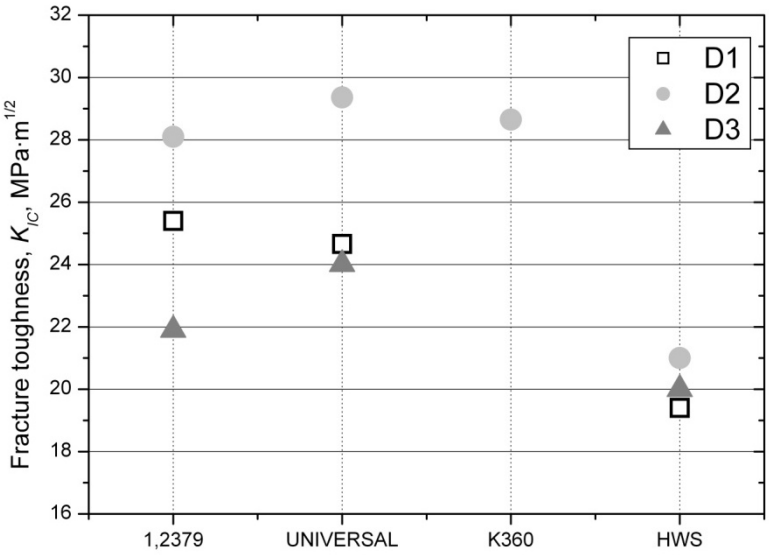

Figure 3.2.10 Fracture toughness, K_{IC}, of 1.2379, UNIVERSAL and HWS in D1, D2 and D3, and K360 D2

3.2.1.4 Fatigue crack propagation threshold, ΔK_{TH}

Fatigue crack propagation threshold, ΔK_{TH}, of 1.2379, UNIVERSAL and HWS D1, D2 and D3, as well as K360 D2, are presented in Figure 3.2.11. All ΔK_{TH} values are comprised between 3 and 5 MPa·m$^{1/2}$ and this range is typical of metallic materials with hardness levels similar to those of this Thesis.

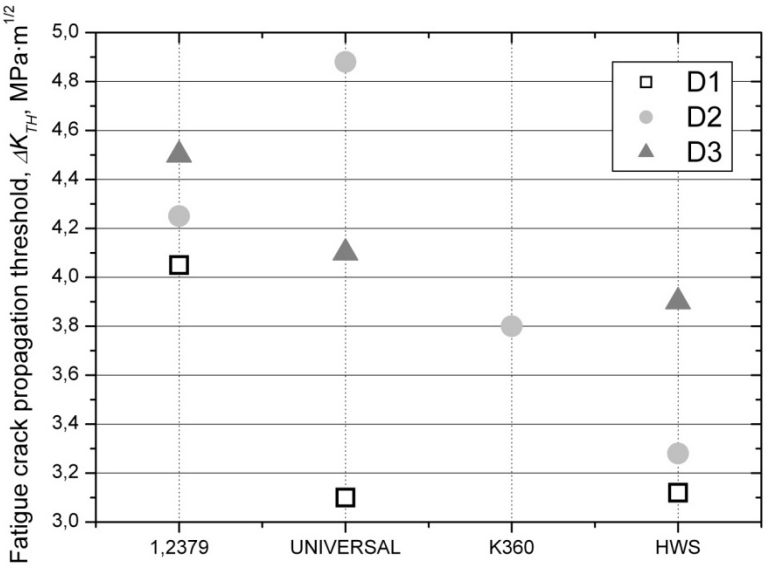

Figure 3.2.11 Fatigue crack propagation threshold, ΔK_{TH}, of 1.2379, UNIVERSAL and HWS in D1, D2 and D3, and K360 D2

The fitting parameters of the Paris curve, *A* and *m*, are presented in Table 3.2.3 and show typical values of metals, too. The physical meaning of the *m* parameter stands for the speed of the crack propagation in the linear Paris regime, i.e. the higher the *m* value, the steeper the slope and the faster the propagation in the stable stage.

Table 3.2.3 Fitting parameters of the Paris curve *A* and *m*

	D1		D2		D3	
	m	*Log A*	*m*	*Log A*	*m*	*Log A*
1.2379	3,4	-11,3	3,1	-11,2	4,6	-12,5
UNIVERSAL	5,1 ± 0,1	-12,2 ± 0,1	4,4 ± 0,5	-12,2 ± 0,5	5,2 ± 0,4	-12,4 ± 0,3
K360	-	-	4,7 ± 0,3	-12,5 ± 0,2	-	-
HWS	8,0 ± 0,9	-13,8 ± 0,6	5,9 ± 0,5	-12,8 ± 0,3	2,8 ± 0,1	-10,7 ± 0,1

3.2.2 Micro-mechanical properties of primary carbides and metallic matrix in ingot cast steels

3.2.2.1 Mechanical properties of primary carbides

The Young's modulus, *E*, hardness, *H*, and fracture toughness, K_C of primary carbides embedded in 1.2379, UNIVERSAL and K360 are presented in Table 3.2.4. Results corresponding to 1.2379 and UNIVERSAL are taken from the work of Casellas et al. [CAS07], while *E*, *H* and K_C of K360 were determined at CTM using the same procedure as described in [CAS07]. (Note: only mechanical properties of M_7C_3 and MC carbides of K360 are presented, since no fractured M_6C carbides have been observed in fracture nor fatigue tested specimens).

E and *H* of M_7C_3 primary carbides in 1.2379 are higher than the M_7C_3 in UNIVERSAL and K360 but lower than the MC of the same steels. In terms of K_C, Casellas et al. already reported on a marked anisotropy of this property in M_7C_3 carbides of 1.2379. These authors showed that cracks emanating from the indenter corners propagate more easily in the direction parallel to the larger edge of the carbide than perpendicular to that. According to these observations, K_C values calculated from cracks propagating parallel to the carbides large edge were lower than 1 MPa·$m^{1/2}$ while the K_C calculated from cracks which run perpendicular to the carbides larger edge was about 2,3 MPa·$m^{1/2}$. In the present work K_C evaluated in the direction perpendicular to the larger edge of the carbide is presented in Table 3.2.4.

Both the M_7C_3 carbides of UNIVERSAL and K360 did not develop cracks after indentation owing to their lower hardness (14,5 and 15,8 GPa respectively). As discussed by Casellas et al., lowering carbide hardness increases the threshold load for generating cracks from the indentation corners. Taking into account the low sizes of these carbides, the load required to generate cracks with a Berckovich indenter may produce indentation imprints which surpass the carbides and therefore, they are no valid.
The calculation of K_C in MC carbides of UNIVERSAL has led to a wide scatter due to their heterogeneous chemical compositions, i.e. the main alloying elements are distributed within carbides in such a way that V- , Cr- or Mo-rich areas are formed. Different cristallographic features in single carbides are then expected, and that directly affects the behaviour of cracks emanating from the indenter corners. A K_C value of these carbides has been given here only for comparison purposes, since current researches at CTM are still focused in determining it accurately.

Table 3.2.4 Mechanical properties of the primary carbides in 1.2379, UNIVERSAL and K360: Young's modulus, *E*, hardness, *H*, and fracture toughness, K_C

Tool Steel	Carbide	*E*, GPa	*H*, GPa	K_C, MPa·$m^{1/2}$
1.2379	M_7C_3	294 ± 17	18,2 ± 2,4	2,3 ± 0,8[(1)]
UNIVERSAL	M_7C_3	270 ± 18	14,5 ± 2,5	-
UNIVERSAL	MC	315 ± 23	25,7 ± 3,6	3,7 ± 0,6[(2)]
K360	M_7C_3	274 ± 15	15,8 ± 1,8	-
K360	MC	308 ± 49	20,6 ± 5,7	2,5 ± 0,6

(1) K_C evaluated in the direction perpendicular to the larger edge of the carbide in 1.2379 steel

(2) Since different crack behaviours are noticed within one single of the MC carbides in UNIVERSAL, further research is been continuously performed to accurately estimate this value

3.2.2.2 Mechanical properties of the metallic matrix

The mechanical properties (*E* and *H*) of the metallic matrix in 1.2379, UNIVERSAL and K360 were determined and the results are very similar in all three cases, as shown in Table 3.2.5: *E* is about 250 GPa while *H* is around 10 GPa.

Table 3.2.5 Mechanical properties of the metallic matrix in 1.2379, UNIVERSAL and K360: Young's modulus, *E*, hardness, *H*

Tool Steel	*E*, GPa	*H*, GPa
1.2379	249 ± 7	9,7 ± 0,3
UNIVERSAL	251 ± 7	9,7 ± 0,3
K360	254 ± 7	10,0 ± 0,3

3.2.3 Crack nucleation and growth under monotonic load

3.2.3.1 Crack nucleation and growth in ingot cast steels

As previously shown in Figure 3.2.3, fracture initiation sites of 1.2379, UNIVERSAL and K360 are located at primary carbides, or agglomerates of them in samples tested under monotonic loads. In order to understand the mechanisms leading to the nucleation and propagation of small cracks in the microstructure of these steels, this part of the Thesis is focused on the analysis of damage at the tensile surface of specimens subjected to stepwise bending tests.

The failure mechanism of ingot cast steels under monotonic loading consists in the nucleation of cracks from broken primary carbides and growth of these through the microstructure. Thus, a critical applied stress value leading to the breakage of carbides can be determined and related to the onset stress for crack nucleation. This stress value is assumed to correspond to the fracture strength of carbides under monotonic tensile loading, and it is referred as σ^{RC}.

As previously discussed in section 1.2, the reason why carbides break is related with dislocations pin ups and cleavage of the matrix at the interface with carbides. These phenomena are highly influenced by the microstructural features since they determine the amount of stresses magnified at the neighbourhood of carbides, with respect to the stress applied macroscopically [RAM99]. Hence, it must be taken into account that in such heterogeneous microstructures as these of the ingot cast steels, with carbides of different shapes, sizes, morphologies and arrangements, σ^{RC} values can vary quite much from a specimen to another.

In Table 3.2.6 σ^{RC} of 1.2379 and UNIVERSAL D2 and D3 are presented, as well as σ^{RC} of K360 D2. The first broken primary carbides identified in 1.2379 D2 are observed when a stress level of 700 – 900 MPa is applied. However, scarce data are available in the literature to contrast this result. Only the work of Fukaura et al. [FUK04] reported on stresses for carbides fracture in SKD11 steel (which is in basis, a steel equivalent to 1.2379). These authors determined by means of AE that the stress for carbides fracture in SKD11 is approximately 1100 MPa, which is quite similar to σ^{RC} determined for 1.2379. It must be taken into account that even though 1.2379 and SKD11 are equivalent in chemical compositions, applied heat treatments and forging processes may have been different and these are in great part, responsible for the

final shape, size and distribution of primary carbides in ingot cast steels. Hence, it is reasonable that σ^{RC} of 1.2379 does not completely coincide with SKD11.

σ^{RC} of M_7C_3 carbides in UNIVERSAL is higher than in 1.2379 (1300 - 1500 MPa vs 700 – 900 MPa), owing to their smaller and rounder shapes. σ^{RC} of the MC carbides in UNIVERSAL is the highest amongst the studied steels and it is comprised between 1600 and 1800 MPa. MC carbides of UNIVERSAL are smaller than the M_7C_3 and they have more regular and rounder shapes indeed. In addition, their intrinsic mechanical properties are also the highest, as shown in Table 3.2.4.

σ^{RC} of K360 M_7C_3 and MC carbides are 500 – 700 MPa and 1300 – 1500 MPa respectively. The shapes of the M_7C_3 carbides are rather irregular and their size is slightly higher than those of 1.2379 (see Table 3.1.2). The MC carbides are rounder and more regular than the M_7C_3, and that is why they show a higher σ^{RC}.

σ^{RC} of 1.2379 and UNIVERSAL D3 are about 200 – 300 MPa lower than D2. Differences between these values are yet not very important, or they are less important than expected after the significantly higher σ^{R} of D2 compared to D3. (Note: in case of 1.2379 D3, the first inspection was at 800 MPa and a high number of carbides were already fractured. Therefore, σ^{RC} was estimated by calculating the stress acting at the furthest broken carbide with respect to the centre of the sample, where the stress is the highest during the test).

Table 3.2.6 Fracture strength of the primary carbides, σ^{RC}, in 1.2379, UNIVERSAL and K360 D2 and D3

Tool Steel	Carbide	σ^{RC}, MPa (D2)	σ^{RC}, MPa (D3)
1.2379	M_7C_3	700 - 900	500 – 700[(1)]
UNIVERSAL	M_7C_3	1300 - 1500	1000 - 1200
UNIVERSAL	MC	1600 - 1800	1400 - 1600
K360	M_7C_3	500 - 700	-
K360	MC	1300 - 1500	-

(1) σ^{RC} was estimated by calculating the acting stress level at the furthest broken carbide from the central position when 800 MPa had been applied

In Figure 3.2.12 some examples of broken carbides are presented. Figures 3.2.12 a), b) and c) show cracks in carbides of 1.2379 D2 at the applied stress level of 700 MPa. Figures 3.2.12 d) and e) show broken M_7C_3 carbides of UNIVERSAL D2 at 1300 MPa, while Figure 3.2.12 f) show cracked MC carbides of UNIVERSAL D2 at 1600 MPa. Finally, in Figures 3.2.12 g) and h) cracks in M_7C_3 carbides of K360 D2 at 500 MPa can be observed, and in Figure 3.2.12 i) a broken MC carbide at 1300 MPa is shown.

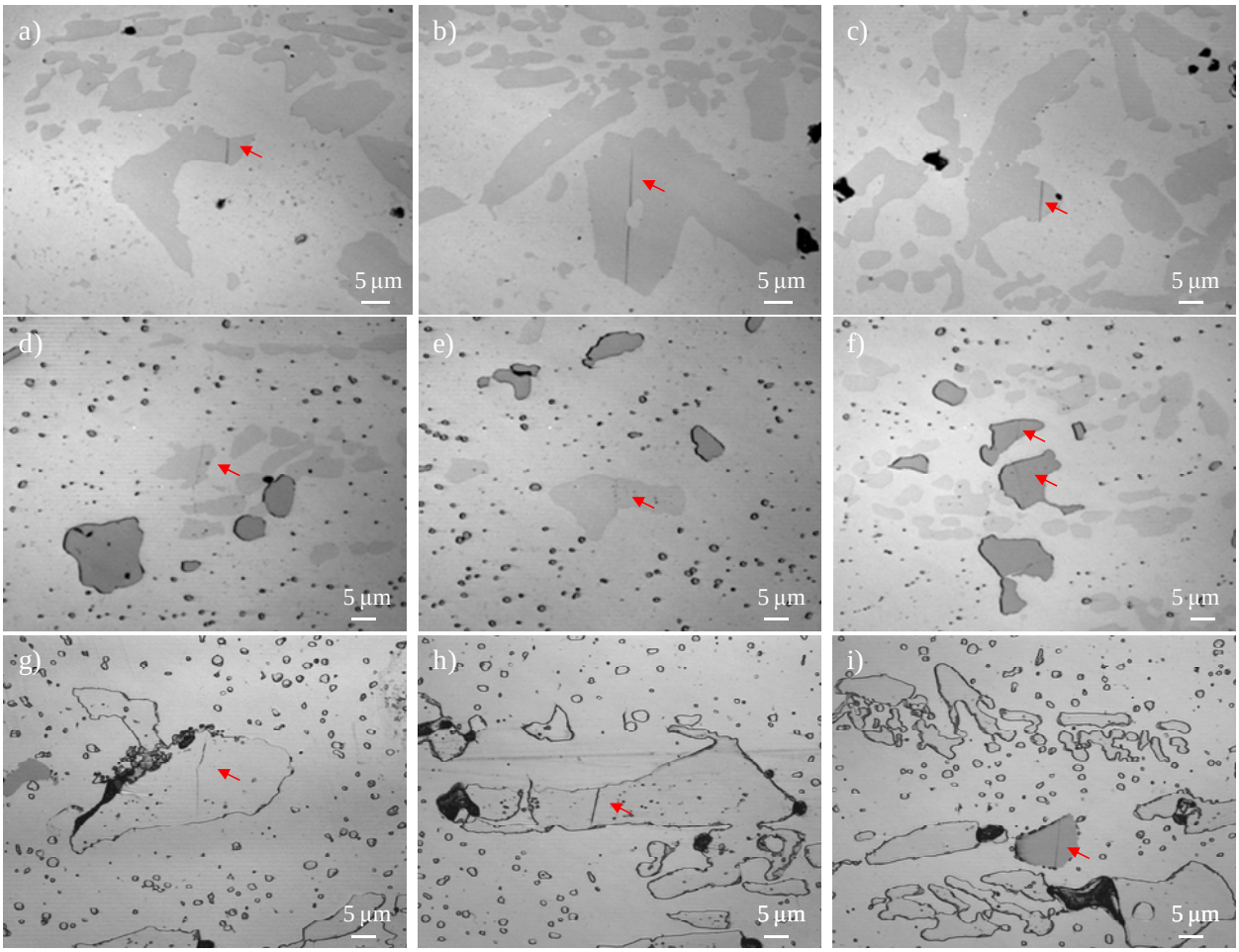

Figure 3.2.12 Broken primary carbides at the surface of D2 specimens tested under monotonic load: a), b) and c) M_7C_3 of 1.2379 at 500 MPa; d) and e) M_7C_3 of UNIVERSAL at 1300 MPa; f) MC of UNIVERSAL at 1600 MPa; g) and h) M_7C_3 of K360 at 500 MPa; i) MC of K360 at 1300 MPa

Figure 3.2.13 presents some of the observed broken carbides in D3 samples. Figures 3.2.13 a), b) and c) in case of 1.2379 at an applied stress of 800 MPa, and in Figure 3.2.13 d) and e) in case of UNIVERSAL M_7C_3 carbides at 1000 MPa. Finally Figure 3.2.13 f) shows MC carbide at 1400 MPa.

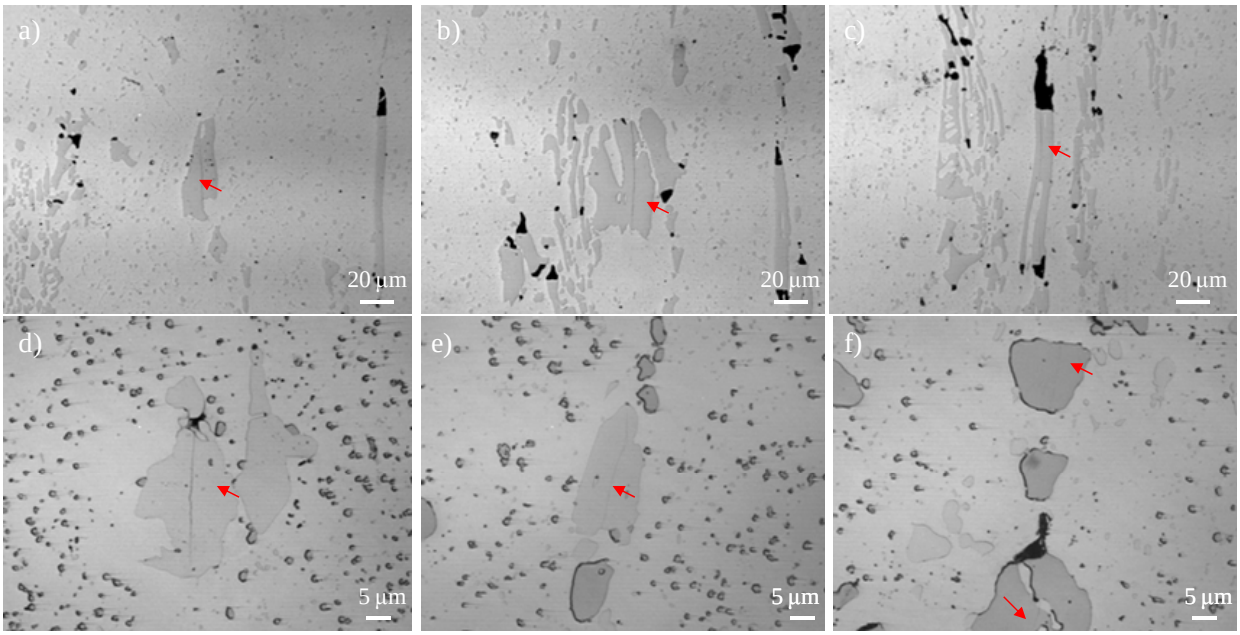

Figure 3.2.13 Broken primary carbides at the surface of D3 specimens tested under monotonic load: a), b) and c) M_7C_3 of 1.2379 at 800 MPa; d) and e) M_7C_3 of UNIVERSAL at 1200 MPa and f) MC of UNIVERSAL at 1400 MPa

In order to help rationalizing D2 and D3 σ^{RC} results, a very simple FE model was developed by the simulation department of CTM. The carbide and the metallic matrix were supposed to be linear elastic with a Young's modulus of 300 and 200 GPa respectively, and the model was axisymmetric. Figure 3.2.14 shows the von Mises stresses at the carbide when a macroscopic applied stress of 1000 MPa is applied. In D2 the stress at the carbide is 1266 MPa (Figure 3.2.14 a)), while in D3 it is 1140 MPa (Figure 3.2.14 b)). In both cases stresses in carbides are slightly higher than the macroscopic applied stress, but none of these results brings any evidence permitting to explain why carbides break at lower applied stresses in D3 than D2.

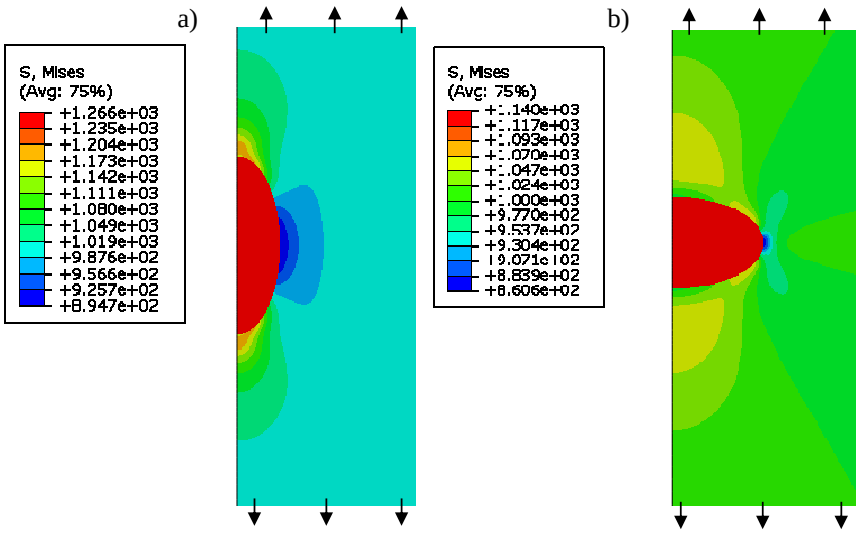

Figure 3.2.14 Von Mises stress distribution in a carbide when a macroscopic tensile stress of 1000 MPa is applied: a) equivalent to D2 and b) equivalent to D3

Results shown above pointed out that not only carbide orientation has to be regarded to understand the experimental σ^{RC} results, but also their intrinsic mechanical properties can bring important information to light. The anisotropy of 1.2379 M_7C_3 carbides may explain that they break at lower stresses in D3 than in D2 since as shown by Casellas et al., K_C for cracks parallel to the longer axis of carbides (D3) are much lower than for cracks which are perpendicular (D2).

However and even though this argument could explain the difference between D2 and D3 σ^{RC} results in 1.2379, no indices of anisotropy could be detected in carbides of UNIVERSAL and they still present lower σ^{RC} in D3 than D2. Then, a second aspect springs to mind and that concerns the fact that carbides have irregular morphologies instead of a linear contour (as it had to be supposed in FE modelling). The shape of carbides certainly contributes localising stresses at the interface with the matrix but, in addition, as carbides are dispersed forming bands aligned with the forging direction, during three points bending tests the microstructure submitted to load is different depending in D2 or D3.

As it can be observed in Figure 3.2.15, in D2 the percentage of carbides in the zone of highest stresses is lower than in D3, since in D2 matrix and carbide bands alternate, while in D3 a whole carbide band is located in this zone. Hence, from a statistical point of view and attending to the results of Rammerstorfer et al. [RAM99] (who showed that there is an influence of the tool steel microstructure on the stresses developed within carbide bands, in the sense that the matrix in the carbide rich layers starts to yield at much smaller macroscopic stress levels than the particle poor layers) is more probable that carbides fail in D3 than in D2. Moreover, as a result of the forging process the matrix is also reinforced in the direction parallel to carbides. Then at equal applied stresses, carbides in D2 may be less constrained because the matrix has greater resistance to deformation, while in D3 the stress is exerted directly to the carbide fibre.
+

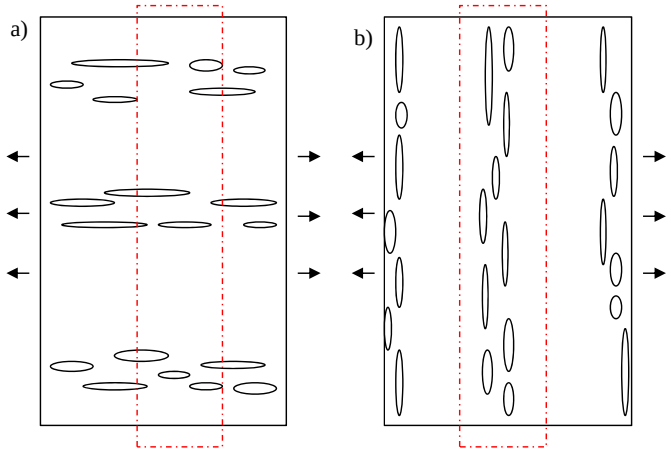

Figure 3.2.15 Schema of the effective microstructure during a three points bending test at the zone subjected to the highest stress: a) D2 sample configuration and b) D3 sample configuration

The next step in the fracture mechanism is the growth of cracks nucleated at broken primary carbides. The presence of cracks in the microstructure of ingot cast steels is directly determined by breakage of primary carbides, as no signs of carbide-matrix decohesion are found at all. By increasing progressively the applied stress it can be observed that cracks grow from the initial carbide to the metallic matrix, as show Figures 3.2.16 to 3.2.18 for 1.2379, UNIVERSAL and K360 D2.

Once cracks are nucleated in carbides and prior to start growing, the matrix ahead of the crack tip is plastically deformed. As Figures 3.2.16 to 3.2.18 were obtained by means of confocal microscopy, plastic zones around cracked carbides can be easily distinguished in blue colour. Deformation follows from a slight sinking of the matrix with respect to the surface (between 200 – 400 nm).

In Figure 3.2.16 it can be observed that in a 1.2379 D2 sample, two initially independent cracks (number 2 of Figure 3.2.16 d) and number 3 of Figure 3.2.16 e)) have coalesced before failure. Figure 3.2.17 shows that in UNIVERSAL D2, first carbides break, then the matrix deforms plastically around this carbides and it is not until the last steps that cracks appear in the matrix. In K360 (Figure 3.2.18) both the two carbides implicated at the fracture event have broken. Then the matrix starts to sink in progressively with the increase of the applied stress until cracks effectively develop.

In all these three cases, crack lengths (*2c*) at the step before fracture could be measured at the surface and compared to the size of the halo once the sample had failed. A zone plastically deformed determined the limit of stable and unstable crack propagation at the fracture surface (as it is shown, for instance, in Figure 3.2.18 f)).

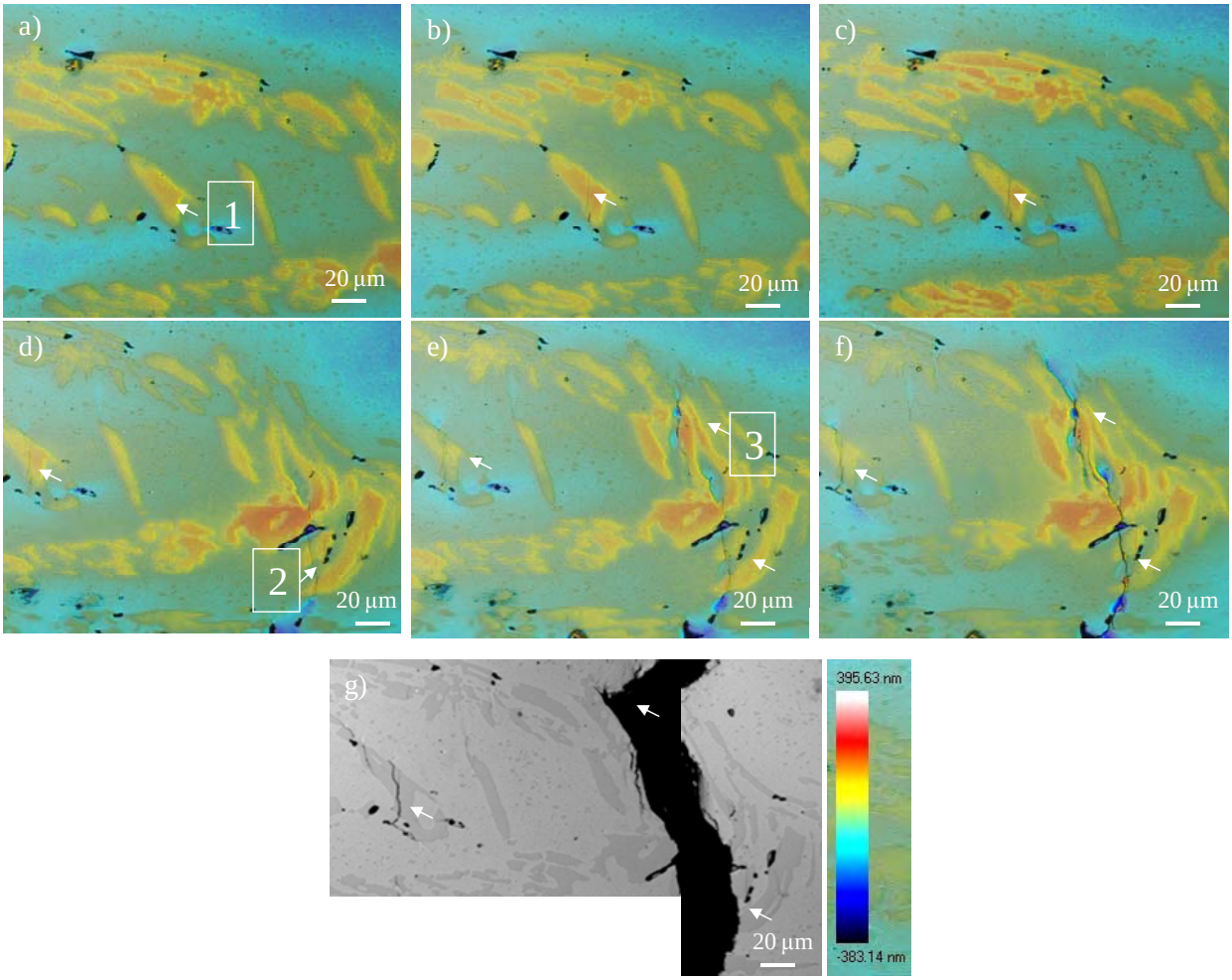

Figure 3.2.16 Evolution of cracks at the surface of the sample 1.2379 D2 at the applied stresses of : a) 900 MPa; b) 1100 MPa; c) 1400 MPa; d) 1700 MPa; e) 2000 MPa; f) 2400 MPa and g) fracture at 2364 MPa

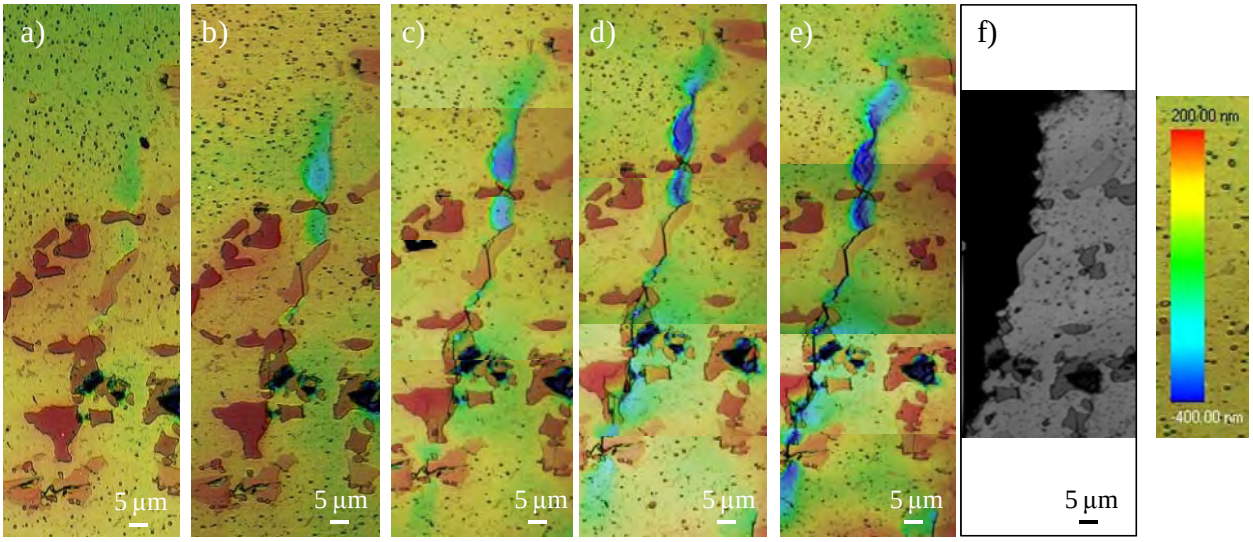

Figure 3.2.17 Evolution of cracks at the surface of the sample UNIVERSAL D2 at the applied stresses of : a) 2400 MPa; b) 2800 MPa; c) 3000 MPa; d) 3200 MPa; e) 3400 MPa and f) fracture at 3521 MPa

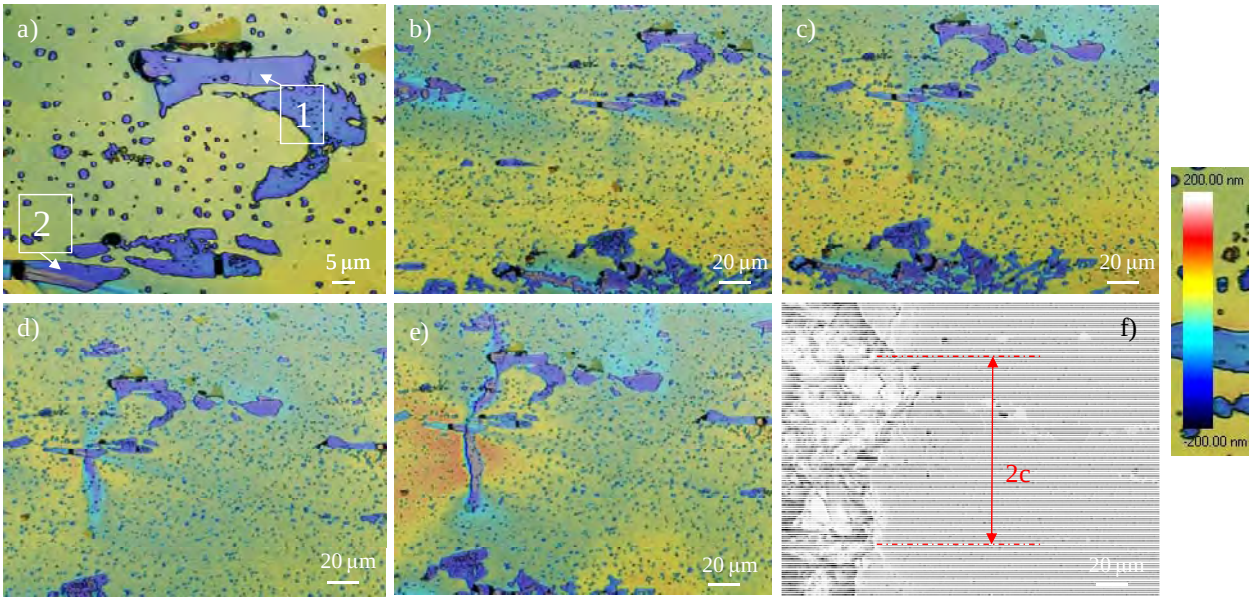

Figure 3.2.18 Evolution of cracks at the surface of the sample K360 D2 at the applied stresses of : a) zoom at 1600 MPa; b) 1600 MPa; c) 1900 MPa; d) 2200 MPa; e) 2600 MPa and f) fracture at 2964 MPa

Figures 3.2.19 and 3.2.20 show the growth of cracks nucleated at primary carbides in 1.2379 D3 and UNIVERSAL D3 respectively. The mechanism of crack growth is very similar to D2; i.e. first, plastic deformation of the matrix occurs at the tip of the cracked carbide and then, cracks develop, grow and coalesce before final fracture. However, as in D3 carbides are aligned following the same direction as cracks, matrix ligaments in-between carbides are very small compared to D2. Hence, nucleated cracks in carbides are close one to each other and as a result, they rapidly coalesce. For this reason, σ^R in D3 is lower than D2, even if σ^{RC} is quite similar in these two.

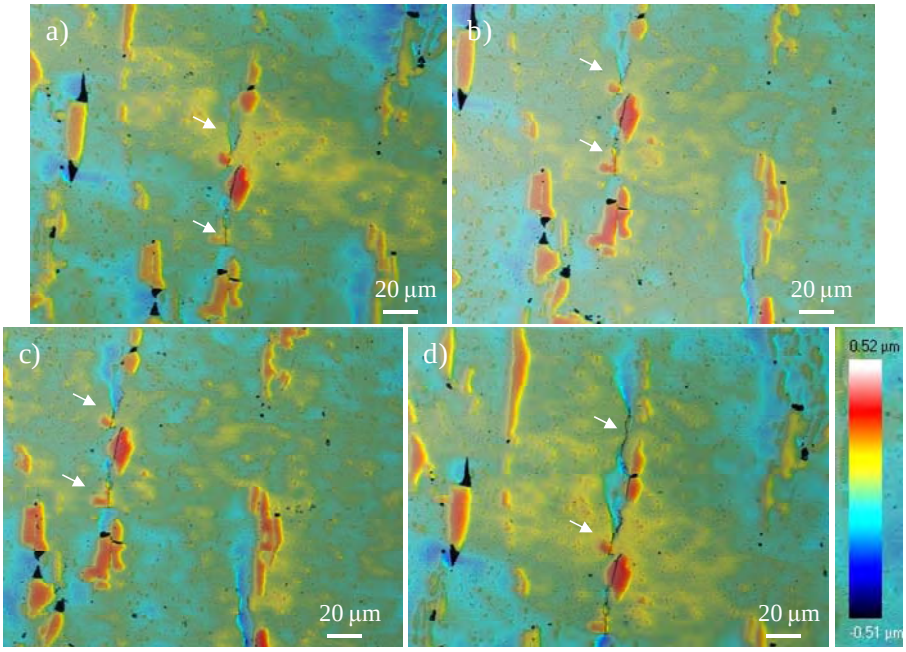

Figure 3.2.19 Evolution of cracks at the surface of the sample 1.2379 D3 at the applied stresses of: a) 900 MPa; b) 1100 MPa; c) 1200 MPa and d) fracture 1310 MPa

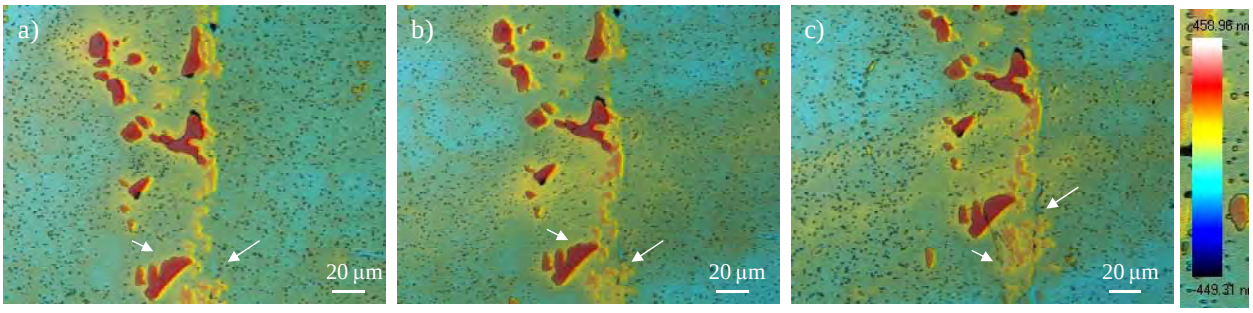

Figure 3.2.20 Evolution of cracks at the surface of the sample UNIVERSAL D3 at the applied stresses of: a) 1600 MPa; b) 1800 MPa and c) 2100 MPa

Plastic deformation of the matrix around broken carbides is attributed to the growth cracks beneath the surface as the applied stress increases, as shows the sequence of images in Figure 3.2.21. In this figure, purple and green cylinders schematise respectively, the resulting two parts of a broken primary carbide. This carbide is embedded in the matrix (grey box), and it has a given, and in principle unknown geometry under the surface (purple and green "clouds"). The mechanism proposed in this figure can be described as follows:

- In Figure 3.2.21 a) it can be observed that first at a certain applied stress, the carbide breaks. Since carbides are hard brittle phases, it is expected that they are all broken at once.
- With the increase of the applied stress, the two faces of the cracked carbide start to separate, as indicated in Figure 3.2.21 b).
- Figure 3.2.21 c) shows that the matrix directly over the opened crack is highly stretched and it evens deforms plastically. As during plastic deformation the volume must be constant, the stretching of the matrix at the surface leads it to sink below the surface.
- With a further increase of applied stress, the crack grows easier inwards the sample than at the surface (Figure 3.2.21 d)). This behaviour is due to the fact that the matrix at the surface is locally under plane stress conditions (as a result of the free stress state perpendicular to the surface) while below the surface, the matrix is under plane strain conditions (as a result of the triaxiality of the stress tensor in front of the crack tip). It is well known that fracture toughness in plane stress conditions is higher than in plane strain (as it was discussed in section 1.2). Therefore, the matrix at the surface has a higher toughness than the matrix which is below this, and it is capable of absorbing more plastic deformation before cracking.
-At the end with the steadily increase of the applied load, the matrix at the surface finally exceeds its fracture toughness and so it breaks, generating the cracks observed at the surface (Figure 3.2.21 e)).

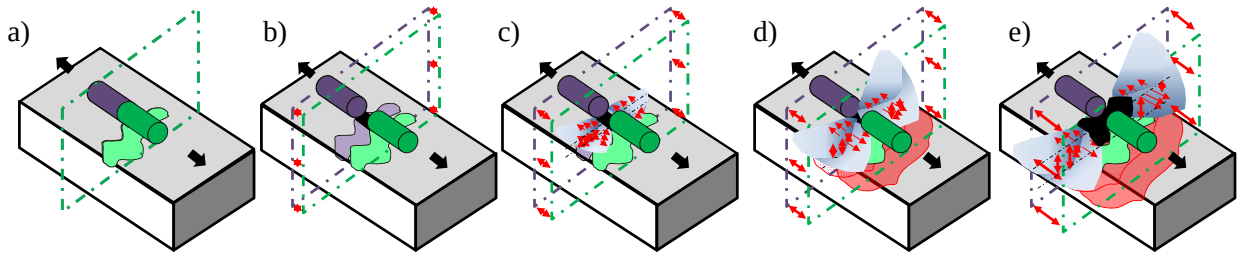

Figure 3.2.21 Mechanism of crack growth and plastic deformation around the cracked carbide. Figures a) throughout e) show the steps of the process at different increasing applied stresses

It is noteworthy to say at this point that the stress intensity of cracks once nucleated at primary carbides is determined by the geometry of carbides, and carbides can be very different depending on the orientation with respect to the surface: parallel (0º) and perpendicular (90º). Then an easier crack propagation below than at the surface may also be explained by a higher K^{90° than K^{0° if the carbide is deeper than wide.

3.2.3.2 Crack nucleation and growth in PM tool steels

Nucleation of cracks in HWS D2 occurs by decohesion or fracture of inclusions and primary carbides, as shown in Figure 3.2.22.

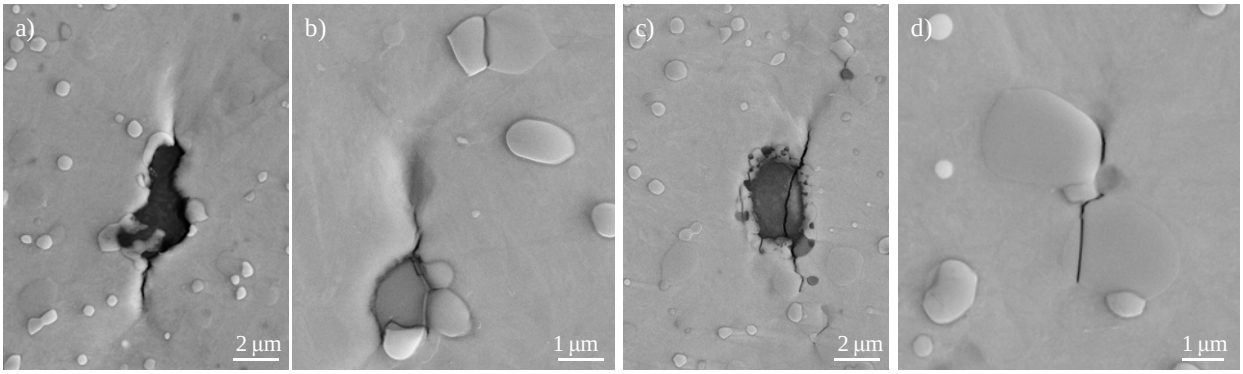

Figure 3.2.22 Cracks nucleated in HWS D2 from inclusion and carbide particles: a) decohesion of an inclusion with an emanating crack at 3500 MPa; b) decohesion of an inclusion with an emanating crack at 3800 MPa; c) fracture of an inclusion and emanating crack at 3800 MPa and d) breakage and decohesion of carbides at 3800 MPa

σ^{RC} is listed in Table 3.2.7 for inclusion and carbide particles respectively. Inclusions fail at slightly lower applied stresses than carbides (3400 - 3600 MPa vs 3800 – 4000 MPa). This can be understood since inclusions, in contrast to carbides, are not well adhered to the matrix and have larger sizes. σ^{RC} in HWS are much higher than in any of the ingot cast steels owing to its finer and more homogeneous microstructure. In addition, the isotropy of HWS implies that the behaviour of D3 is equivalent to D2 (that is why it was only evaluated in D2). Nevertheless, inclusions are weak points of PM steels when it

comes to nucleate cracks; therefore the size and distribution of these particles can strongly affect their fracture behaviour.

Table 3.2.7 Fracture strength of inclusions and primary carbides, σ^{RC}, in HWS D2

Tool Steel	Type of particle	σ^{RC}, MPa (D2)
HWS	Inclusion	3400 – 3600
HWS	Carbide	3800 - 4000

Growth of cracks in HWS is hardly observed since they nucleate at very high stresses, near those of unstable fracture. As shown in Figure 3.2.23, the few cracks observed are very small, but their growth seems to call the same steps as in 1.2379, UNIVERSAL and K360: nucleation of cracks in particles, plastic deformation of the surrounding matrix and development of cracks.

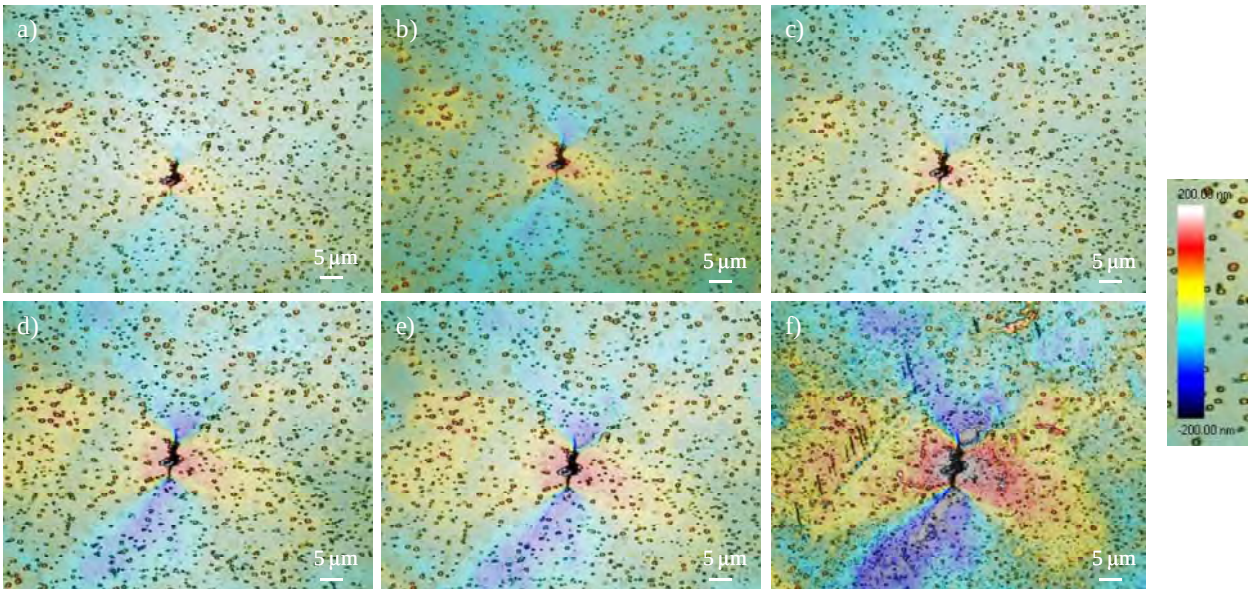

Figure 3.2.23 Evolution of a crack nucleated at an inclusion in HWS D2: a) at 3483 MPa; b) at 3582 MPa; c) at 3781 MPa; d) at 3980 MPa; e) at 4179 MPa and f) fracture at 4319 MPa

Fracture of PM steels can be due to two different processes: either an inclusion at the surface or inside the material breaks under the applied stress and the sample rapidly fractures, or no inclusions with the appropriated size are present and then small cracks nucleate at carbides, coalesce and give birth to larger cracks which lead to failure, too. As a difference to ingot cast steels, in HWS the time between nucleation and unstable fracture is very short. This means that even if the resistance to crack nucleation in PM steels is very high, they are very sensitive to the growth of these cracks as well.

3.2.4 Monitoring micro-damage using Acoustic Emission techniques

As shown in section 3.2.3, the interaction between the two main constituents of tool steel microstructures; i.e. primary carbides and metallic matrix, determine the mechanical properties of these materials and hereby, a proper comprehension of the micro-mechanical mechanisms leading to damage in the microstructure prior to failure is required. The gain of this knowledge concerns the identification, localization and quantification of the phenomena being involved in the process when a certain load is applied. In order to reach this goal, an innovative field-based approach is undertaken in this investigation, combining notions of fracture mechanisms with Acoustic Emission (AE) monitoring and wave signal analysis. This approach permits to obtain in situ data characterization, unique providing wave-like information of damaging mechanisms in tool steels.

3.2.4.1 Identification of characteristic AE signal patterns in bending tests of 1.2379 under monotonic loading

Figure 3.2.24 a) shows the results of the AE signals registered in bending tests under monotonic loading of 1.2379. This diagram plots the cumulative number of hits in function of the stress applied and the location of each signal on the sample surface (with respect to the centre of the sample). As it can be observed, the highest amount of signals is generated at the centre of the sample (where the applied stress is the highest during the three point bending test), and the quantity of emitted signal continuously increases with the applied stress.

A closer gaze to the AE signals allows to classify them into two categories depending on their characteristic patterns. As shown in Figure 3.2.24 b), at the beginning of the test, no AE signals are detected, but at a certain applied stress level, a first type of AE signal starts to be recorded (green line in Figure 3.2.24 b)). These signals are not continuous but they are emitted in a burst-like manner, and the quantity of hits registered increases along with the applied stress. As the stress increases, a second type of signal is distinguished (red line in Figure 3.2.24 b)). This signal also increases in number of hits together with the applied stress, but at the moment of final fracture it attains lower hit values than the first signal.

These two signals identified not only differ because of the number of hits, but also they have very different characteristic frequencies and waveforms. As shows Figure 3.2.24 c), the first type of signal has a main frequency of 280 kHz, while the frequency of the second type is around 650 kHz. These different frequency ranges of the two signals indicate that the responsible mechanisms for emitting them take place at different velocities in the microstructure, i.e. the second mechanism is much faster than the first one.

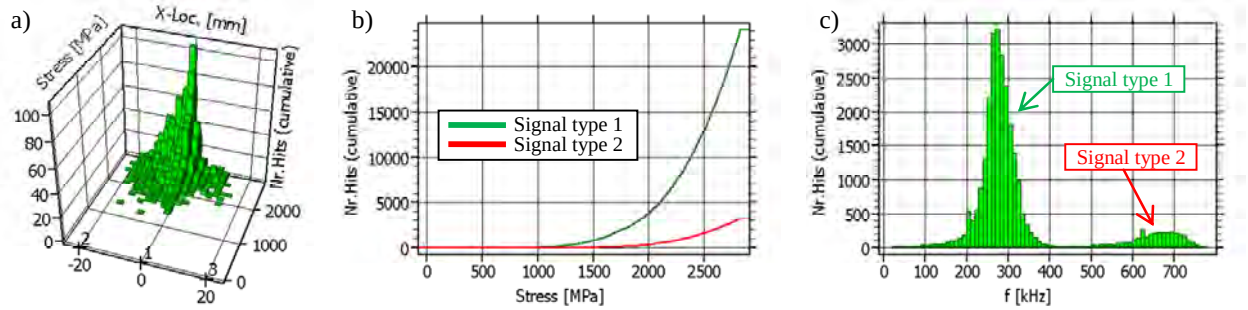

Figure 3.2.24 a) Cumulated number of hits in function of the stress applied during the bending test and the location of the signals at the sample surface; b) cumulated number of hits vs applied stress during a monotonic bending test in which two different types of AE signals can be observed; c) cumulated number of hits vs frequency for the two signals registered

Stepwise bending tests permitted to inspect the tensile surface of the samples at different increasing stress levels, and correlate the registered AE data (namely the two different identified signal types presented in Figure 3.2.24 b) and c)) to the micro-damage observed in the microstructure. In Figure 3.2.25 a) the cumulated number of hits in function of the stress applied at the first load step can be observed. This test was stopped at 800 MPa, in the moment in which the first signals were detected for this sample. These signals answer to the same pattern as those of type 1 identified before. However, no damage is observed at the sample surface, as shown in Figure 3.2.26 a); likely something happened at the microstructure but it could not be optically detected yet, such as phenomena involving the small secondary carbides or dislocations movement.

The next test was stopped at 2200 MPa, when a higher quantity of AE signal was detected. Practically all signals correspond to the characteristics of the type 1, and only a few hits of characteristic type 2 signals are detected (Figure 3.2.25 b)). In this case, the first cracks are observed in the microstructure and they are located at primary carbides (Figure 3.2.2 6 b) and c)). However and despite many carbides are broken, none of the cracks observed have started growing through the matrix. The last load step at 2600 MPa reveals a notable increase of type 2 signals, even though the number of hits of the type 1 has not ceased to increase (Figure 3.2.25 c)), as well as the number of broken carbides in the sample. The inspection of the surface shows that some cracks have now grown through the metallic matrix (Figure 3.2.26 d)).

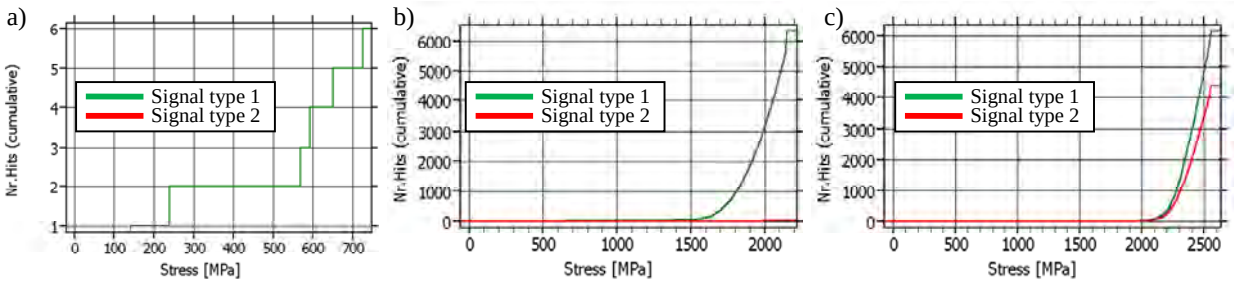

Figure 3.2.25 AE signal results of monotonic stepwise tests in 1.2379 in terms of the cumulated number of hits vs applied stress to: a) 800 MPa; b) 2200 MPa and c) 2600 MPa

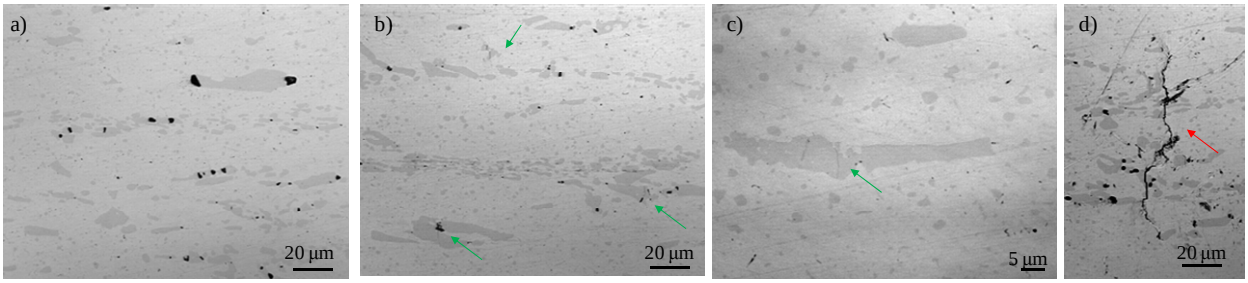

Figure 3.2.26 Images of the microstructure of 1.2379 at: a) 800 MPa; b)-c) 2200 MPa and d) 2600 MPa

As it follows from these results, the first and the second AE signal types can be related to different damaging mechanisms occurring in 1.2379 as the applied stress increases. The first type corresponds to the breakage of carbides in the microstructure, i.e. nucleation of cracks, while the second type is emitted by the subsequent growth of these cracks through the metallic matrix.

3.2.4.2 Influence of the tool steel microstructure on the acquired AE signals

Signals registered by means of AE reproduce with good accuracy micro-mechanical phenomena that take place in tool steel, even though if due to the heterogeneity that characterises their microstructure, significantly different AE results are obtained in samples of a same material. Figures 3.2.27 a) throughout c) show an example of such differences amongst three samples of 1.2379. As it can be observed in Figure 3.2.27 a), the maximum number of registered hits for the signal type 1 is very high at the end of the test, even though this sample did not break when the load was stopped. In Figure 3.2.27 b) it can be observed that the AE activity of another 1.2379 sample is significantly lower than the previous one with regard to both type 1 and type 2 signals, and this sample did neither break when the test was halted. A third 1.2379 sample shows the lowest cumulated number of hits for the signal of type 1, but it registers relatively high activity for the type 2. This sample in turn, had failed at the end of the test.

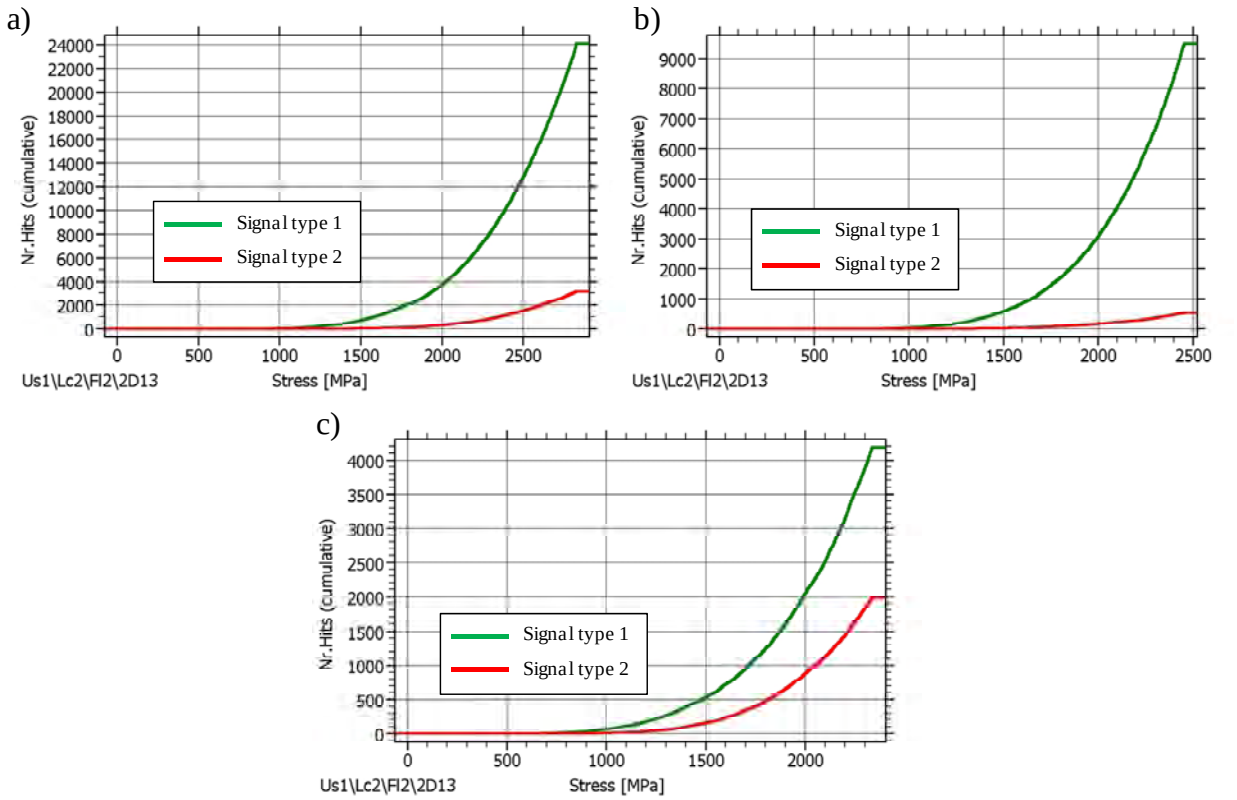

Figure 3.2.27 Cumulative number of AE hits for the two signal types vs the applied stress for: a), b) and c) three different 1.2379 samples

Figure 3.2.28 shows the microstructure of the three aforementioned samples at the end of the tests. Figure 3.2.28 a) shows the microstructure of the first sample (in correspondence with Figure 3.2.27 a)), and it can be observed that according to its high AE activity, multiple cracks have certainly nucleated at broken carbides. However, only a few amongst these cracks have grown through the matrix and they are mainly very small. Figure 3.2.28 b) shows an image of the second sample (in correspondence with Figure 3.2.27 b)). In this case it is concluded that even if some cracks have nucleated, there is a lower number of broken carbides than at the previous sample, and this is in agreement with the lower AE activity. In Figure 3.2.28 c) it is shown that in case of the third sample (in correspondence with Figure 3.2.27 c)), practically no broken carbides exist, but a long crack is observed near to the fracture surface, what correlates well to lowest AE activity but the highest number of hits of type 2.

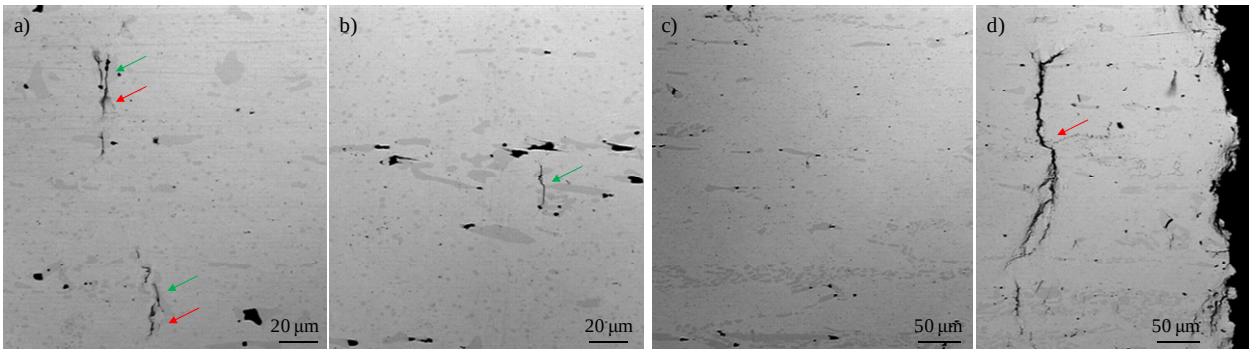

Figure 3.2.28 Micrographs of the surface of the three different 1.2379 samples whose AE results are shown in Figure 3.2.27: a) sample corresponding to the AE results of Figure 3.2.27 a), where lots of broken primary carbides are observed; b) sample corresponding to the AE results of Figure 3.2.27 b), where a lower number of broken primary carbides is present; c) and d) sample corresponding to the AE results of Figure 3.2.27 c), where practically no broken carbides are identified but a long crack is found near to the fracture surface

These results prove that there is very good correlation between the AE results registered during a bending test and the effective damage generated in the microstructure. They also point out the validity of the AE technique to detect the breakage of carbides and the propagation of cracks from them.

From this standpoint, it is possible to characterise the behaviour of steels showing different microstructural features by means of the analysis of the signals emitted during a mechanical test. With this aim, Figure 3.2.29 a), b) and c) compare the AE results obtained for samples of 1.2379, UNIVERSAL and HWS, respectively. As it can be observed, the same two characteristic AE patterns are identified in all materials, but the stress levels at which they start to be recorded differ significantly, according to the different fracture mechanisms observed in these steels.

On the one hand, 1.2379 and UNIVERSAL show a high AE activity both concerning signals of type 1 and type 2. This is in agreement with the fracture mechanisms discussed in section 3.2.3 in the sense that in 1.2379 and UNIVERSAL, a high number of broken carbides with cracks emanating from them are present in the microstructure. In addition, the stress at which the signal type 1 starts to be recorded correlates well to σ^{RC} as presented in Table 3.2.6. In this way, σ^{RC} values determined by optical inspection of the surface of samples are validated.

On the other hand, HWS shows a very poor AE activity (Figure 3.2.29 c), but according to the observations of section 3.2.3, the first cracks are not observed until more than 3000 MPa are applied. In this case however, the stress at which the first AE signals are detected is lower than the values of σ^{RC} presented in Table 3.2.7. This can be understood in two different ways: either AE is able to register signals emitted by mechanisms not observed in the examination of the surface (which are quite probable to have been left given the small size of carbides and inclusions) or the signals registered have no relationship at all with microstructural features.

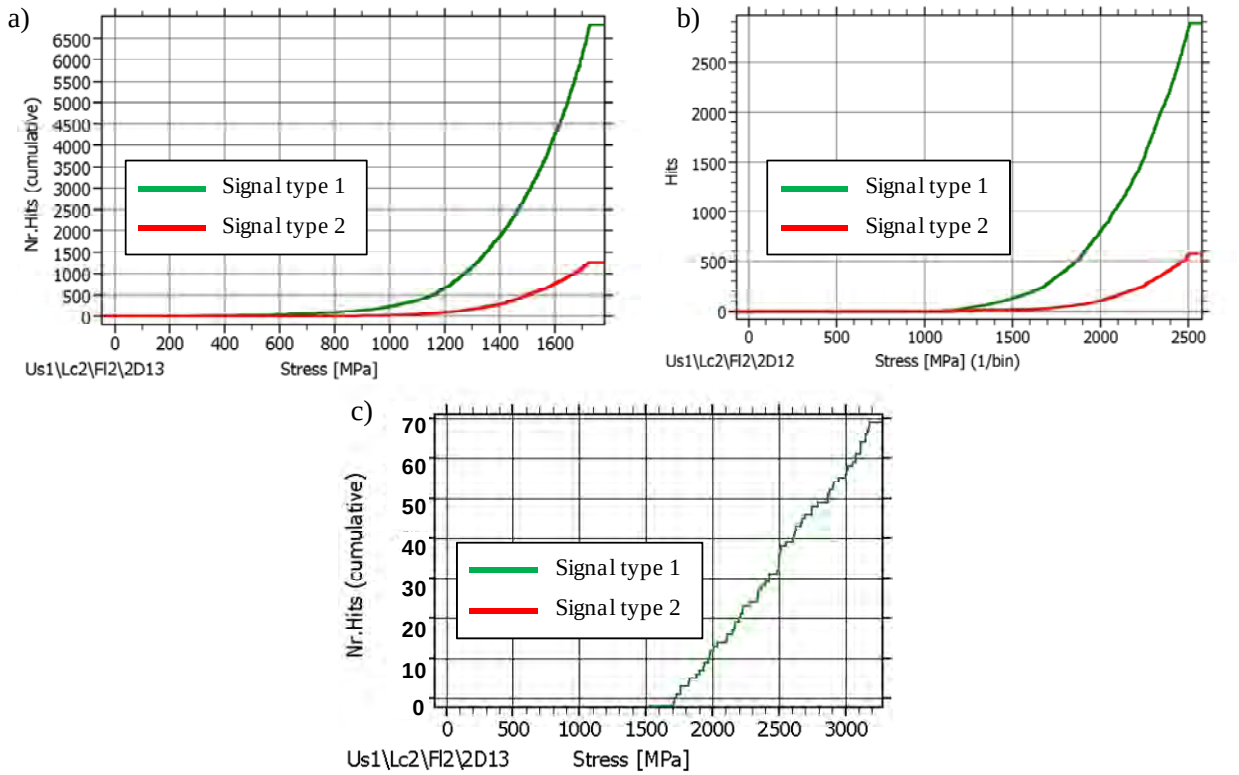

Figure 3.2.29 Cumulative number of AE hits vs applied stress for: a) 1.2379; b) UNIVERSAL and c) HWS

Figure 3.2.30 shows that in this HWS sample whose AE results are presented above, cracks at primary carbides and inclusion particles are present at the surface. There are only a few cracks and they are very small but nonetheless, it is possible that the generated signals in HWS are so small that they are well under the working amplitudes of the AE sensors. Thus an action to be taken into account for further work is the use of sensors specially adapted for low amplitude signals, so that any possible signal coming from the microstructure can be detected.

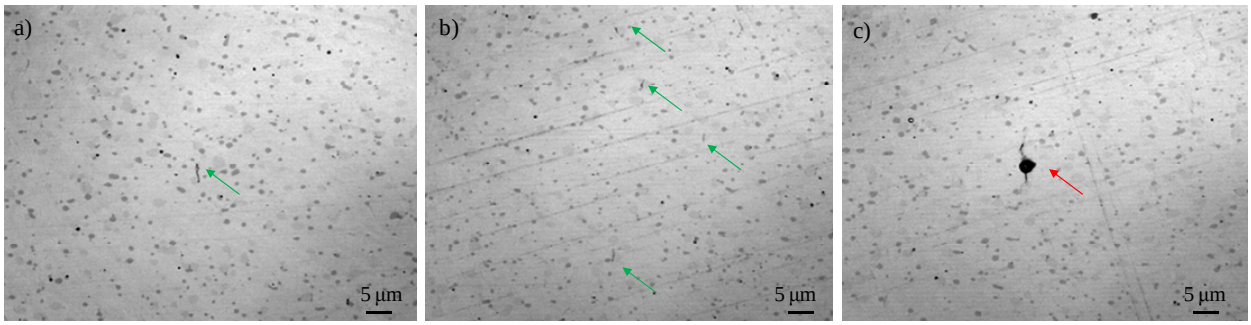

Figure 3.2.30 Images of the microstructure of HWS whose AE results are shown in Figure 3.2.29

3.2.5 Crack nucleation and propagation mechanisms under cyclic load

The objective of the present section is to study in depth the mechanisms of fatigue crack nucleation and propagation in ingot cast and PM steels. As discussed in section 3.2.1, fatigue failure initiation sites of ingot cast tool steels are primary carbides, or agglomerations of them. In case of HWS, fatigue origins are inclusions directly at the surface or inside the material. However, as follows from section 3.2.3 the stresses at which primary carbides and inclusions start to break under monotonic loads are higher than the applied fatigue stress amplitudes. If the properties of primary carbides are assumed to not deteriorate as a consequence of fatigue (what seems plausible for hard ceramic phases), there is no reason for which carbides can break in fatigue at applied stresses lower than σ^{RC}; e.g. $\Delta\sigma^{fat}$ of 1.2379, UNIVERSAL and K360 lies between 500 and 900 MPa while σ^{RC} ranges between 500 and 1800 MPa. In HWS σ^{RC} and σ^{R} are around the 4000 MPa while $\Delta\sigma^{fat}$ is between 900 and 1200 MPa.

The aforementioned observation indicates that the mechanisms governing fracture processes under monotonic loads are different to those controlling the cyclic ones, thus, the latter need to be clarified. This investigation has also permitted to assess if the nucleation and growth of small cracks in fatigue is governed by microstructural parameters rather than the macroscopic material properties. In this sense, fatigue properties which hold for long cracks (ΔK_{TH}, m and A) are contrasted with respect to those determined for the small ones.

3.2.5.1 Fatigue crack propagation threshold and shapes of small cracks in ingot cast steels

The first set of fatigue tests was carried out using 1.2379 D2 and examining the surface regularly after certain numbers of cycles with the aim to identify the first nucleated cracks. After 10000 cycles at a stress amplitude, $\Delta\sigma$, of 720 MPa the first broken primary carbides are observed, as show Figures 3.2.31 a-1) throughout a-3). With the subsequent increase of the number of cycles to 20000, 45000 and 745000, no crack propagation was detected (see Figures 3.2.31 b-1) to b-3), c-1) to c-3) and d-1) to d-3)).

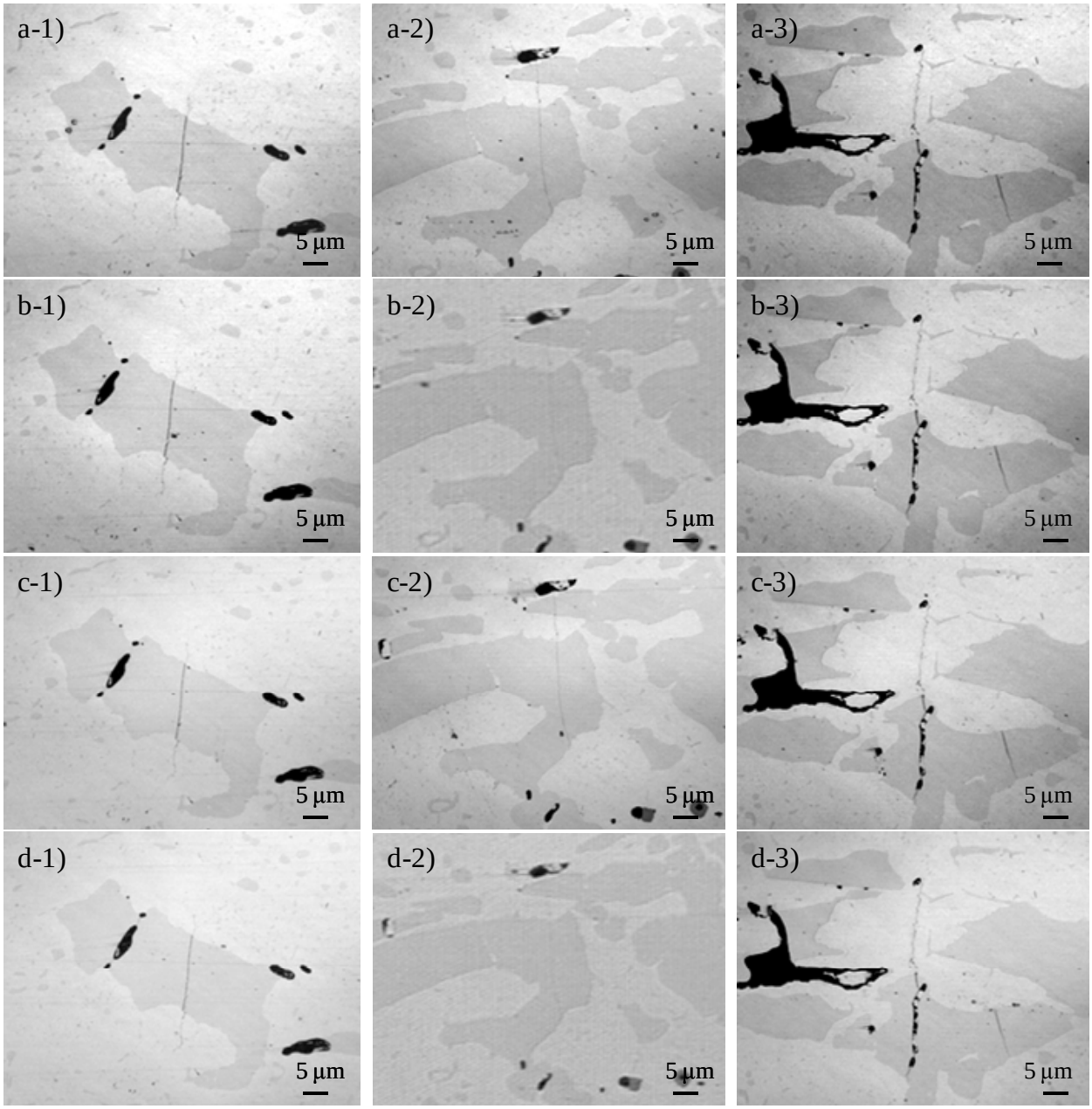

Figure 3.2.31 Three different broken carbides (1, 2, 3) in 1.2379 D2 at *Δσ* 720 MPa and after: a) 10000 cycles; b) 20000 cycles; c) 45000 cycles and d) 745000 cycles

In an attempt to rationalize these results, fracture mechanics was used to calculate the applied stress intensity factor, *ΔK*, of the cracks considered in Figure 3.2.31. Table 3.2.8 shows the stress amplitude, *Δσ*, (estimated for each crack taking into account its distance with respect to the centre of the sample, where stresses are the highest), the length of each crack at the surface, *2c*, and the corresponding *ΔK* values assuming different crack shapes. As the depth of these cracks, *a*, is not known, typical semi-circular cracks (*a/c* 1*)* and a shallow cracks (*a/c* 0,5 and 0,3) were assumed.

Table 3.2.8 *ΔK* of the three cracks in Figure 3.2.31, assuming *a/c* ratios of 1, 0,5 and 0,3

Crack	$\Delta\sigma$, MPa	$2c$, µm	ΔK, MPa·m$^{1/2}$ (a/c 1)	ΔK, MPa·m$^{1/2}$ (a/c 0,5)	ΔK, MPa·m$^{1/2}$ (a/c 0,3)
1	605	28	2,92	1,98	1,33
2	640	26	2,98	2,01	1,36
3	679	35	3,66	2,48	1,67

As no crack growth is observed, it is assumed that the threshold for propagation has not been attained. It is not clear at this point if the threshold for propagation of short cracks coincides with ΔK_{TH} determined for long cracks, but ΔK remains below ΔK_{TH} of 1.2379 D2 (4,25 MPa·m$^{1/2}$) in all cases. These results point out that at certain $\Delta\sigma$ carbides can certainly break and cracks can be nucleated, but this condition is not enough to observe crack propagation. Crack propagation requires an additional condition which is that $\Delta K \geq \Delta K_{TH}$. If none of these cracks has the minimal size to accomplish this condition at the $\Delta\sigma$, even if the number of cycles increases, cracks show exactly the same size as in the moment of being nucleated. Therefore, the size of carbides is crucial determining not only the onset for crack nucleation but also the shape of the generated cracks and as a result, if they propagate or remain arrested at certain applied stress amplitude.

In a second set of tests, $\Delta\sigma$ was increased to 820 MPa in order to force those cracks already nucleated to propagate through the matrix. Figure 3.2.32 shows cracks number 1, 2 and 3 (Figures 3.2.32 a), b) and c)) respectively) after 3000 cycles and it can be observed that only crack number 3 has propagated (compare Figure 3.2.32 d-3) to Figure 3.2.32 c)).

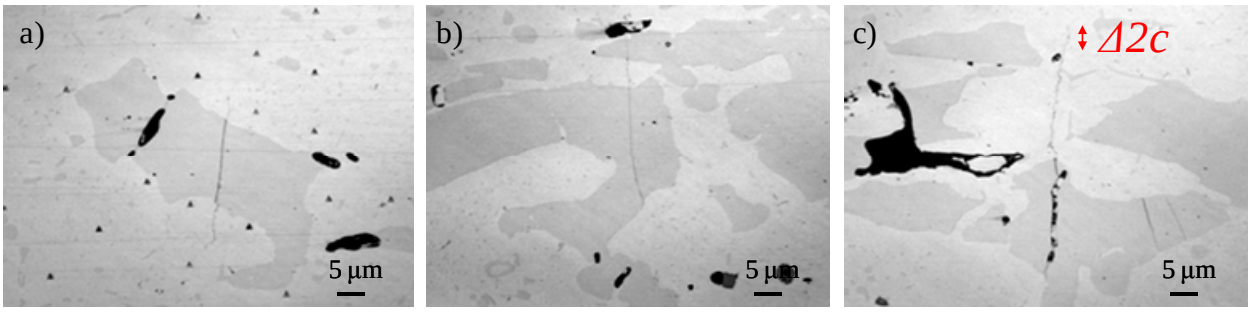

Figure 3.2.32 The three broken carbides in 1.2379 D2 now at *Δσ* 820 MPa and after 3000 cycles: a) crack number 1; b) crack number 2 and c) crack number 3

Table 3.2.9 summarises ΔK values calculated at the stress level of 820 MPa for the three considered cracks. In this case and since crack 3 has propagated, it was reasonable to think that some of its calculated ΔK's has exceeded the threshold for propagation.

Table 3.2.9 *ΔK* of the three cracks in Figure 3.2.32, assuming *a/c* ratios of 1, 0,5 and 0,3

Crack	*Δσ*, MPa	*2c*, µm	*ΔK*, MPa·m$^{1/2}$ (*a/c* 1)	*ΔK*, MPa·m$^{1/2}$ (*a/c* 0,5)	*ΔK*, MPa·m$^{1/2}$ (*a/c* 0,3)
1	680	28	3,28	2,22	1,50
2	720	26	3,35	2,27	1,53
3	856	35	4,62	3,12	2,11

In a third set of tests, *Δσ* was increased to 855 MPa so that crack 1 and crack 2 could also propagate. As it can be observed in Figure 3.2.33, crack 1 remains arrested after 3000 and 13000 cycles (Figure 3.2.33 a-1) and b-1) respectively). Only crack 2 has propagated (Figure 3.2.33 a-2) and b-2)) as well as crack 3, which continues to grow further (Figure 3.2.33 a-3) and b-3)).

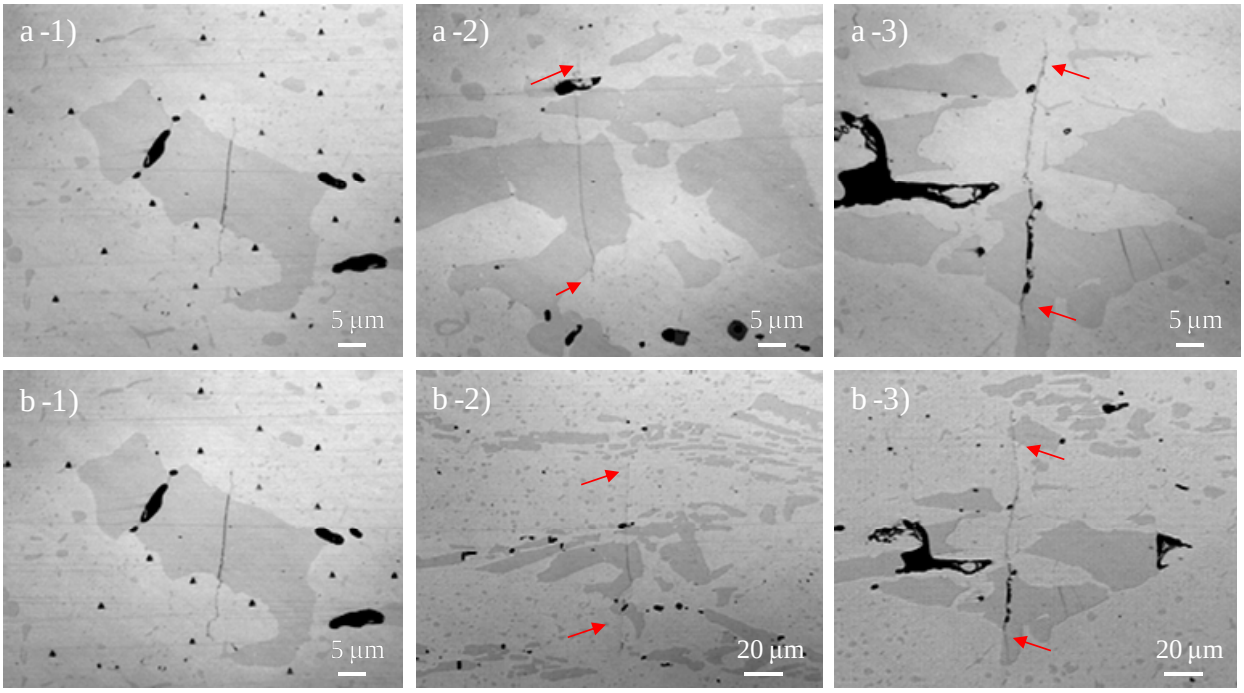

Figure 3.2.33 The three broken carbides (1, 2 and 3) in 1.2379 D2 now at *Δσ* 855 MPa after: a) 3000 cycles and b) 13000 cycles

Table 3.2.10 summarises the *ΔK* values calculated at the stress level of 855 MPa for cracks 1 and 2 (crack 3 was not considered since it had already started propagating at the last applied stress amplitude).

Table 3.2.10 *ΔK* of the three cracks in Figure 3.2.33, assuming *a/c* ratios of 1, 0,5 and 0,3

Crack	*Δσ*, MPa	*2c*, µm	*ΔK*, MPa·m$^{1/2}$ (*a/c* 1)	*ΔK*, MPa·m$^{1/2}$ (*a/c* 0,5)	*ΔK*, MPa·m$^{1/2}$ (*a/c* 0,3)
1	718	28	3,47	2,35	1,58
2	760	26	3,53	2,39	1,61

Since now crack 2 has also propagated, it is reasonable to say that the threshold for small crack propagation is comprised between ΔK values of crack 1 and crack 2. However, as carbides can have very irregular geometries (especially if they are arranged forming clusters, as it could be the case of cracks number 2 and number 3), cracks nucleated from them may not necessarily present the same shapes; e.g. crack 1 could present an *a/c* ratio of 0,5 while crack number 3 could have *a/c* equal to 1, or they could even have an *a/c* larger than 1.

Given the uncertainties originated to estimate the real shape of cracks at their very initial stages, the sizes of carbides at the fracture origins of fatigue samples were measured in order to have an idea of possible *a/c* ratios for this material. As shown by the results listed in Table 3.2.11, the shapes of the initial cracks differ substantially, and so they do the calculated initial stress intensity factors.

Table 3.2.11 Shape of carbides at the failure initiation sites of fatigue samples and corresponding ΔK values

Sample	$\Delta\sigma$, MPa	$2c$, μm	a, μm	a/c	ΔK, MPa·m$^{1/2}$
1	810	75	55	1,5	8,24
2	720	20	50	5,0	4,73
3	630	48	30	1,3	4,85
4	855	42	18	0,9	5,21

As follows from results of Table 3.2.11, initial ΔK of nucleated cracks in carbides is very different from one case to another but in all cases reported in this Thesis, $\Delta K > \Delta K_{TH}$ of 1.2379 D2, so the propagation threshold determined for long cracks can be a good approximation to the that of small cracks. Thus, even if the mechanisms regulating the threshold for crack propagation of small cracks in ingot cast tool steels are dictated by local microstructural parameters, i.e. the size and shape of the broken primary carbides, ΔK_{TH} determined for long cracks using E647-00 can be employed to estimate crack propagation of small cracks provided that that the shape of the crack is previously known.

3.2.5.2 Stable fatigue crack propagation and shapes of "medium" sized cracks in ingot cast steels

Stable fatigue crack growth is understood here as the propagation of cracks from the initial carbide, or carbide cluster, towards the matrix ahead. These cracks are longer than those considered in the previous section and this is why they are referred as "medium" sized cracks. Shapes of small cracks are influenced by the initiating carbide geometry but the question now is whether these cracks evolve during fatigue tests (and into which geometries) as they grow in the metallic matrix.

Halos, i.e. rings with a different texture in the fracture surface, are observed around fatigue cracks as shown in Figure 3.2.34. Halos are associated with a sequential formation of fracture surface markings that emanate from a strength limiting flaw when the material is loaded in tension. In case of ingot cast tool steels, fatigue samples present halos that emanate from initial broken primary carbides as a result of stable crack propagation through the matrix. These halos permit to estimate the final shape of fatigue precracks before fracture with rather good accuracy. As illustrate the examples of Figure 3.2.34, fatigue precracks have semi-circular shapes with *a/c* values very close or equal to 1.

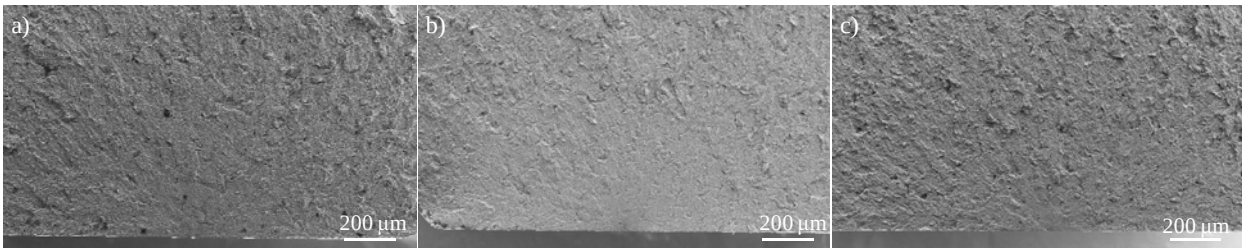

Figure 3.2.34 Fatigue halos observed at the fracture surface of 1.2379 D2 samples: a) *Δσ* 810 MPa, N 11195 cycles, *a* 335 µm, *2c* 690 µm and *a/c* 0,97; b) *Δσ* 720 MPa, N 29375 cycles, *a* 841 µm, *2c* 1740 µm and *a/c* 0,97 and c) *Δσ* 630 MPa, N 83329 cycles, *a* 922 µm, *2c* 1844µm and *a/c* 1

These results show that even if shapes of small cracks are very irregular and highly dependent on the initiating carbide or carbide cluster, as these cracks grow they tend to have semi-circular shapes regardless of the microstructure ahead. In order to shed light in the process by which cracks evolve from irregular to semi-circular shapes, a 1.2379 D2 sample was tested at *Δσ* 855 MPa and it was stopped after 13000 cycles when several cracks were observed at the surface, as illustrates Figure 3.2.35.

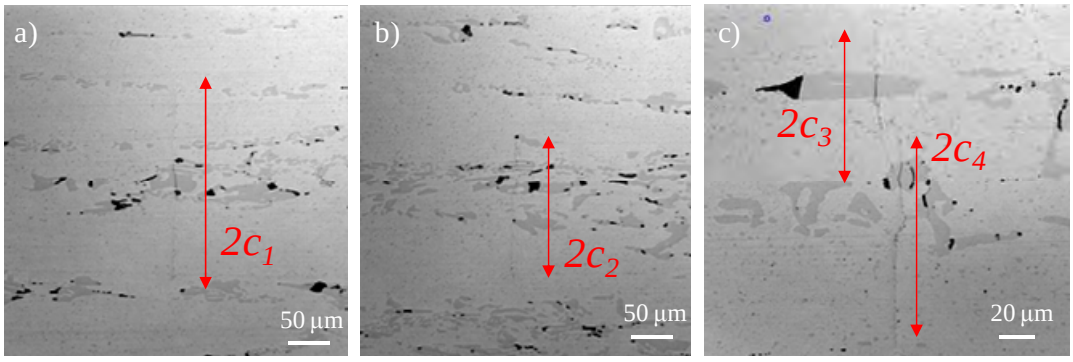

Figure 3.2.35 Cracks developed at the surface of the 1.2379 D2 sample at *Δσ* 855 MPa and after 13000 cycles: a) $2c_1$ 262 µm; b) $2c_2$ 197 µm and c) $2c_3$ 83 µm and $2c_4$ 114 µm

In an attempt to determine the shape of these “medium” sized cracks, this sample was directly broken monotonically to measure the halo of the fatigue precrack at the origin of failure. Figure 3.2.36 shows that the crack presented in Figure 3.2.35 a) caused the failure when the applied stress reached 1625 MPa. The halo left by the fatigue precrack is clearly distinguished in Figures 3.2.36 a) and b), and it has already a close to semi-circular shape with an *a/c* ratio of 0,9.

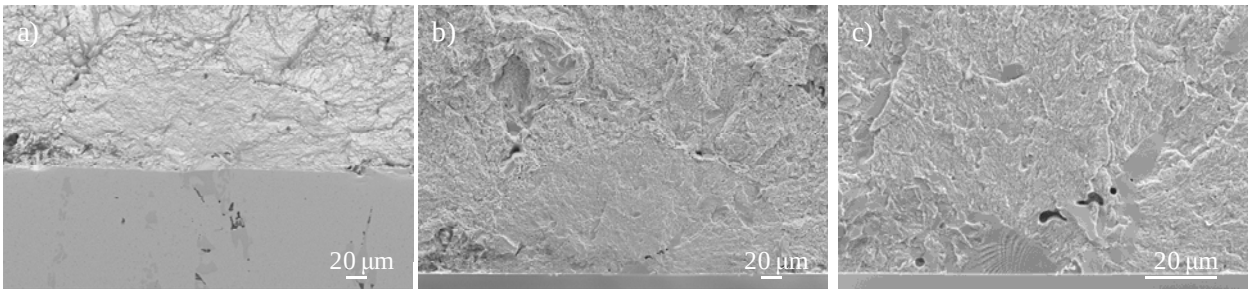

Figure 3.2.36 Fracture surface of the 1.2379 D2 broken monotonically after some cracks had been nucleated in fatigue. The halo of the fatigue precrack has the following dimensions: *a* 122 µm and *2c* 262 µm (*a/c* 0,9)

These results evidence that fatigue cracks have regular shapes which tend to reach *a/c* ratios equal to 1. Therefore, crack shapes are very irregular only during the stages in which cracks remain within their carbide band. Once they propagate to the metallic matrix in-between bands, irregularities in crack geometries are compensated in favour of more stable semi-circular shapes.

Once “medium” sized cracks have been shown to tend to semi-circular shapes, their fatigue crack growth parameters are determined and compared to those obtained for long cracks. *m* and *A* of the Paris law are determined for cracks in UNIVERSAL D2 at $\Delta\sigma$ 990 MPa. The evolution of a crack from its initial stage to the moment when the sample broke can be observed in Figures 3.2.37 a) throughout i). This crack was identified after 15000 cycles, even though in a previous examination after 10000 cycles nothing could be observed. Likely the crack was yet not formed at 10000 cycles, meaning that it had an incubation period comprised between 10000 and 15000 cycles.

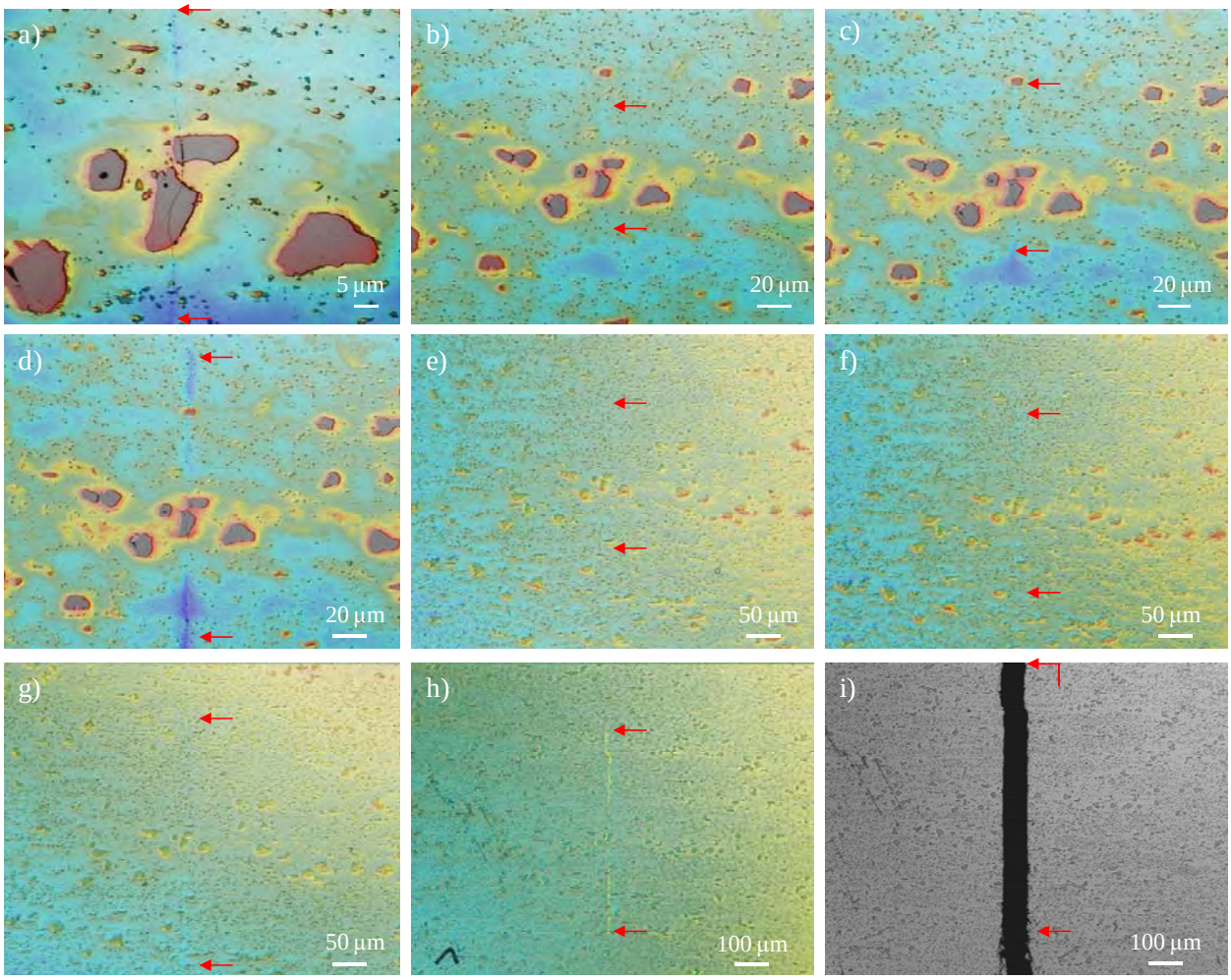

Figure 3.2.37 Stable crack growth in the UNIVERSAL D2 sample at *Δσ* 990 MPa (red arrows indicate the length of the crack, *2c*): a) 1500 cycles, *2c* 61 µm; b) 16000 cycles, *2c* 69 µm; c) 18000 cycles, *2c* 96 µm; d) 21000 cycles, *2c* 169 µm; e) 22000 cycles, *2c* 211 µm; f) 23000 cycles, *2c* 247µm; g) 24300 cycles, *2c* 330 µm; h) 26300 cycles, *2c* 566 µm and i) final fracture after 27664 cycles and *2c* 819 µm

Figure 3.2.38 shows the evolution of the crack from the last time that it could be measured (Figure 3.2.38 a)) to the moment when it fractured (Figures 3.2.38 b), c) and d) from different views). The crack length, *2c*, is also indicated by red arrows, as well as the crack depth, *a*, in Figure 3.2.38 d). The halo at the fracture surface evidences that the fatigue precrack has a semi-circular shape, with *a/c* equal to 1.

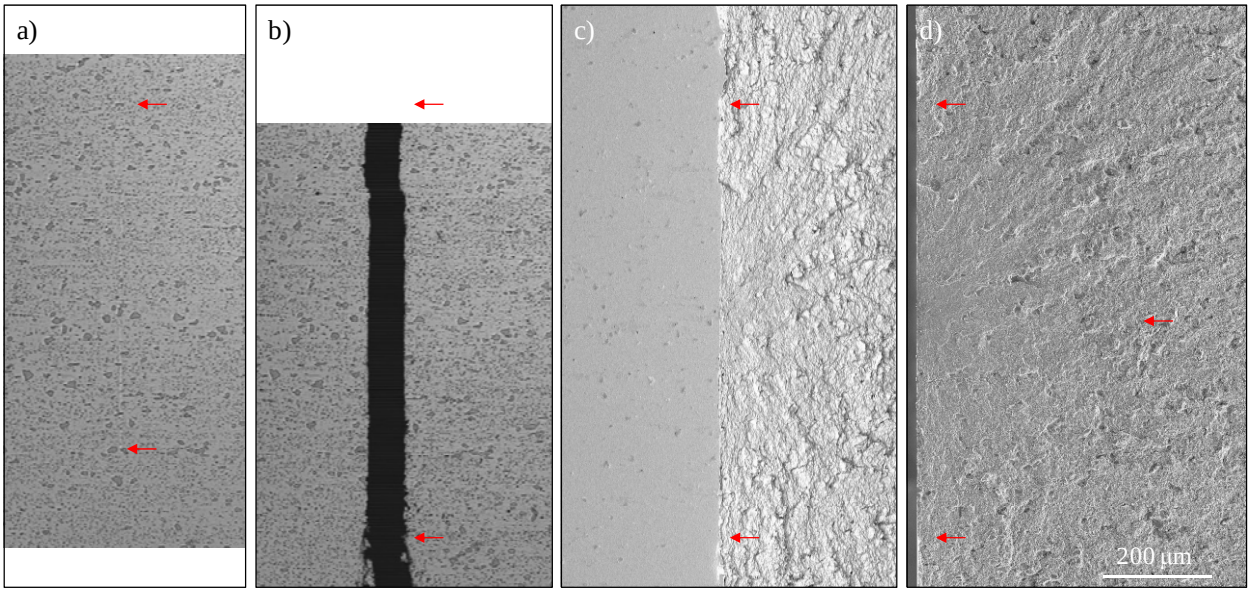

Figure 3.2.38 Evolution of the crack in the UNIVERSAL D2 sample loaded at *Δσ* 990 MPa: a) at the last inspection of the surface (N 26300 cycles and *2c* 566 µm) to b), c) and d) the moment when the sample broke (N 27664 cycles, *2c* 819 µm and *a* 423 µm)

Data on crack growth permits to plot the diagram shown in Figure 3.2.39 relating the crack propagation rate, *da/dN*, to the applied stress intensity factor, *ΔK*. *ΔK* values are calculated under the assumption that the crack shape has an *a/c* ratio equal to 1. That seems plausible even for the first step of propagation contemplated here (Figure 3.2.37 a)), as this crack had already propagated out of its carbide band the first time that it was observed.

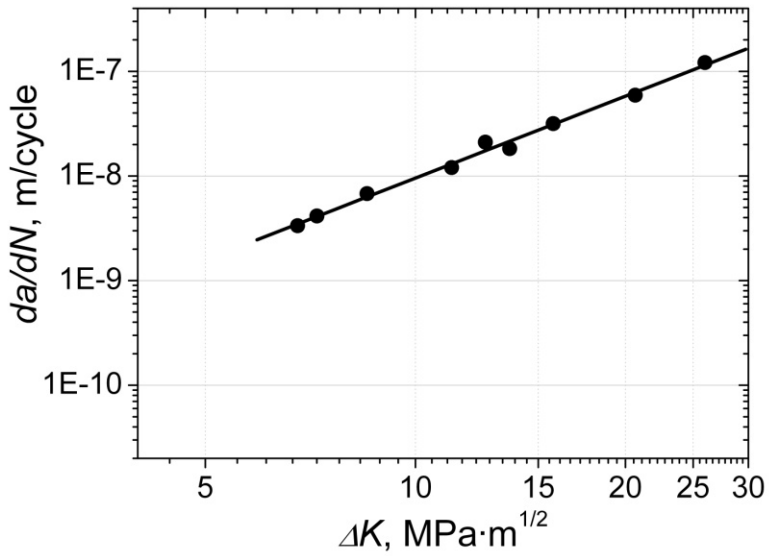

Figure 3.2.39 Crack propagation rate, *da/dN*, vs the stress intensity factor, *ΔK*, of the crack studied in the UNIVERSAL D2 sample

Crack propagation is very good approximated by a lineal regression, meaning that even if the growth of cracks is somewhat tortuous at the beginning when they are still confined in the carbide band, they tend to rapidly evolve into more stable shapes and grow steadily. The parameters *m* and *A* (in terms of *Log A*) resulting from the linear fitting are 2,60 ± 0,08 and -10,62 ± 0,09 respectively. These values are lower than those determined for long cracks in UNIVERSAL D2: 4,4 ± 0,5 and -12,2 ± 0,5 respectively, as shown in Table 3.2.3.

In order to ascertain the validity of such experimental results, this analysis was performed in another crack of the same sample so that the *m* and *A* values could be contrasted. This crack however, was smaller than the previous one, since the sample broke when it had just started its stable propagation stage. Figure 3.2.40 shows its evolution from the first time that it could be identified (Figure 3.2.40 a) at 21000 cycles) to the end of the test when the sample broke (Figure 3.2.40 f) at 27664 cycles). This crack required thus, a nucleation period comprised between 18000 and 21000 cycles.

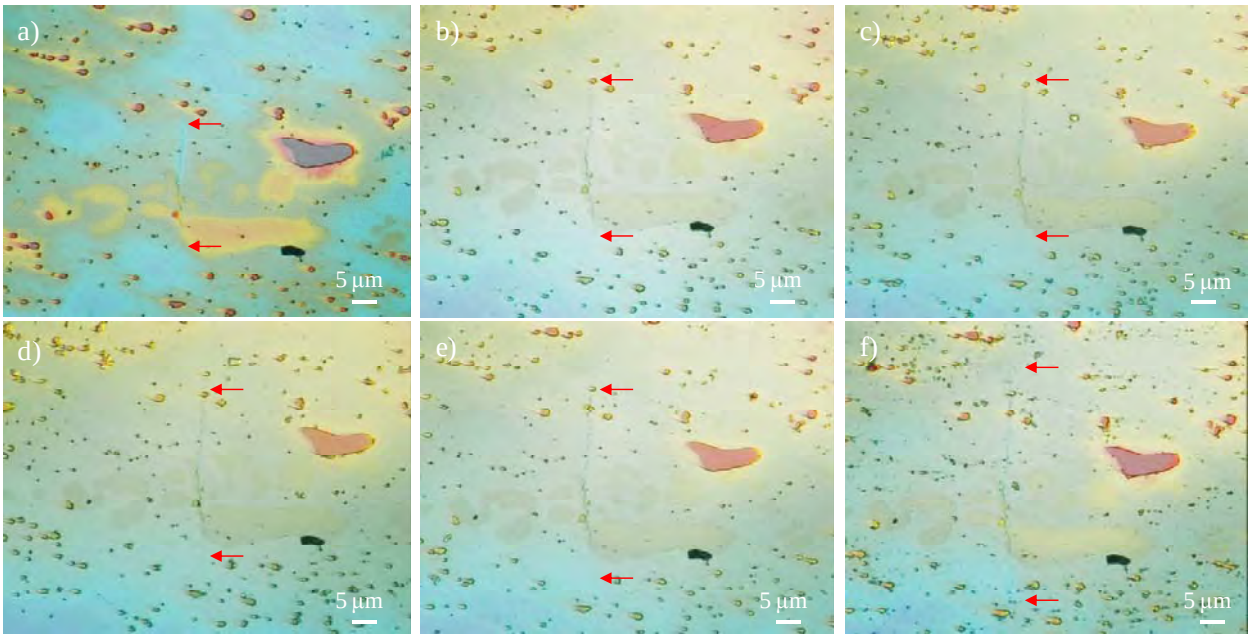

Figure 3.2.40 Stable crack growth in the UNIVERSAL D2 sample at *Δσ* 990 MPa: a) 21000 cycles, *2c* 27 µm; b) 22000 cycles, *2c* 29 µm; c) 23000 cycles, *2c* 29µm; d) 24300 cycles, *2c* 32 µm; e) 26300 cycles, *2c* 37 µm and f) final fracture after 27664 cycles and *2c* 44 µm

da/dN and *ΔK* are plot in Figure 3.2.41 assuming an *a/c* ratio equal to 1, even if at the first points of the curve (in which the crack is still confined in the carbide band) it can have an irregular shape likely different to 1. Figure 3.2.40 and 3.2.41 show that this crack has a tortuous beginning to propagation since it is not until attaining a certain size that it is able to propagate without too much influence of the microstructure. At 24300 cycles it had a length of 32 µm (Figure 3.2.40 d)) and it is considered to start propagating stably.

The first *da/dN* value obtained for this crack is very low (close to 10^{-10} m/cycle), hence the corresponding ΔK value can be an estimation of the crack propagation threshold of this crack. ΔK (assuming *a/c* equal to 1) is 4,7 MPa·$m^{1/2}$, very close to that determined for long cracks in UNIVERSAL D2: 4,9 MPa·$m^{1/2}$. Therefore, once again is shown that ΔK_{TH} of small cracks can successfully be estimated by values determined for long cracks.

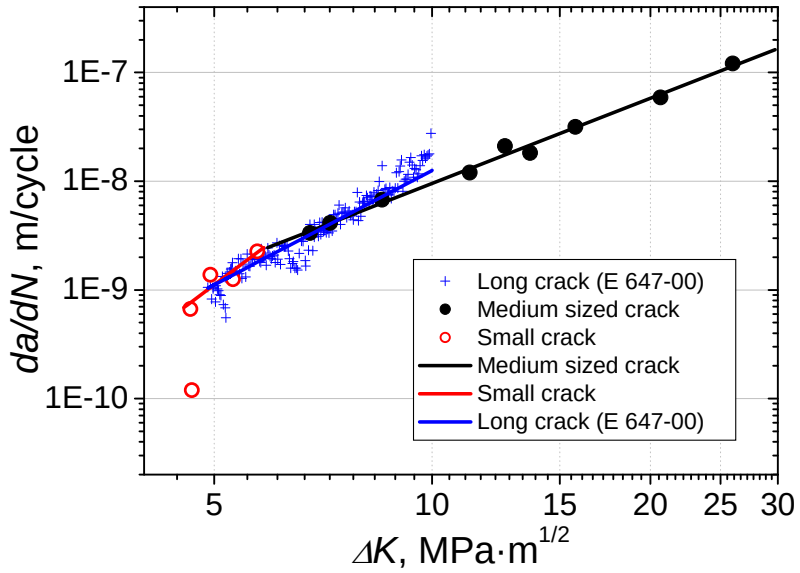

Figure 3.2.41 Crack propagation rate, *da/dN*, vs the stress intensity factor, *ΔK*, of the cracks studied in the UNIVERSAL D2 steel

As the crack presented in Figure 3.3.40 was small when the sample failed, only a few points could be used to estimate the parameters of the Paris curve (red dots in Figure 3.2.41). However, when plotting together in Figure 3.2.41 the results of crack propagation for the small, the "medium" sized and the long crack (E 647-00), it can be observed that they almost coincide. Although the parameters of the Paris law are slightly different (as shown in Table 3.2.12) their behaviours are comparable and the differences can be explained by scattering, typical of such heterogeneous microstructures.

Table 3.2.12 Fitting parameters of the Paris curve *A* and *m* for the different cracks studied

Crack type	*m*	*Log A*
Small	5,0 ± 1,6	-12,5 ± 1,12
Medium	2,6 ± 0,8	-10,6 ± 0,1
Long (E 647-00)	4,4 ± 0,5	-12,2 ± 0,5

3.2.5.3 Fatigue crack nucleation in ingot cast steels

After revising fatigue crack propagation mechanisms in ingot cast tool steels, the corresponding crack nucleation processes are tackled within this section. It is shown that the presence of cracks in fatigue samples implies the breakage of carbides even though in some cases, $\Delta\sigma$ is lower than σ^{RC}.

Two different cases should be distinguished to discuss about crack nucleation in carbides under cyclic loadings, as show Figure 3.2.42. On the one hand 1.2379 D2 and D3, UNIVERSAL D3 and K360 D2 present similar σ^{RC} and σ^{max}. On the other hand, UNIVERSAL D2 shows $\sigma^{RC} > \sigma^{max}$. (Note: σ^{max} refers to $\Delta\sigma^{fat}$ in terms of the maximum applied stress, and this parameter is used to compare with σ^{RC} since it is assumed that if fracture of carbides takes place, it happens at the maximum stress during the fatigue test.

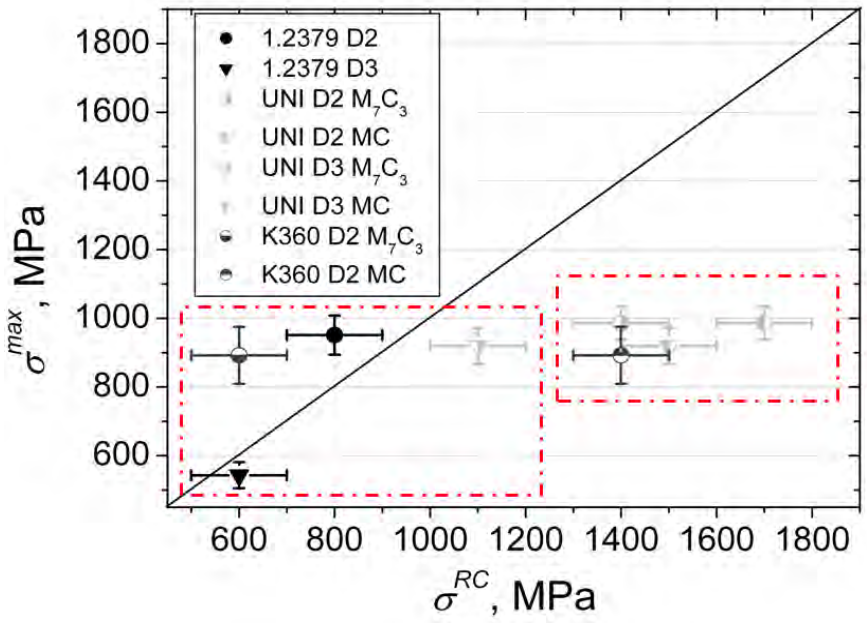

Figure 3.2.42 Fatigue limit, in terms of σ^{max}, vs fracture strength of primary carbides, σ^{RC}, for the considered ingot cast tool steels in D2 and D3 configurations

Concerning the first case, if σ^{RC} and σ^{max} occupy more or less the same level at a stress scale, it is reasonable that the crack nucleation mechanism is the failure of carbides, and that it occurs already when the first load cycle is applied (since σ^{max} can exceed σ^{RC}). However, it is observed that the fracture of carbides is a necessary but not sufficient condition for cracks to start propagating, since they can remain arrested in carbides independently of the number of cycles applied but provided that $\Delta K < \Delta K_{TH}$. This indicates that either (or at least) one crack is formed at the cycle number one that has the appropriated ΔK to start propagating, or this sample cannot fail at the applied $\Delta\sigma$. Certainly, this statement is not entirely true, since carbides are observed to be broken when the fatigue test has run a certain number of cycles. Hence, there must be some additional mechanism by which carbides break in fatigue.

This additional mechanism also regards the second case of Figure 3.2.42, when $\sigma^{max} < \sigma^{RC}$, as in UNIVERSAL D2. It is important to underline the fact that $\sigma^{max} < \sigma^{RC}$ is not a guarantee that any carbide breaks at cycle number one in this UNIVERSAL D2. Given the scatter of σ^{max} and σ^{RC} and their dependence on microstructural parameters, the differences between these values are not as important as to justify that carbides breakage is impossible. It is just a question of probabilities, i.e. the probability to find a carbide with the proper characteristics to fail, for instance in 1.2379 D2, is significantly higher than in

UNIVERSAL D2 due to the most refined microstructure of this one. Hence, both the first mechanism (carbide breakage at the first cycle) and the second one (carbide breakage after a certain number of cycles) are plausible to take place in all steels regarded.

The reason to say that some cycles must be applied so that the mechanism number two is effective is that this one involves the degradation of the metallic counterpart (the matrix) as the number of cycles increases. As discussed in chapter 1.2, the degradation of the matrix properties can result in cyclic hardening and softening phenomena. Given the over-tempered condition of these steels, it is plausible that if their properties are to be modified during the fatigue life, they lead to cyclically softening rather than cyclically hardening, as postulated by Fukaura et al. [FUK04]. Softening of the metallic matrix is understood by Fukaura et al. if the tempered martensite structure is destabilized by strain localisation processes, such as persistent slip bands (PSBs) and vein structure formation. Unfortunately, the evaluation of such phenomena to ascertain that it is at the origin of cyclic softening and carbide breakage requires much additional work, which was in priory not contemplated in the course of this Thesis. However, it can certainly constitute the motivation of future research in this field, since some indices of structures recalling those of PSBs are identified at the surface of fatigue samples using SEM, as shown in Figure 3.2.43.

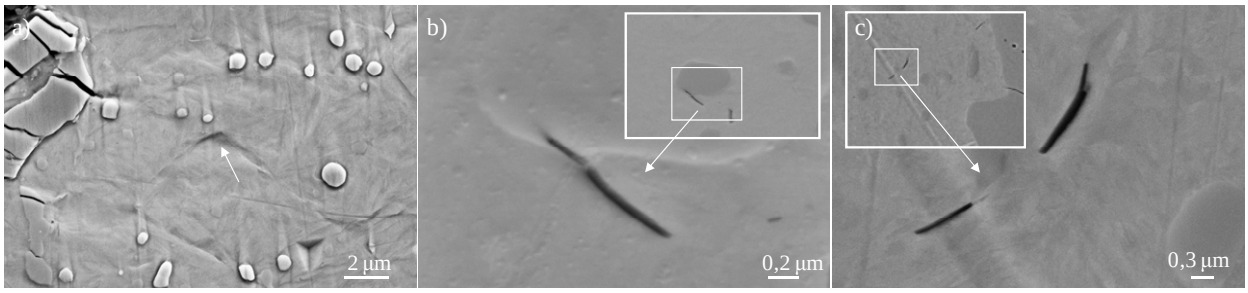

Figure 3.2.43 Different forms of damage in the matrix of a 1.2379 D2 fatigue sample

It must be said that the solely presence of these structures in the matrix cannot directly explain that carbides break. But if they are at the origin of softening processes, they may lead to conclude that the matrix has certainly softened. If this is the case, at an equal applied load to the beginning of the test (since the tests were run under load control), the matrix can undergo further deformation. But as carbides are embedded in the matrix (and very well adhered indeed) and they allow just very small amounts of deformation, the local increase of strain can lead the carbides to break.

These two mechanisms described above may be effective depending on the stress level applied: the higher the applied maximum stress, σ_a^{max}, the more probable carbides break at the first cycle because $\sigma_a{}^{max} > \sigma^{RC}$; and the lower the σ_a^{max}, the more probable carbides break after some cycles as the condition underlined before cannot be accomplished, but because the matrix progressively softens with the number of cycles and $\varepsilon^{msoft} > \varepsilon^{RC}$ (where ε^{msoft} is the corresponding strain value of the softened matrix at $\sigma_a{}^{max}$ and ε^{RC} is the strain at which a carbide fails).

Last but not least, a third option for crack nucleation should be regarded. If the $\sigma_a{}^{max}$ is so low that neither the first nor the second mechanisms described above are effective, then it is probable that if the test is run to $2 \cdot 10^6$ cycles (as in this investigation), no fracture is observed. However, if the test could have been run to giga-cycle fatigue regimes, as performed by Shiozawa et al. [SHI01, SHI06-1 and SHI06-2] or Sohar et al. [SOH08-1, SOH08-2 and SOH08-3] then fracture could have finally taken place by the mechanisms of GBF formation and fish-eye, as described in chapter 1.3 and section 3.2.1. In this mechanism the matrix locally degrades at the surrounding of a particle (either inclusion or primary carbide), in a way that small cracks start to nucleate by decohesion of secondary carbide precipitates. The cohesion of these cracks around the particle induces the fracture of this one, and the creation of a facet in the fracture surface with a special texture (the GBF).

In conclusion, several possibilities must be regarded concerning crack nucleation processes in ingot cast steel microstructures under cyclic loadings. The occurrence of one mechanism or another is related to the level of the applied stress amplitude in correspondence to the microstructural parameters of the steel which is considered. Depending on the size, shape and arrangement of its primary carbides, three different stress levels corresponding to the three different types of crack nucleation mechanisms can be identified:

- At the highest stress levels ($\sigma_a{}^{max} \geq \sigma^{RC}$) crack nucleation takes place at broken primary carbides.
- Below such stress levels ($\sigma_a{}^{max} < \sigma^{RC}$) crack nucleation must happen because of some degradation of the matrix properties resulting to cyclic softening, which leads in turn, to the breakage of carbides since at equal applied loads to the beginning of the test, $\varepsilon^{msoft} > \varepsilon^{RC}$.
- When none of these circumstances are encountered (i.e. $\sigma_a{}^{max} < \sigma^{RC}$ and $\varepsilon^{msoft} < \varepsilon^{RC}$) then failure takes place because of the formation of GBFs and fish-eye phenomena.

3.2.5.4 Fatigue crack nucleation and propagation in HWS

Under monotonic loading, the nucleation of cracks in the microstructure of HWS samples is due to the fracture and decohesion of inclusions and/or carbides from the metallic matrix. However, as follows from the conclusions of the last paragraph, the nucleation mechanism by which at the first applied load cycle,

fracture and decohesion of these particles take place, is directly disregarded for HWS since $\sigma_a^{max} << \sigma^{RC}$ (see the third square of Figure 3.2.44).

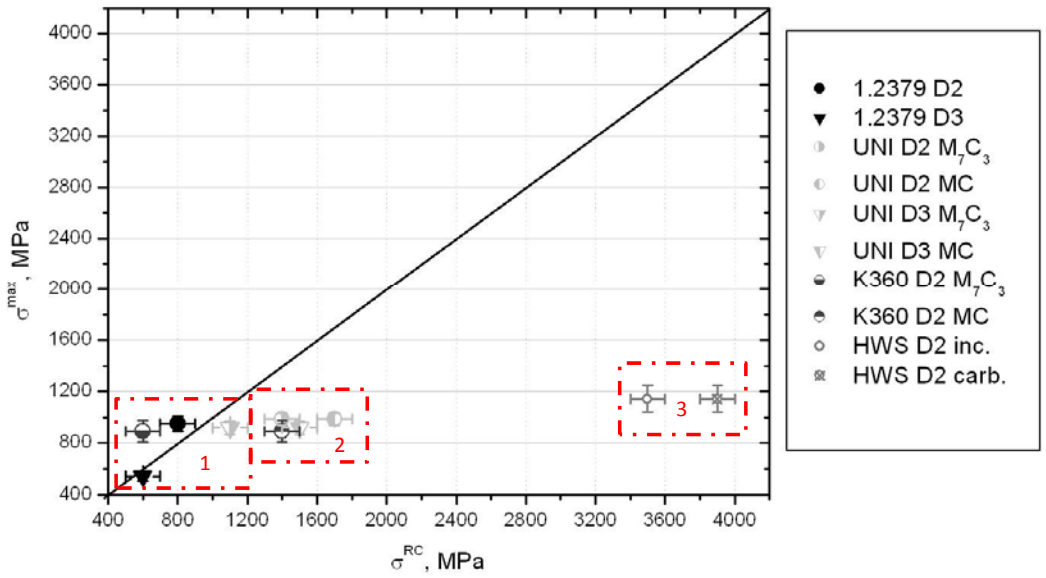

Figure 3.2.44 Fatigue limit, in terms of σ^{max}, vs fracture strength of primary carbides and inclusions, σ^{RC}, for the ingot cast tool steels under D2 and D3 configurations and for HWS D2

Despite the aforementioned observations, initial sites of fatigue failure in samples of HWS are inclusion particles, as shown in Figure 3.2.45.

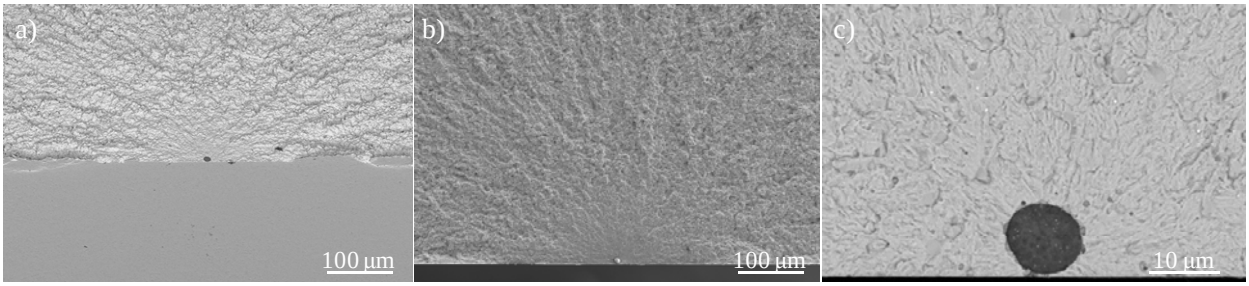

Figure 3.2.45 Example of a fracture surface of an HWS fatigue sample in which an inclusion is the crack initiating site

Thus, it follows that the nucleation of cracks at such particles requires an incubation period in which the matrix progressively loses its properties (and which can be very long depending on the stress amplitude applied). Given the very fine microstructure of HWS, inclusions act as stress concentrators and hence, their surroundings are preferential locations in which the matrix degrades. Inclusions are scarcely distributed in the matrix and they have very different shapes and sizes. That is the reason why sometimes, fracture initiation sites are located at the interior of samples even though the stresses are higher at the surface (likely no inclusions with the required size are present at the surface). In addition, inclusions opposite to carbides, are not well adhered to the matrix and so detachment at the interface is prone to take

place as the number of cycles increases during a test. Finally, analogous to ingot cast steels, GBFs and fish-eye phenomena may occur when there is a lack of inclusions which break or detach in the microstructure under a certain applied load.

Concerning crack propagation mechanisms, in HWS and opposite to ingot cast steels, the sizes of inclusions (which can attain more than 10 μm) is sufficiently high to give birth to propagating cracks in the microstructure once they are nucleated. ΔK_{TH} determined for long cracks is 2,8 MPa·m$^{1/2}$ and as it can be observed in Table 3.2.13, the estimated ΔK for some of the identified inclusion particles are higher than this value.

Table 3.2.13 Shape of initiating inclusion particles and corresponding *ΔK* values in HWS fatigue samples

Sample	$\Delta\sigma$, MPa	$2c$, μm	a, μm	a/c	ΔK, MPa·m$^{1/2}$
1	1350	9,6	10,0	2,0	4,46
2	1350	20,0	10,0	1,0	5,50
3	1400	5,0	11,3	1,3	3,31
4	1400	22	23,8	2,2	6,98

Stable propagation of such cracks nucleated from inclusions is expected to be attained already at the very initial stages of crack growth. In HWS and in opposition to ingot cast steels, the microstructure ahead of the crack tip is homogeneous since the beginning (there are no carbide bands in through which the crack must first propagate), and so cracks easily develop semi-circular shapes (the most common crack shape observed at the fractured surfaces), as it can be observed for instance, in Figure 3.2.45 b).

Even though in this investigation a total number of 12 HWS D2 samples were used in order to try to follow, step by step, the crack nucleation and propagation mechanisms (a study similar to that carried out with 1.2379 D2 and UNIVERSAL D2), none of the samples permitted to obtain any concluding results; either they broke suddenly when no damage had been detected at the previous step, or they run to $3{\cdot}10^6$ cycles and did not fail. This leads to conclude that not only nucleation processes in these samples are very time consuming at the stresses applied but also, they are strongly dependent on the microstructure (i.e. on the probability to find an inclusion which can break under the applied load). Additionally, cracks propagate easier through the microstructure than in ingot cast steels and once they are nucleated, they rapidly grow to fracture.

Given the results of this section, the reason why the tool steels studied in this work show very similar $\Delta\sigma^{fat}$ but different σ^R can now be understood. Both under monotonic and cyclic loads, crack nucleation requires the breakage of carbides or breakage/detachment of inclusion particles. Under monotonic load the stress level at which it occurs is dictated by the size, shape, arrangement and intrinsic properties of the particle. Under cyclic load, even though certain particles can certainly break at the first applied cycle if

they have the sufficient requirements ($\sigma_a{}^{max} > \sigma^{RC}$), it is often the case that $\sigma_a{}^{max} < \sigma^{RC}$ and then, fracture of these particles cannot take place until the matrix softens to a certain extent in which $\varepsilon^{msoft} > \varepsilon^{RC}$.

As shown in Figure 3.1.1 and Tables 3.1.2 and 3.2.5, the size, arrangements, shapes and properties of carbides are very different in the four steels considered, then it can be understood that they lead to different σ^{RC} and σ^{R} values. In contrast, the properties of the metallic matrix of these steels are rather similar, as shown in Table 3.2.5, and even if the features of the particles influence the time in which the matrix is softened enough to lead them to break (since they act as stress concentrators), the onset for this mechanism is dictated by the matrix in itself. Since the matrixes are very similar, it is reasonable that the differences observed in fatigue resistances among the studied steels are much diminished compared to the results of fracture strength.

3.2.6 Monotonic subcritical crack growth in tool steels

As it has been shown through this chapter, in ingot cast steels cracks nucleate in carbides (hard phases) and propagate within a carbide band towards the metallic matrix (which is more ductile). The existence of these two phases with markedly different crack growth resistances may induce fracture instability to take place well after crack initiation due to the occurrence of subcritical crack growth, i.e. stable crack growth at $K < K_{IC}$, when the effective fracture toughness increases along with the crack growth. This phenomenon is mainly studied in ceramics, polymers or composite materials, but in this part of the Thesis the crack growth resistance or *R*-curve, of tool steels is aimed at being determined.

The *R*-curve generally entails the measurement of the crack driving force, *K* or *G*, as function of stable crack extension, Δa or Δc (see chapter 1.2). Unstable fracture occurs when the materials resistance to fracture ceases to increase faster than the driving force for crack propagation; this corresponds to the driving force as function of crack size being tangent to the crack growth resistance curve. As schematised in Figure 3.2.46 [RIT08], for a material that has a flat *R*-curve, a single value of toughness unambiguously characterises the material, as there is no stable crack extension and the initial crack size, a_0, is the same as the critical size, a_c. For a material with a rising *R*-curve there is no single value of toughness that characterises the material, as the driving force for unstable crack propagation depends on the extent of crack growth, and the final toughness depends on the tangent condition (which varies in function of a_0). In these materials crack growth resistance measurements are needed to determine how the resistance to fracture evolves with crack extension, since stable crack growth occurs and the critical crack size will be larger than the initial crack size.

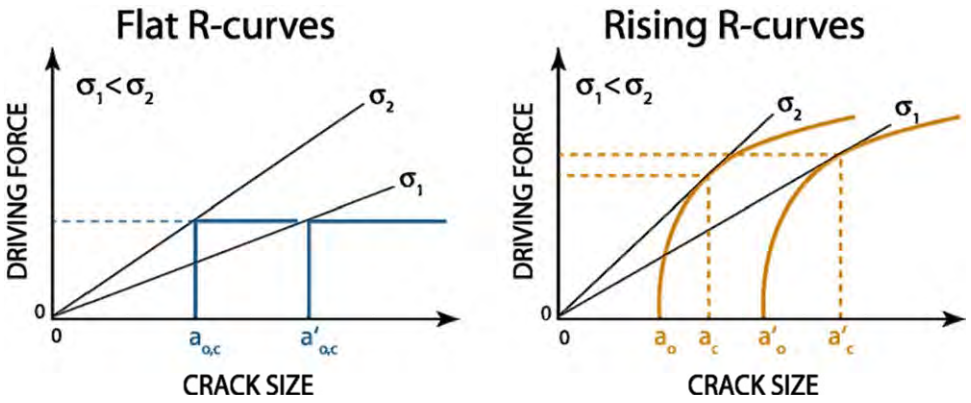

Figure 3.2.46 Schematic description of flat and rising R-curves in terms of the driving force, *K* or *J*, vs the crack size, *a* [RIT08]

In this part of the investigation, stepwise monotonic subcritical crack growth was evaluated in order to measure the stress intensity factor as function of stable crack extension, permitting to plot the *R*-curves of 1.2379, UNIVERSAL and K360 D2 and D3, as well as HWS D2. Under increasing monotonic stresses, it was already observed that crack nucleation and growth in 1.2379, UNIVERSAL and K360 takes place at stresses below those for yielding or fracture. Gomes et al. [GOM97] indicated that fracture of T42 high speed steel samples occurred while the cracks were still in the microstructurally short regime: ~ 20 - 100 μm in length, meaning that *R*-curve behaviour was exhibited with estimated maximum *K* as low as 0,5K_{IC} (K_{IC} is the toughness value determined for long cracks in standard E 399-90 measurement tests).

Knowledge on crack geometries is required so that the applied *K* values, K_a, are determined with accuracy. However, crack geometries are usually unknown since they run inwards the sample. Gomes et al. found that all non-propagating cracks were extremely shallow (0,1 < *a*/*c* < 0,5), what contrasted with the approximately semi-circular crack geometries that were generally observed at the failure initiating sites. Gomes et al. assumed semi-circular crack shapes (*a* /c = 1) to build their *R*-curves although they pointed out the uncertainties regarding crack geometries in which, according to their results, microcracks could be initially shallow but then they could attain semi-circular geometries before failure.

Owing to such uncertainties on the real geometry of cracks, in this investigation stepwise polishing is performed in samples prior to build the *R*-curves. By these means the depth of cracks under the surface is determined and K_a is calculated to plot the *R*-curves. Acoustic Emission is used during the three-point bending tests in order to anticipate the unstable fracture and stop the test just before failure. In this way, data about geometries and K_a of cracks with sizes very close to those leading to final fracture are obtained.

3.2.6.1 Geometry of microcracks under monotonic loading

Fracture normally starts from approximately semi-circular "thumbnail" regions, sometimes with characteristic "river markings" radiating from them (Figure 3.2.47 a)). As shown in Figure 3.2.47 b) the final length of cracks is delimitated by high plastically deformed zones at the fracture edge. However, as it can be seen in Figure 3.2.47 c), the final depth of the crack is hardly identified.

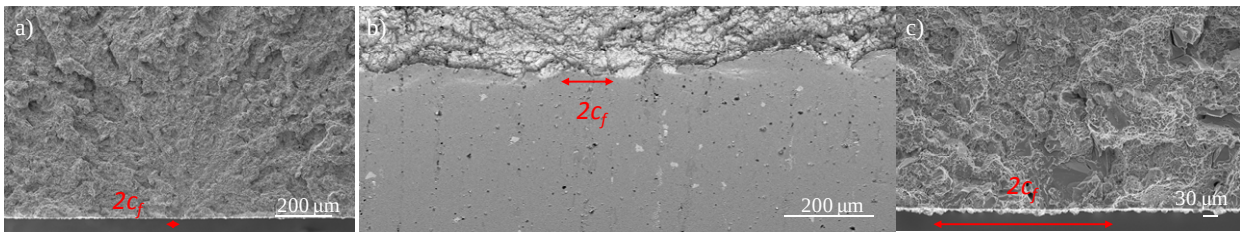

Figure 3.2.47 Failure initiation site showing: a) "river markings"; b) the crack length at the surface delimited by a high plastically deformed zones a the fractured edge and c) the initial precracked carbide in which the final depth of the crack is difficult to be identified

In order to shed light on crack geometries and their evolution as cracks grow; stepwise polishing was performed in a UNIVERSAL D2 sample. Using Acoustic Emission, this sample was loaded to a stress level which was near that of unstable fracture. When inspecting the surface, many cracks were detected as shown in Figure 3.2.48. Crack number 1 had a length, *2c*, equal to 192 µm (Figure 3.2.48 a)); cracks number 2 and 3 were very close one to each other but they had not coalesced at the surface, their *2c* was 124 µm and 154 µm respectively (Figure 3.2.48 b); finally, crack number 4 had a *2c* of 103 µm (Figure 3.2.48 c)).

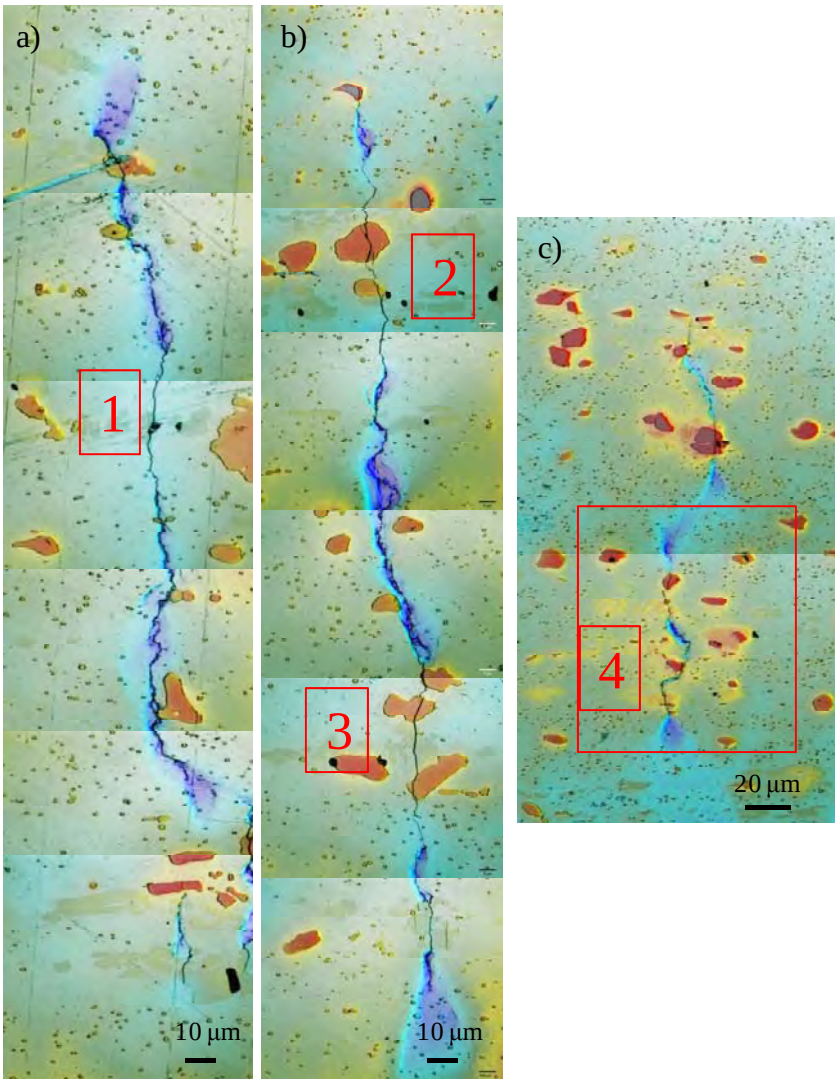

Figure 3.2.48 Cracks observed at the surface of the UNIVERSAL D2 sample tested under monotonic loading and stopped before failure: a) crack number 1: *2c* 192 µm; b) cracks number 2 and 3: *2c* 124 µm and 154 µm respectively, c) crack number 4: *2c* 103 µm

Figure 3.2.49, 3.2.50 and 3.2.51 show the evolution of cracks 1, 2-3 and 4 respectively at different increasing depths from the initial sample surface.

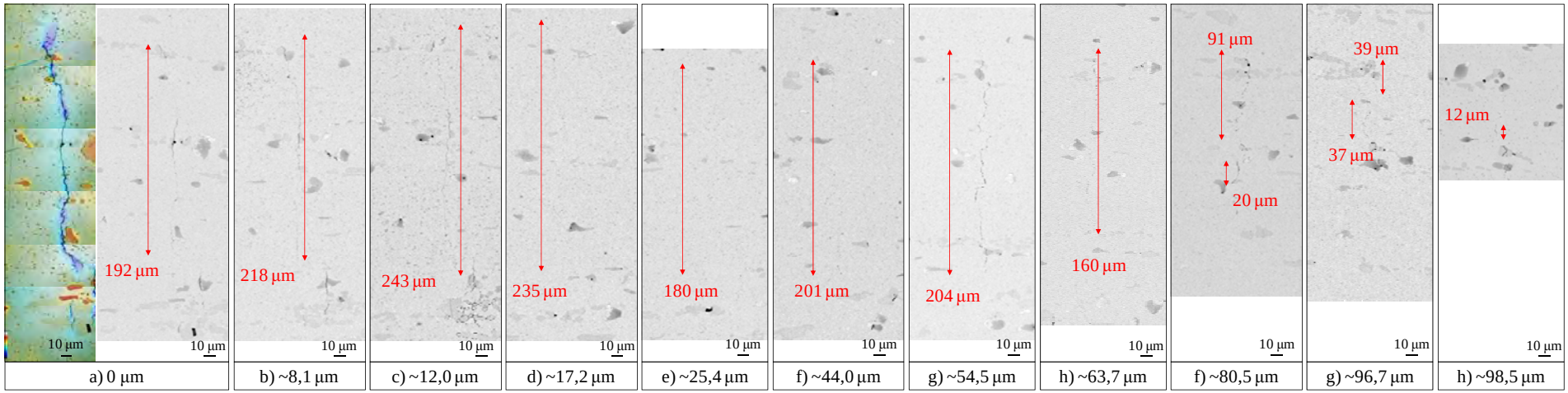

Figure 3.2.49 Stepwise polishing results of crack number 1, from a) throughout h) sequence of crack images at increasing depths from the initial surface

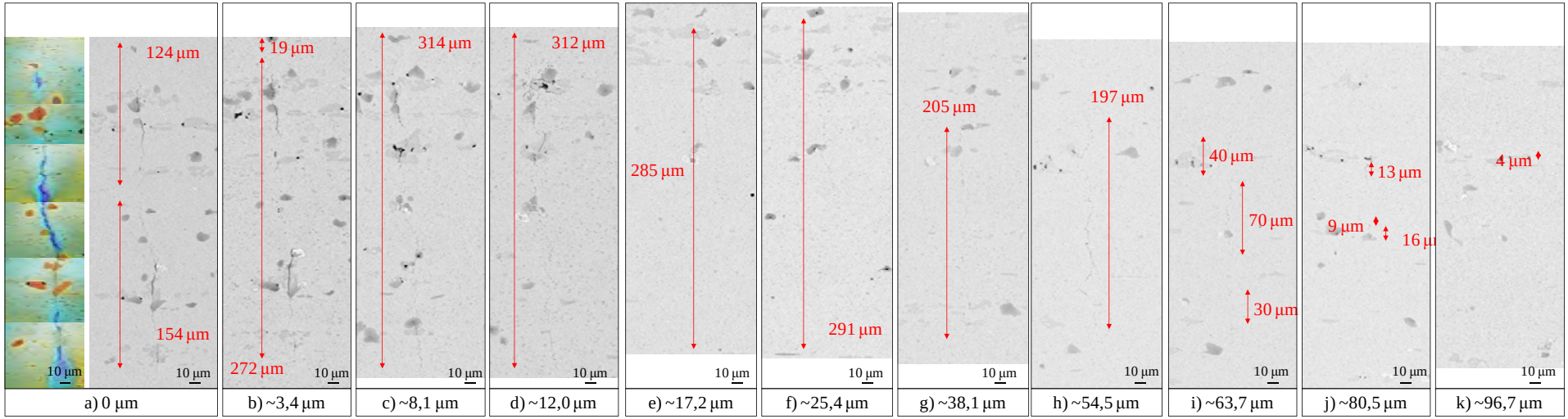

Figure 3.2.50 Stepwise polishing results of cracks number 2-3, from a) throughout k) sequence of crack images at increasing depths from the initial surface

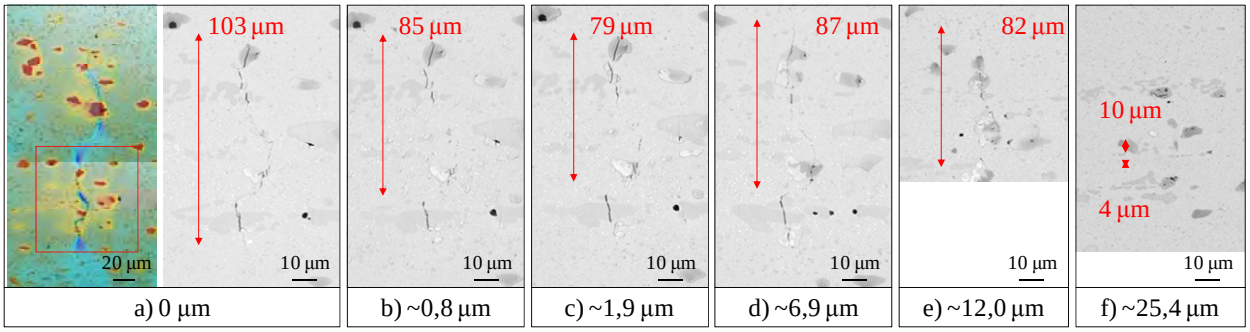

Figure 3.2.51 Stepwise polishing results of crack number 4, from a) throughout f) sequence of crack images at increasing depths from the initial surface

From the data collected in the previous figures, the geometry of cracks 1, 2-3 and 4 could be estimated respectively, as shown in Figure 3.2.52.

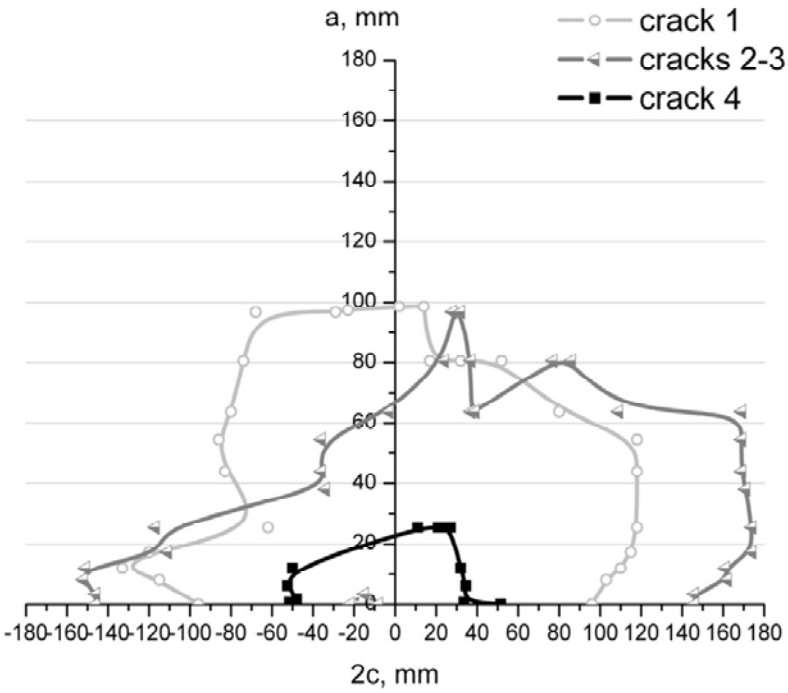

Figure 3.2.52 Geometry of cracks 1, 2-3 and 4 in terms of *a* (depth of the crack, or material removed at each polishing step) vs *2c* (length of the crack, or measured length at each polishing step)

Table 3.2.14 summarises for each of the studied cracks the local applied stress, σ_a, the length of the crack at the surface, *2c*, its total depth, *a*, the corresponding *a/c* ratio and the calculated applied stress intensity factor, K_a. As shown in Figure 3.2.52, crack geometries are rather tortuous and since it is difficult to determine objectively *a* values, they are calculated as the minor axis of the equivalent semi-ellipse which fits the plot of each crack. To estimate K_a of cracks 2 and 3, the small discontinuity which separates them at the surface is not considered, so it is assumed that they form only one crack.

Table 3.2.14 Local applied stress, σ_a, length of the crack at the surface, *2c*, its total depth, *a*, the corresponding *a/c* ratio and the calculated applied stress intensity factor, K_a, for each one of the cracks studied

Crack	σ_a, MPa	*2c*, μm	*a*, μm	*a/c*	K_a, MPa·m$^{1/2}$
1	2604	192	96	1,00	32[(1)]
2-3	2217	292	73	0,50	23
4	2501	103	21	0,41	13

[(1)] K_a is higher than K_{IC} of UNIVERSAL D2 (32 vs 29 MPa·m$^{1/2}$) even though this sample does not fail. This can be understood by the heterogeneity of microstructures that characterise ingot cast steels (even if the same materials and configurations are considered), but also due to the experimental error when estimating the amount of removed material (i.e. *a* values) measuring the diameters of the Rockwell indentations

As follows from these results and in agreement with the work of Gomes et al., non propagating cracks, i.e. cracks having not yet gone out from the limits of the carbide band, are initially shallow (like crack number 4), but the propagating ones, i.e. cracks crossing the matrix band, tend to evolve to $a \sim c$ before fracture (like crack number 1). From this standpoint, an interesting observation is that assuming that cracks 2 and 3 have completely coalesced, what it would have been expected in fact, if the test was followed to higher loads, the whole geometry of the crack is that of *a/c* 0,5, as shows Table 3.2.14. However, Figure 3.2.53 shows that in agreement with the aforementioned arguments, if the two original cracks are considered separately, crack number 2 which is confined within its carbide band is quite shallow (*a/c* 0,41 as in case of crack number 4), while crack number 3 which has started propagating through the metallic matrix has nearly attained the semi-circular shape (*a/c* 0,90, very close to 1).

Table 3.2.15 Length of the crack at the surface, *2c*, its total depth, *a*, the corresponding a/c ratio for cracks number 2 and 3

Crack	*2c*, μm	*a*, μm	*a/c*
2	124	26	0,41
3	154	69	0,90

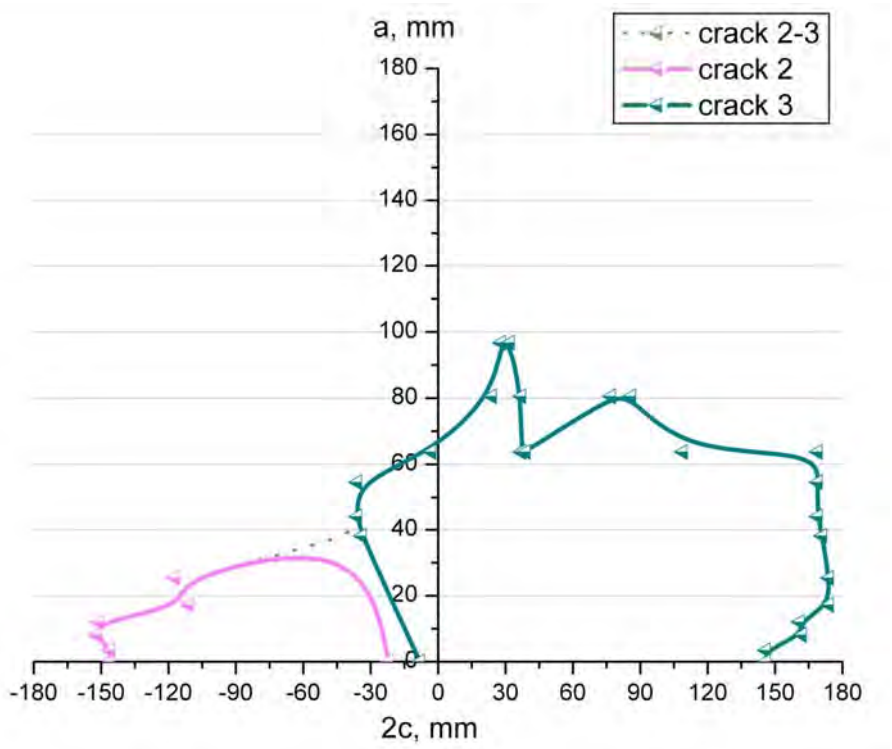

Figure 3.2.53 Estimated geometry of cracks number 2 and number 3

The longest cracks, such as number 1 or number 3 are difficult to be observed at the surface by means of stepwise monotonic tests because they rapidly lead to fracture instability, and this may explain why they could not be detected by Gomes et al. Therefore, only by coupling acoustic emission techniques and analysing the type of signals registered it is possible to successfully anticipate unstable failures and stop tests when crack are still propagating. This information is precious shedding light to the effective crack geometries before unstable fracture under monotonic loads and to well estimate the *R*-curve behaviour.

Cracks are initially shallow while they are kept within a carbide band, but they tend to evolve towards more stable forms of propagation such as that of $a = c$ as the load progressively increases. However, given the high number of cracks nucleated at different zones of the surface, coalescence of cracks (as it occurs with cracks number 2 and 3) is very likely to take place. When two or more cracks coalesce, the shape of the resulting crack is deviated from the equilibrated $a = c$ since the crack length at the surface may increase further than its depth (the length of the resulting crack is the sum of the initial ones, but the depth is that of the deepest crack).

The shape of the crack (a/c ratio) determines the K values at 0º and 90º from the surface. The computation of K^{90} and K^{0} for shallow cracks ($a/c < 1$) gives $K^{90} > K^{0}$, meaning that shallow cracks grow preferentially perpendicular to the surface and in consequence, the a value increases faster than the c one. When the ratio a/c approaches to 1, then K^{90} and K^{0} are similar and so it is the crack growth in 90º and 0º directions.

The final geometry of cracks is strongly influenced by the local microstructure ahead of the crack tip. The reasons why some cracks would run deeper and faster than some others can be related on the one hand, to the size of the carbide band in which they are initially embedded but on the other, to the probability of finding the next carbide band. For instance, Figure 3.2.49 shows that crack number 1 encounters practically no obstacles (i.e. other bands of carbides) from 17,24 μm to 80,54 μm in depth, meaning that it can propagate stably through the matrix. The same applies for crack 3, since as shown in Figure 3.2.50, from 12,01 to 80,54 μm there are no major microstructural impediments ahead of the crack tip. Both cracks number 1 and number 3, the only cracks which propagate through the matrix, are arrested just when encountering the next carbide band in the depth direction, while crack number 2 and 4 have not yet surpassed the initial carbide band in which they are nucleated.

Finally, propagating cracks show balloon-like shapes instead of the semi-circular ones typically assumed. As discussed in section 3.2.3, at the surface the matrix is under plane stress conditions while below this it is under plane strain. As a result, it has locally higher fracture toughness at the surface than inside the material and hereby, it is able to absorb more deformation before fracture. Thus, cracks propagate easier below the surface than what they expand on it, and this balloon shape is due to the fact that the matrix at the surface ahead of the crack tips is plastically deformed before cracking.

3.2.6.2 R-curve behaviour

R-curve behaviour of 1.2379, UNIVERSAL, K360 D2 and D3, and HWS D2 are assessed by measuring the increase of crack lengths at the surface of samples and estimating the corresponding K_a. Figure 3.2.54 plots the *R*-curve of these materials in D2 and in terms of K_a vs $\Delta 2c$. As the real geometry of cracks gradually turns from very shallow ($a/c < 1$) into semi-circular ($a/c = 1$) three possible *R*-curves are constructed for each material, assuming a/c 0,3, 0,5 and 1.

The sizes of halos measured in fatigue failed samples are included in *R*-curve plots in order to take into account K_a values of cracks longer than those observed under monotonic loads. As follows from the work of Casellas [CAS00], the law proposed by Evans (Equation 3.2.1) describes with good accuracy the *R*-curve behaviour in the following way:

$$K_a = K_0 + C_1 \cdot atan\left(\frac{\Delta a}{C_2}\right) \qquad (3.2.1)$$

Where K_0, C_1 and C_2 are constants relating K_a and Δa. (Note: according to the plots of K_a vs $\Delta 2c$ of Figure 3.2.54, this expression has been rewritten in terms of $\Delta 2c$ assuming a/c = 0,3, 0,5 or 1). K_0, C_1 and C_2 determined for 1.2379, UNIVERSAL, K360 and HWS D2 are summarised in Table 3.2.16.

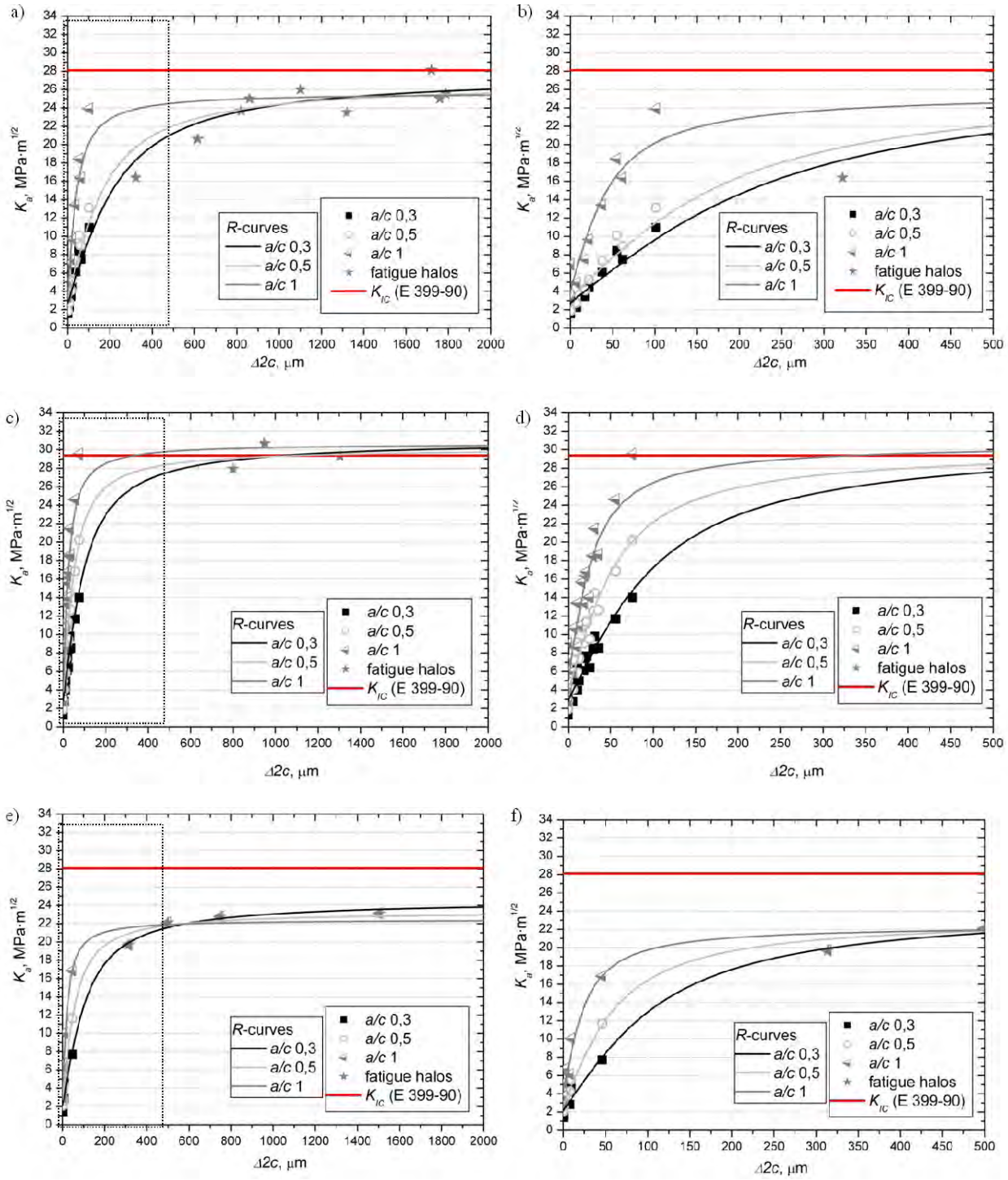
a)
b)
c)
d)
e)
f)
K_a, MPa·m$^{1/2}$
Δ2c, μm
R-curves
a/c 0,3
a/c 0,5
a/c 1
fatigue halos
K_{IC} (E 399-90)

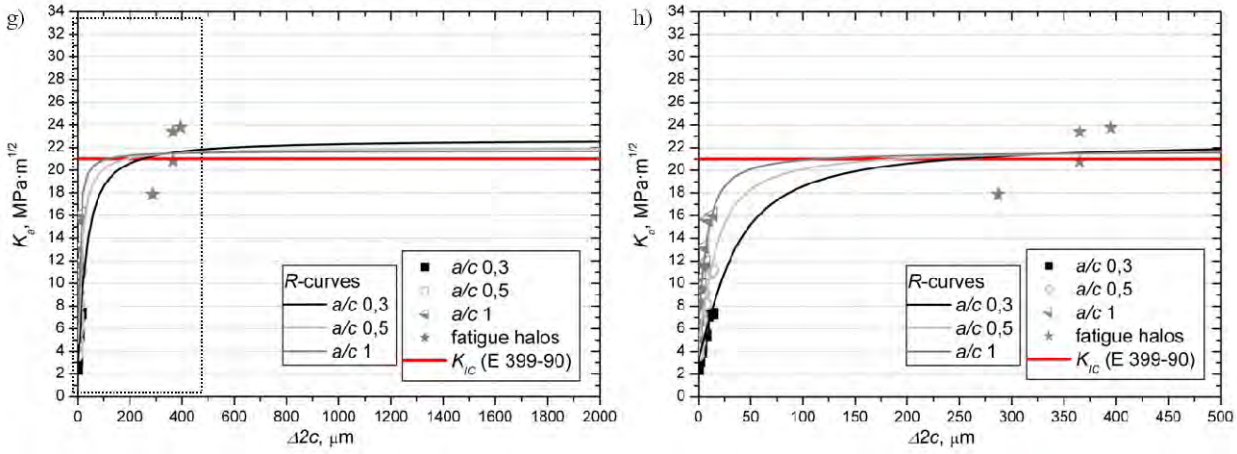

Figure 3.2.54 Estimated *R*-curves considering different *a/c* ratios (0,3, 0,5 and 1) for the studied steels: a) 1.2379 D2 and b) zoom in 1.2379 D2; c) UNIVERSAL D2 and d) zoom in UNIVERSAL D2; e) K360 D2 and f) zoom in K360 D2; g) HWS D2 and h) zoom in HWS D2

Table 3.2.16 Parameters of the Evans equation, K_0, C_1 and C_2, for the four considered steels in D2 configuration and for *a/c* equal to 0,3, 0,5 and 1

Crack	*a/c*	K_0, MPa·m$^{1/2}$	C_1, MPa·m$^{1/2}$	C_2, µm
1.2379 D2	0,3	2,8 ± 0,6	15,1 ± 0,1	217,7 ± 35,4
	0,5	3,2 ± 0,8	15,3 ± 0,6	165,6 ± 32,8
	1	4,1 ± 1,3	13,3 ± 1,4	42,4 ± 11,4
UNIVERSAL D2	0,3	2,9 ± 0,4	17,9 ± 0,5	96,9 ± 9,5
	0,5	3,8 ± 0,54	16,8 ± 0,6	51,8 ± 5,4
	1	5,0 ± 0,9	16,3 ± 1,0	26,6 ± 3,9
K360 D2	0,3	2,1 ± 0,3	14,7 ± 0,4	106,2 ± 14,3
	0,5	2,8 ± 0,2	13,1 ± 0,3	58,2 ± 6,5
	1	4,3 ± 0,7	11,6 ± 0,6	23,8 ± 5,9
HWS D2	0,3	3,2 ± 0,4	12,4 ± 0,5	34,6 ± 8,6
	0,5	4,6 ± 0,5	11,1 ± 0,5	17,5 ± 3,3
	1	6,4 ± 0,6	9,8 ± 0,6	8,3 ± 1,5

As shown in Figure 3.2.55, K_0 is the K_a value of the initial crack, or in other words, the K_a of the crack at the initial broken primary carbide. C_1 and C_2 give information about the shape of the *R*-curve: its height and rising slope respectively. Higher C_1 values indicate higher K_a for a given $\Delta 2c$, while higher C_2 values indicate more pronounced *R*-curve behaviours (i.e. K_a depends more on the crack growth extent).

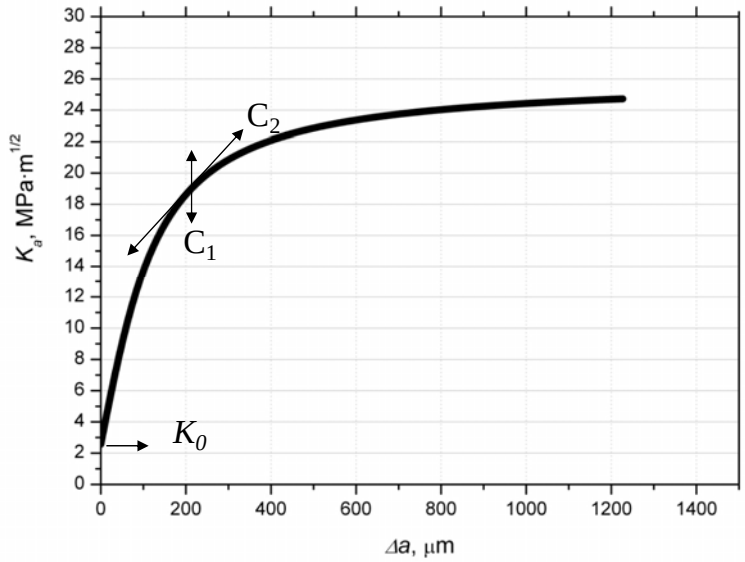

Figure 3.2.55 Significance of the parameters of the Evans equation on the *R*-curve

In Figure 3.2.54 it can be observed that even if the *R*-curves of *a/c* = 0,3, 0,5 and 1tend to converge to the same K_a at high $\Delta 2c$ values (i.e. for long cracks), at lower $\Delta 2c$ values shallow cracks (*a* /c = 0,3 and 0,5) have lower K_a values than semi-circular cracks (*a/c* = 1). That is to say, K_a values of semi-circular cracks have less dependency with respect to the crack size than shallow cracks, since semi-circular cracks attain the plateau at lower $\Delta 2c$.

Regardless of the *a/c* ratio, 1.2379 D2 shows a more rising *R*-curve behaviour (i.e. more dependency between K_a and $\Delta 2c$) than K360 D2 or UNIVERSAL D2. HWS D2, in turn, practically shows a flat *R*-curve, with the highest K_0 and the lowest C_2 values amongst the studied steels. 1.2379 D2 and K360 D2 attain the plateau in the *R*-curve at lower K_a values than K_{IC}, while in UNIVERSAL D2 and HWS D2 the plateau coincides with K_{IC}. This means that even for the longest cracks considered in *R*-curve plots, cracks in 1.2379 D2 and K360 D2 can lead to failure at lower K_a values than K_{IC}.

In Figure 3.2.54 it can be observed that the Evans equation fits quite well the experimental results of K360 D2 and HWS D2. However, in case of 1.2379 D2 and UNIVERSAL D2, the highest K_a values calculated for *a/c* = 1 deviate from the estimated *R*-curve (experimental results have higher K_a values than what is described by the Evans equation). That can indicate that either the considered cracks must have *a* < *c* in order to fit to the shape of the *R*-curve, or that the crack growth behaviour in these steels does not follow an *R*-curve of this type.

In order to assess the validity of the *R*-curves estimated for 1.2379 D2 and UNIVERSAL D2, Figure 3.2.56 re-plots their *R*-curves incorporating the halos of samples fractured monotonically in section 3.2.3, and 3.2.6.1 and cyclically in section 3.2.5.1. In Figure 3.2.56 a) it can be observed that in case of 1.2379 D2, both the sample fractured monotonically in section 3.2.3 (light grey dot with *a/c* 0,54), and the

sample with a fatigue precrack of section 3.2.5.1 (dark grey star with *a/c* 0,90), are well within the limits of the *a/c* 1 and a/c 0,3 *R*-curves. However, Figure 3.2.56 b) shows that in case of UNIVERSAL D2, samples fractured monotonically in section 3.2.3 (light grey dots with *a/c* 0,75 ± 0,07) and crack number 1 of section 3.2.6.1 (black rhombus with *a/c* 1) show K_a values higher than those described by the *R*-curve.

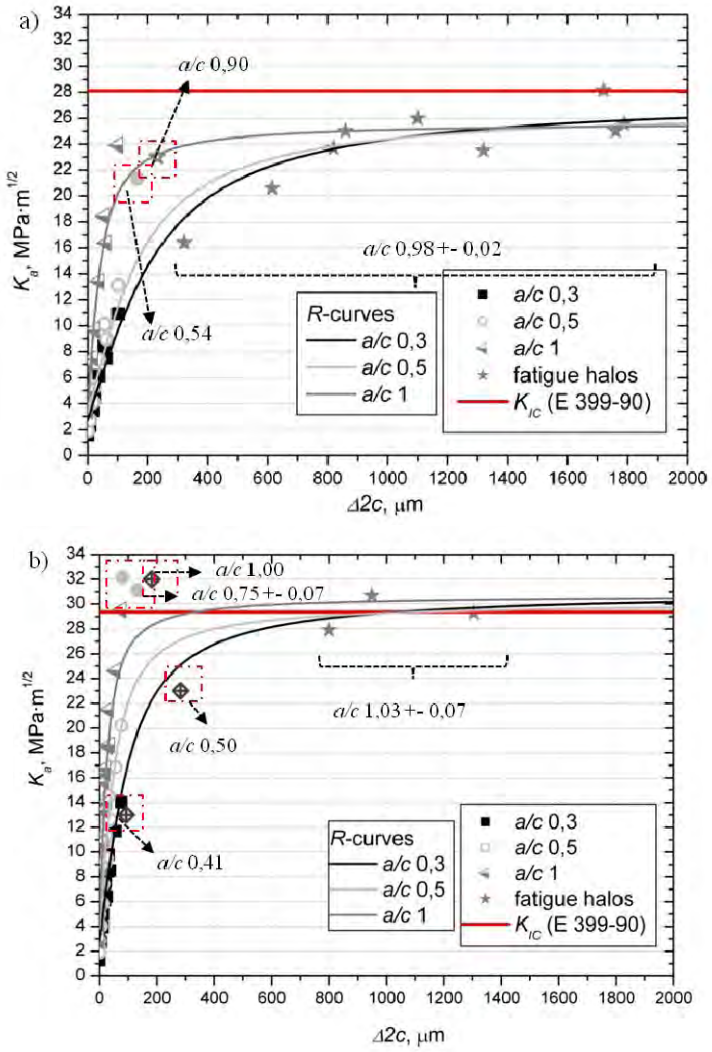

Figure 3.2.56 *R*-curve plots with the experimental results of sections 3.2.3, 3.2.6.1 and 3.2.5.1 for a) 1.2379 D2, with the results of samples broken in section 3.2.3 (light grey dot with *a/c* 0,54) and section 3.2.5.1 (dark grey star with *a/c* 0,90); b) UNIVERSAL D2 with the results of samples broken in section 3.2.3 (light grey dots with *a/c* 0,75 ± 0,07) and section 3.2.6.1 (dark grey rhombi with: crack number 1 *a/c* 1, crack number 2-3 *a/c* 0,50 and crack number 4 *a/c* 0,41)

This seems to indicate that in case of UNIVERSAL D2 and likely in case of 1.2379 D2, *R*-curves may be steeper than predicted by the Evans equation. Nevertheless, it must be taken into account that the measurement of halos in samples fractured monotonically is always a source of experimental error and can explain the slight deviations between K_a values and modelled *R*-curves.

R-curves of 1.2379, UNIVERSAL and K360 D3 are presented in Figure 3.2.57 and K_0, C_1 and C_2 parameters are summarised in Table 3.2.17. No K360 D3 samples were available to determine K_{IC}, but as K_{IC} of K360 D2 is almost the same as 1.2379 D2 (28 vs 29 MPa·m$^{1/2}$), it is assumed K360 D3 has the same K_{IC} as 1.2379 D3 (22 MPa·m$^{1/2}$). In D3 fracture is initiated at multiple sites and it is difficult to identify the failure origins and measure the corresponding halos. Even in fatigue samples the measure of halos is hardly possible. Thus, only data on cracks propagating at the surface before unstable fracture are used to plot the *R*-curves of Figure 3.2.57.

Despite the aforementioned limitations to estimate the *R*-curves, 1.2379, UNIVERSAL and K360 D3 show more rising *R*-curves than the respective D2.

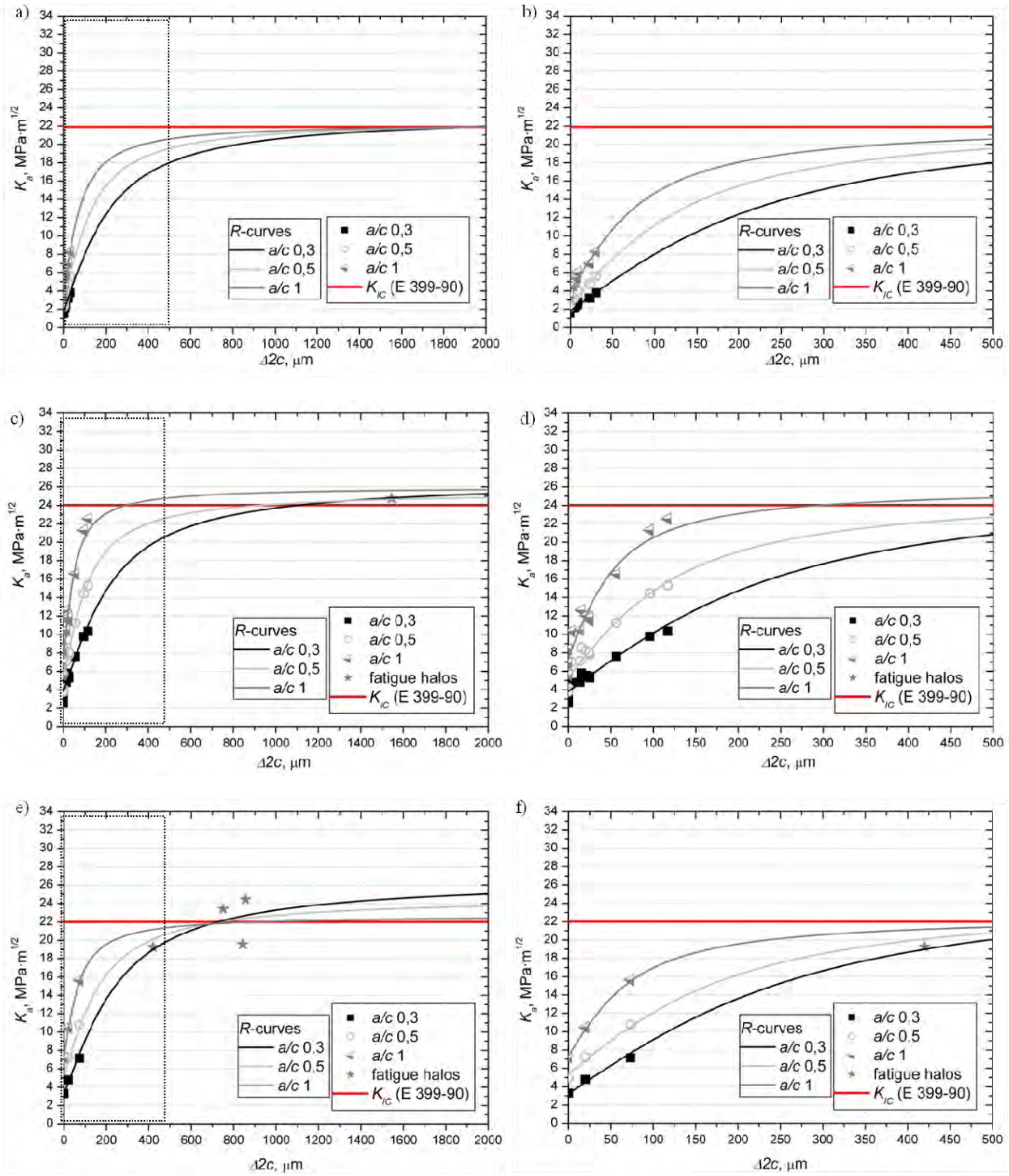

Figure 3.2.57 Estimated *R*-curves considering different *a/c* ratios (0,3 – 0,5 – 1) for the studied steels: a) 1.2379 D3 and b) zoom in 1.2379 D3; c) UNIVERSAL D3 and d) zoom in UNIVERSAL D3; e) K360 D3 and f) zoom in K360 D3

Table 3.2.17 Parameters of the Evans equation: K_0, C_1 and C_2, for the considered ingot steels in D3 configuration and for a/c = 0,3, 0,5 and 1

Crack	a/c	K_0, MPa·m$^{1/2}$	C_1, MPa·m$^{1/2}$	C_2, µm
1.2379 D3	0,3	1,8 ± 0,2	13,7 ± 0,2	205,8 ± 23,8
	0,5	2,7 ± 0,2	12,8 ± 0,2	127,8 ± 14,5
	1	3,9 ± 0,2	11,7 ± 0,3	77,0 ± 8,7
UNIVERSAL D3	0,3	3,8 ± 0,2	14,7 ± 0,5	226,9 ± 23,2
	0,5	5,4 ± 0,4	12,9 ± 0,7	112,5 ± 14,3
	1	7,5 ± 0,7	11,8 ± 0,9	50,3 ± 10,0
K360 D3	0,3	3,2 ± 1,4	15,0 ± 1,9	242,4 ± 28,4
	0,5	5,4 ± 1,8	12,3 ± 1, 9	165,8 ± 92,9
	1	7,4 ± 1,9	9,8 ± 1,4	66,8 ± 35,8

The K_a values at which unstable fracture occurs, from now on K_R, are estimated for different initial crack lengths, $2c_0$, and for a/c = 0,5 and 1 (a/c = 0,3 is not considered since as it was observed in section 3.2.6.1, final crack geometries are comprised between 0,5 and 1). As it can be observed in Figure 3.2.58 and 3.2.59 for D2 and D3 respectively, fracture instability corresponds to K_a in function of $\Delta 2c$ being tangent to the R-curve.

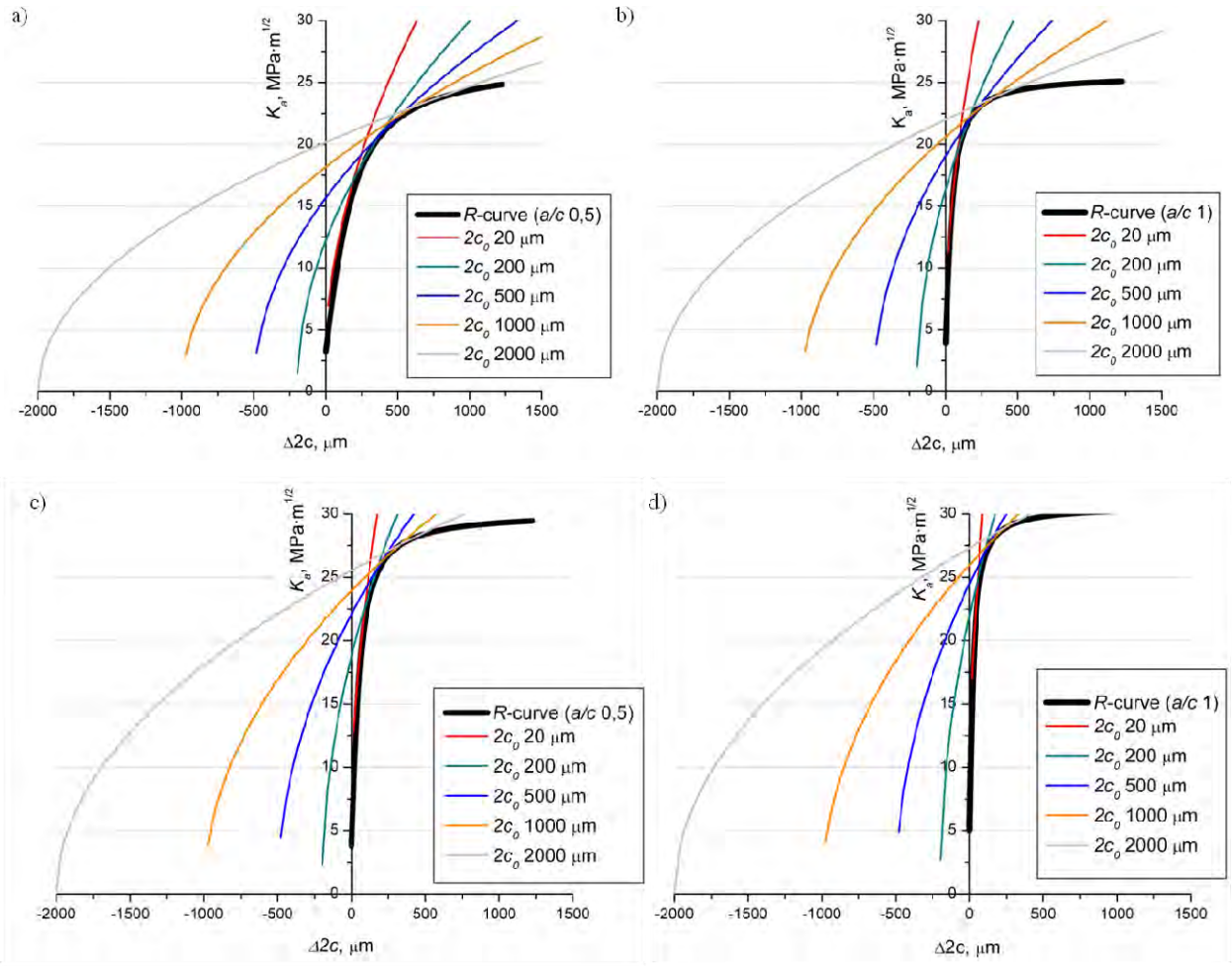

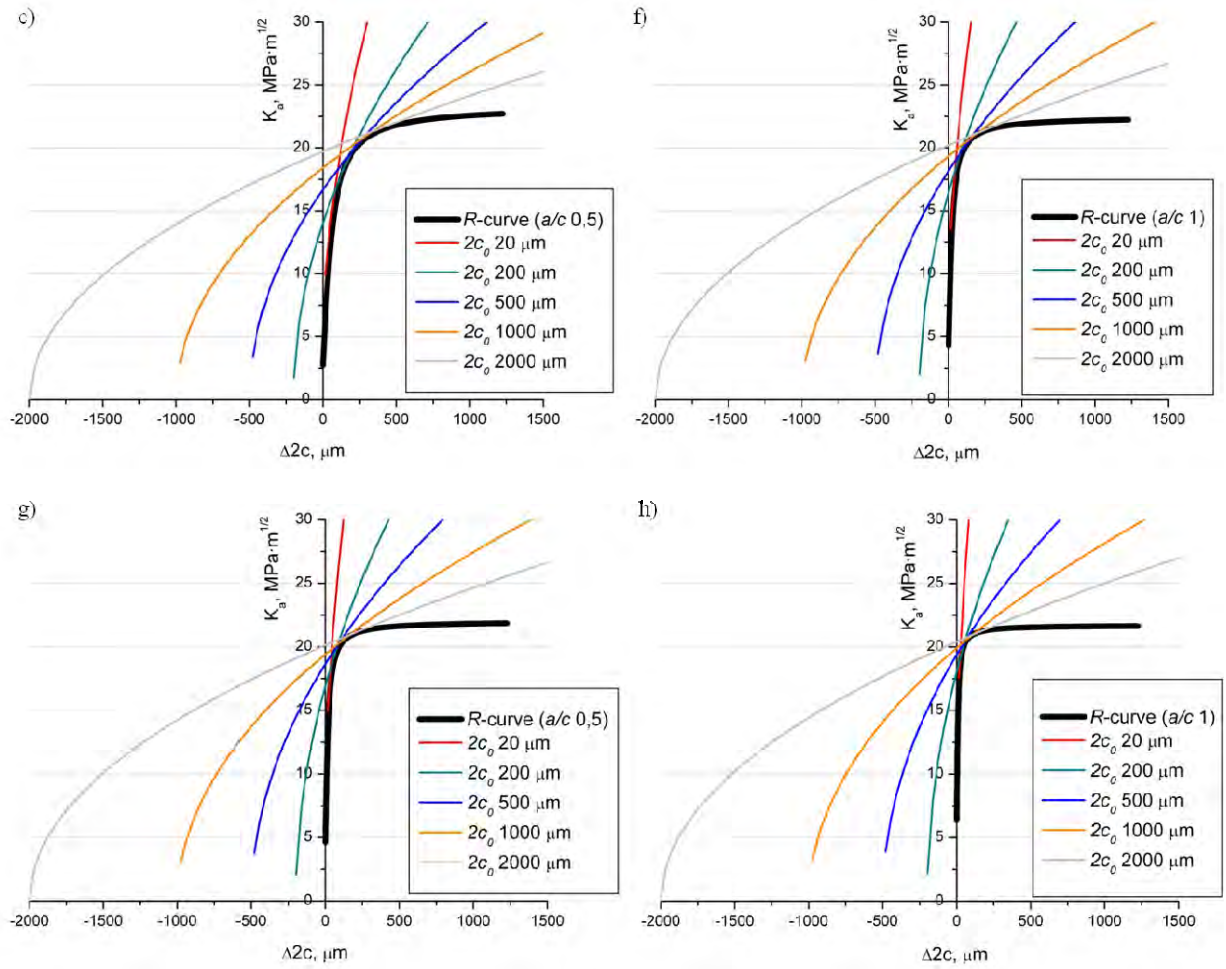

Figure 3.2.58 Unstable fracture for different initial crack lengths, $2c_0$, and *a/c* ratios: a) 1.2379 D2 and *a/c* = 0,5; b) 1.2379 D2 and *a/c* = 1; c) UNIVERSAL D2 and *a/c* = 0,5; d) UNIVERSAL D2 and *a/c* = 1; e) K360 D2 and *a/c* = 0,5; f) K360 D2 and *a/c* = 1; g) HWS D2 and *a/c* = 0,5 and h) HWS D2 and *a/c* = 1

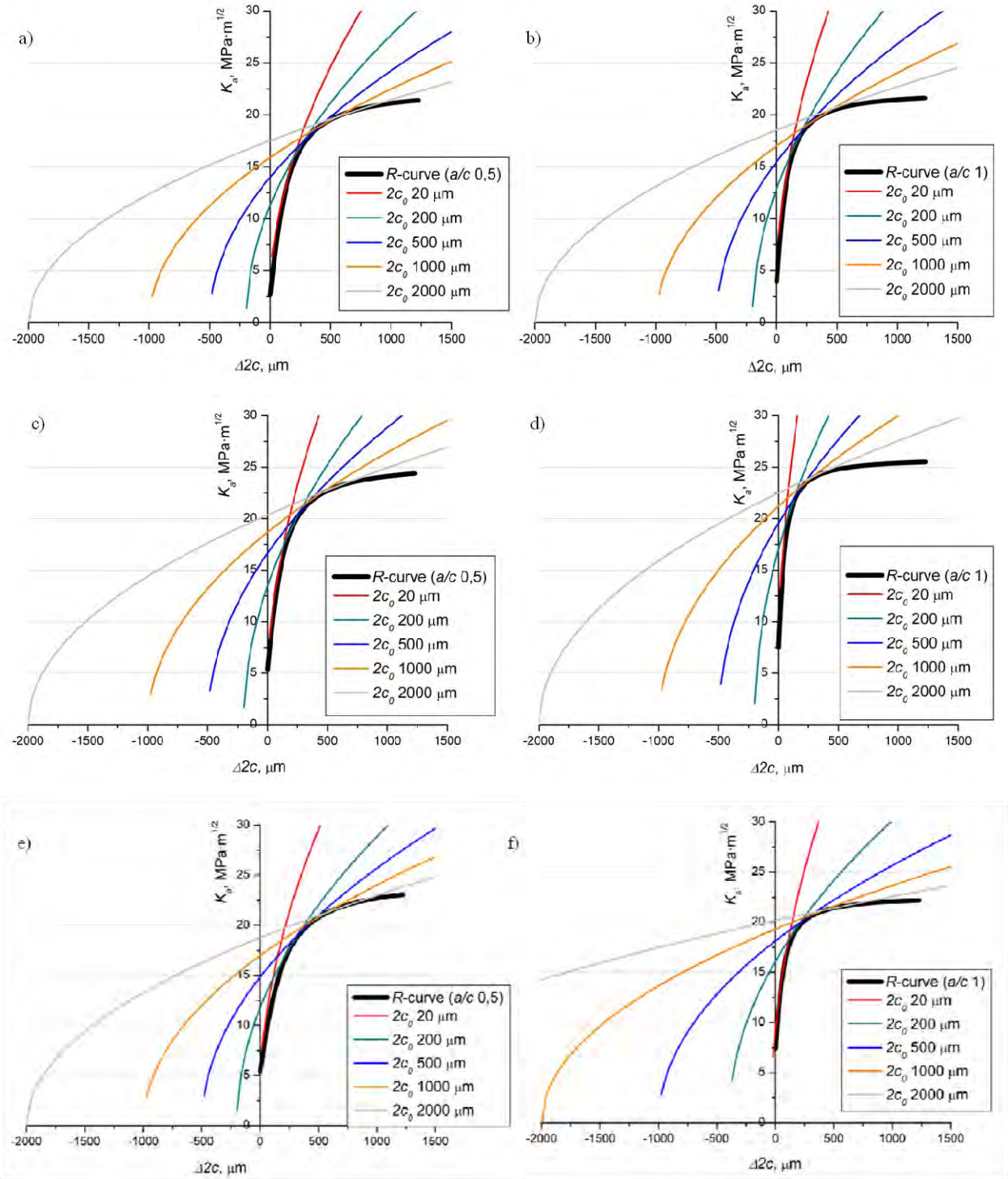

Figure 3.2.59 Unstable fracture for different initial crack lengths, $2c_0$, and *a/c* ratios: a) 1.2379 D3 and *a/c* = 0,5; b) 1.2379 D3 and *a/c* = 1; c) UNIVERSAL D3 and *a/c* = 0,5; d) UNIVERSAL D3 and *a/c* = 1; e) K360 D3 and *a/c* = 0,5; f) K360 D3 and = *a/c* 1

K_R as well as the applied stress corresponding to unstable fracture, σ_r, for the considered $2c_0$ values are plotted in Figures 3.2.60 a) and b) for a/c = 0,5 and 1 respectively.

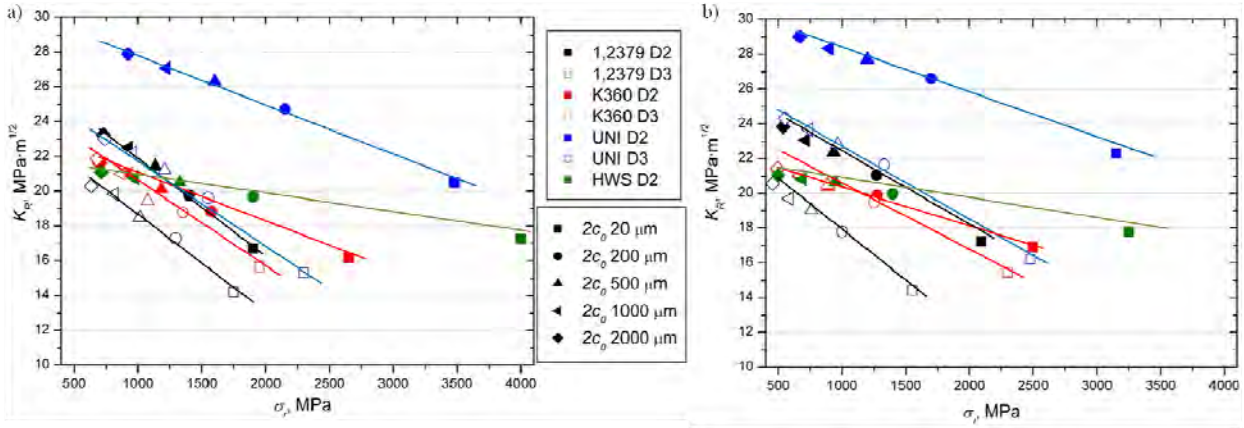

Figure 3.2.60 Applied stress intensity factors for unstable fracture, K_R, vs the corresponding applied stresses, σ_r, considering different $2c_0$ values: a) for a/c 0,5 and b) for a/c 1

As it can be observed in the previous figure, K_R in function of σ_r follows a linear inverse relationship which can be described by:

$$K_R = -A \cdot \sigma_r + B \tag{3.2.2}$$

where A and B are the fitting parameters. A describes the crack growth behaviour by the increase of K_R when σ_r decreases or $2c_0$ increases. In this way, a material with a flat R-curve shows an A parameter equal to 0 (meaning that K_R does not vary with the stress applied or the crack size), while the higher the A value, the higher the differences between K_R of small and large cracks (so the more rising the R-curve). In contrast, B lacks of physical meaning since if σ_r = 0 MPa, it has no sense to talk about K_R (i.e. Equation 3.2.2 is valid only if $K_R \leq K_{IC}$).

As theoretically K_{IC} is the maximum K_R at which cracks show fracture instability in materials with R-curve behaviour, Figure 3.2.61 plots K_{IC} in function of A for a/c = 0,5 and a/c = 1 respectively. The lower the A values, the more independent are toughness and the extent of crack length and the higher the K_{IC}, the higher is the toughness of long cracks.

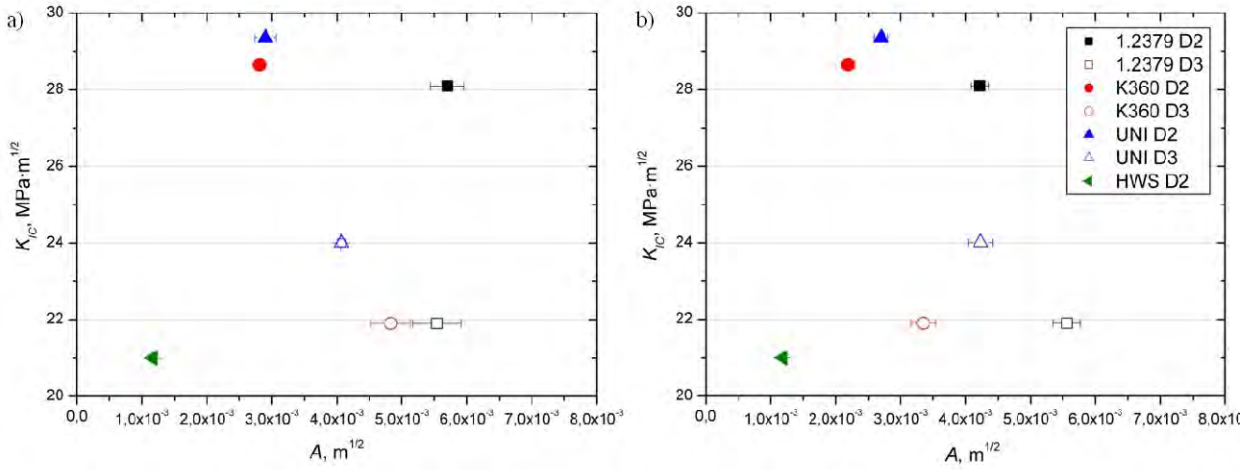

Figure 3.2.61 K_{IC} (E 399-90) in function of the A parameter: a) for a/c 0,5 and b) for a/c 1 (note that the K_{IC} value of K360 D3 was not calculated, in these diagrams it was assumed that it had the same value than in 1.2379 D3)

Thus, ideal materials are aimed at showing A close to 0 and K_{IC} as high as possible. However, none of the considered steels shows such a particular combination of A and K_{IC} values. 1.2379 D2 (full black squares) shows quite high K_{IC} but it also has one of the highest A). This means that if small cracks or high stresses are involved in the fracture process, the effective toughness is considerably reduced compared to that measured for long cracks. K360 D2 (full red dots) has a similar K_{IC} to 1.2379 D2, but A is lower. This means that even if K_{IC} of these two steels is similar, if small cracks or high loads are involved in the fracture process, cracks in K360 can show fracture instability at higher effective toughness than 1.2379 D2.

UNIVERSAL D2 (full blue triangles) shows the highest K_{IC} value (so the highest toughness for long cracks), and its A value is similar to that of K360 D2. Thus, UNIVERSAL D2 shows the closest to ideal behaviour amongst the ingot steels considered. HWS D2 (full green triangles), in turn, shows very low A values according to the practically flat R-curves observed, which mean that small cracks in HWS D2 already develop the K_{IC} values calculated for long cracks. However, K_{IC} of this steel is rather low compared to the values of the ingot steels.

In case of 1.2379, UNIVERSAL and K360 D3, it must be recalled that the results plotted in Figure 3.2.57 give an orientation of the behaviours but they cannot be used to ascertain the materials' behaviours (as a low amount of experimental data was available to plot the R-curves). Nevertheless, it can be observed that the A parameter in all D3 cases is higher than the corresponding in D2. Thus, D3 is more sensitive to the behaviour of small cracks than D2 since R-curves are more rising.

In conclusion, the results of this part of the Thesis indicate that R-curves must be taken into consideration in ingot cast steels, especially in case of 1.2379 and K360, since if small cracks or high stresses are involved in the fracture process, fracture instability can occur at lower K_R than K_{IC} (which is the property

typically measured to assess the fracture toughness of tool steels). HWS shows a practically flat *R*-curve with very low dependency of K_R with the applied stress or the initial crack size. As it follows from this observation and although K_{IC} of HWS is lower than that of ingot cast steels, it is possible that if small cracks are concerned HWS shows higher toughness than ingot cast steels. Then this chapter evidences that the behaviour of materials in front of small cracks can be different than that governed by the nucleation and growth of long cracks. Thus, when it comes to design considerations, the effective material properties for small cracks must be regarded in order to optimise the performance of the final application of the material.

3.3 Mechanical and tribological behaviour of tools working in industrial conditions

3.3.1 Main failure mechanisms of tools in forming and shearing operations

The main failure mechanisms observed in tools for forming and shearing UHSS can be summarized in fracture and wear related phenomena, as detailed below:

- Fracture by fatigue: when the nucleation of cracks at the subsurface and their growth under the cyclically applied loads makes them come to the surface (Figure 3.3.1 a)). Large fatigue cracks are also be observed, as shown in Figure 3.3.1 b), when being initiated at the surface from machining grooves or wear patterns, they propagate inwards up to fracture (cracks change their direction of growth to 45º from the crack plane, and/or they coalesce with perpendicular crossing cracks).

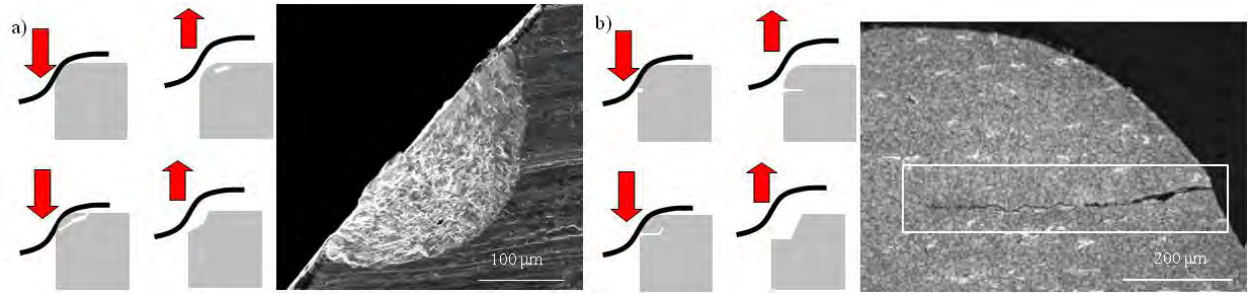

Figure 3.3.1 Fracture by fatigue: a) when cracks are nucleated at the subsurface and grow to come to the surface and b) cracks initiated at surface flaws propagate inwards

- Micro-chipping: this mechanism consists in the nucleation, coalescence and growth of many microcracks in the microstructure under the high cyclic applied loads (Figure 3.3.2).

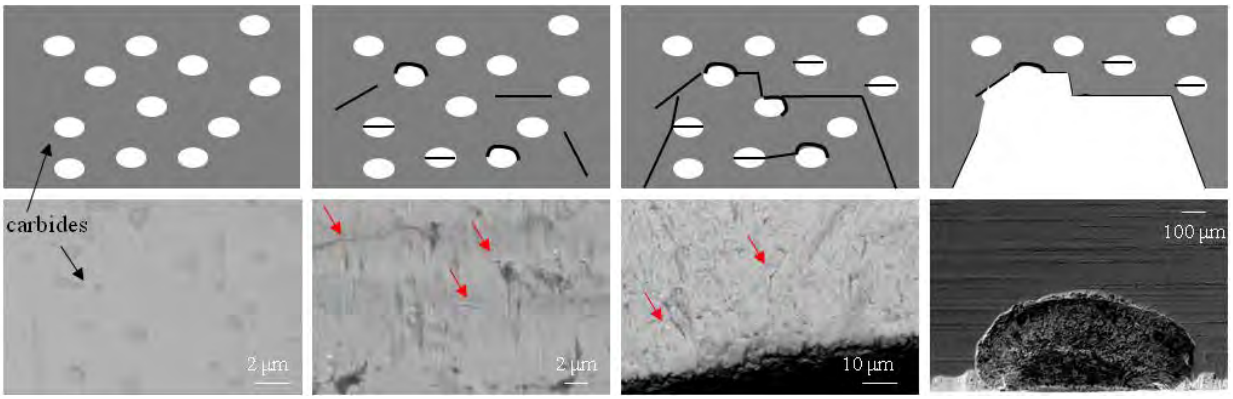

Figure 3.3.2 Micro-chipping in PM steels: many cracks nucleate from broken carbides, decohesion at the carbide-matrix interface and in the metallic matrix; the cracks coalesce and grow to final fracture

- Chipping: when fracture takes place after very short numbers of strokes, i.e. in low cycle fatigue (LCF) regimes, due to overloads, local stress magnifications and stress concentrators (sharp-angled shearing edges), or lack of toughness at the surface, i.e. if the heat treatment was not the appropriated for the application) (Figure 3.3.3 a)).
- Plastic deformation and sinking: opposite to chipping, plastic deformation and most of times, sinking in, takes place because of the lack of hardness of the tool steel, i.e. the heat treatment was not the appropriated for the application (Figure 3.3.3 b)).

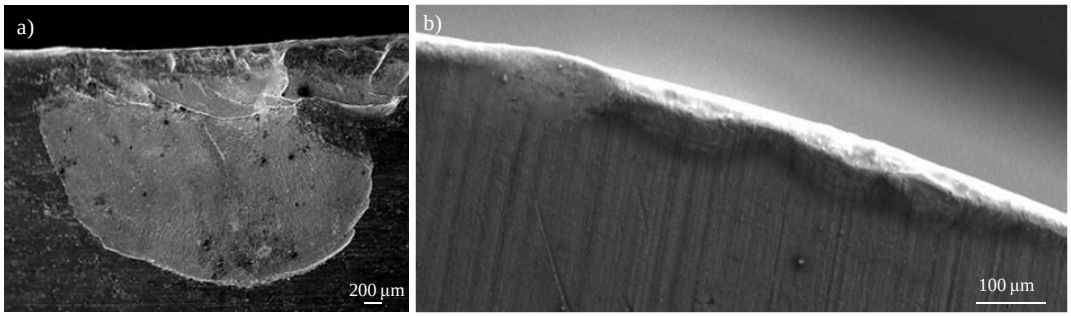

Figure 3.3.3 a) Chipping; b) plastic deformation at the cutting edge and sinking in

- Accidents: or fractures due to sheet debris entrapped between tools, presence of threads, holes and all types of stress concentrators (Figure 3.3.4 a)).
- Fracture due to machining defects (grooves and craters): they act like stress concentrators and shorten the time for crack nucleation (Figure 3.3.4 b)).

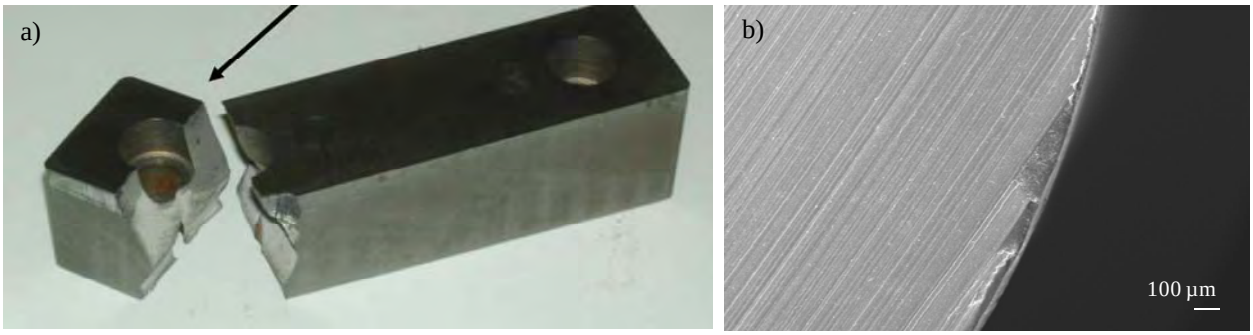

Figure 3.3.4 a) Fracture due to the presence of threads; b) fracture due to machining grooves

- Abrasive wear: when abrasive particles, such as oxides, contact to the tools (that is especially important in non-coated sheets) (Figure 3.3.5 a)).
- Adhesive wear: when the sheet material (usually coated) adheres to the tool surface. Adhesive wear can lead to local decreases of clearance, which increases the stresses in tools and accelerates fracture (Figure 3.3.5 b)).
- Severe wear (adhesive + abrasive): it takes place when contact pressures at the tools surface are extremely high (Figure 3.3.5 c)).

Figure 3.3.5 Wear related phenomena in tools: a) abrasive wear; b) adhesive wear; c) severe wear (abrasive + adhesive)

3.3.2 Characterization of the damaging processes and their evolution with the number of strokes in tools working in industrial conditions: relationship between the microstructure and the failure mechanisms of tool steels

The aim of this section is to identify the most relevant failure mechanisms acting in tools during different forming operations of UHSS carried out under industrial conditions and understand the underlying mechanisms from a microstructural point of view. For that, the three different tests described in section 2.5.2 will be discussed respectively in sections 3.3.2.1, 3.3.2.2 and 3.3.2.3.

3.3.2.1 Trimming of press hardened boron steel, 2 mm thick (at SEAT S.A.)

The damaging mechanisms observed in tools for trimming press hardened steel are different depending on the tool steel employed. A detailed SEM examination shows that after 10000 strokes, the cutting edge of tools made of HS6-5-4 (AISI M4) and DIN 1.3202 (AISI T15) is severely affected by fracture and wear. Some zones are fractured (as shown in Figure 3.3.6 a)), while in others many cracks are observed (Figure 3.3.6 c)). Two types of mechanisms can explain the presence of these fractures and cracks: on one hand, local overloads at the cutting edge (presence of sheet welded joints, vibrations due to load recovery after cutting, accidents, entrapment of particles, lack or inhomogeneous clearance, etc.), and on the other hand, nucleation and propagation of cracks by low cycle fatigue.

Severe wear is also observed at the surface with mixed patterns of abrasion and adhesion. Figure 3.3.6 b) shows that sheet metal and Al-Si coating material are weld at the surface of the HS6-5-4 tools, while the abraded surface of 1.3202 tools reveals the small carbides embedded (Figure 3.3.6 d)).

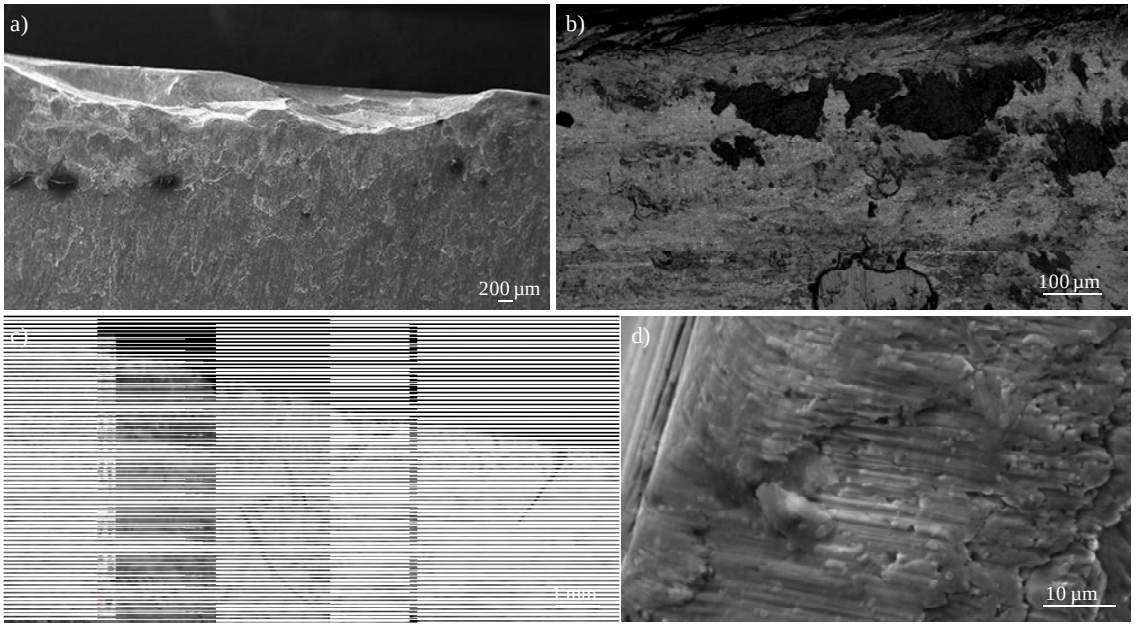

Figure 3.3.6 Damage at the cutting edge: a) fracture and b) wear (adhesion of sheet metal and Al-Si material) in HS6-5-4 tools; c) cracks and d) abrasive wear at the surface of 1.3202 tools

After 10000 strokes, VANADIS 4 EXTRA and HWS in turn, show damage due to plastic deformation as well as accelerated wear at the cutting edge (mainly loss of sharpness). In Figures 3.3.7 a) and b) plastic deformation of VANADIS and HWS tools is shown respectively. No fractures are observed at the cutting edge of HWS, while the corner of the B tool of VANADIS is broken, as it can be observed in Figure 3.3.7 c). Figure 3.3.7 d) shows that the cutting edge of HWS is rounded.

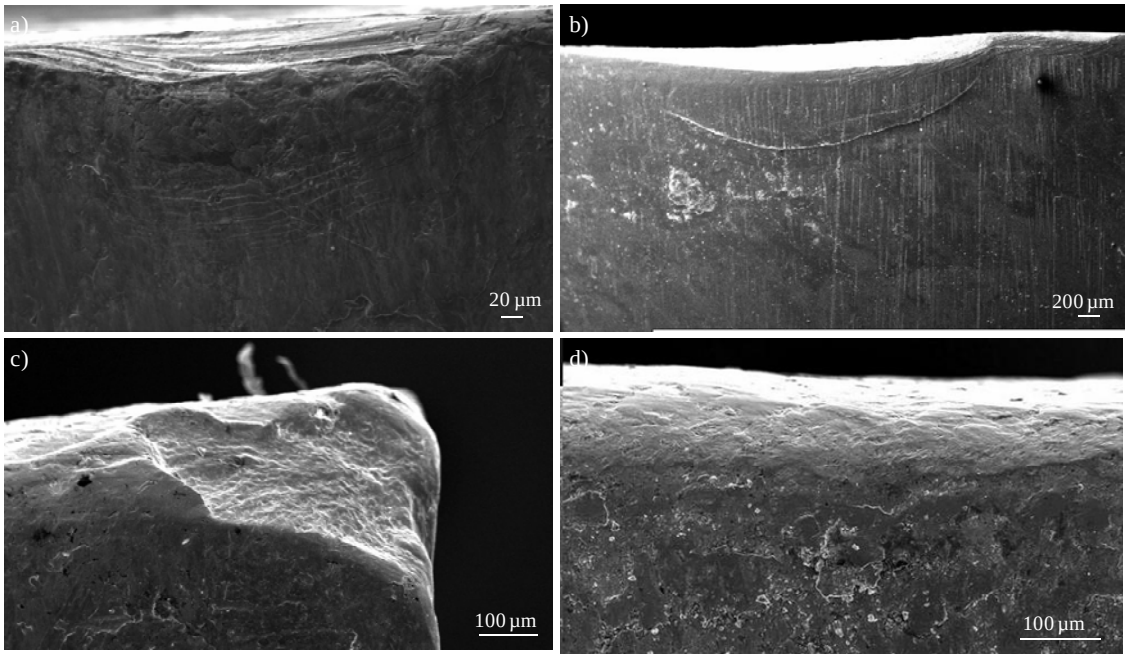

Figure 3.3.7 Damage at the cutting edge: plastic deformation at a) VANADIS 4 EXTRA and b) HWS; c) breakage of VANADIS 4 B tool and d) loss of sharpness of HWS tools

Figure 3.3.8 a) shows the maximum values of von Mises stresses registered at each node during one stroke of the cutting operation. It can be observed that in the most mechanically demanded zone (at the corner of the B tool) von Mises stresses estimated by means of FE exceed the 2500 MPa. This result is in agreement with the experimental observations at the cutting edge, since fractures take place in this zone (see Figures 3.3.8 b), d) and e) in case of HS6-5-4, VANADIS 4 EXTRA and 1.3202 respectively). In contrast, HWS shows good resistance against fracture, as shown in Figure 3.3.8 c). However, not only the stresses at the corner of B tools are high, but also the values registered all along the cutting edge are far from negligible (around 1600 - 1700 MPa). Such high stress values repeatedly applied with each stroke may explain the accelerated failure of these tools.

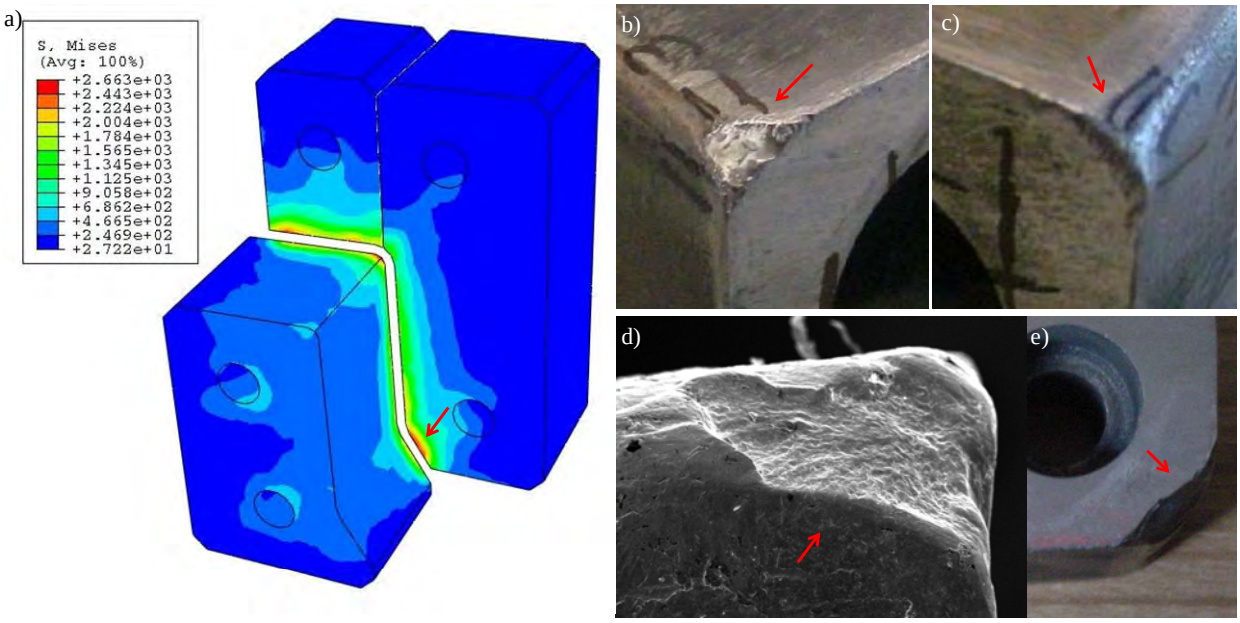

Figure 3.3.8 a) Von Mises stresses determined by means of FE-simulation; corner of the B tool b) HS6-5-4, c) HWS, d) VANADIS 4 EXTRA and e) 1.3202

The reason for the different failure mechanisms observed may lie in the different hardness levels of tools. As it was reported by Horton and Child [HOR83], hardness influences toughness in an inverse proportional manner, i.e. high hardness values use to correspond to low toughness and vice versa. This statement is completely in agreement with the experimental findings of this investigation, where HS6-5-4 tools at 63 – 65 HRC are extremely sensitive to breakage and HWS at 59 – 60 HRC show almost no cracks but plastic deformation instead.

A detailed inspection of the surface near the cutting edge of tools reveals the presence of broken carbides, as shown in Figure 3.3.9 in red arrows for a) HS6-5-4 and b) 1.3202 respectively. As follows from the chemical composition of the tool steels and the backscattering diffraction data, fractures are observed mainly at V-Cr carbides (grey colour), while the white carbides (W and W-Mo carbides) do not seem to be damaged. Broken carbides could have acted as crack initiation sites, from which cracks could have started propagating to the surrounding matrix under the cyclic applied loads and led to the fractures observed at the cutting edge. In case of VANADIS 4 EXTRA and HWS, no broken carbides are observed despite they were not easily distinguishable due to the rounding and deformation at the surface near the cutting edge.

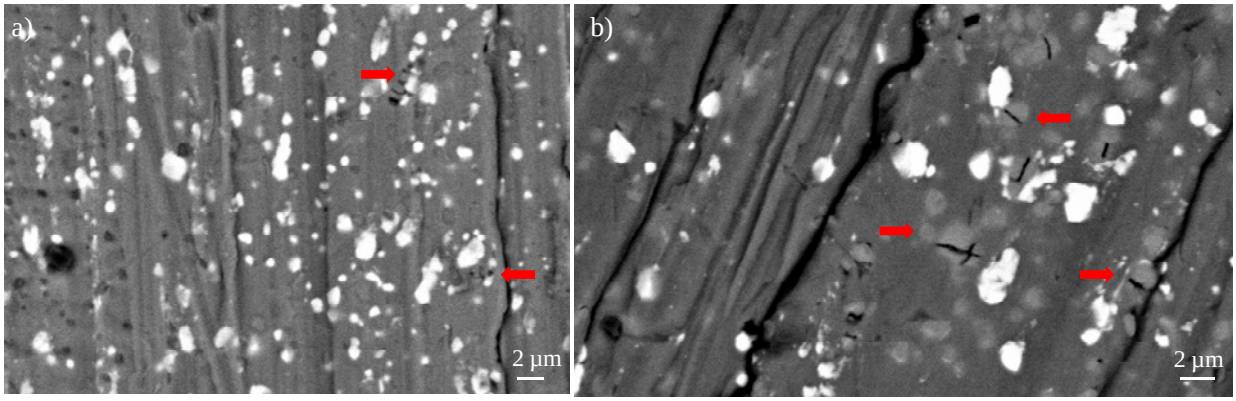

Figure 3.3.9 Broken carbides observed in the surface near the cutting edge: a) HS6-5-4 and b) 1.3202 tools

An estimation of the loss of material at the cutting edge was performed in B tools of HS6-5-4 and HWS steels after 2500 and 5000 strokes. Six different zones along the cutting edge were selected and the variation of area under the edge profiles was estimated with the increasing number of strokes, following the procedure described in section 2.5.1.

In Figure 3.3.10 it can be observed that the punch made of HWS has lost more material after 2500 and 5000 strokes than that of HS6-5-4. Therefore, tools with higher hardness values (as HS6-5-4) show good response against wear (in terms of material loss at the cutting edge, i.e. loss of sharpness) despite they suffer from early fractures by low cycle fatigue and chipping. In the meanwhile, tools with lower hardness values (as HWS) show poor surface integrity after a few strokes, but they are not damaged by chipping or fatigue. (Note: profiles obtained from fractured zones at the cutting edge of HS6-4-5 were not taken into account to evaluate the amount of material lost by wear in Figure 3.3.10 b)).

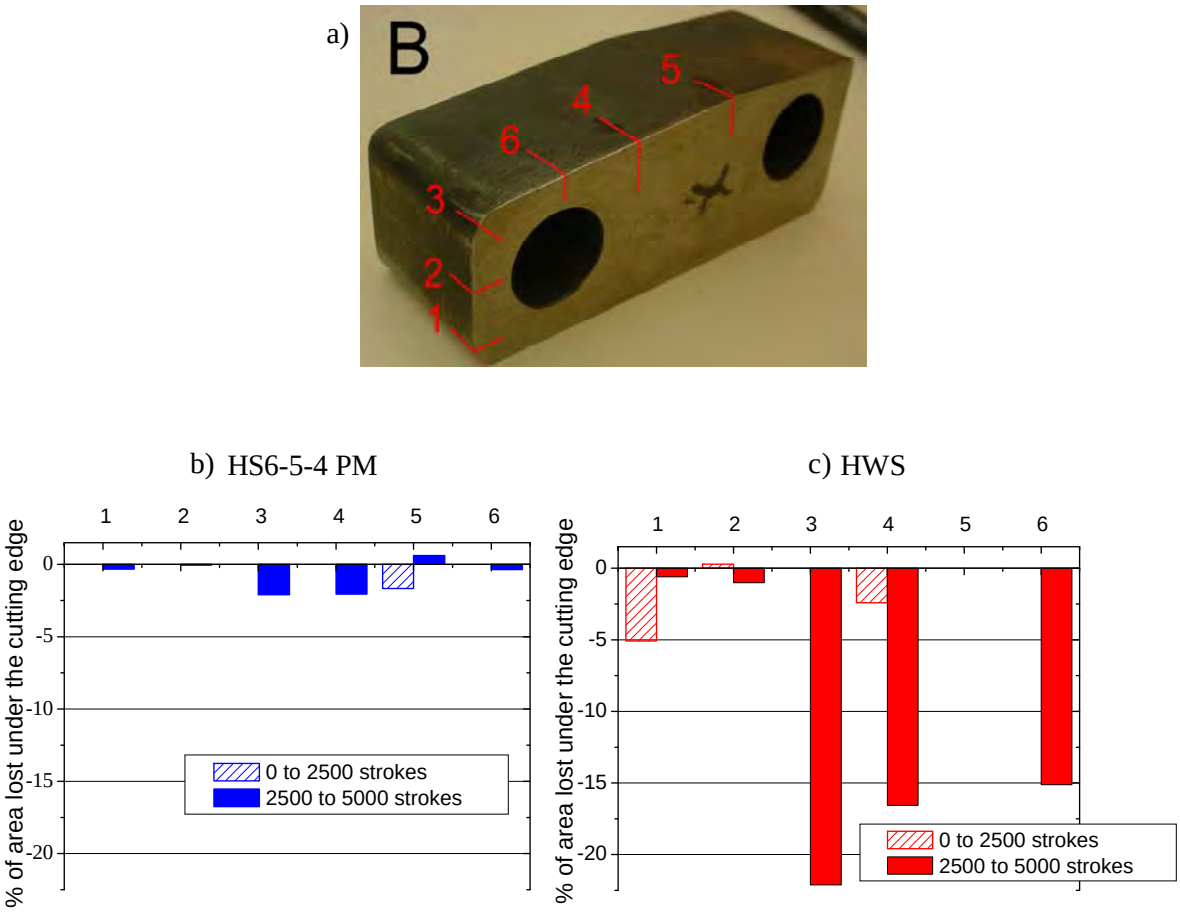

Figure 3.3.10 a) Schema of the studied zones at the B tool; b) variation of the area under the cutting edge for each zone after 2500 and 5000 strokes in HS6-5-4 and c) HWS

Therefore, the hardness level is relevant determining the mechanical and tribological behaviour of tools. A proper choice of the hardness is required to ensure the optimal relationship between fracture toughness, yield stress (which determines the onset for plastic deformation of the cutting edge) and wear (abrasion, adhesion and also material loss under the cutting edge). In addition, as only one type of primary carbides has broken, the micro-mechanical properties of these are also an important factor determining the presence of cracks in tools. In this sense, carbides with higher E, H, K_C and σ^{RC} are desired in the microstructure of tool steels.

The presence of large fractures at the cutting edge of HS6-5-4 and 1.3202, as well as the plastically deformed zones and loss of sharpness of VANADIS and HWS can generate burrs or large rollover and fracture zones at sheet edges. Thus, as a result of these tests punches with intermediate hardness of 62 HRC could help to obtain a good compromise between fracture and wear resistance.

3.3.2.2 Punching of MS-W1200, 2 mm thick (at AUTOTECH ENG.)

As described in section 2.5.2.2, four different sets of HWS punches at 62 HRC are studied with the objective to discern the evolution of damaging mechanisms at several increasing numbers of strokes. A first damage exploration by SEM in one of the sets after 15000 strokes shows that wear is the phenomenon with the most detrimental effects on the punch as shown in Figure 3.3.11.

In zone 1, two craters formed as a consequence of detachment of wear particles are present at the flank face (Figure 3.3.11 a)). Zones 2 and 3 (Figures 3.3.11 b) and c)) look similar to each other and show two types of surface damage: a highly worn and smooth surface near the cutting edge and a rougher one, starting from 400 μm below, produced by a combination of wear and local plastic deformation. This type of damage is also observed in zones 4 and 5 (Figures 3.3.11 d) and e)). Zone 6 shows the most severe damage since the sheet welded joints have larger dimensions and some of them have already detached (Figure 3.3.11 f)). In addition, cracks parallel to the cutting edge are also identified.

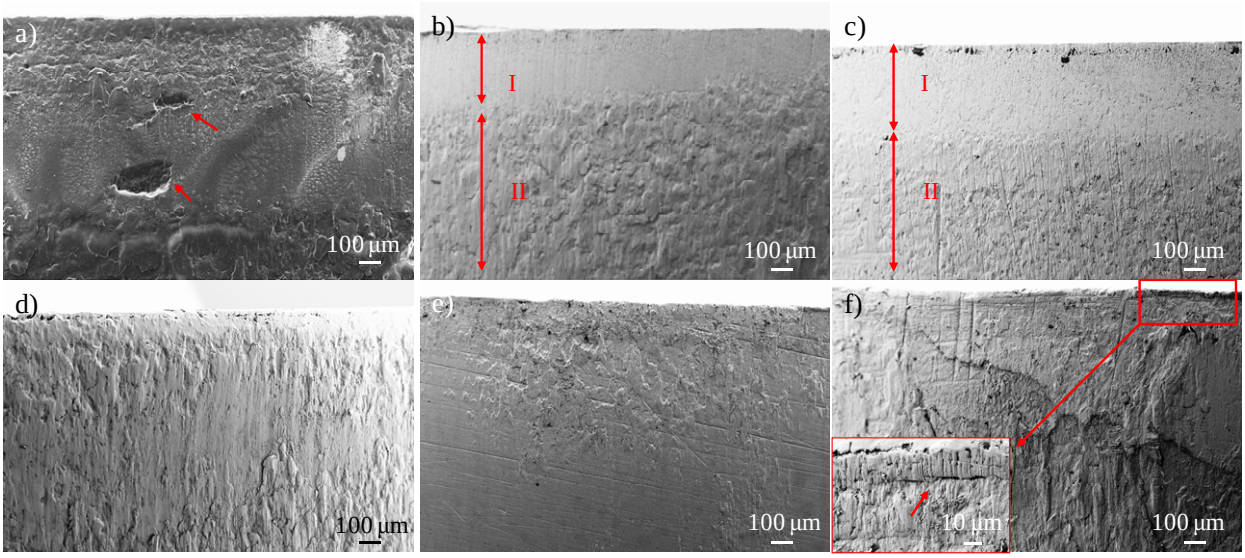

Figure 3.3.11 Damage at the flank face of the HWS 62 HRC punch after 15000 strokes: a) zone 1; b) zone 2; c) zone 3; d) zone 4; e) zone 5 and f) zone 6

Another set of tools was studied up to the 40000 strokes with an intermediate SEM examination at 9800 strokes (Figure 3.3.12). The flank face of the punch shows the same type of wear as in Figure 3.3.11, but in this case in a lower amount. Zone 1 and 2 show fractures and zones 3 and 5 show plastic deformation. Additionally, numerous cracks running parallel to the cutting edge are observed in zone 1 (Figure 3.3.12 a)). However, these cracks do not seem to be responsible of the fractures observed since as follows from the shape of fractures, they are likely produced during the grinding process (Figure 3.3.13).

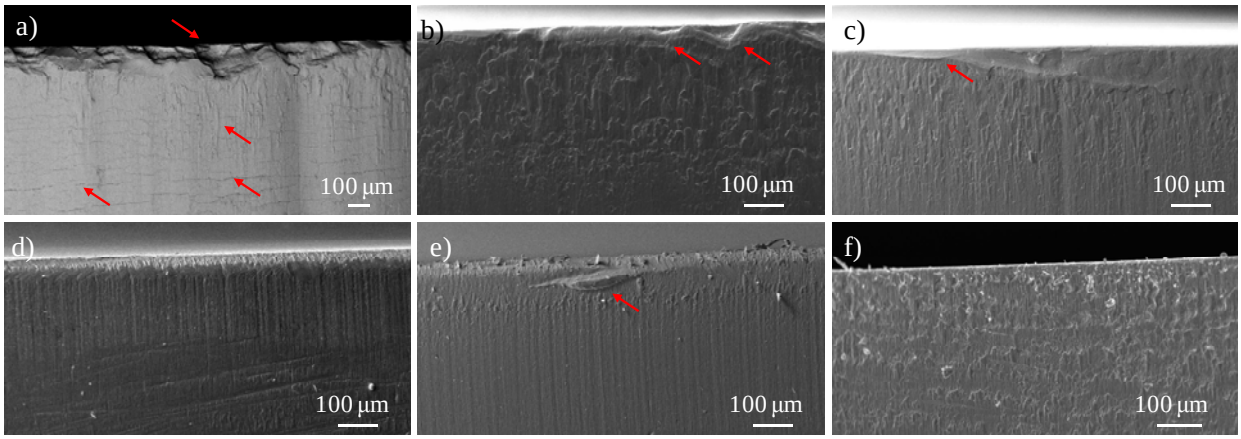

Figure 3.3.12 Damage at the flank face of the HWS 62 HRC punch after 9800 strokes: a) zone 1; b) zone 2; c) zone 3; d) zone 4; e) zone 5 and f) zone 6

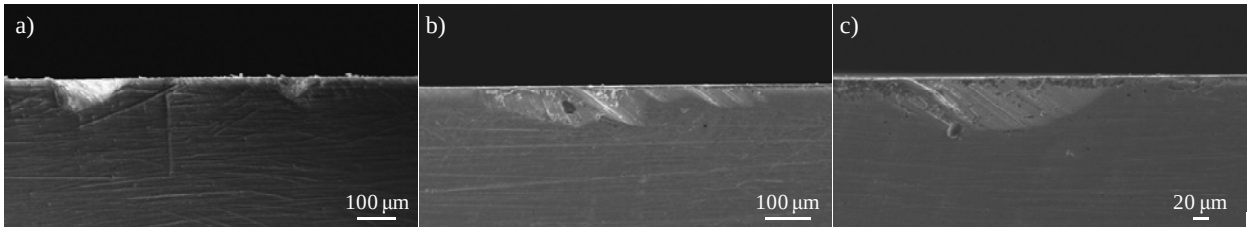

Figure 3.3.13 Damage at the flank face of the HWS 62 HRC punch at its initial state: a) zone 1; b) zone 5 and c) zone 6

After 40000 strokes wear is more accentuated, as shown in Figure 3.3.14. But no additional fractures are observed.

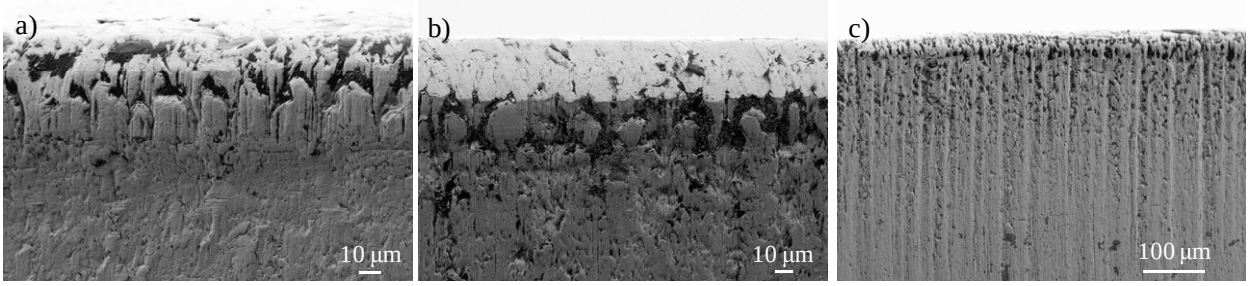

Figure 3.3.14 Damage at the flank face of the HWS 62 HRC punch after 40000 strokes: a) zone 4; b) zone 5 and c) zone 6

A third set of tools was studied up to 100000 strokes with an intermediate SEM inspection at 65000 strokes. Figure 3.3.15 shows that after 65000 strokes, wear is once again the main acting damaging mechanism. However, in zone 5 there is a fatigue crack (Figure 3.3.15 e)) which propagates perpendicular to the cutting edge. As a result of the repetitive action of sliding, friction and contact pressures, the smooth zone near the cutting edge identified in Figure 3.3.11 is now completely rounded, while the rougher zone has turned into smoother.

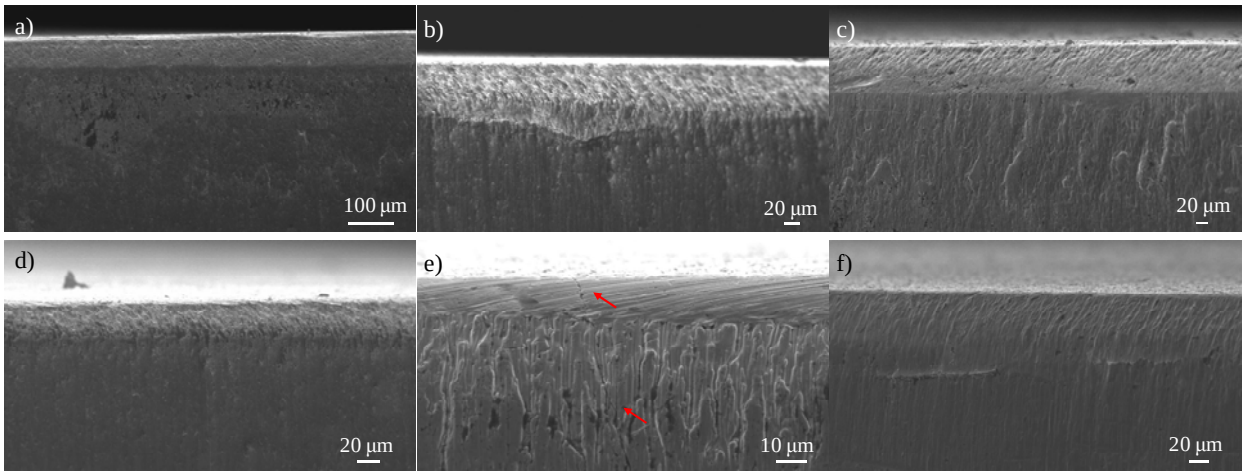

Figure 3.3.15 Damage at the flank face of the HWS 62 HRC punch after 65000 strokes: a) zone 1; b) zone 2; c) zone 3; d) zone 4; e) zone 5 and f) zone 6

Figure 3.3.16 shows that after 100000 strokes, the flank face is polished almost everywhere due to the repetitive action of contact pressures, but other lumps adhere on the worn surface, until they are polished and once again, new ones are adhered.

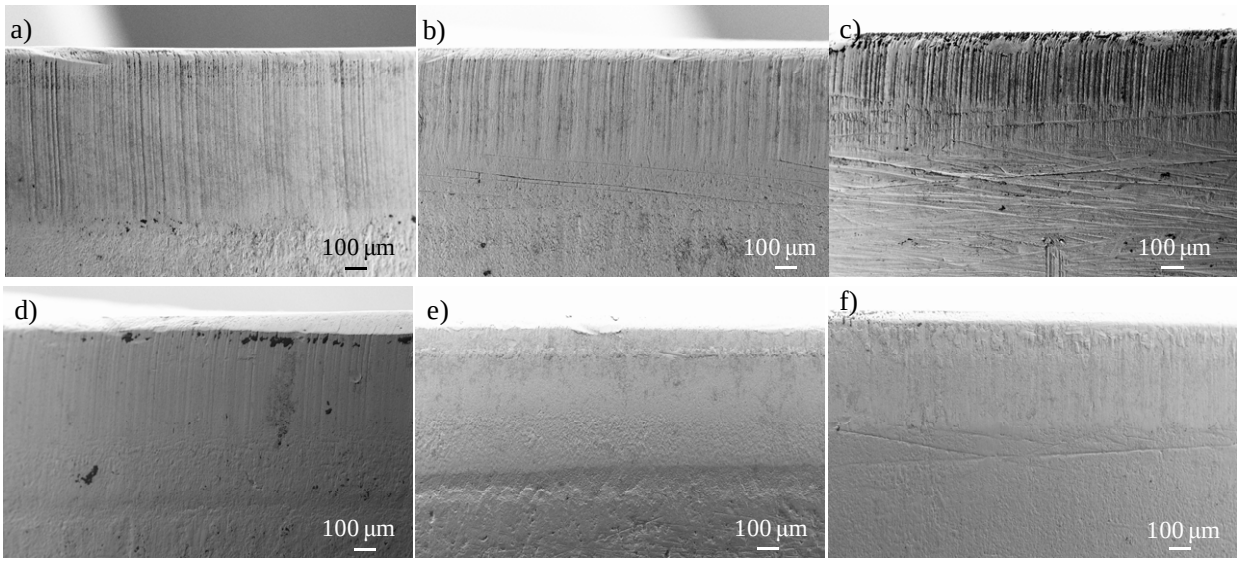

Figure 3.3.16 Damage at the flank face of the HWS 62 HRC punch after 100000 strokes: a) zone 1; b) zone 2; c) zone 3; d) zone 4; e) zone 5 and f) zone 6

Finally, the set of punches coated with CrN-AlCrN was analysed. Although wear is the main failure mechanism identified in these type of punches, the examination of the coated ones reveals that even if the coating successfully prevents some of the adhesion on the surface, it starts detaching and wearing out rather early after only 10000 strokes (Figure 3.3.17). Additionally, Figures 3.3.17 c) and f) show cracks in the substrate in those places where the coating is removed.

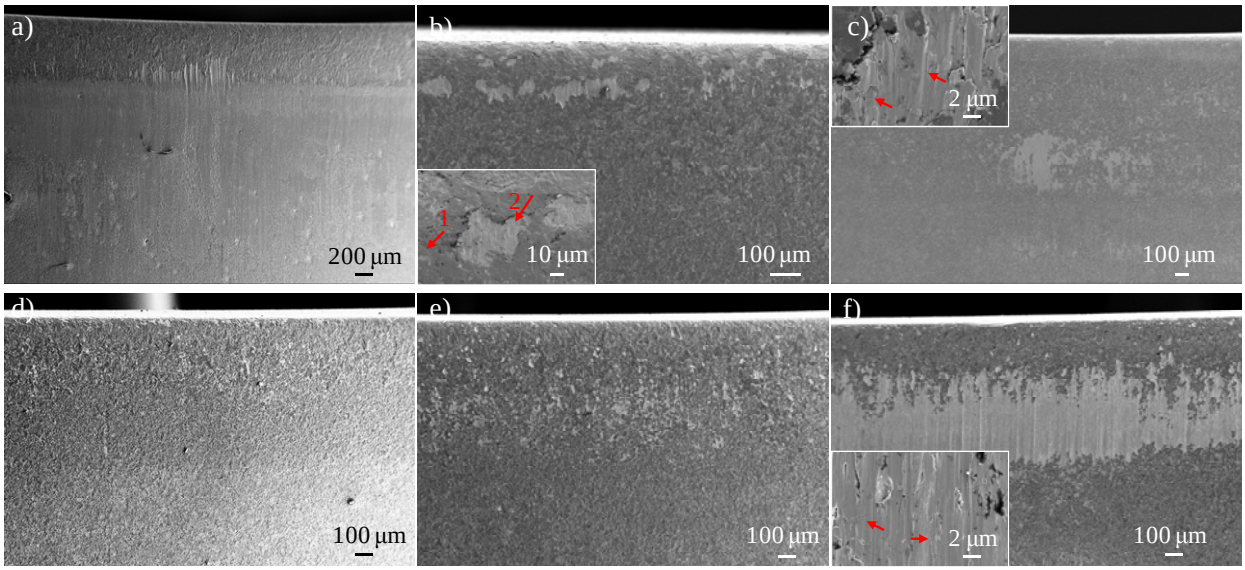

Figure 3.3.17 Damage at the flank face of the coated CrN-AlCrN HWS 62 HRC punch after 10000 strokes: a) zone 1; b) zone 2 (arrow number 1 shows adhered material and arrow number 2 shows the substrate tool steel); c) zone 3; d) zone 4; e) zone 5 and f) zone 6

After 30000 strokes, the coating is almost detached in zones 1, 3 and 6 (Figures 3.3.18 a), c) and f)) and the substrate which appears beneath is highly damaged by numerous cracks. In addition, sheet adhesion on the coating is observed to increase with respect to 10000 strokes. Therefore, this type of coating is far from being recommended for this type of application even if the main failure mechanisms observed in nude punches is wear.

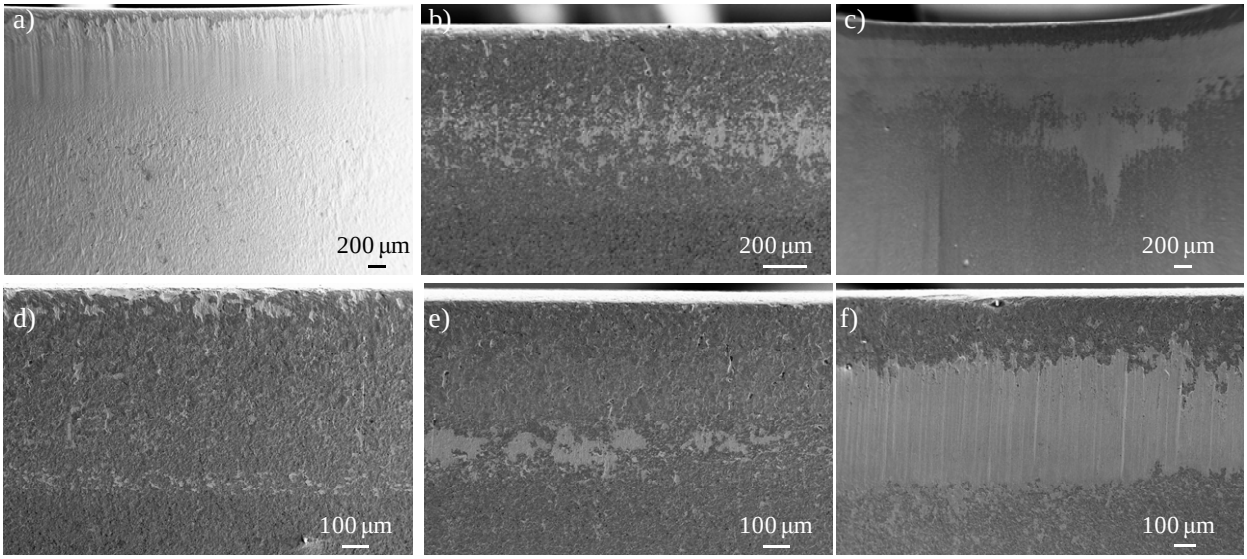

Figure 3.3.18 Damage at the flank face of the coated CrN-AlCrN HWS 62 HRC punch after 30000 strokes: a) zone 1; b) zone 2; c) zone 3; d) zone 4; e) zone 5 and f) zone 6

Such behaviour of the HWS punches can be rationalized in basis of the acting stresses, their distribution and level, which have been determined by means of FE-simulation. As shown in Figure 3.3.19, the highest von Mises stresses are located at a very narrow zone at the cutting edge and they attain 1700 MPa. However, they decrease rapidly to 1000 MPa within a short distance from the edge (less than 400 μm).

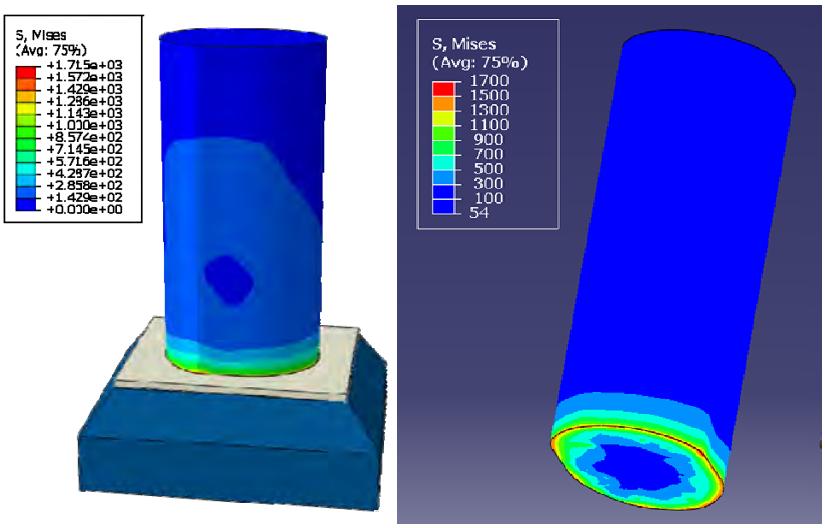

Figure 3.3.19 Von Mises stresses estimated in the punch by means of FE-simulation

As follows from the results obtained in these tests, HWS at 62 HRC is a good choice for this punching operation of MS-W1200. No chipping, fatigue failure nor severe plastic deformation affects the punches and thus, many strokes have been performed without affecting the sheet edge quality. Tools have worked up to 100000 strokes (what is considered a huge amount of strokes for this type of processes) and they have continued to be employed at AUTOTECH ENG. after this investigation. Only wear has been identified at the punches surface. However, typical means to reduce it, such as through the application of a hard PVD-coating, have not shown successful results. The coating has detached prematurely from the surface due to the high contact pressures.

3.3.2.3 Matriu de Dany Accelerat (MDA): forming and punching TRIP 800 and DP1000, both 2 mm thick (at TROE S.L.)

This part of the Thesis is focused on drawing tools (step number 4), bending (step number 6), and punching (steps number 5, 8 and 9) of the MDA, as specified in Figures 2.5.12 and 2.5.13. The damaging mechanisms depend on the type of forming process; hereby they are classified in two main groups, drawing and bending, and punching. The MDA and its processes were specially conceived to accelerate any damaging mechanism taking place in tools, therefore the number of strokes in which damage was observed within this Thesis cannot be compared to real tool lives in the industry but it only can be used as representative of it. These tests aim at evaluating different tool steel performances and familiarising as well as understanding, the damaging mechanisms of tools.

- Drawing and bending tools

The main failure mechanism in drawing and bending tools of the MDA is wear, as no fractures, plastic deformation or fatigue cracks are observed. As described in section 2.5.2.3, wear has been evaluated in terms of the variation of the drawing and bending tool radii, by means of measured surface profiles. From now on, drawing tools are identified with the code “240” and bending tools with “250”.

Wear of drawing tools has been characterised at the radius of the lower tool. Figure 3.2.20 shows that von Mises stresses determined by means of FE-simulation attain the highest values in this radius. However, as shown in Figure 3.3.21, even after the two series of tests using TRIP800 and DP1000 (both 2 mm thick) wear at this radius is not appreciated on no matter what the tool steel is considered (Figure 3.3.21 for 240H and Figure 3.3.22 for 240A).

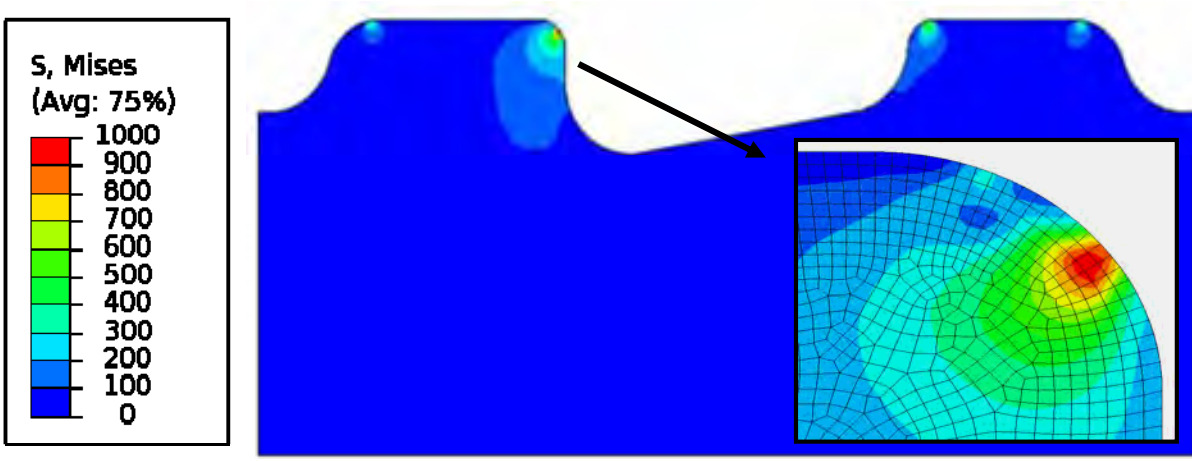

Figure 3.3.20 Von Mises stresses at drawing tools determined by means of FE-simulation

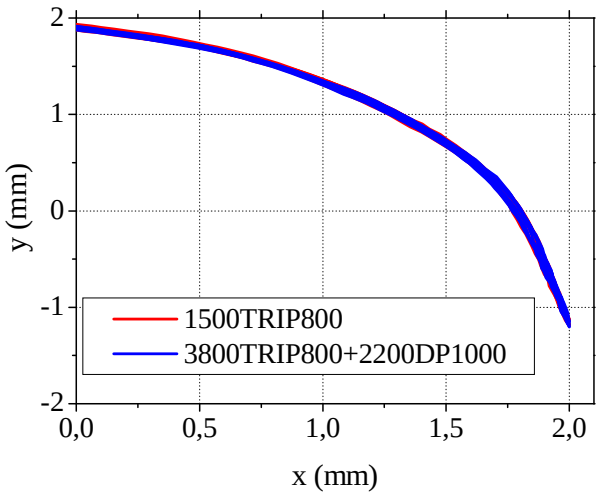

Figure 3.3.21 Measured profiles in the drawing 240H tools radii after different numbers of strokes with TRIP800 and DP1000 2 mm thick

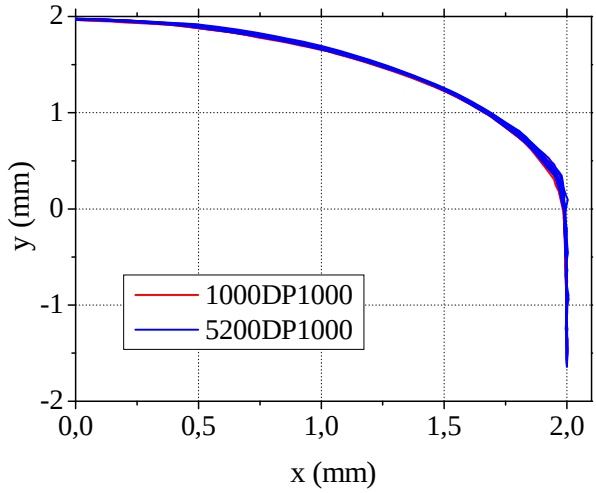

Figure 3.3.22 Measured profiles in the drawing 240A tools radii after different numbers of strokes with TRIP800 and DP1000 2 mm thick

Using FE-simulation, an estimation of wear at this radius was also performed by Ricardo Hernández within the frame of his doctoral thesis, considering TRIP800 as sheet steel and 1.2379 and HWS as tool steels. The results obtained help rationalizing the experimental findings since only slight variations of the tool radii are predicted after 80000 strokes, as shown in Figure 3.3.22.

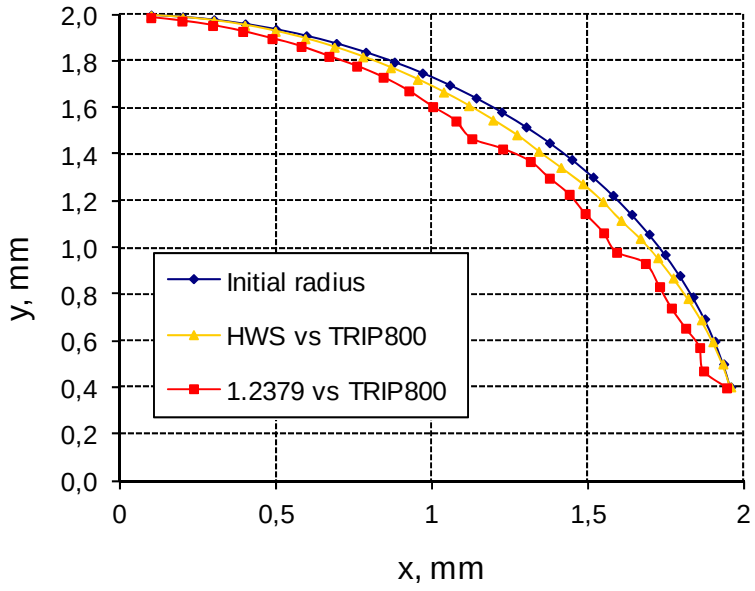

Figure 3.3.23 Radius of the drawing tool at the initial state (blue line) and after 80000 strokes with TRIP800: HWS (yellow line) and 1.2379 (red line)

In bending the maximum von Mises stresses are registered at the radius of the upper tools, and they are higher than those in drawing tools, as shown in Figure 3.3.24.

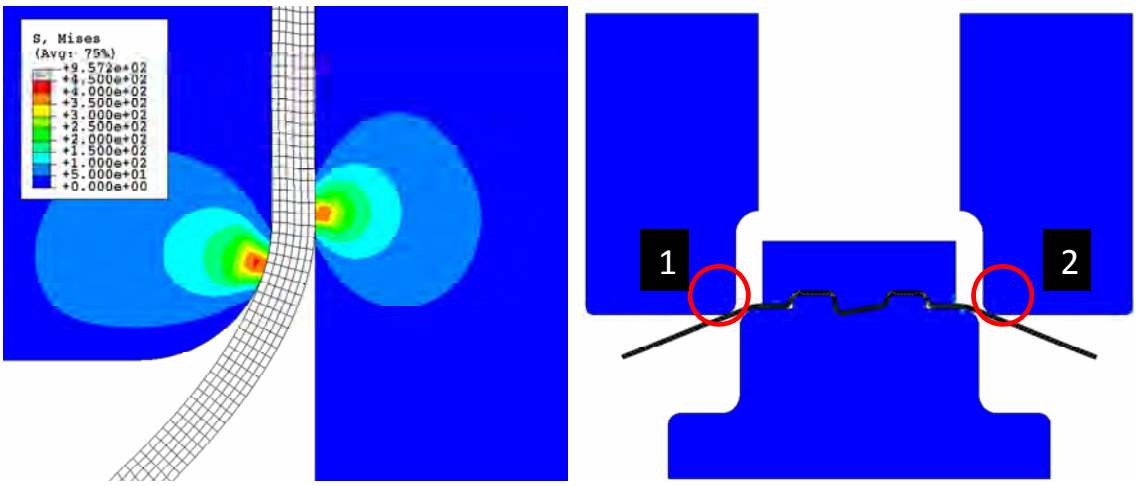

Figure 3.3.24 Von Mises stresses registered in bending tools determined by FE-simulation

Radii profiles measured after different numbers of strokes in tools 1 and 2 of 250A and 250U are shown in Figure 3.3.25, together with the deviation of the measured radii with respect to the theoretical radii of the tool (6 mm).

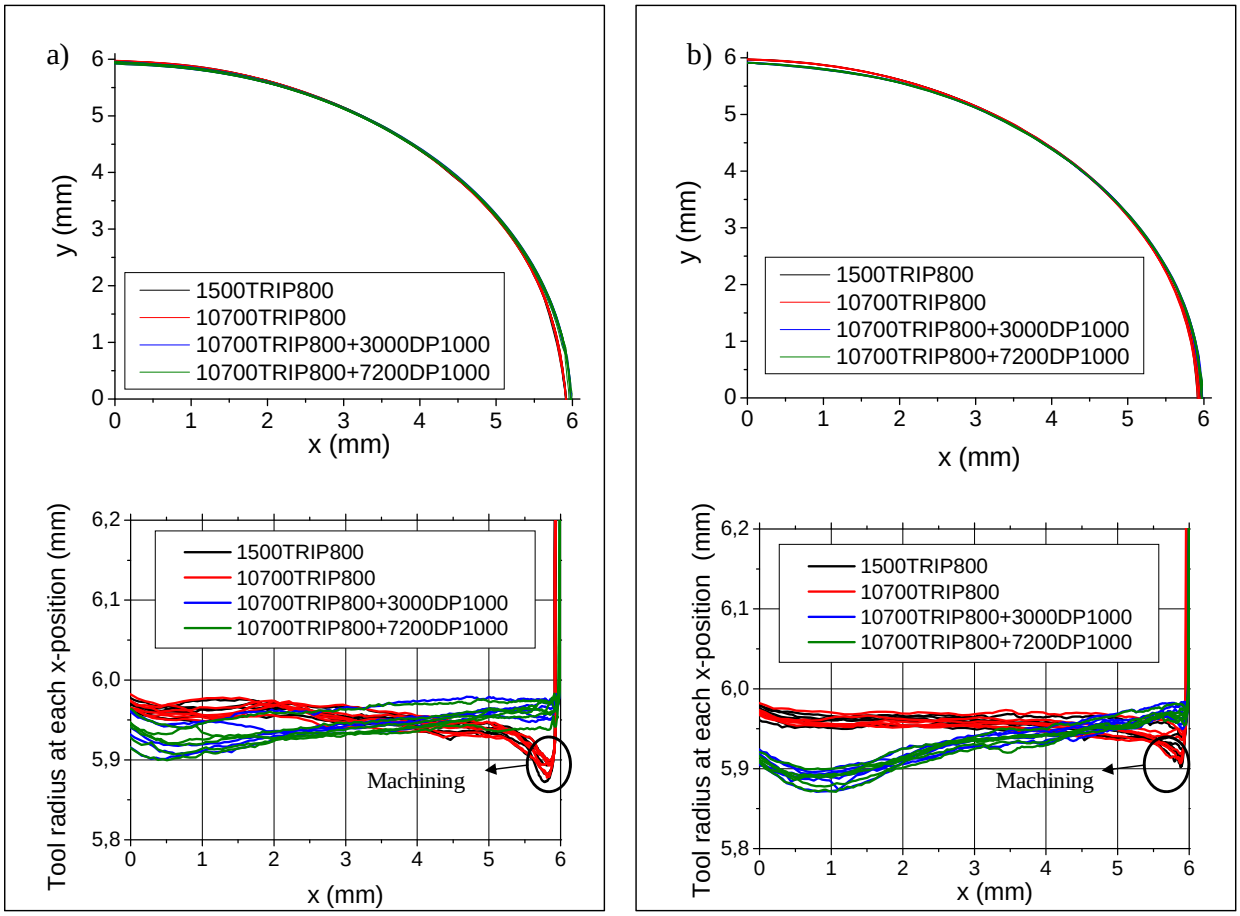

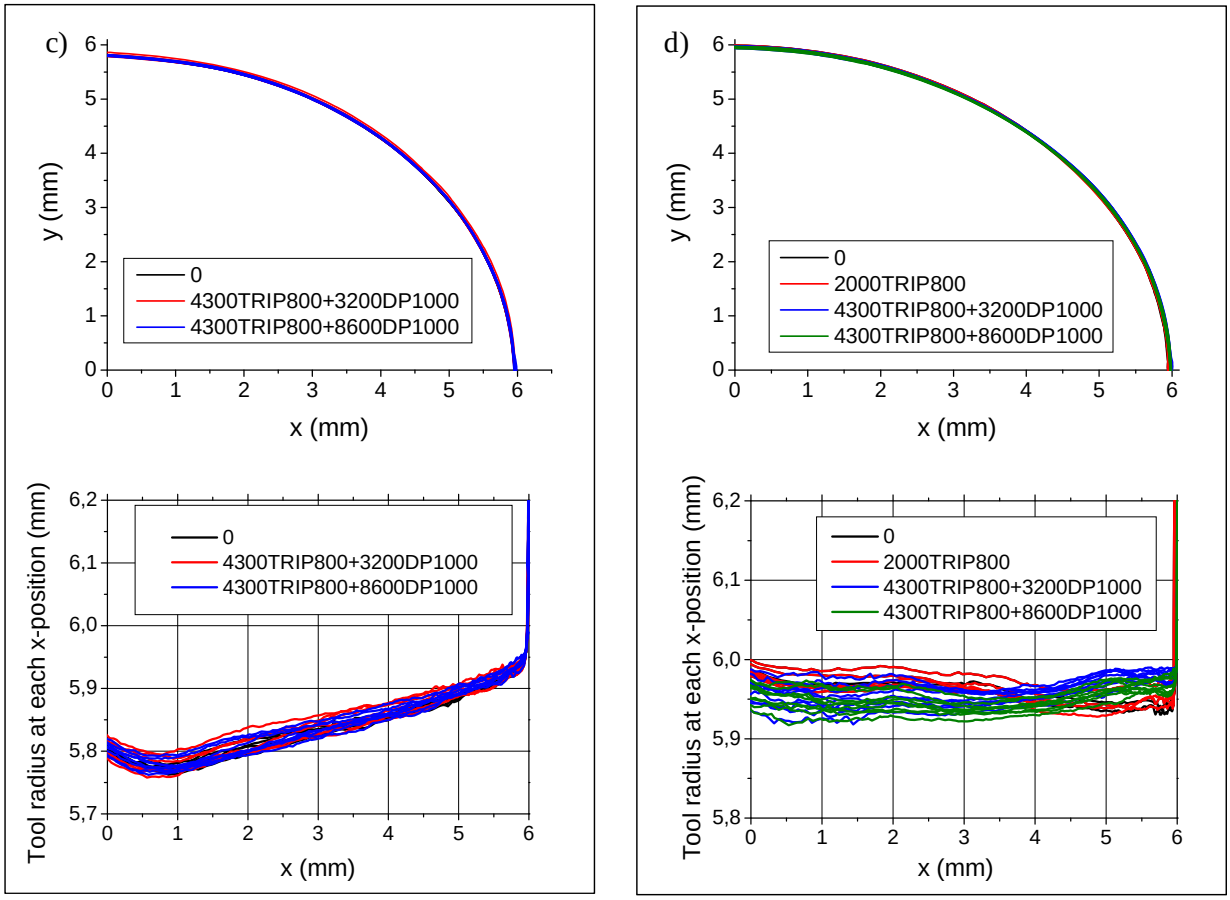

Figure 3.3.25 Tool radii profiles and deviation from the initial radius for 1.2379 (250A) and UNIVERSAL (250U): a) 250A tool 1; b) 250A tool 2; c) 250U tool 1; d) 250U tool 2

In 250A tools there is an initial deviation in the radius probably due to machining, which is removed as the number of strokes increases. At the highest numbers of strokes it can be observed that the first part of the profile has lost material at the beginning of the radius curvature (up to 2 mm in x-axis and with a loss of 800 μm approximately) but a gain of material is observed nearly at the end (between 5,5 and 6 mm in x-axis). In 250U tool 1 neither loss nor gain of material can be appreciated. In 250U tool 2 and similar to 250A, a loss of material of nearly 500 μm is observed up to 2 mm, as well as a slight gain nearly at the end.

The gain of material at the end of the tools radii is attributed to adhesion of sheet material at the tool surface due to the high contact pressures during bending, as shown in Figure 3.3.26.

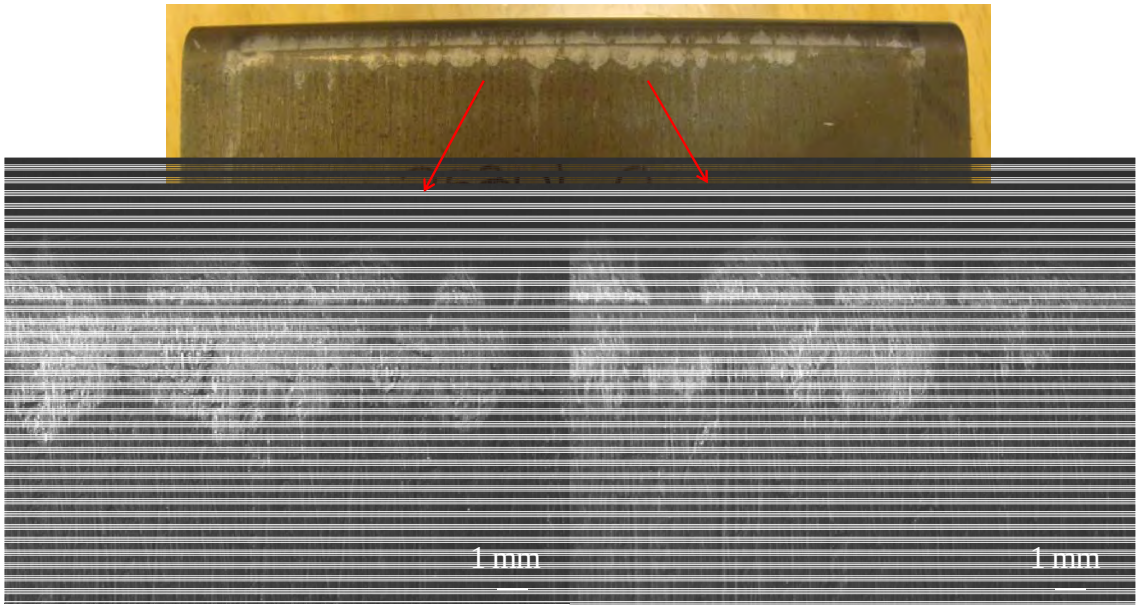

Figure 3.3.26 Adhesion of sheet material at the surface of the 250U tool number 2 after 4300 strokes with TRIP800 and 1500 with DP1000

- Punching tools

Two types of punching tools are studied, as schematized in Figure 3.3.27. The first type corresponds to step number 8 and it is referred as “922”; the second type corresponds to steps number 5 (the two outer holes) and step number 9 (the central hole), and the code is “917”.

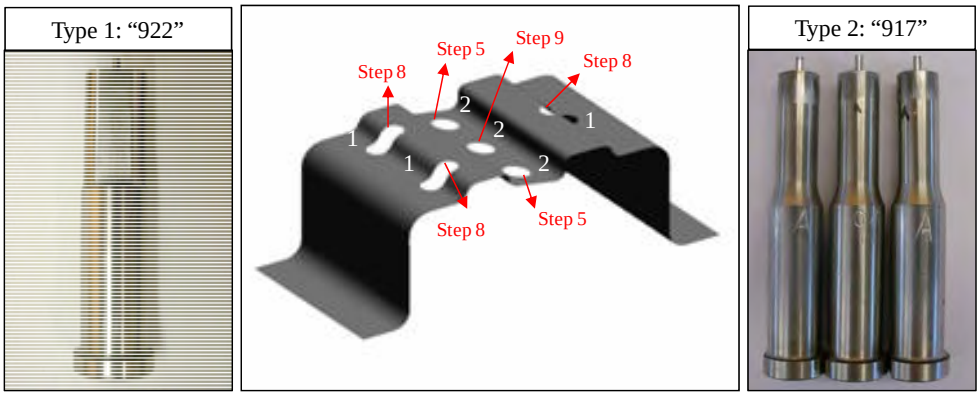

Figure 3.3.27 Schema of the two types of punching tools: type 1 “922” punch, and type 2 “917” punches

The first tests are performed using TRIP800 2 mm thick as sheet material and 5 % of the sheet thickness as cutting clearance. Fractographic inspection of “922” and “917” punches built of different materials reveals that chipping, sinking in and plastic deformation are the most important damaging mechanisms.

917A punches (made of 1.2379 at 60 – 62 HRC) show large fractures by chipping all along the cutting edge, as shown in the sequence of Figures from 3.3.28 a) throughout e) for increasing numbers of strokes. Chipping is observed at the first hundreds of strokes (between 200 and 700) but fractures grow progressively with the increasing numbers of strokes. Also, new chippings continuously appear in other zones all around the punch and in comparison to the other tool steels, 917A punches show the most severe damage and at the lowest numbers strokes.

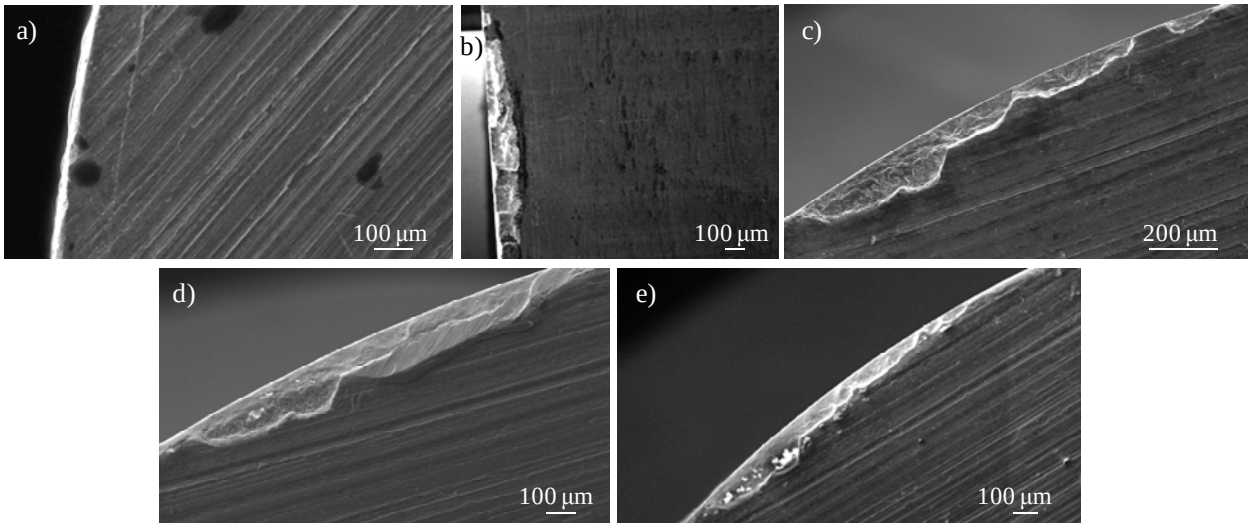

Figure 3.3.28 Chipping evolution at the cutting edge of a 917A punch after: a) 200 strokes; b) 700 strokes (image of the flank face); c) 1500 strokes; d) 3100 strokes and e) 6100 strokes with TRIP800 2 mm thick

As it can be observed in Figure 3.3.29 a), the cutting edge of 917B punches (1.2379 58 – 60 HRC) is plastically deformed and rather worn out, but small fractures by chipping start to appear at 4500 strokes. Both 917U (UNIVERSAL 61 – 62 HRC) and 917H (HWS 61 – 62 HRC) punches show small fractures by chipping at the cutting edge at the first thousands of strokes, as illustrated in Figures 3.3.29 b) and c) respectively.

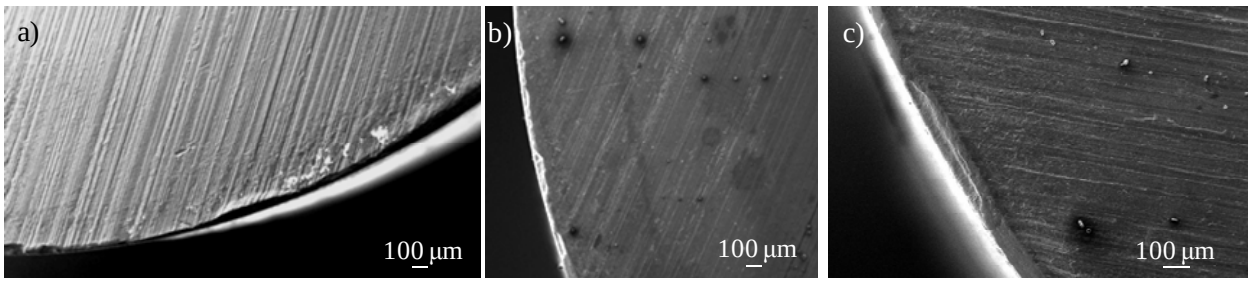

Figure 3.3.29 Damage observed in punches of different tool steels: plastic deformation in 917B after 4500 strokes; b) chipping in 917U after 4400 strokes and c) chipping in 917H after 4000 strokes with TRIP800 2 mm thick

An examination of the flank face of HWS punches at 2000 strokes allows to identify fatigue cracks (as shown in red arrows in Figure 3.3.30), which propagated parallel to the cutting edge at a distance of approximately 50 μm. Imperfections at the flank face (as those indicated by the blue arrow of Figure 3.3.30 b) which may have been formed after release of wear particles) may have influenced the nucleation of these cracks at the surface and subsequent fractures by chipping, even though direct relationship between these craters and nucleation of cracks from them cannot be ascertained by experimental observations.

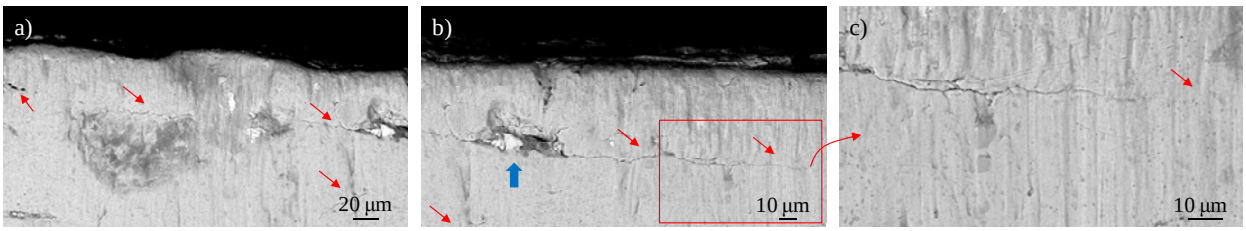

Figure 3.3.30 Fatigue cracks (red arrows) observed in the flank face of a 917H punch. These cracks could have been nucleated from surface defects (shown by the blue arrow)

The examination of "922" punches shows different types of damage at different locations at the punch cutting edge, as it is schematically described in Figure 3.3.31. Independently of the tool steel, one of the semi-circular areas is always almost broken before one thousand strokes, while the other one is first plastically deformed and later, at more than two thousand strokes fractures start to appear. Such differences can be understood because punching was performed at two levels (the piece had a step in the middle of the punched hole). The first level is more severe than the second one because the sheet has to be fractured, while in the second it is only torn. In the straight areas, chipping and cracks are observed after 700 – 800 strokes. As shown in Figure 3.3.31 d), cracks are nucleated from damage at the cutting edge (which act as small notches) and from there they propagate inwards.

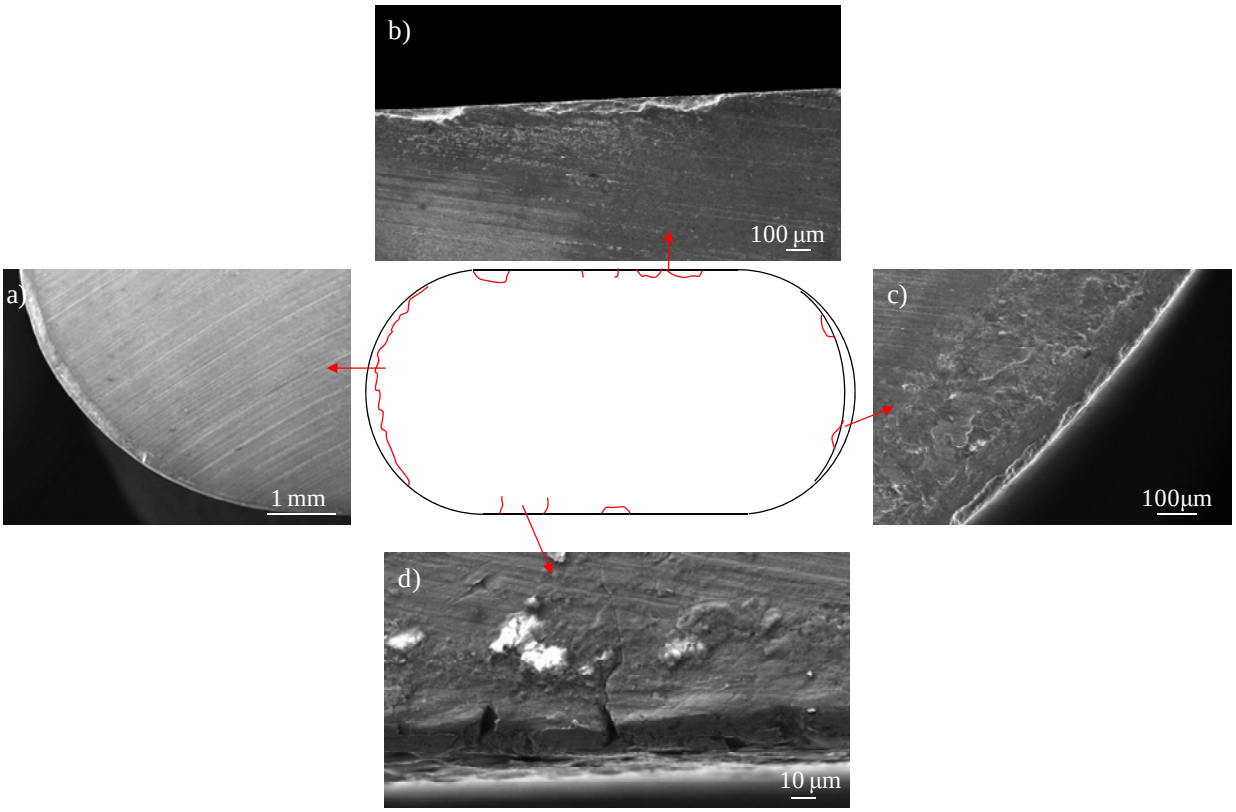

Figure 3.3.31 Damaging mechanisms observed in "922" punches: a) one of the semi-circular areas is almost fractured; b) and c) fractures by chipping and cracks at straight areas and d) plastic deformation and then chipping at the other semi-circular area of the punch

Figure 3.3.32 a) shows a zone near the cutting edge where fracture was about to take place (blue arrows). The main crack (red arrow number 1 in Figure 3.3.32 b)), which propagates parallel to the cutting edge, bifurcates in cracks number 2 and 3. Crack number 3 continues propagating in parallel to the cutting edge and bifurcates to two more cracks (number 4 and 5). Crack number 2 propagates towards the surface instead. Figure 3.3.32 c) also shows cracks, which propagate at 45 º and perpendicular to the cutting edge respectively. Fracture was observed to take place 2000 strokes later, as illustrated Figure 3.3.32 d).

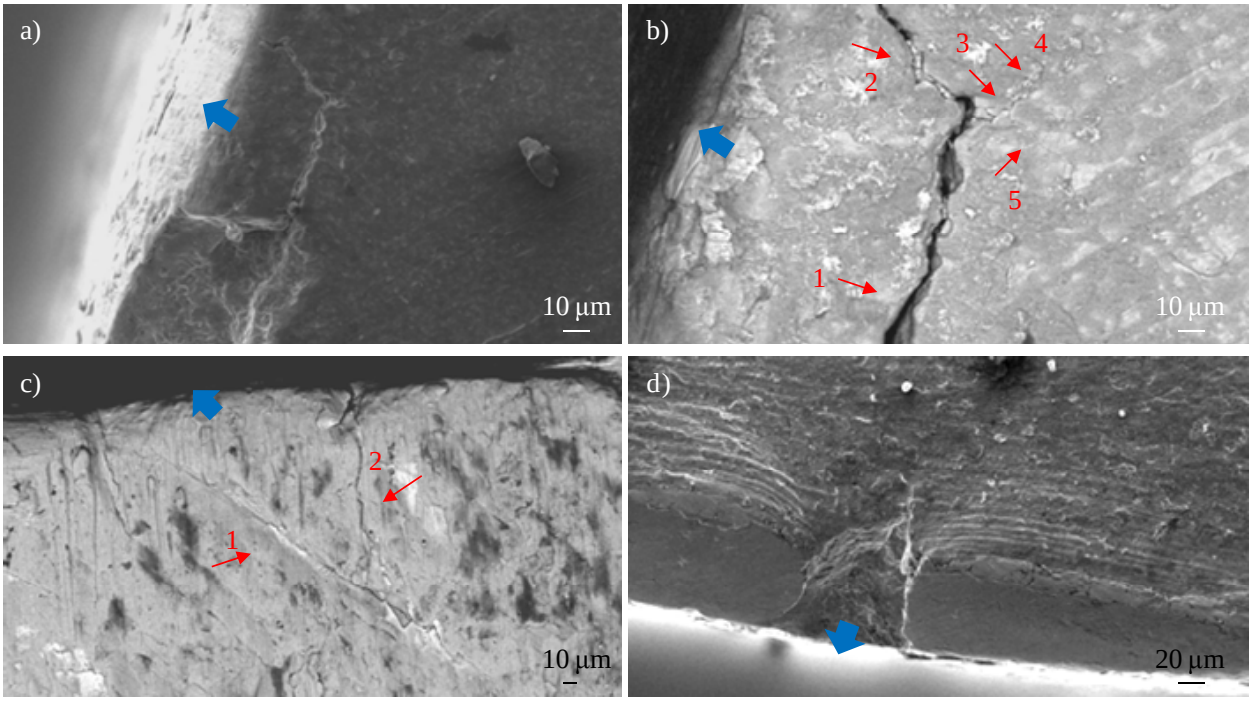

Figure 3.3.32 Cracks and fractures at "922" punches: a) and b) secondary and backscatter electron images of a 922A punch after 4600 strokes; c) and d) backscatter and secondary images of a 922B punch before and after fracture at 2000 and 4000 strokes respectively. All the images correspond to punching TRIP800 2 mm thick

The second tests are performed using DP1000 2 mm thick and a cutting clearance of 10 % of the sheet thickness. Fractographic results of tools agree with those previously obtained using TRIP800: chipping is the main acting failure mechanism regardless of the tool steel microstructure but in this case, it starts at lower numbers of strokes than for TRIP800 (as it could be expected due to the higher strength of DP1000). As shown in Figures 3.3.33 a), b) and c), fracture at the cutting edge of a "917" punch increases progressively with the number of strokes, from 500 to 1500 and 3500 respectively.

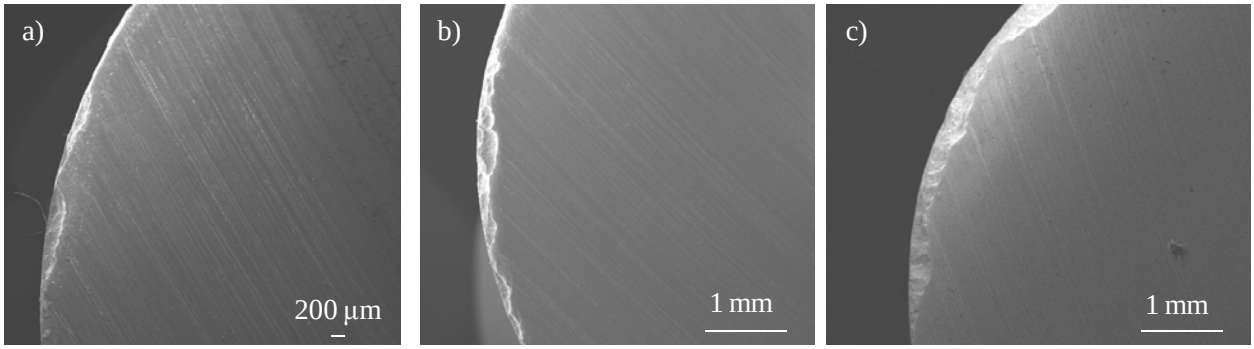

Figure 3.3.33 Fractures at a "917A" punch when punching DP1000 2 mm thick: a) after 500 strokes; b) after 1500 strokes and c) after 3500 strokes

Crack nucleation and propagation mechanisms are assessed in 1.2379, UNIVERSAL and HWS punches. In Figure 3.3.34, propagating cracks in the matrix, cracks in broken carbides and cracks nucleated from inclusions are distinguished by different arrow colours: red in the first case, blue in the second and green in the third one. Figures 3.3.34 a) and b) show that most of the primary carbides near the cutting edge of 917A punches are broken, each carbide presenting multiple cracks oriented parallel to the edge. In 917U punches (Figures 3.3.34 c) and d)) carbides are also broken in cracks parallel to the cutting edge, and they are observed to coalesce with each others and give rise to longer cracks which propagate through the microstructure.

At the surface of 917H punches, cracks are difficult to be identified due to the deep machining grooves, which create rather high peaks and deep valleys compared to the very fine carbide dispersion. The examinations required very high magnifications and considering that they were performed directly on the tool surface (with no special sample preparation other than as much cleansing as possible) it was difficult to obtain images of high quality. Nevertheless, a few cracks can be identified, as shown in Figures 3.3.34 e), f) and g). These cracks seem nucleated or at least, to pass through brittle inclusions (the two black particles shown by green arrows in Figure 3.3.34 g)). Even though it is difficult to ascertain whether the crack is nucleated in the surface or it is nucleated at a certain depth inside the material and it just has come out, slight patterns of what seems possible plastic deformation are identified directly at the surrounding of the crack, and crack bifurcation takes place at both tips of the crack. Also, some carbides look like broken at the neighbourhood of this crack (see Figure 3.3.34 g)).

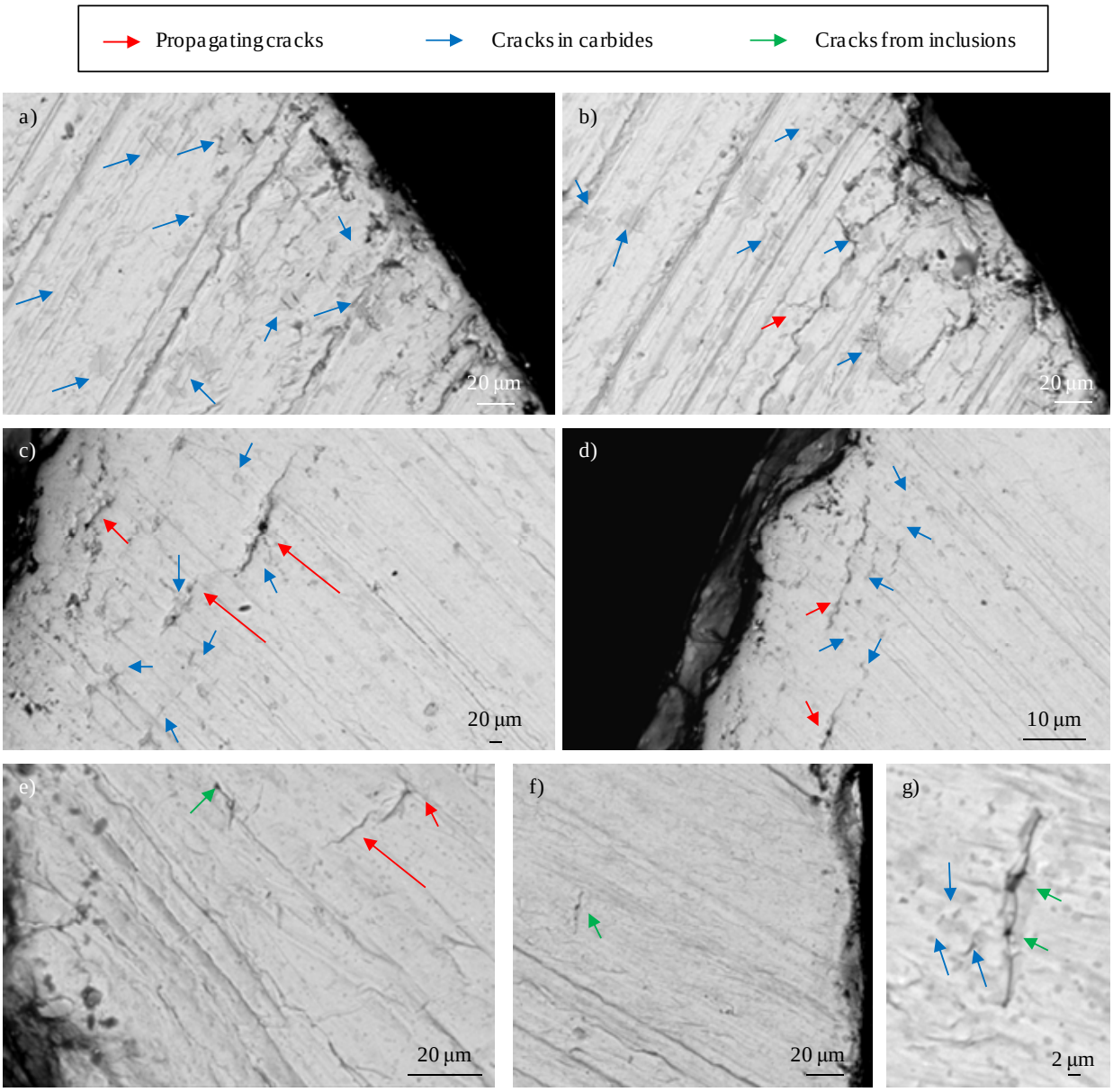

Figure 3.3.34 Cracks identified after 1500 strokes near the cutting edge of: a) and b) a 917A punch; c) and d) a 917U punch and e), f) and g) 917H punch when punching DP1000 2 mm thick

Regarding the fractographic inspection of "922" punches, damage by chipping is identified already from the first 500 strokes. Damage distribution around the punch reminds that schematised in Figure 3.3.32 when punching TRIP800. However, in the punching operation of DP1000 tool fracture mechanisms are even more accelerated, as shown in Figure 3.3.35. The cutting edge of a 922A punch shows a large fatigue crack at one of the semi-circular zones at 1500 strokes (Figure 3.3.35 a)) and as it can be observed in Figure 3.3.35 b), at 3500 strokes it is completely broken. In 922U punches such fractures are not identified even if chipping at smaller scale has also taken place at the cutting edge (Figure 3.3.35 c)). In 922H early chipping is observed at 500 strokes (Figure 3.3.35 d)) and it increases progressively with subsequent strokes (Figures 3.3.35 e) and f) at 1500 and 3500 strokes respectively).

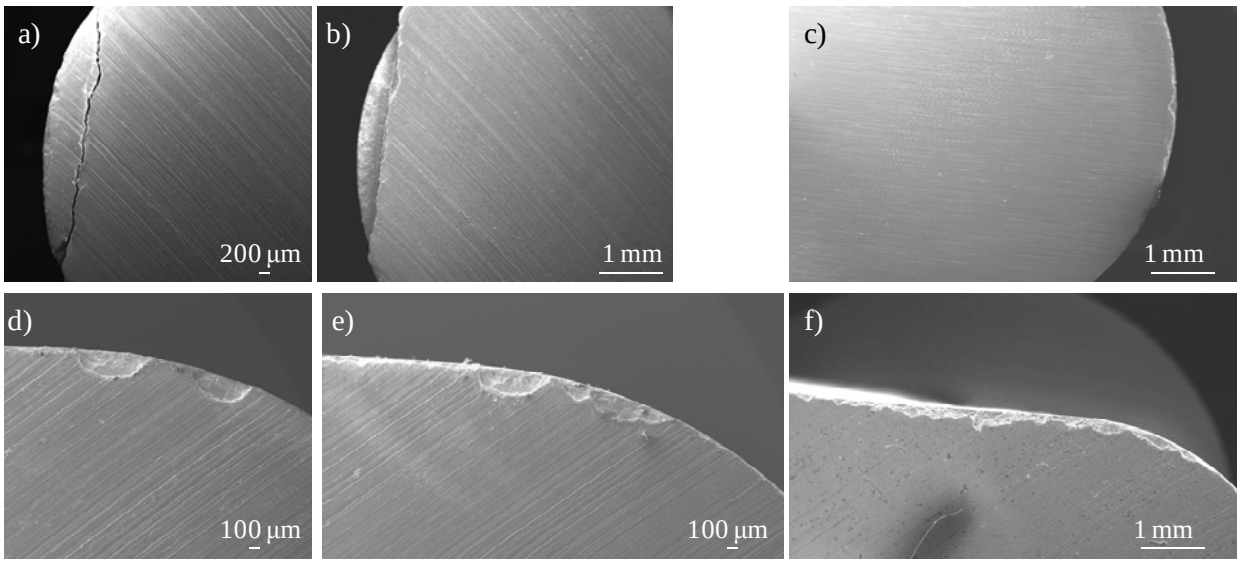

Figure 3.3.35 Fractography of different punches: a) 922A at 1500 strokes; b) 922A at 3500 strokes; c) 922U at 3500 strokes; d) 922H at 500 strokes; e) 922H at 1500 strokes and f) 922H at 3500 strokes when punching DP1000 2 mm thick

The large breakage at 922A is understood by the nucleation and propagation of small cracks by fatigue. In Figure 3.3.36 a) it can be observed that in parallel to the main crack, smaller cracks have nucleated from broken carbides and they have coalesced with each others. In 922U the same mechanism can explain the presence of chipping at the cutting edge; small cracks start from broken carbides, propagate and coalesce prior to fracture (Figure 3.3.36 b)). In 922H the mechanisms are different; cracks are nucleated from defects at the cutting edge, generated either by machining flaws, wear or small fractures. In addition, cracks propagate easily following the machining grooves. As shown in Figure 3.3.36 c), d) and e) cracks can bifurcate and change their direction, leading to fracture.

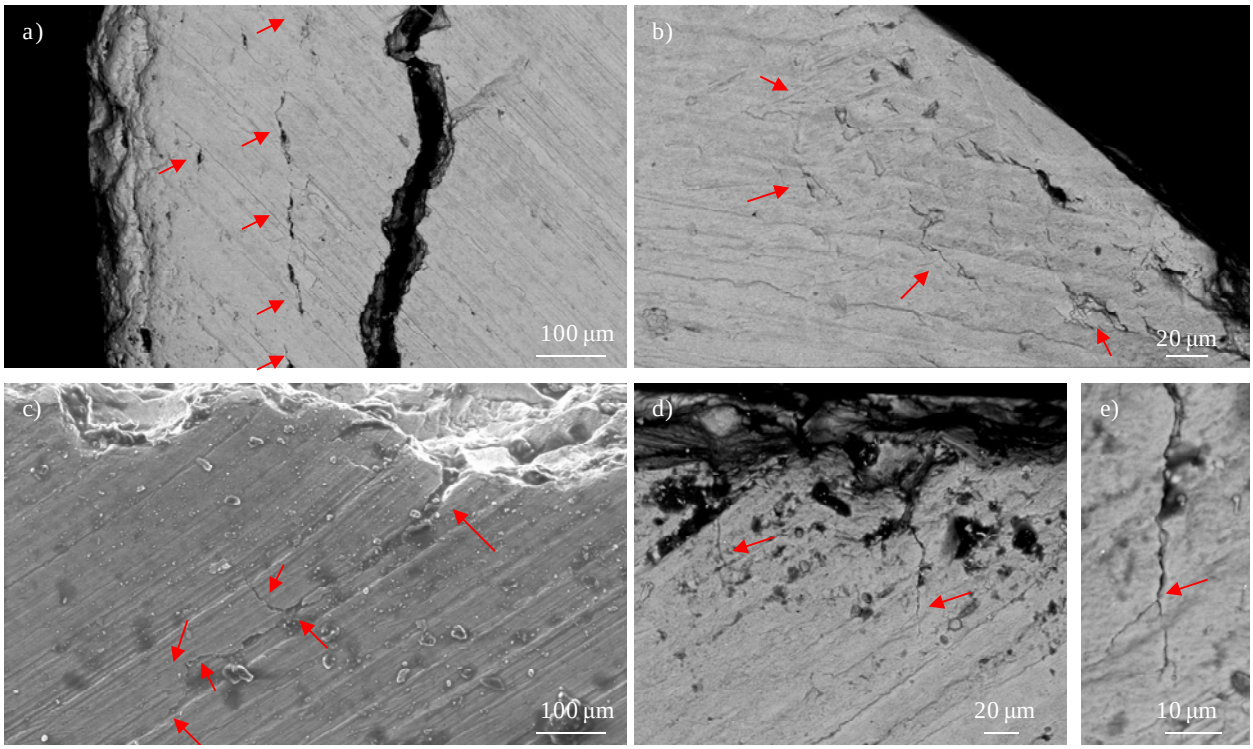

Figure 3.3.36 Fracture mechanisms in punching DP1000 2 mm thick: a) 922A punch at 1500 strokes; b) 922U at 3500 strokes; c); d) and f) 922H at 3500strokes. The red arrows indicate the presence of cracks

3.3.3 Analysis of the performance of shearing tools: relationship between the acting mechanical solicitations and damage in the microstructure

As described in section 2.5.3, the HPC was conceived, designed and built for bench testing at CTM, in order to reproduce the mechanical solicitations of industrial tools but under controlled laboratory conditions. These tests were supervised in situ and tools were easily replaced for examination. In view of the results observed in tools working in industrial conditions (section 3.3.2), shearing instead of forming operations were chosen to be studied in the HPC due to their more detrimental effects on tools. Thus, punching and slitting processes of DP1000 2 mm thick (see Figure 2.5.15 c) and Figure 2.5.16 a) and b)) were analysed and the obtained results will respectively be presented in this section.

3.3.3.1 Damage mechanisms in punching tools

Mechanical solicitations of punches working in the HPC are rationalized through the estimated stress state and level, determined by means of FE-simulation. As shown in Figure 3.3.37, von Mises stresses are confined in a narrow area near the cutting edge, which measures approximately 600 µm (in radial direction). As shown in Figure 3.3.37, the maximum stress level at the cutting edge is attained below the surface.

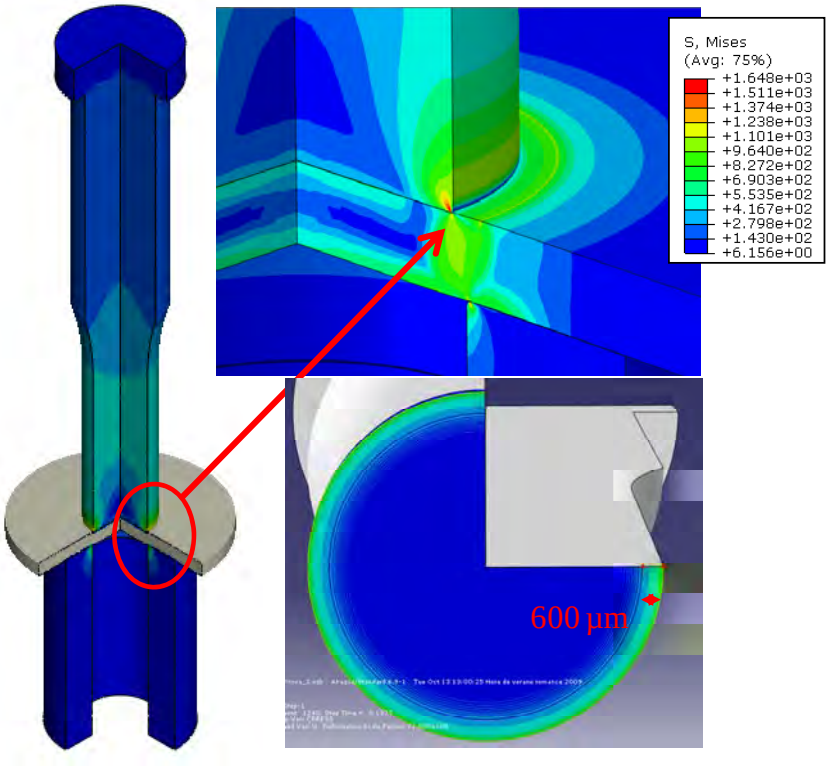

Figure 3.3.37 Von Mises stress distribution and level in the punch. Stresses are confined in a narrow area near the cutting edge (600 µm) and the highest stresses are found below the surface

A closer gaze into the zone where stresses are maximal (Figure 3.3.38) reveals that von Mises stresses reach 2000 MPa at approximately 20 µm from the cutting edge. However, the stresses decrease steadily and they reduce to 1000 MPa at 200 µm from the cutting edge.

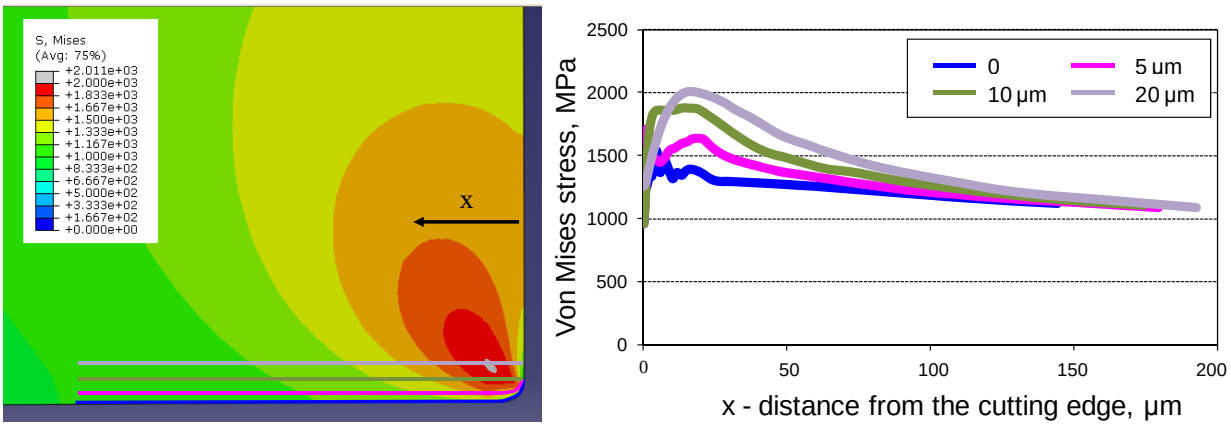

Figure 3.3.38 Von Mises stress distribution and level in the punch at the cutting edge

Fractographic inspection of punching tools reveals severe damage by fracture and plastic deformation (sinking in) at the cutting edge, depending on the considered tool steel. After 50 strokes, 1.2379A punches show fracture almost all around the cutting edge (Figure 3.3.39 a)), while in 1.2379B sinking instead of fracture has affected the punch edge (Figure 3.3.39 b)). K360 shows deformation and sinking at the nearest regions of the cutting edge (Figure 3.3.39 c)). UNIVERSAL does neither show fracture nor plastic deformation at these numbers of strokes (Figure 3.3.39 d)). Finally, in HWS some deformation and sinking can be observed at the cutting edge (Figure 3.3.39 e)).

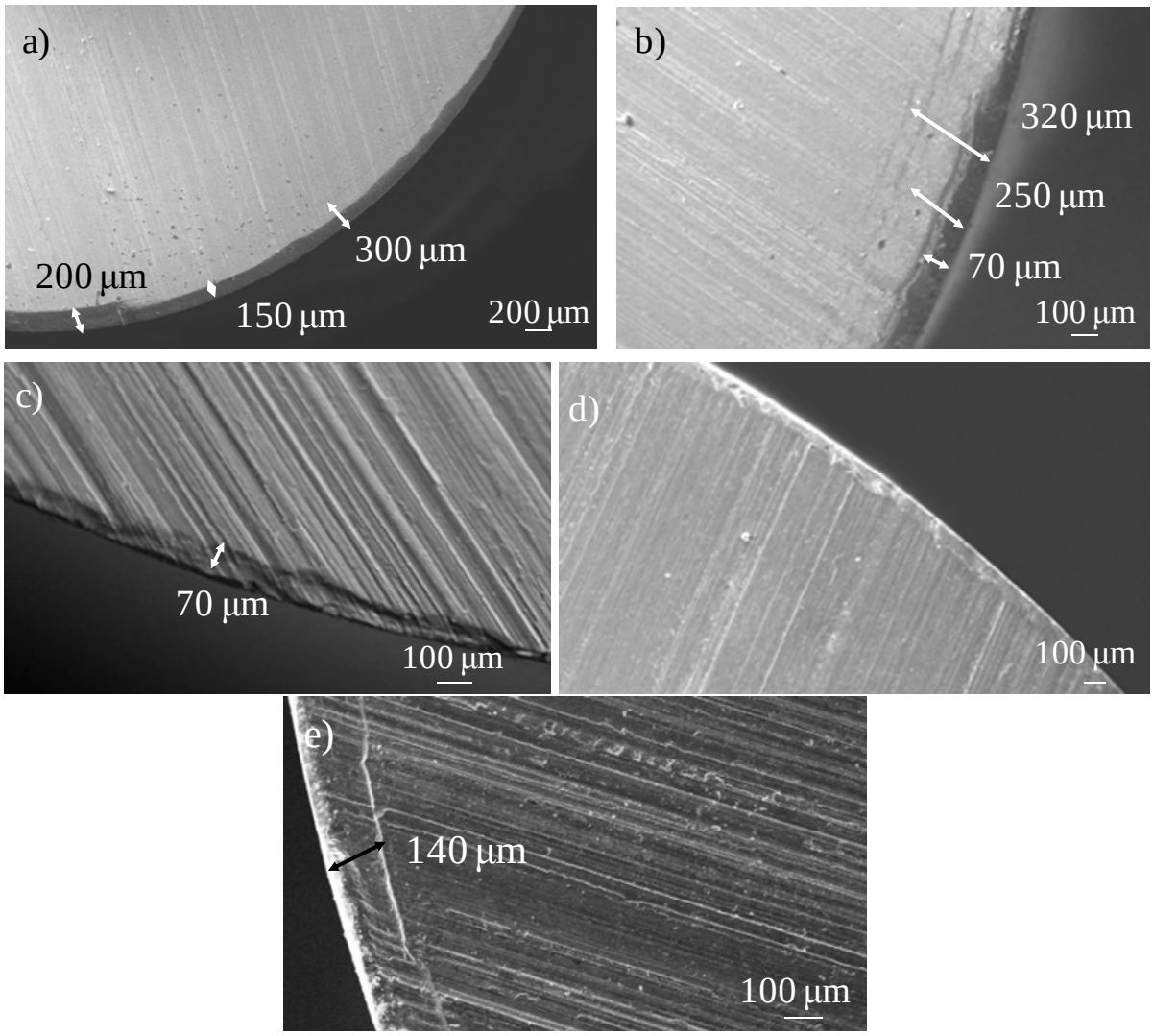

Figure 3.3.39 Fractography after 50 strokes: a) 1.2379A (fracture); b) 1.2379B (sinking); c) K360 (deformation and sinking); d) UNIVERSAL (-); e) HWS (deformation and sinking)

- Punches of 1.2379A

After 50 strokes, in 1.2379A fracture expands up to 200 µm far from the cutting edge, as shown in Figure 3.3.39 a). 1.2379A punches show the widest fractured zone and after the stress diagram plotted in Figure 3.3.38, it can be said that almost all the area subject to von Mises stresses higher than 1000 MPa is broken. Fractographic results at such low numbers of strokes show no signs of fatigue; on the contrary, the large fractured area observed can likely have taken place in a rather brittle manner, by rapid crack nucleation and propagation in low cycle fatigue. However, with the subsequent increase of strokes, the evolution of damage is almost inappreciable at the cutting edge. As shown in Figure 3.3.40 from a) throughout e), the cutting edge is rounded and rather worn, but the fractured zone has not increased its size.

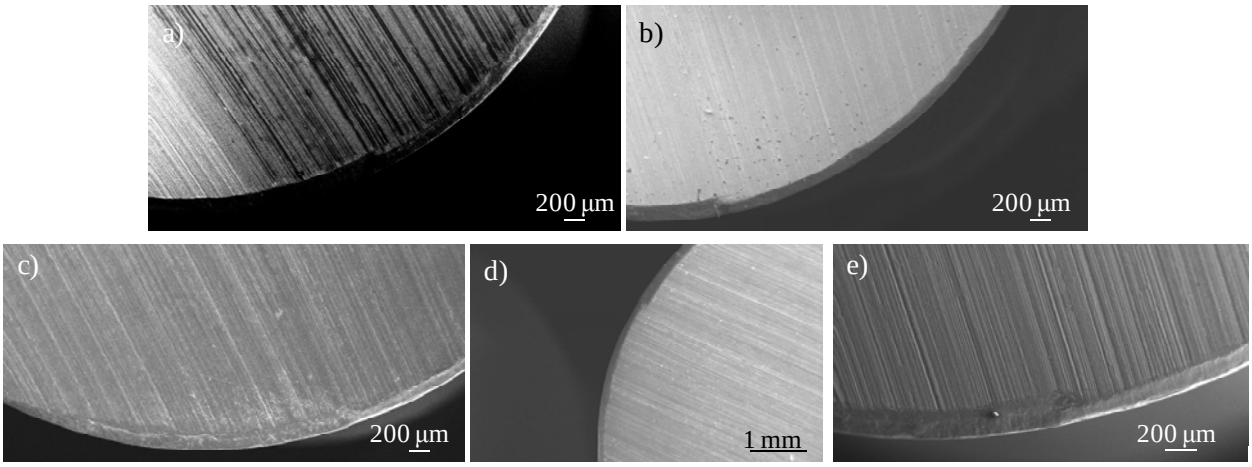

Figure 3.3.40 Fractography of 1.2379A punch after: a) 50 strokes; b) 3000 strokes; c) 17000 strokes; d) 26000 strokes and e) 31000 strokes

This behaviour is understood if stresses decrease once the cutting edge has lost its sharp shape. In order to quantify the reduction of stresses, the topography of the fracture was measured using confocal microscopy, as shown in Figure 3.3.41 a), and the resulting geometry was modelled by FE-simulation. Assuming the same fracture height, two cases were simulated: in the first one the punch had a slant edge (slope 10 º with respect to the sheet) (Figure 3.3.41 b)), and in the second the edge had a flat step (Figure 3.3.41 c)). In both cases, maximum von Mises stresses are 1600 MPa in the tool radii, being hence considerably lower compared to the sharp edge (2000 MPa).

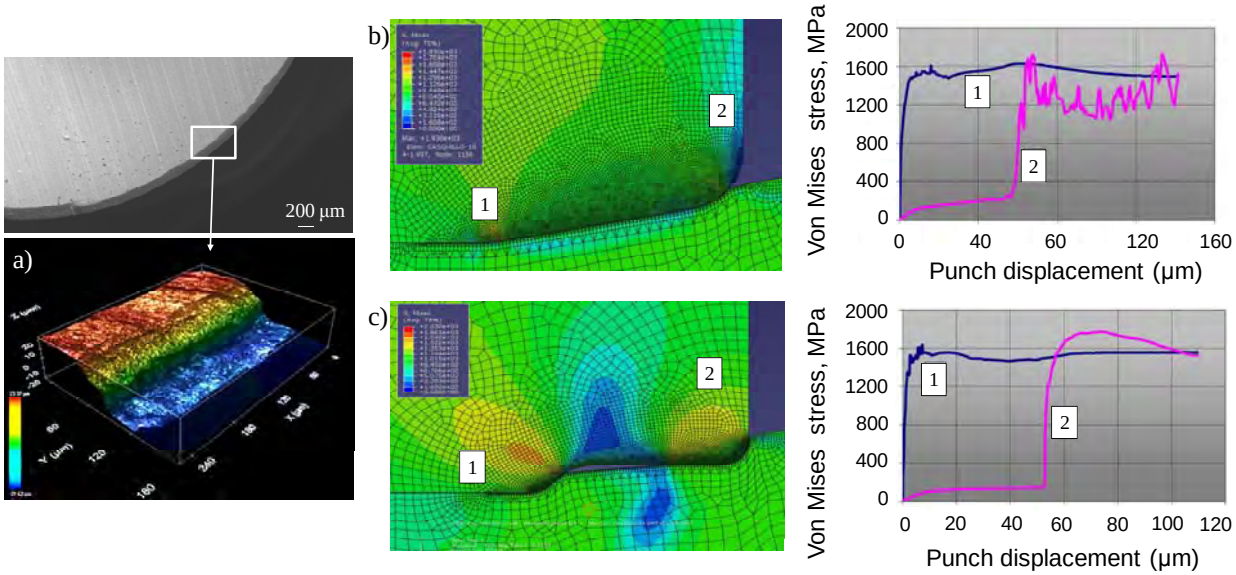

Figure 3.3.41 a) Topographic image of the fracture at the cutting edge of the 1.2379A punch; b) FE-simulation results of von Mises stresses assuming a slant fractured edge and von Mises stress evolution with the penetration of the punch at points "1" and "2"; c) the same than b) but assuming a flat step fractured edge

At 31000 strokes, chipping is observed at those scarce zones of the cutting edge which have survived from fracture at the earliest strokes. As shown in Figure 3.3.42 a), fracture is found to take place following the marked machining grooves at the surface. In parallel, at this number of strokes the flank face of the punch is severely damaged by wear, as it can be observed in Figure 3.3.42 b) and some cracks propagate parallel to the cutting edge (Figure 3.3.42 c)).

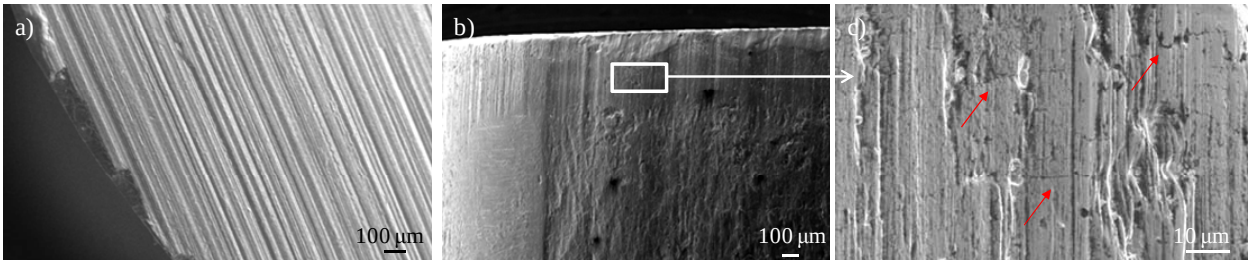

Figure 3.3.42 a) Chipping of 1.2379 A punch along the machining grooves after 31000 strokes; b) wear at the flank face of the punch after 31000 strokes and c) cracks at the flank face of the punch after 31000 strokes

SEM inspection of the punch cutting edge in cross section view (from the punch cut slices after 31000 strokes) reveals that a small area under the cutting edge is damaged by the presence of broken carbides (Figures 3.3.43 a) and b)). Different cracks are also identified: some of them are very shallow and have likely nucleated at the surface; these can be the same than the previously observed at the flank face, in Figure 3.3.42 c). Other cracks are nucleated from broken carbides at the subsurface, and they likely propagate outwards up to reach the surface, leading to fracture (Figure 3.3.43 d)).

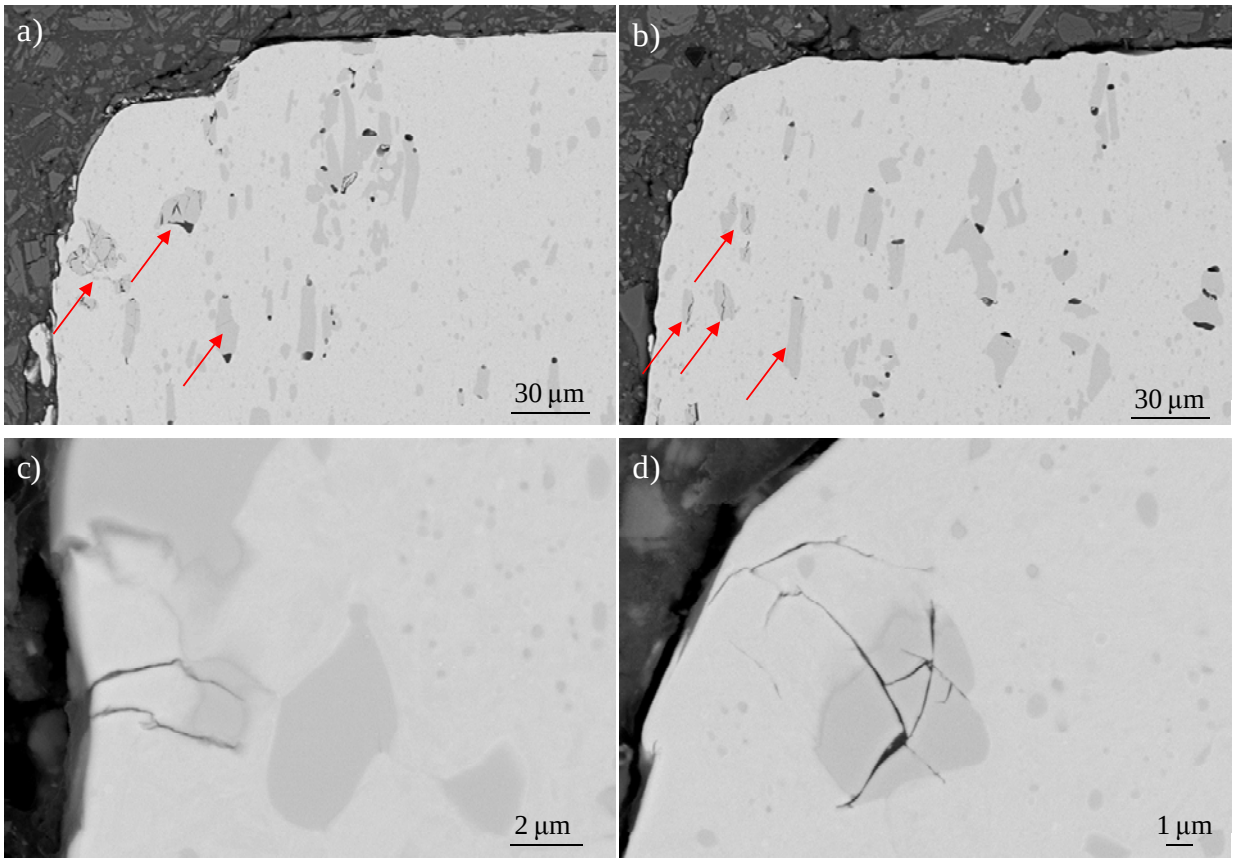

Figure 3.3.43 Cross sectional images of the punch cutting edge: 1.2379A after 31000 strokes; a) and b) carbides are broken at the subsurface of the cutting edge; c) cracks nucleated at the surface and propagating inwards and d) cracks nucleated at the subsurface from broken carbides and propagating outwards

A closer gaze to other regions of the punch cross section shows that apart from the damaged microstructure directly beneath the cutting edge (Figure 3.3.44 a)), broken carbides at the subsurface are also present in very shallow zones near the rake and the flank faces (Figures 3.3.44 b) and c) respectively). However, any kind of damage can be identified at the inner microstructure of the punch (Figure 3.3.44 d)), nor at other positions than a), b) or c). Damage at the cutting edge is rather expected after the high acting stresses; but the observed broken carbides directly beneath the rake and flank face, far from the cutting edge, cannot be explained after FE-simulation results since after Figure 3.3.37 stresses at these locations are to be very low.

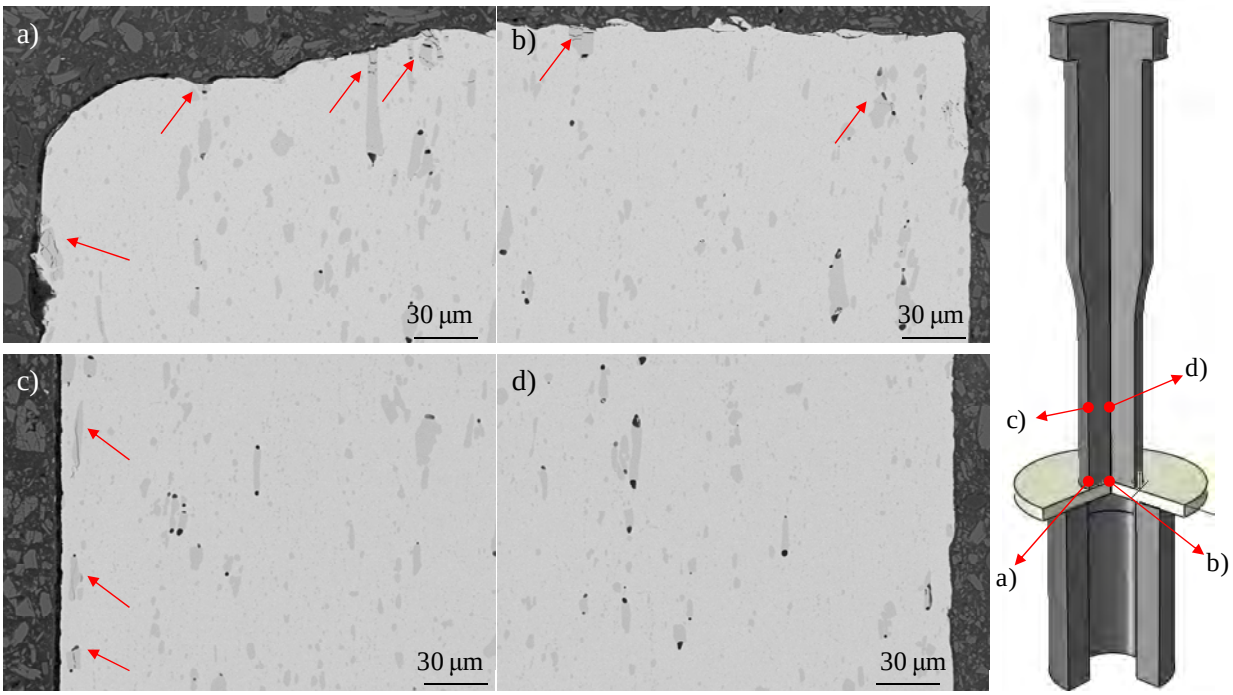

Figure 3.3.44 Cross sectional images of the punch cutting edge: 1.2379A after 31000 strokes at different positions of the punch; a) cutting edge; b) rake face at the middle of the punch; c) flank face and d) punch inner position

-Punches of 1.2379B

After 50 strokes, 1.2379B show sinking by plastic deformation at the cutting edge, as shown in Figure 3.3.39 b). No brittle fracture can be observed, opposite to 1.2379A, even though similar areas in 1.2379A and 1.2379B punches are affected by damage. Broken primary carbides are identified in the highly deformation zone and cracks emanating from them propagate parallel to the cutting edge (red arrows in Figure 3.3.45). Blue arrows in Figure 3.3.45 indicate the presence of cracks propagating following the machining grooves. Green arrows denote damage in the metallic matrix caused by microcracks, which might have nucleated under such high plastic deformation.

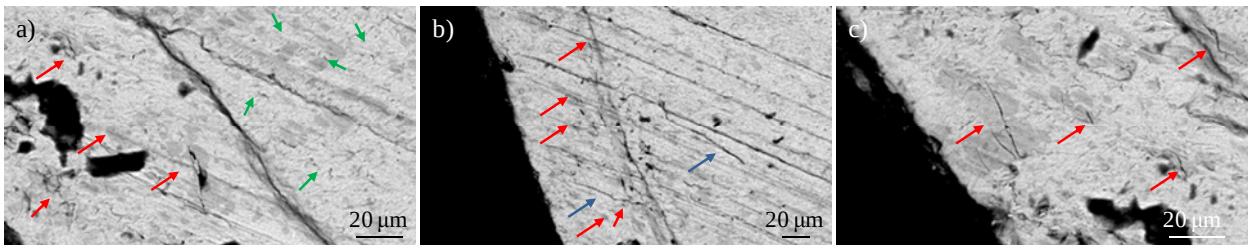

Figure 3.3.45 Cracks in 1.2379B punch nucleated in broken carbides in the plastically deformed zone near the cutting edge after 3000 strokes

Chipping starts to be observed at the cutting edge after 3000 strokes, as shown in Figure 3.3.46 a), and new chippings are continuously detected after 17000 (Figure 3.3.46 b)), 26000 (Figure 3.3.46 c) and 31000 (Figure 3.3.46 d)).

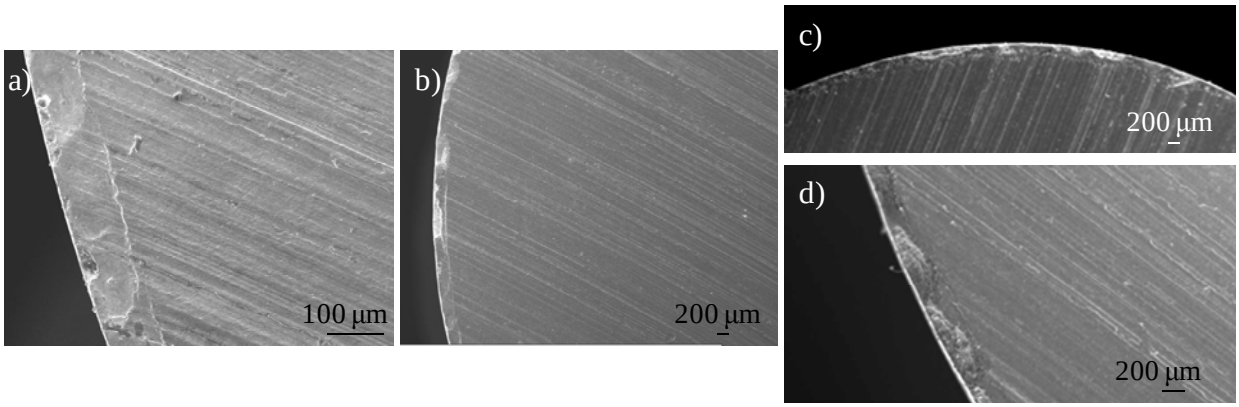

Figure 3.3.46 Fractography of 1.2379B punch after: a) 3000; b) 17000; c) 26000 and d) 31000 strokes

As shown in Figures 3.3.47 a), b) and c), some large propagating cracks are detected at the rake face of the 1.2379B punch after 26000 strokes. These cracks may explain the new fractures identified at 31000 strokes. The flank face of this punch is severely affected by wear and plastic deformation (Figure 3.3.47 d) after 31000 strokes) and some cracks parallel to the cutting edge can be observed (red arrows in Figure 3.3.47 e)).

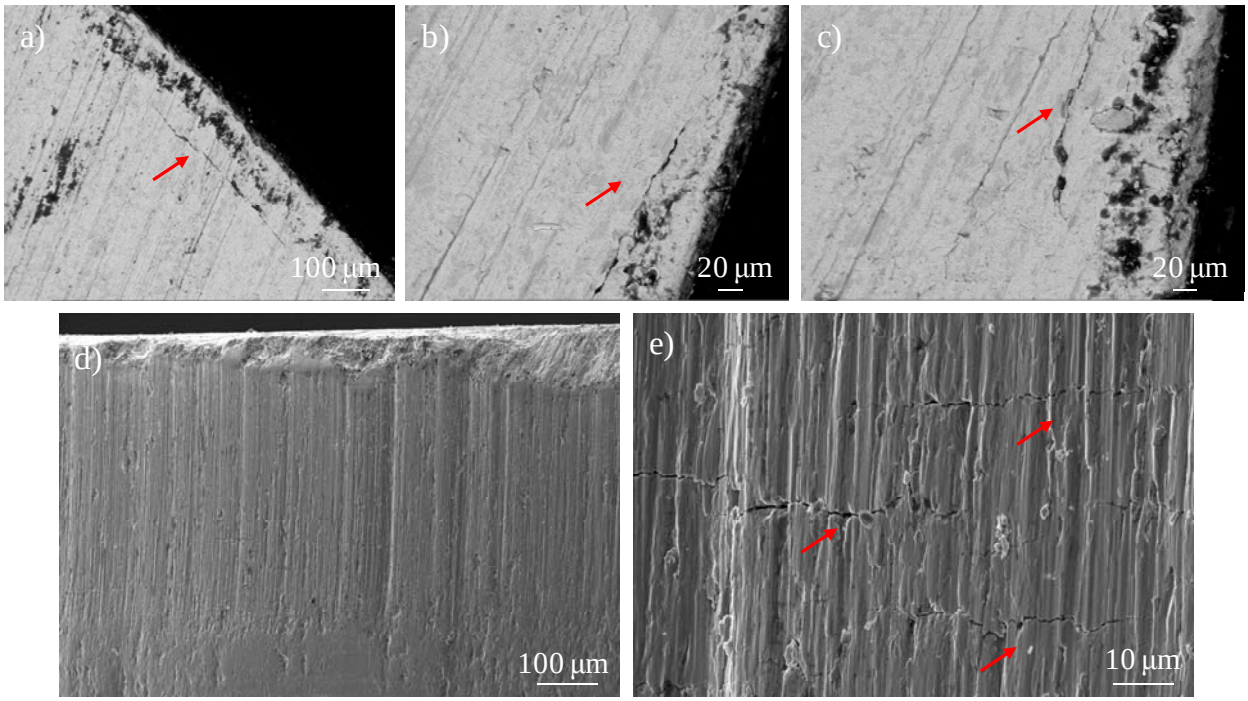

Figure 3.3.47 Fractography of 1.2379B punch: a), b) and c) cracks at the rake face after 2600 strokes; d) and e) wear, deformation and cracks at the flank face after 31000 strokes

Similar to 1.2379A, in 1.2379B microstructural damage caused by broken carbides is found at positions a), b) and c) (in reference to the punch schema depicted in Figure 3.3.44); while no damage can be seen in position d). Figure 3.3.48 a) shows a crack which is successfully captured prior to leading to failure at the cutting edge (indicated by the black square). This crack is possibly nucleated at the rake face and then it propagates in-wards, as shown in detail in Figure 3.3.48 b), while at the same time it tries to modify its direction towards the flank face. The surface of this punch has severely been affected by wear, as already shown in Figures 3.3.47 d) and e), hence the region directly below the surface (both at the rake and the flank faces) is highly damaged. Figures 3.3.48 c) and d) illustrate respectively the rake face and the flank face and in both cases, broken carbides and shallow cracks are identified. It is noteworthy that some submicrometric scale cracks are identified in the metallic matrix almost everywhere where some damage is encountered (black arrows in Figure 3.3.48 b)). These cracks can be the predecessors of microcracks, and their presence can be understood by fatigue damage of the metallic matrix.

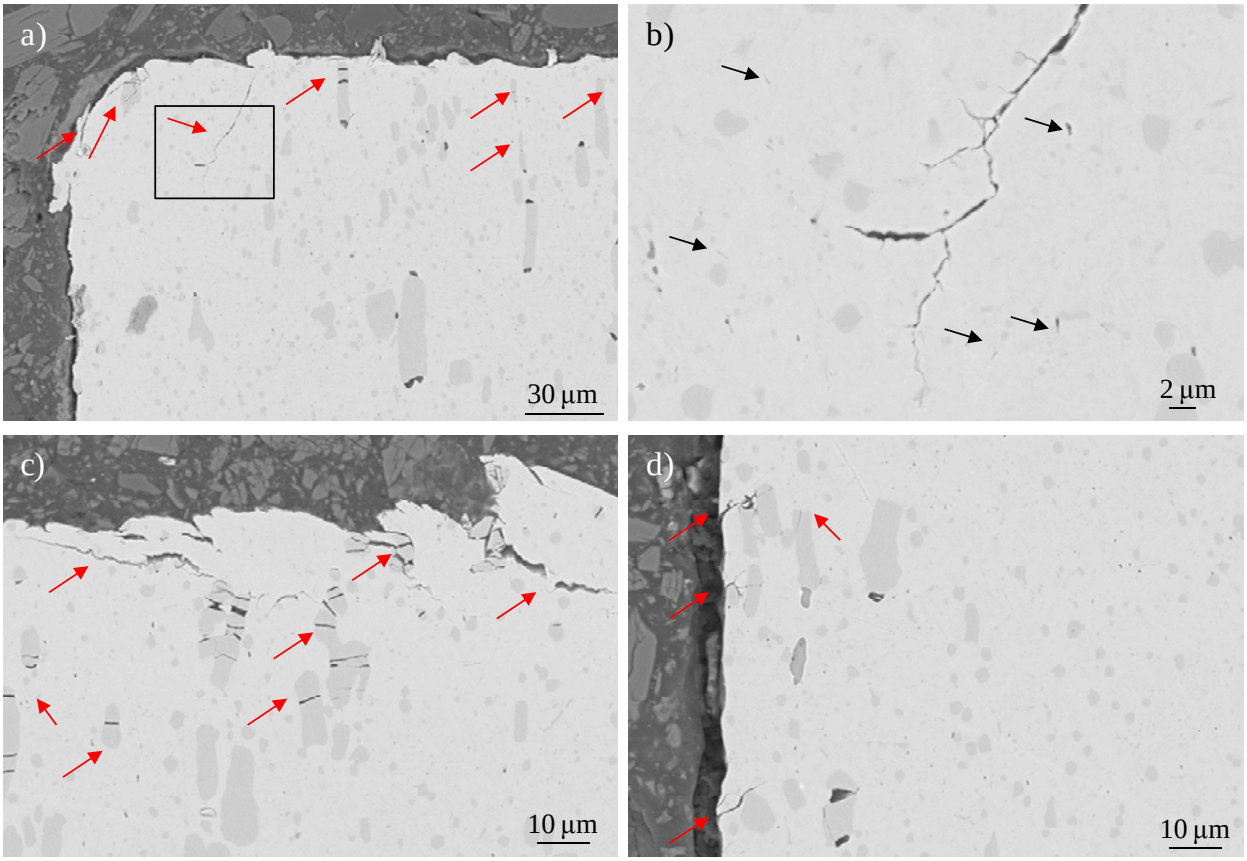

Figure 3.3.48 Cross sectional images of the punch cutting edge: 1.2379B after 31000 strokes; a) carbides are broken at the subsurface of the cutting edge and a crack propagates through the microstructure; b) zoom of this crack; c) cracks and broken carbides below the rake face and d) shallow cracks nucleated at the flank face

- Punches of K360

As shown in Figure 3.3.39 c), the cutting edge of K360 punches shows some plastic deformation at 50 strokes. Fractographic results after 5000 strokes are presented in Figure 3.3.49 and in Figure 3.3.49 a) it can be observed that the surface at the cutting edge is severely damaged by wear. Chipping is also observed at such highly worn areas, as illustrate Figures 3.3.49 b) and c), following the orientation of machining grooves.

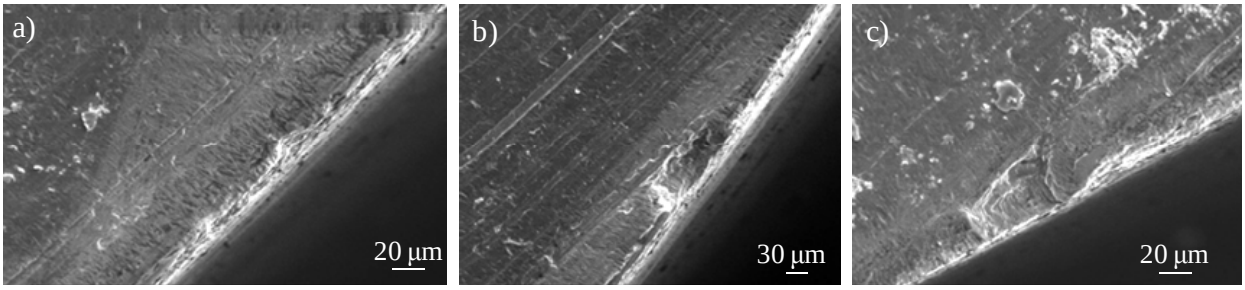

Figure 3.3.49 Fractography of a K360 punch after 5000 strokes: a) wear at the cutting edge; b) and c) chipping at the highly worn areas and fracture following machining grooves

- Punches of UNIVERSAL

After 50 strokes no damage is observed in punches made of UNIVERSAL, as shown in Figure 3.3.39 c). After 3000 strokes wear starts to affect the surface of the punch (Figure 3.3.50 a)) but no fracture is observed yet. At 17000 strokes, a few microcracks are discerned at the surface (Figure 3.3.50 b) in red arrows) and the cutting edge starts to be affected by small fractures (Figure 3.3.50 c)). With the increasing number of strokes, the observed microcracks coalesce and few chippings are identified at the cutting edge (Figure 3.3.50 d) after 26000 strokes). Wear at the flank face is also observed (Figure 3.3.50 e)), as well as the presence of cracks parallel to the cutting edge (Figure 3.3.50 f) in red arrows).

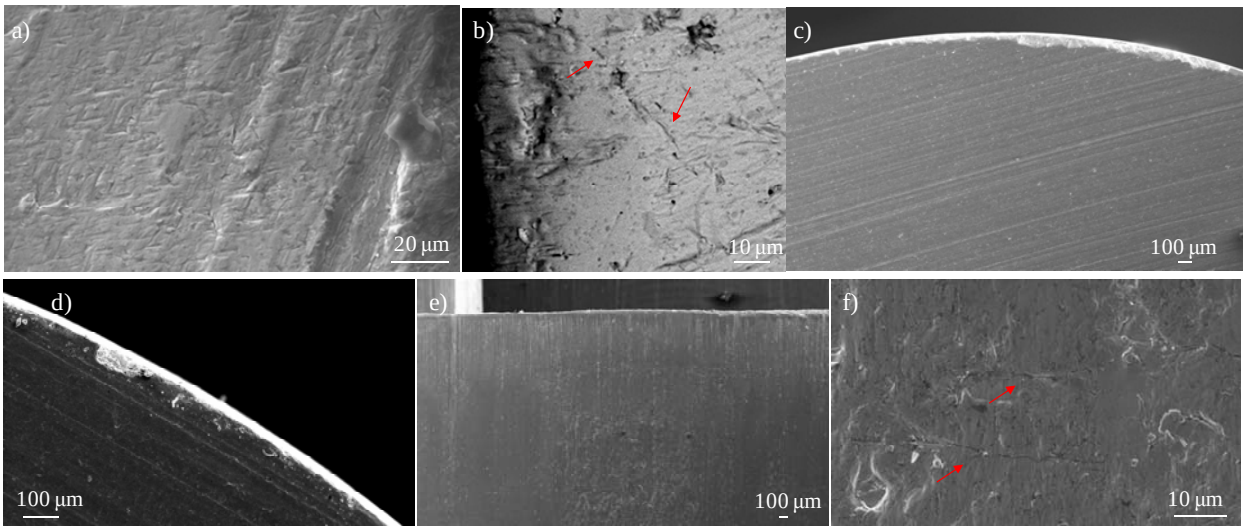

Figure 3.3.50 Fractography of an UNIVERSAL punch: a) wear after 3000 strokes; b) microcracks after 17000 strokes; c) small fractured area after 17000 strokes; d) chipping after 26000 strokes; e) wear at the flank face after 26000 strokes and f) cracks at the flank face parallel to the cutting edge

The cross sectional inspection of UNIVERSAL punches shows that few carbides are broken under the cutting edge after 26000 strokes (Figure 3.3.51 a)). Some cracks propagate at the subsurface near to the flank and the rake faces (Figures 3.3.51 b) and c) respectively), and Figure 3.3.51 b) also shows a piece of material about to detach from the surface. In figure 3.3.51 d) shallow cracks can be observed at the flank face.

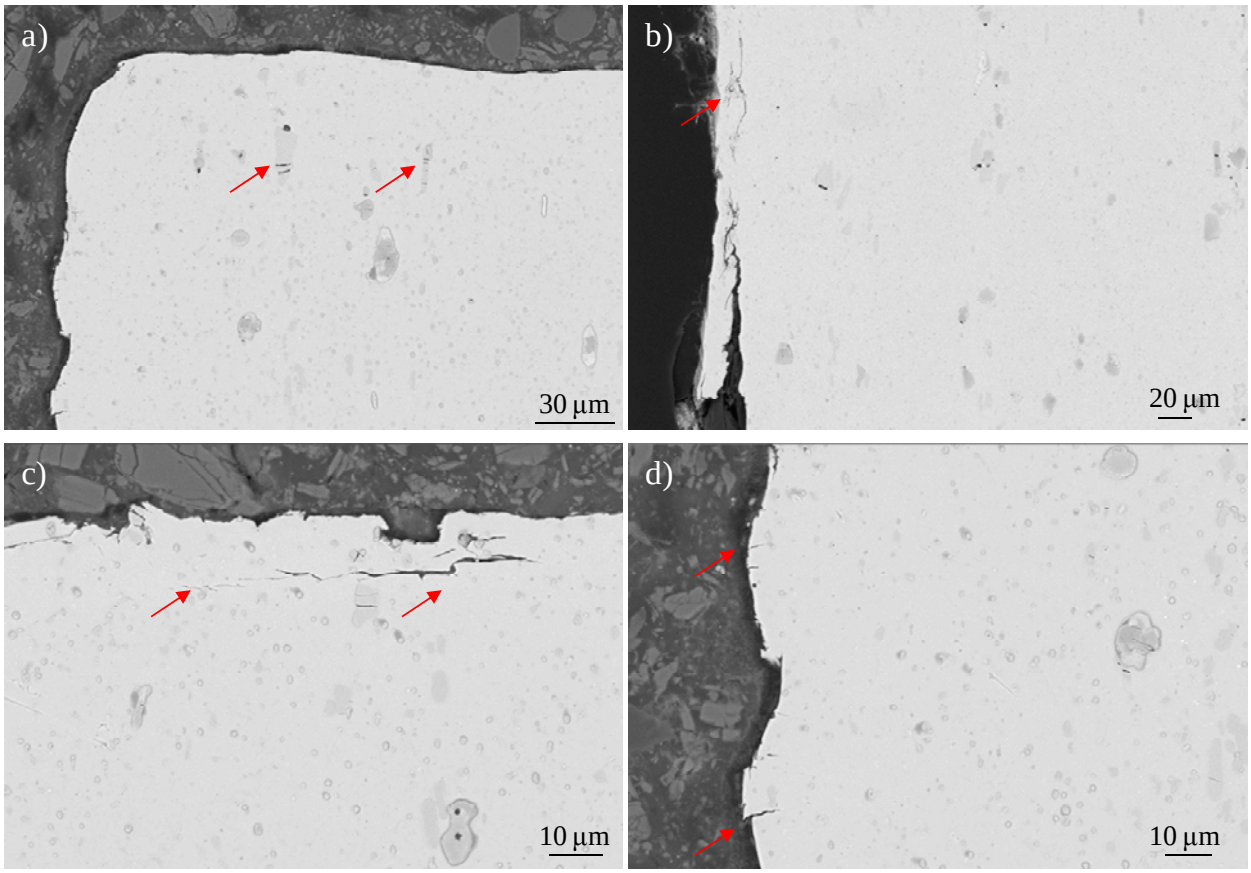

Figure 3.3.51 Cross sectional images of a UNIVERSAL punch after 26000 strokes; a) a few carbides are broken below the the cutting edge; b) subsurface cracks at the flank face and material about to detach; c) subsurface cracks and broken carbides at the rake face and d) shallow cracks nucleated at the flank face

- Punches of HWS

At 50 strokes, HWS punches show sinking in some regions of the cutting edge, as it shown in Figure 3.3.39 e). With the successive number of strokes, the cutting edge is rounded and highly worn out (Figure 3.3.52 a) and b), respectively). In the region where sinking is previously observed, chipping appears at 17000 strokes (Figure 3.3.52 c)). Damage in this region does not evolve at 26000 strokes with respect to 17000 (Figure 3.3.52 d)), but new chippings can identified at other regions of the cutting edge (Figure 3.3.52 e) oriented following the machining grooves).

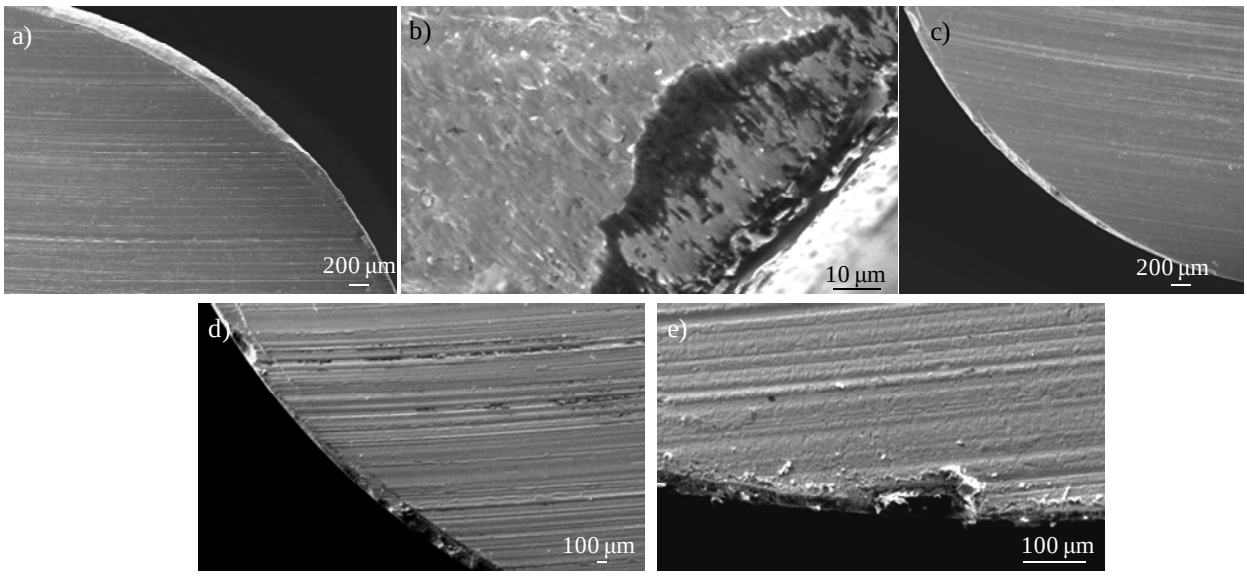

Figure 3.3.52 Fractography of an HWS punch: a) rounding of the cutting edge after 17000 strokes; b) wear at the surface after 17000 strokes; c) fractures by chippings at a previously sunk zone after 17000 strokes; d) the same zone than (c) but at 26000 strokes and e) new chipping at 26000 strokes

- PVD coated punches

AlTiN and W:C-H PVD coatings are tested on UNIVERSAL and HWS substrate punching tools. Figure 3.3.53 shows the flank face of the UNIVERSAL punch coated with W:C-H at 1500 strokes. In Figure 3.3.53 a) it can be observed that near to the cutting edge, the coating has worn out (white marks in the light gray coating surface). In this zones, sheet material is preferentially adhered (dark gray lumps in Figures 3.3.53 b) and c)). Many cracks are identified at the coating and in some cases, coating detachment reveals that a few cracks are also nucleated in the substrate (Figures 3.3.53 d) and e)).

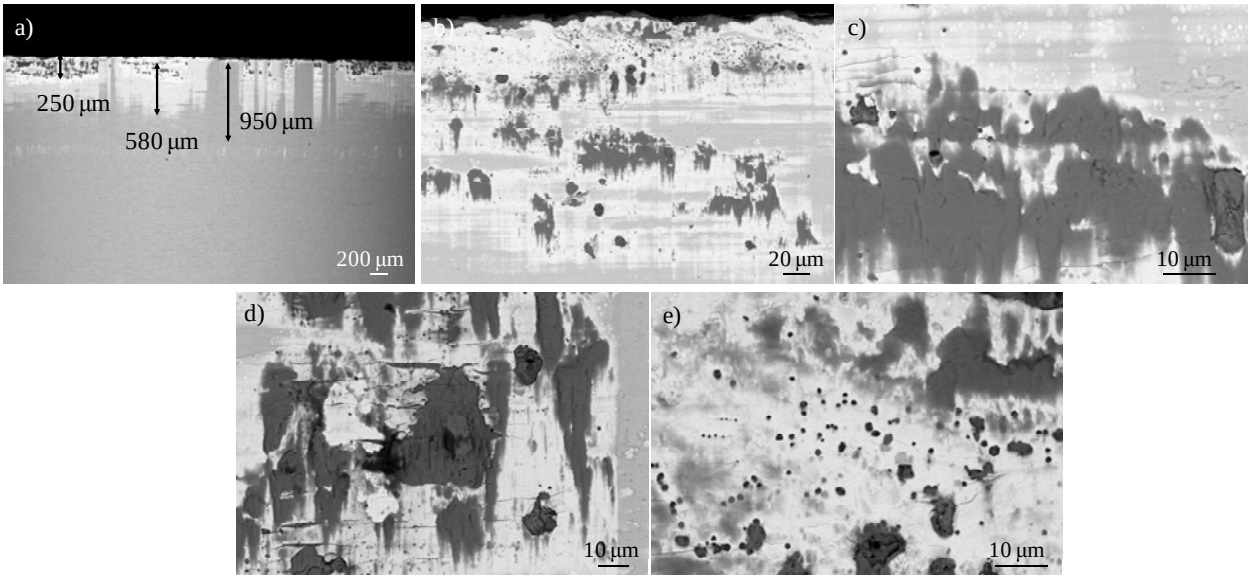

Figure 3.3.53 Fractography of the UNIVERSAL punch coated with W:C-H; flank face at 1500 strokes

The HWS punch coated with W:C-H shows very similar trends than the UNIVERSAL at 1500 strokes, even though it shows better performance since it starts showing wear at shorter distances from the punch edge (at 250 μm compared to 580 μm in UNIVERSAL). As shown in Figure 3.3.54, the coating is progressively worn out going close to the cutting edge (Figure 3.3.54 a)) and sheet material is preferentially adhered in those places where the coating is being removed (Figure 3.3.54 b)).

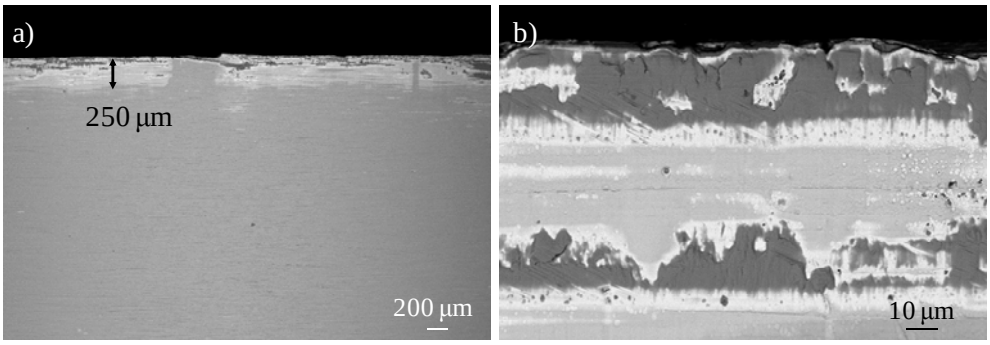

Figure 3.3.54 Fractography of the HWS punch coated with W:C-H; flank face at 1500 strokes

Chipping is observed at 1500 strokes at both W:C-H coated UNIVERSAL and HWS punches (Figures 3.3.55 a), b), c) and d), e), f) respectively), and cracks use to follow the direction of machining grooves. It is worth to say that the initial surface roughness of tools has detrimental effects on the coating deposition; i.e. the high peaks and valleys (grooves) created during machining processes make difficult the homogeneous repartition of the coating (see for instance Figure 3.3.55 a), where deep valleys between machining grooves are not successfully coated).

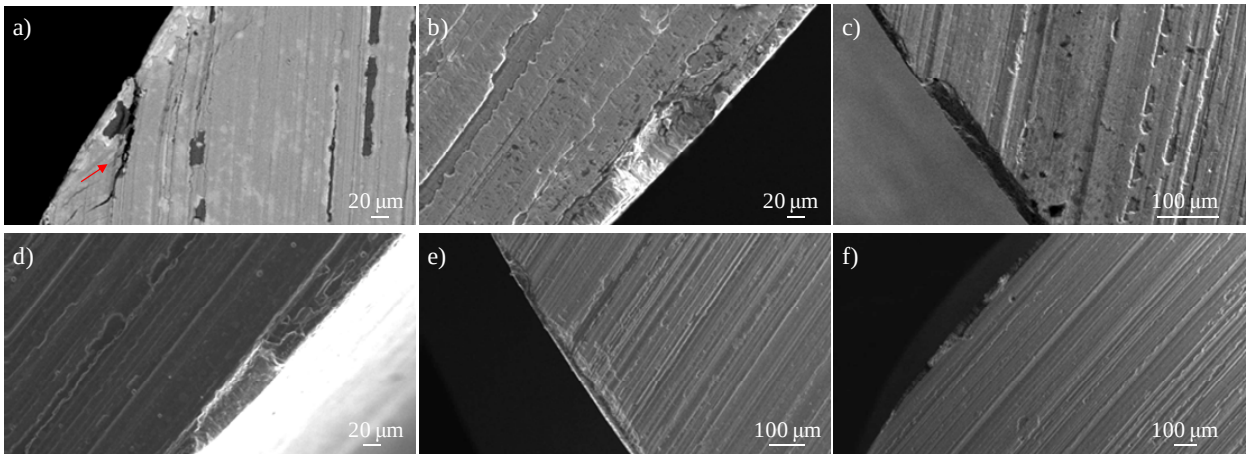

Figure 3.3.55 Fractography of the UNIVERSAL (a), b) and c)) and HWS (d), e) and f)) punches coated with W:C-H; rake faces at 1500 strokes

Punches coated with AlTiN, in turn, are analysed at 5000 strokes and the fractographic results are reassembled in Figure 3.3.56 in case of UNIVERSAL and Figure 3.3.57 in case of HWS. AlTiN on UNIVERSAL shows scarce performance since it is practically removed even as far distances from the cutting edge as 2000 µm (Figure 3.3.56 a)). There is a gradual deconvolution of the coating (Figures 3.3.56 b) and c)) and in those zones where it has completely disappeared, microcracks in the tool steel microstructure are observed (some of them are shown in red arrows in Figure 3.3.56 d)).

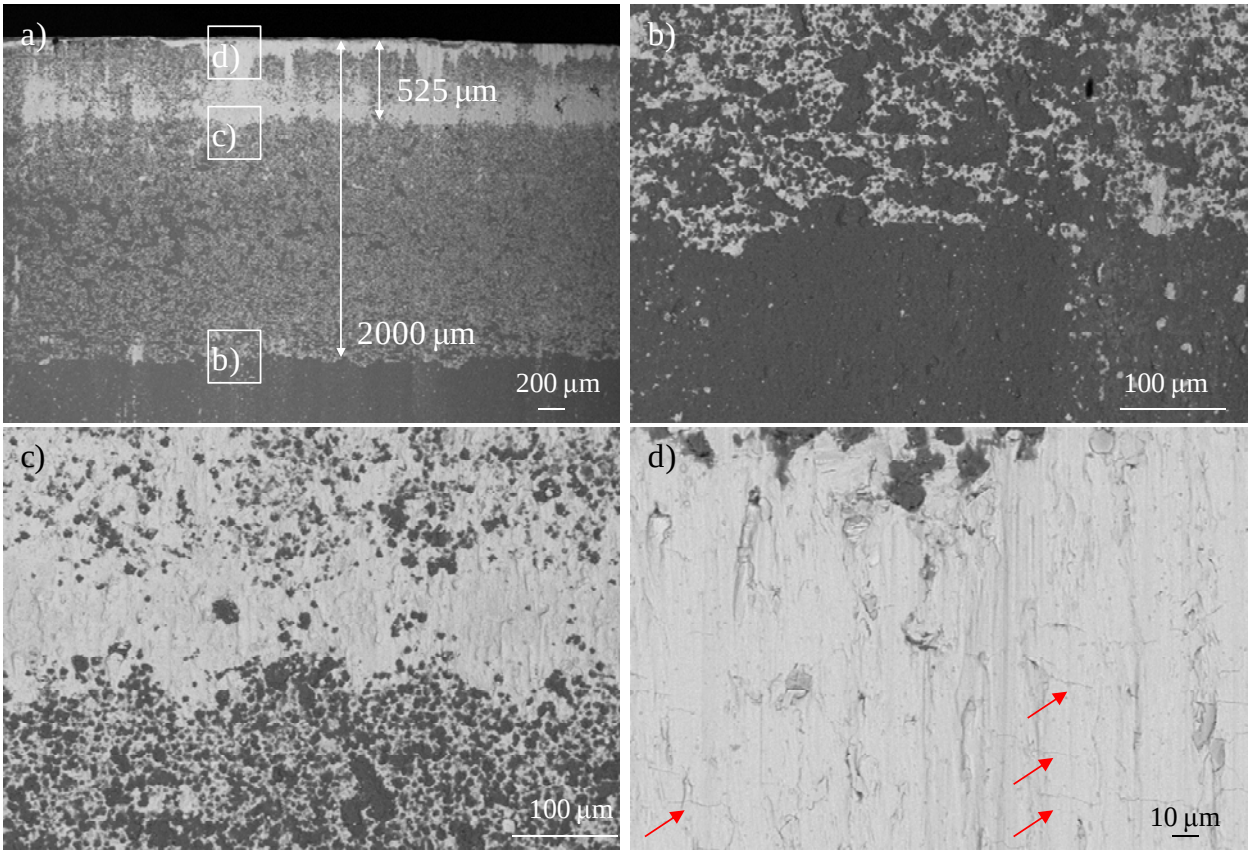

Figure 3.3.56 Fractography of the UNIVERSAL punch coated with AlTiN; flank face after 5000 strokes

For HWS, the same behaviour as in case of UNIVERSAL is observed (Figures 3.3.57 a) throughout d)).

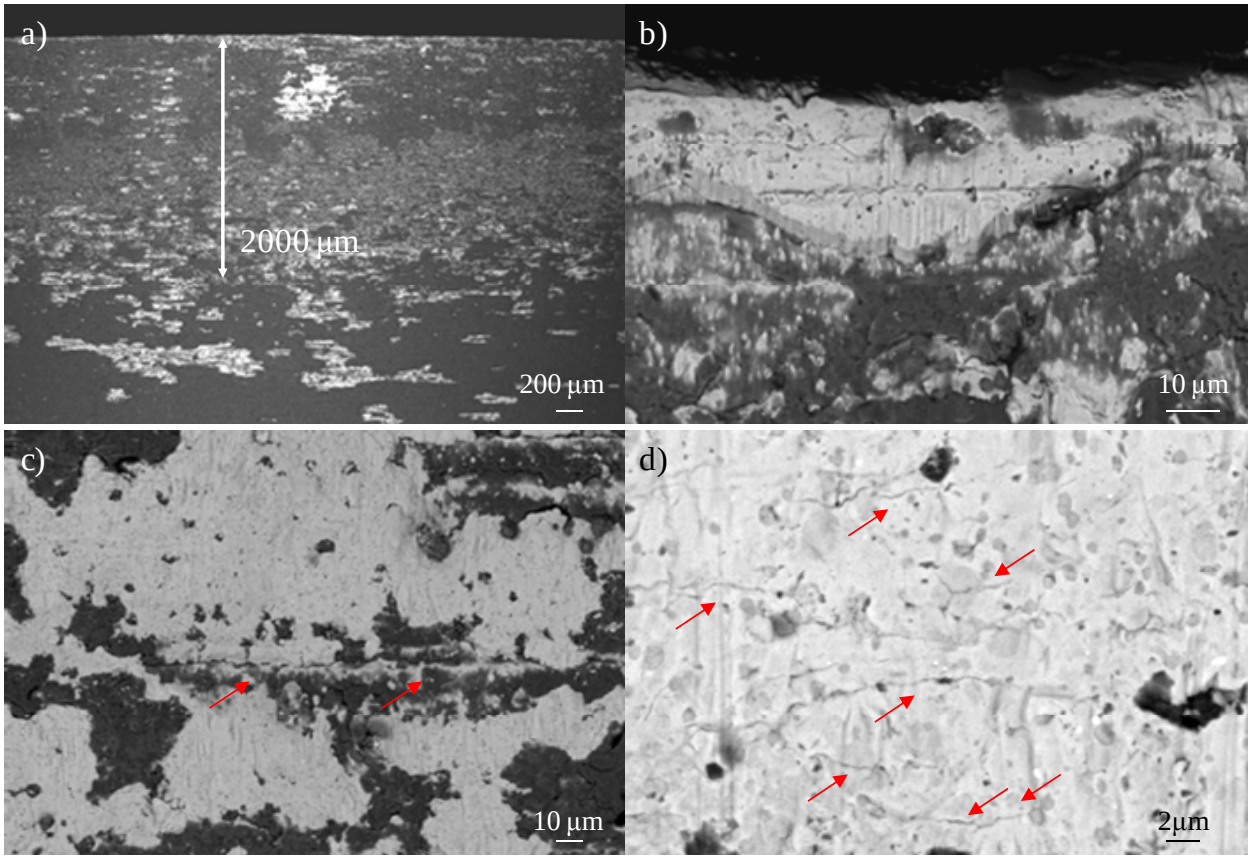

Figure 3.3.57 Fractography of the HWS punch coated with AlTiN; flank face after 5000 strokes

Fractographic inspection also reveals that chipping takes place in few occasions in case of the UNIVERSAL punch (Figure 3.3.58 a)). In the HWS, a bad deposition of the coating is evident at the rake face (Figure 3.3.58 b)), but no chipping is observed (3.3.58 c)).

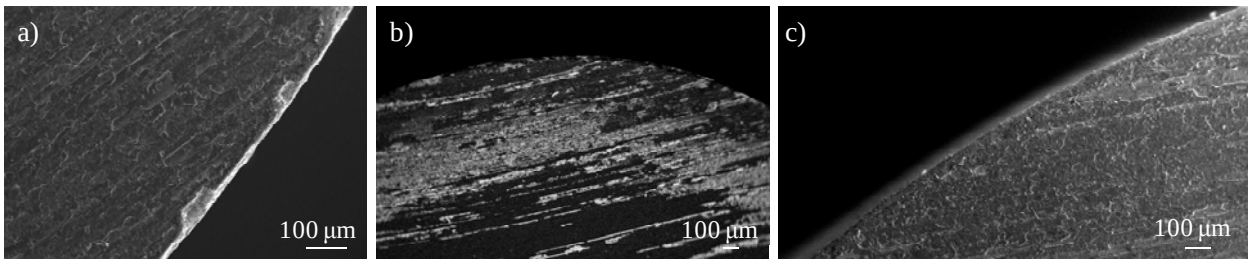

Figure 3.3.58 Fractography of the a) UNIVERSAL; b) and c) HWS punches coated with AlTiN; rake face after 5000 strokes

The W:C-H coating on UNIVERSAL punch as substrate at 5000 strokes shows better performance than the AlTiN at the same number of strokes. As illustrated in Figure 3.3.59 a), b) and c), gradual wearing of the coating is observed at closer distances from the cutting edge than in case of the AlTiN coated punches. Several cracks are however, detected at the regions where the coating has completely been detached (Figure 3.3.59 d)). Fracture occurs at the cutting edge as shown in Figure 3.3.60 a), b) and c).

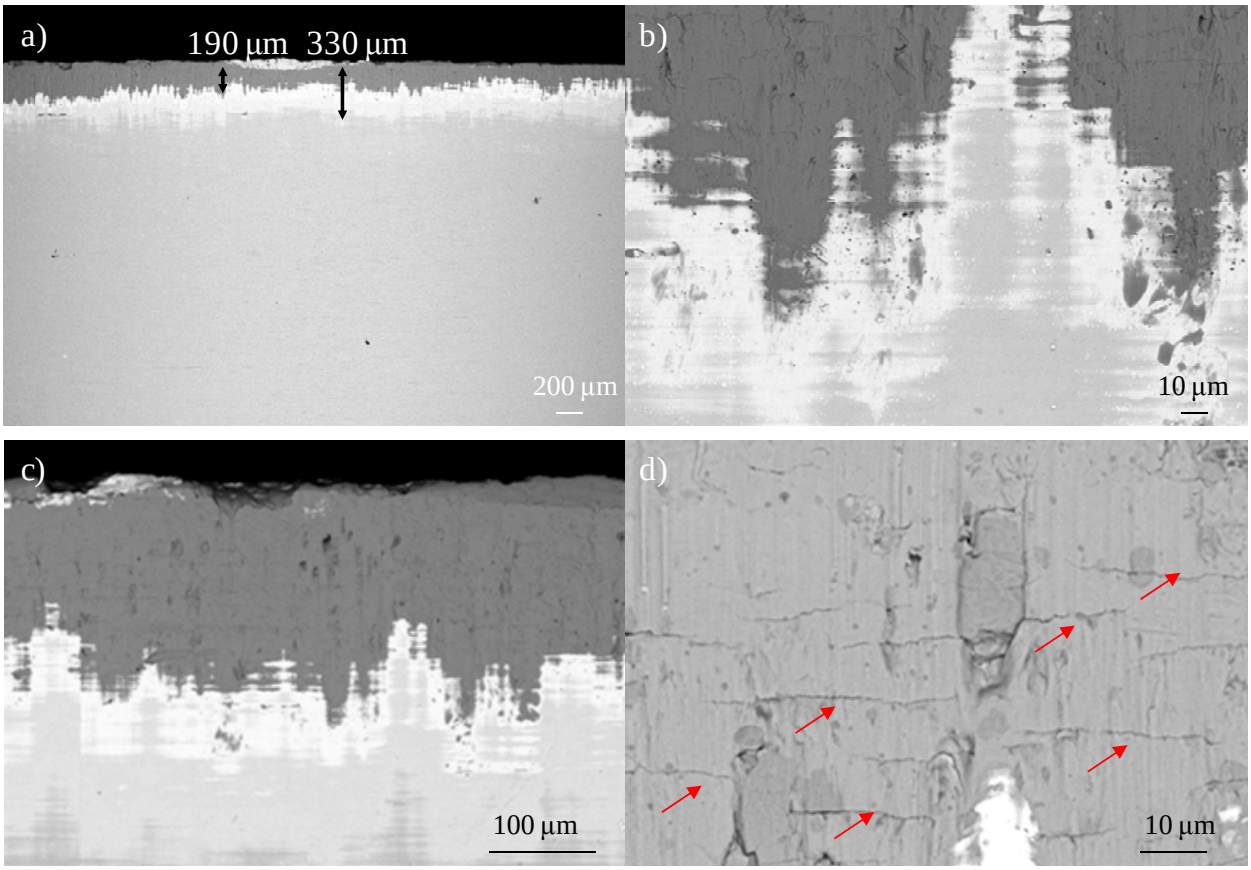

Figure 3.3.59 Fractography of the UNIVERSAL punch coated with W:C-H; flank face after 5000 strokes

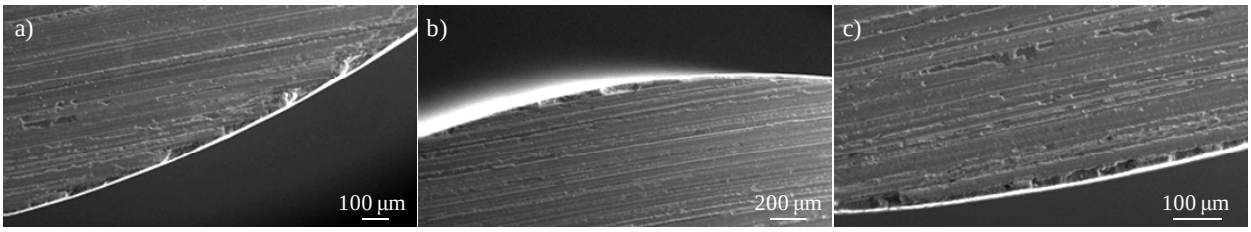

Figure 3.3.60 Fractography of the UNIVERSAL punch coated with W:C-H; rake face after 5000 strokes

Regarding the HWS punch coated with W:C-H at 5000 strokes, it also shows a better performance compared to the AlTiN (in terms of the distance from the cutting edge at which it is worn, Figure 3.3.61 a) and b)). Several cracks are always detected at the regions where the coating has completely been detached (Figure 3.3.61 c)) and lumps of sheet material are adhered directly on the worn coating (Figure 3.3.61 d)).

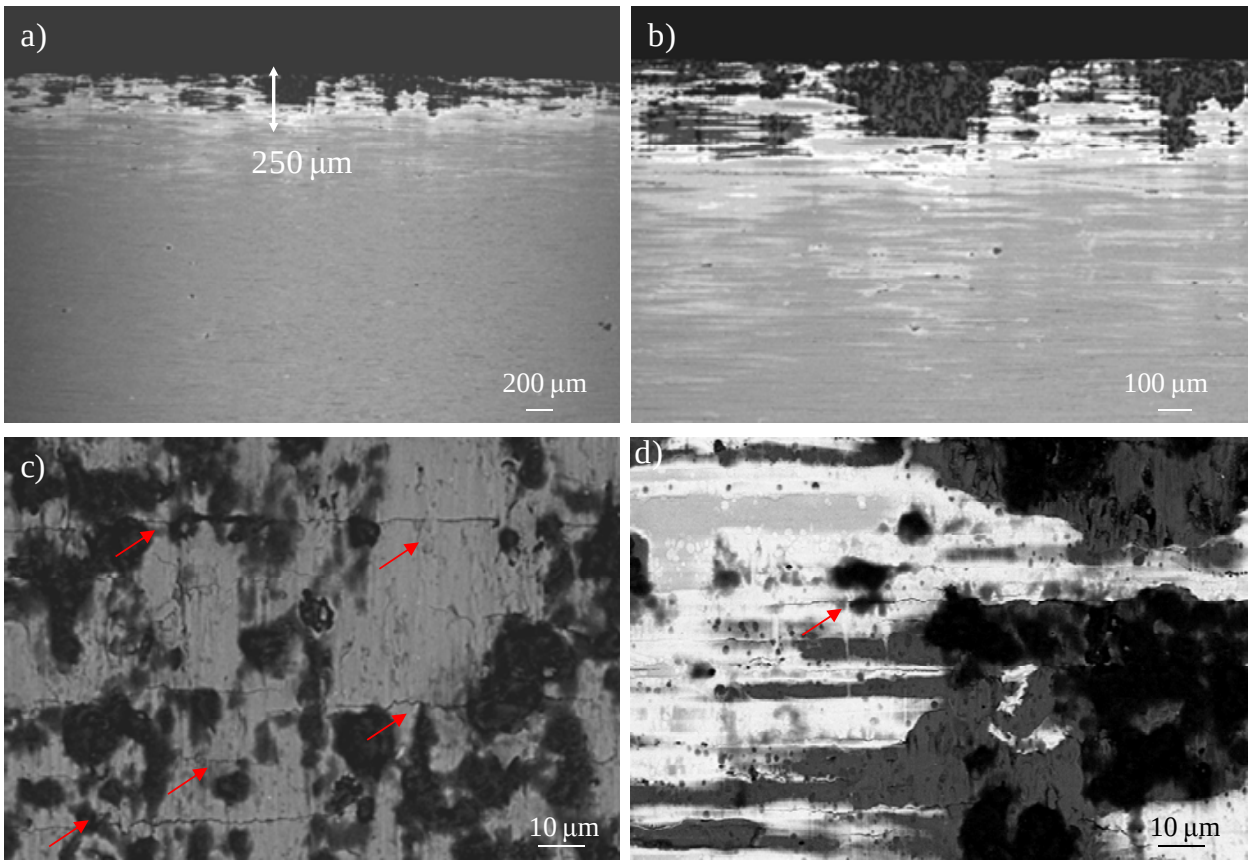

Figure 3.3.61 Fractography of the HWS punch coated with W:C-H; flank face after 5000 strokes

Once again the inspection of the rake face reveals a non homogeneous deposition of the W:C-H coating at the surface, namely due to the deep grooves produced by machining processes (Figure 3.3.62 a)). Chipping and several small fractures (also influenced by the machining grooves) are observed at the cutting edge (Figures 3.3.62 b) and c)).

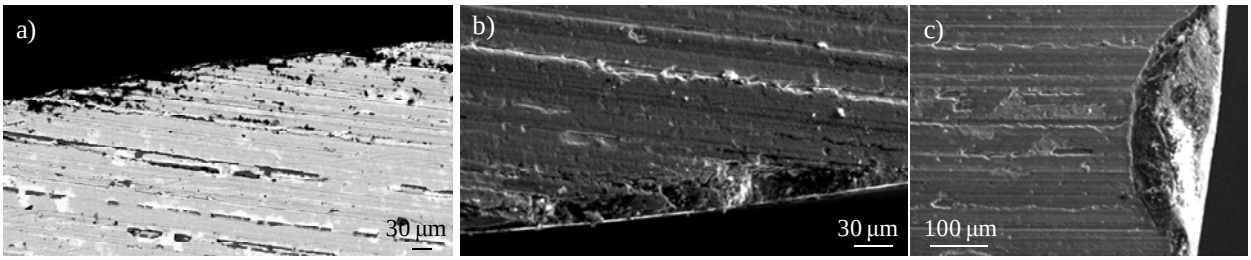

Figure 3.3.62 Fractography of the HWS punch coated with W:C-H; rake face after 5000 strokes

After 12000 strokes, chipping is observed in the UNIVERSAL W:C-H punch cutting edge (Figure 3.3.63 a) and b)). Some cracks are identified at the coating surface (red arrows in Figure 3.3.63 c)), and they can have likely been the reason for crack nucleation and propagation through the substrate, at the origin of the fractures observed. In the HWS punch coated with AlTiN, chipping is not observed at 12000 strokes (Figure 3.3.63 d) throughout f)) and the entire cutting edge remains in good quality (even though the coating is prematurely worn, as observed in Figure 3.3.57).

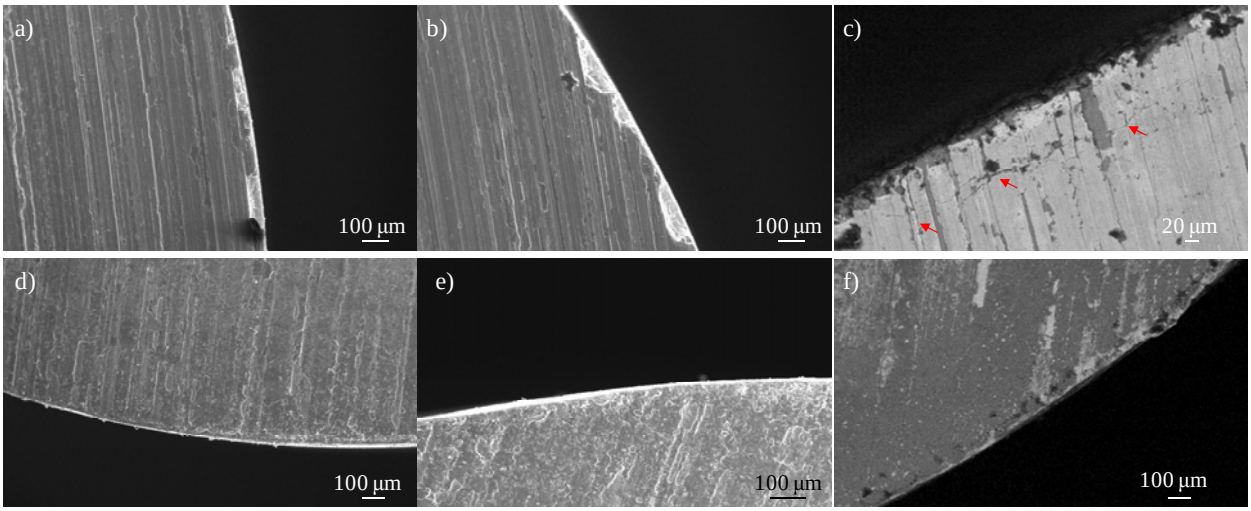

Figure 3.3.63 Fractography of the rake face in UNIVERSAL W:C-H punch (a) throughout c)) and HWS – AlTiN punch (d) throughout f)) at 12000 strokes

As follows from the results obtained in this investigation, the application of such PVD coatings does not improve the performance of tools compared to nude substrates. A reason for that is that the tools initial roughness is very high due to deep machining grooves. PVD coatings possess internal compressive stresses of the order of 1 – 5 GPa. This stresses act positively for the coating cohesion, but negatively on its adhesion to the substrate. In combination with a rough substrate, excessively high compressive stresses may cause spontaneous detachment without any external loads. Lateral compressive stresses in the coating combined with a rough substrate generate tensile stresses across the coating - substrate interface as illustrated in Figure 3.3.64. These ridges are the result of a too rough grinding process or incorrect grinding parameters. Consequently, most of the common PVD coatings employed in operations with UHSS rather fail by fatigue and discrete delamination or detachment than removal by slow gradual wear (that has also been shown in section 3.3.2.2 when punching MS-W1200). Once the coating is removed, the wear mechanisms of coated tools are the same as those of uncoated, although more severe because the nude substrate is already damaged.

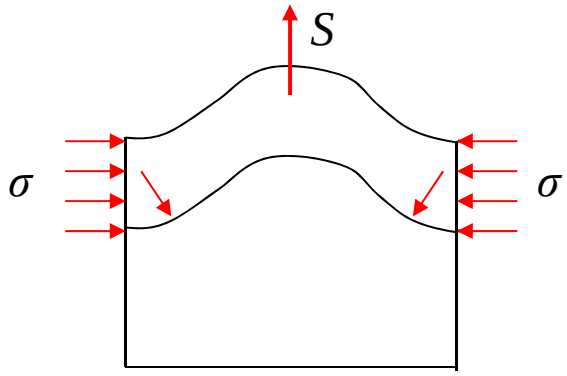

Figure 3.3.64 The lateral compressive stresses state *σ* present in most PVD coatings generates interfacial stresses *S*. At the top of e.g. grinding ridges this stress is a tensile "lift off" stress that may reach the same order of magnitude as the residual stress *σ*

3.3.3.2 Damage mechanisms in slitting tools

Von Mises stresses acting in slitting tools of the HPC are shown in Figure 3.3.65. Maximum stresses are registered below the cutting edge of the lower tool and they attain more than 2000 MPa. Stresses in the upper tool are lower, they attain between 800 and 1000 MPa below the cutting edge.

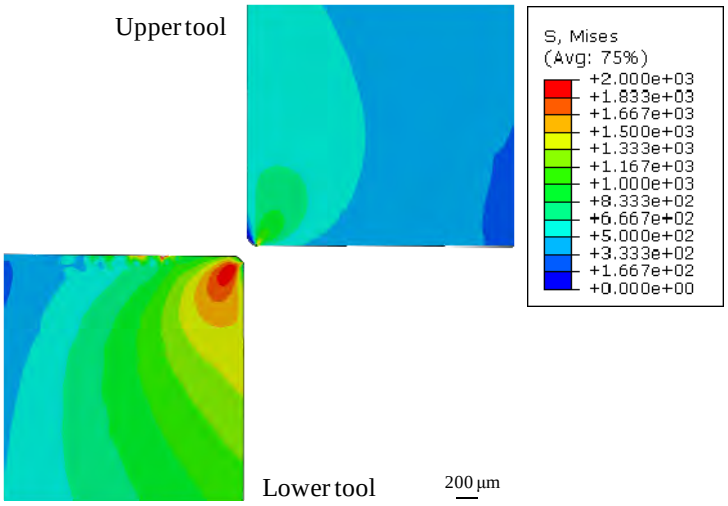

Figure 3.3.65 Von Mises stresses determined by means of FE-simulation in the HPC slitting tools. Slitting DP1000 2 mm thick with a clearance of 10 %

The stress distribution in tools before the fracture of the sheet, i.e. until the force attains its maximum value, was analysed by Nothhaft [NOT10]. Even though in Nothhaft's work the sheet analysed was press hardened 22MnB5 1,75 mm thick, the results obtained by this author help figuring out the stress evolution during one stroke in HPC tools for DP1000 2 mm thick. As follows from the work of Nothhaft, Figure 3.3.66 shows the stress distribution at different steps of the cutting process, as well as the maximum stress (dashed line) and the load (solid line) in function of the tool displacement. The location of maximum stresses evolves during the process from the surface in contact with the sheet (at the first step of rollover zone formation), to the interior of the tool moving towards the flank face (at the stage of bright zone formation).

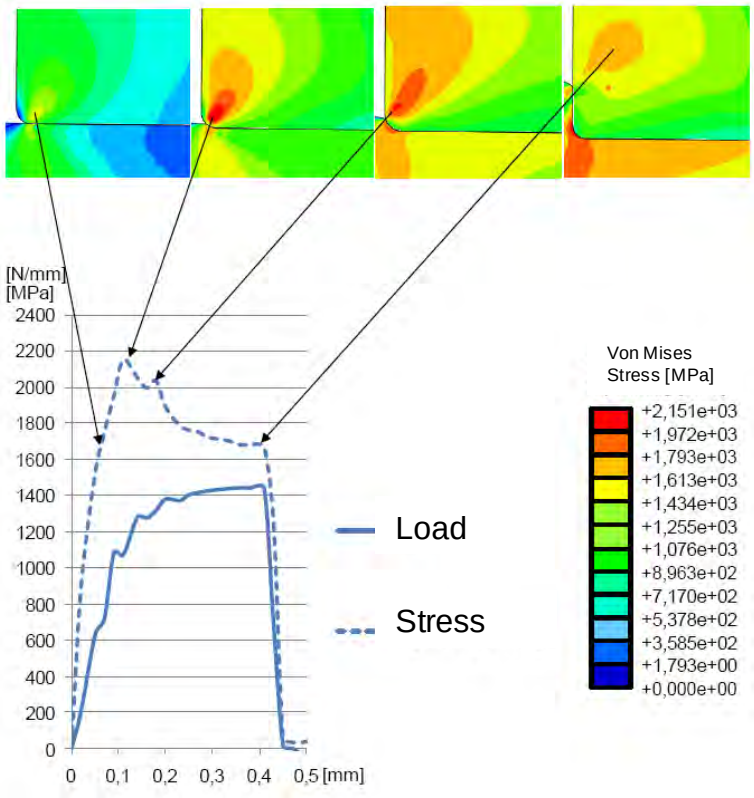

Figure 3.3.66 Location of the maximum stress in the upper blade during the slitting process of 22MnB5 1,75 mm thick with a cutting clearance of 15 %. Comparison between stress (dashed line) and load (solid line) in function of displacement [NOT10]

The main damaging mechanisms of slitting tools are shown in Figure 3.3.67 for 1.2379 tools after 36000 strokes. The fractographic inspection reveals that the upper tool is affected by wear, while the lower tool shows premature fracture by chipping. Figure 3.3.67 shows that besides fractures, the rake face of the lower tool is highly worn. This type of wear may be attributed to the extremely high contact forces which appear between the sheet and the tool surface during the cutting process.

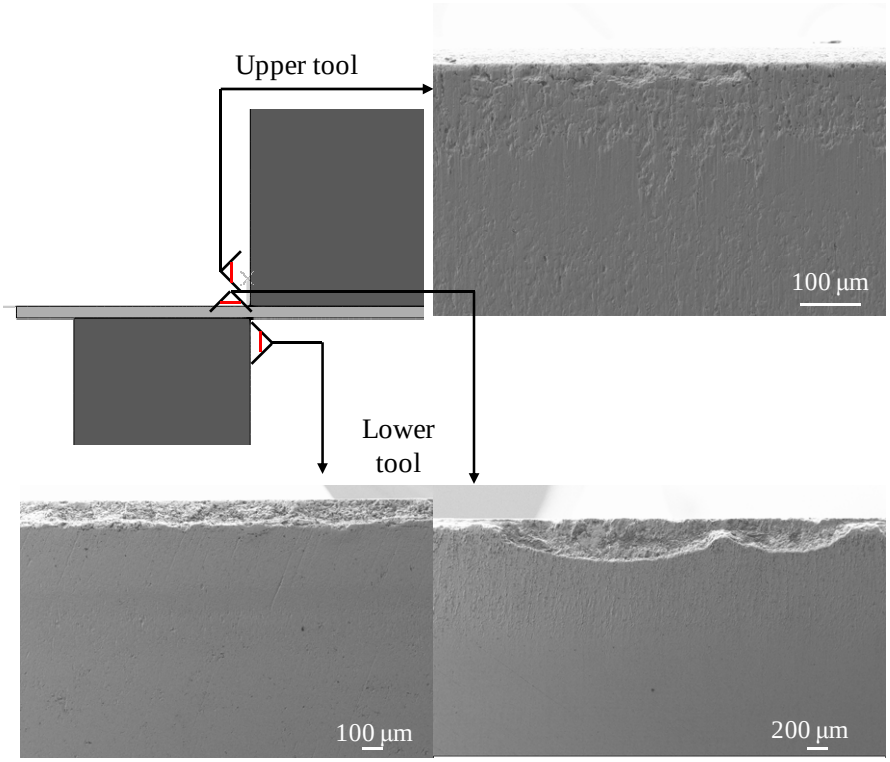

Figure 3.3.67 Fractographic inspection of the 12379 upper and lower slitting tools

Figure 3.3.68 illustrates, in turn, that in the 1.2379 lower tool long cracks nucleate and propagate at the flank face, parallel to the cutting edge. These cracks are observed at an approximated distance of 150 µm from the cutting edge, as shows Figure 3.3.68 b) at 8000 strokes. This distance is in agreement with the size of the fractured zone observed at higher number of strokes, as depicted in Figure 3.3.68 c) for 22000 strokes.

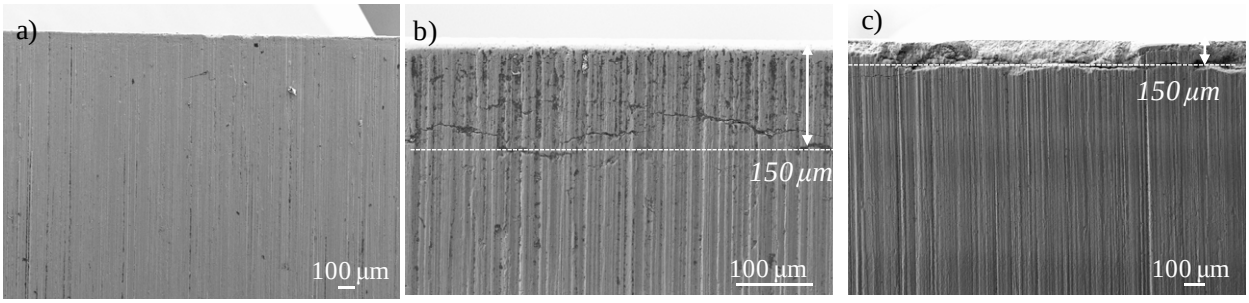

Figure 3.3.68 Fractographic images of the 1.2379 lower tool observed using SEM after a) 0 strokes; b) 8000 strokes and c) 22000 strokes

Figure 3.3.69 shows the evolution of the surface of the upper tool at increasing number of strokes, from 16000 to 36000. Wear, mainly due to a combination of adhesion and abrasion, is the main damaging mechanism observed at the cutting edge.

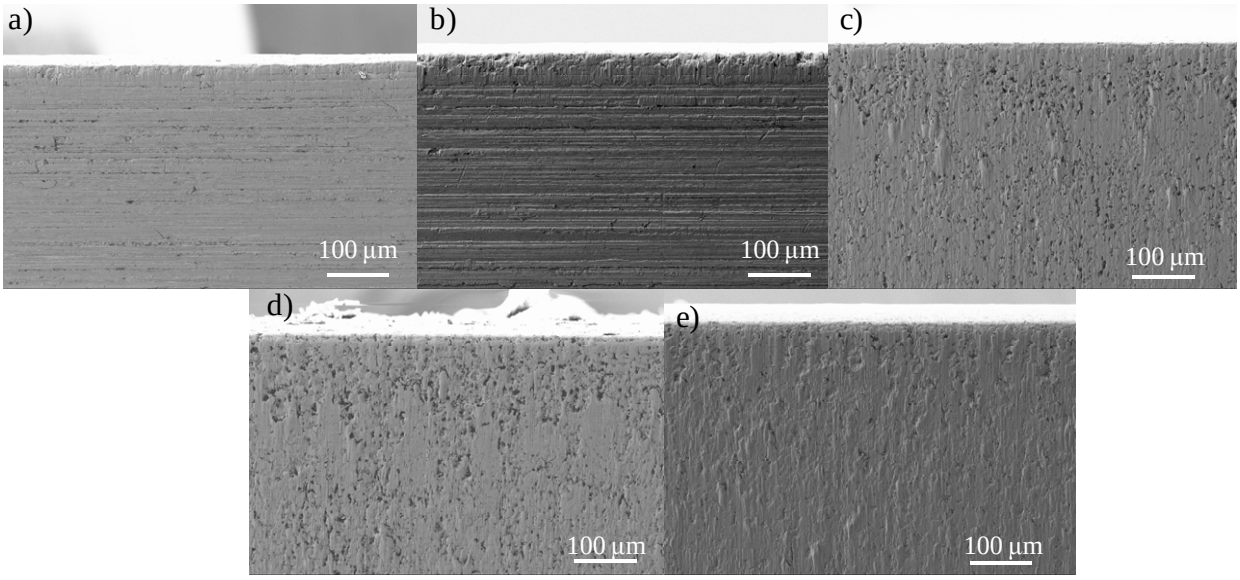

Figure 3.3.69 Fractography of the 1.2379 upper tool at increasing number of strokes: a) 16000; b) 22000; c) 26000; d) 31000 and e) 36000

The microstructure of two 1.2379 pair of tools was inspected in cross section, after 22000 and 36000 strokes, as shows the Figure 3.3.70 a)-b) and c)-d) respectively. In this figures it can be observed that according to the conclusions of the fractographic analysis presented above, in the lower tools many cracks nucleate and propagate (Figures 3.3.70 a) and c)), while the upper tools show practically no damage (Figures 3.3.70 b) and d)). In the lower tools, two different types of cracks can be identified: the first ones consist in cracks at broken carbides and they are, in all cases, aligned parallel to the stroke direction (red arrows in Figure 3.3.70); while the second type of cracks seems to have probably nucleated at the flank face of the tool and propagated perpendicular to the stroke by fatigue (blue arrows in Figure 3.3.70) (these cracks correspond to those observed previously in the fractographic inspection of the flank face, as show the images of Figure 3.3.68). Notice that none of the cracks nucleated at broken primary carbides propagate through the matrix in the samples examined.

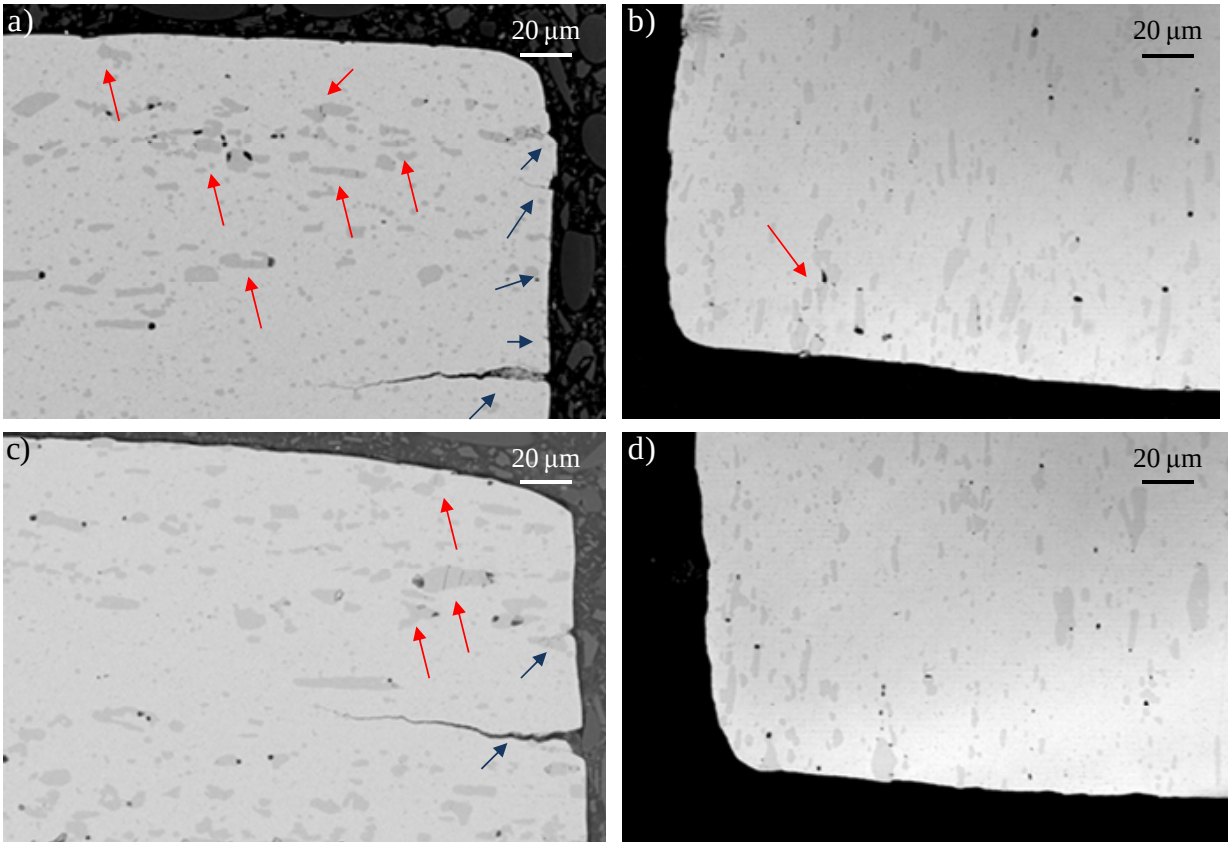

Figure 3.3.70 Microstructural inspection of the cross section of 1.2379 slitting tools: a) lower tool at 22000 strokes; b) upper tool at 22000 strokes; c) lower tool at 36000 strokes and d) upper tool at 36000 strokes

The analysis of the microstructure in the cross section of tools reveals that they have been machined, by mistake, with different carbide orientations. In lower tools the carbide bands are aligned perpendicular to the stroke direction while in the upper ones, the carbides are aligned parallel to this. Such observation may help explaining that the lower tool presents fractures while the upper one does not (since as discussed in section 3.2.1, 1.2379 is markedly anisotropic).

With reference to the effect of the type of tool steel microstructure to the failure mechanisms observed, at the same number of strokes as 1.2379, the UNIVERSAL tools show a better behaviour. As shown in Figure 3.3.71, at 10000 strokes the flank face of the 1.2379 lower tool shows many cracks and also some fractures at the cutting edge (Figure 3.3.71 a)), while in the UNIVERSAL only some small fractures at the cutting edge are observed, with no long horizontal cracks (Figure 3.3.71 b)).

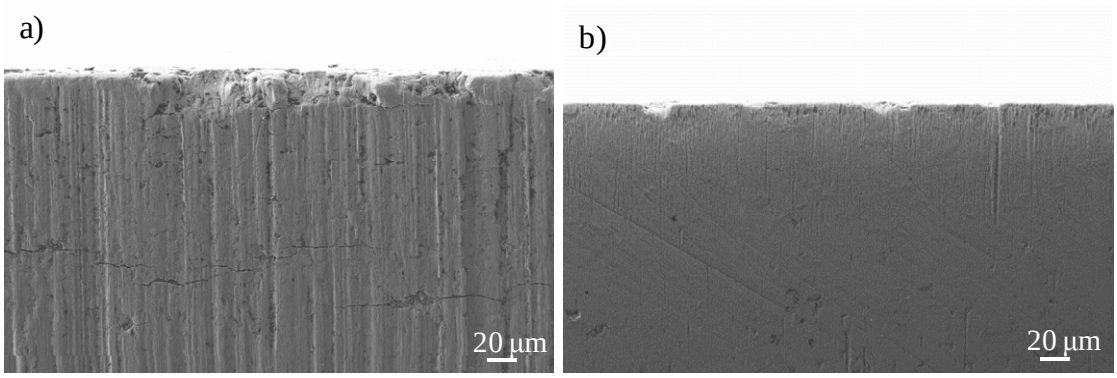

Figure 3.3.71 Images of the flank face of the lower tool at 10000 strokes: a) 1.2379 and b) UNIVERSAL

However, a closer gaze to the surface of the UNIVERSAL lower tool reveals that some cracks have actually nucleated and started propagating, as shows Figure 3.3.72. These cracks are rather small yet and they are located at very short distances from the cutting edge (at approximately 20 µm). As it can be observed in Figures 3.3.72 b) and c), these cracks may be nucleated due to the presence of a damaged zone at the surface (probably originated by wear).

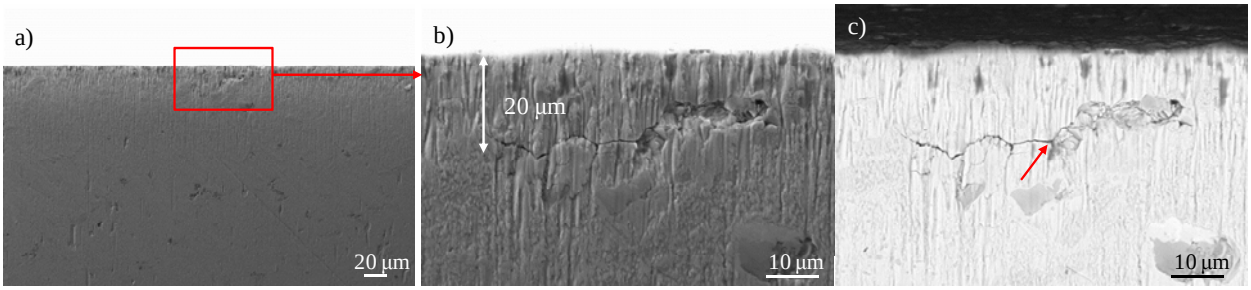

Figure 3.3.72 Images of the flank face of the UNIVERSAL lower tool at 10000 strokes: a) low magnification image; b) zoom in the zone indicated in a) and c) backscattered image of b)

After 15000 strokes, no relevant damage is observed in the UNIVERSAL lower tool compared to 10000 strokes, except for some small cracks observed previously which have propagated further. Figure 3.3.73 shows an example of a crack which, similar to that shown in Figure 3.3.72, it is nucleated from a defect at the surface.

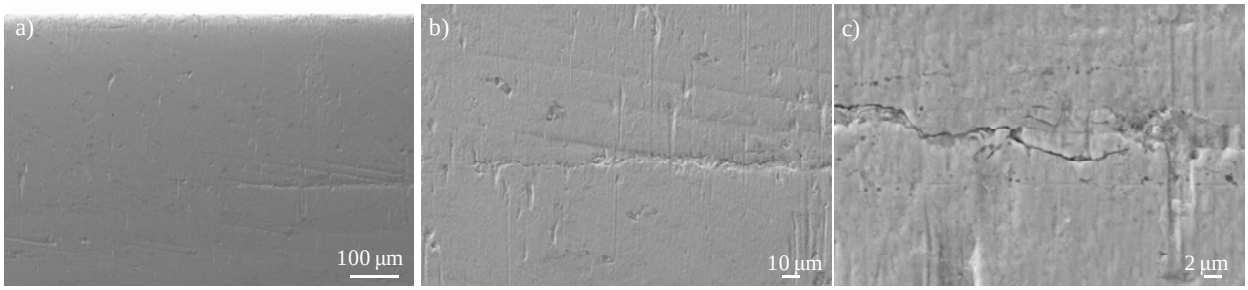

Figure 3.3.73 Images of the flank face of the UNIVERSAL lower tool at 15000 strokes: a) to c) different increasing zooms of the same crack

In the rake face of the same tool, no cracks are detected, only some small fractures are observed, as shown in Figure 3.3.74 a) after 5000 strokes. Figures 3.3.74 b) and c) show that some cracks are nucleated at primary carbides, even though these cracks do not propagate through the matrix.

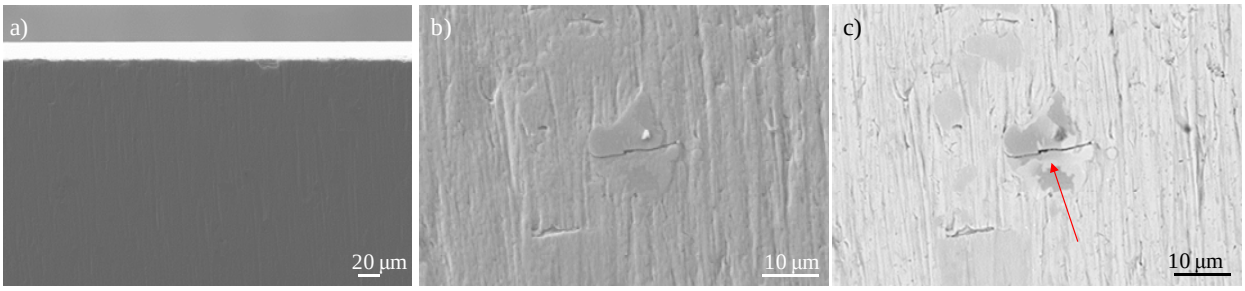

Figure 3.3.74 Images of the rake face of the UNIVERSAL lower tool at 5000 strokes: a) general overview; b) and c) crack observed at the surface in a primary carbide

With the increase of the number of strokes from 5000 to 10000 and 15000, mainly the rake face of the UNIVERSAL lower tool has been affected by wear, i.e. no propagating cracks can be observed in this case (see Figure 3.3.75).

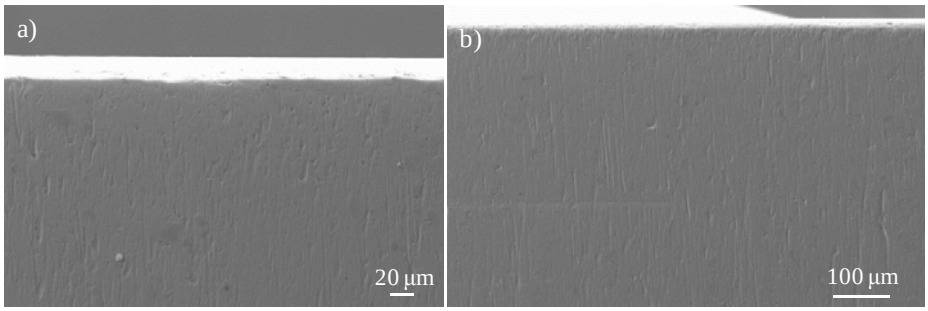

Figure 3.3.75 Images of the rake face of the UNIVERSAL lower tool at: a) 10000 strokes and b) 15000 strokes

In case of the UNIVERSAL upper tool, the main mechanism observed with the increase of the number of strokes is the same as in 1.2379: wear at the surface, as shown in Figure 3.3.76 a) throughout c) at 0, 10000 and 15000 strokes respectively. Neither cracks nor fractures are observed at the cutting edge of this tool.

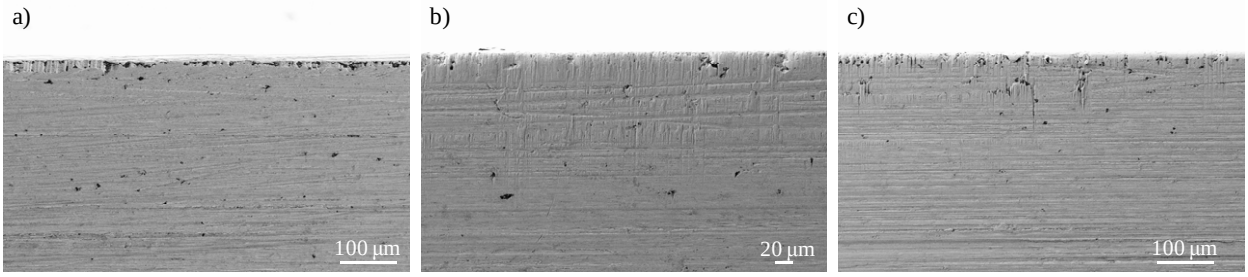

Figure 3.3.76 Images of the flank face of the UNIVERSAL upper tool at: a) 0 strokes; b) 10000 strokes and c) 15000 strokes

The cross sectional inspection of the UNIVERSAL lower and upper tools at 15000 strokes reveals that carbides are also broken in this steel, as shown by red arrows in Figure 3.3.77 a) and b) respectively. Although as shown previously some cracks are identified at the lower tool, none of the cross sectional samples analysed shows these cracks and therefore, they are not observed. It must be said, however, that due to the low number and small sizes of these cracks, especially in comparison to those identified in 1.2379, the probability to encounter one of them in the UNIVERSAL lower tool is very low. Notice that in this case, and opposite to what it is revealed for 1.2379, the carbide configuration of tools with respect to the stroke direction is the same for the lower and the upper one: perpendicular to the stroke direction.

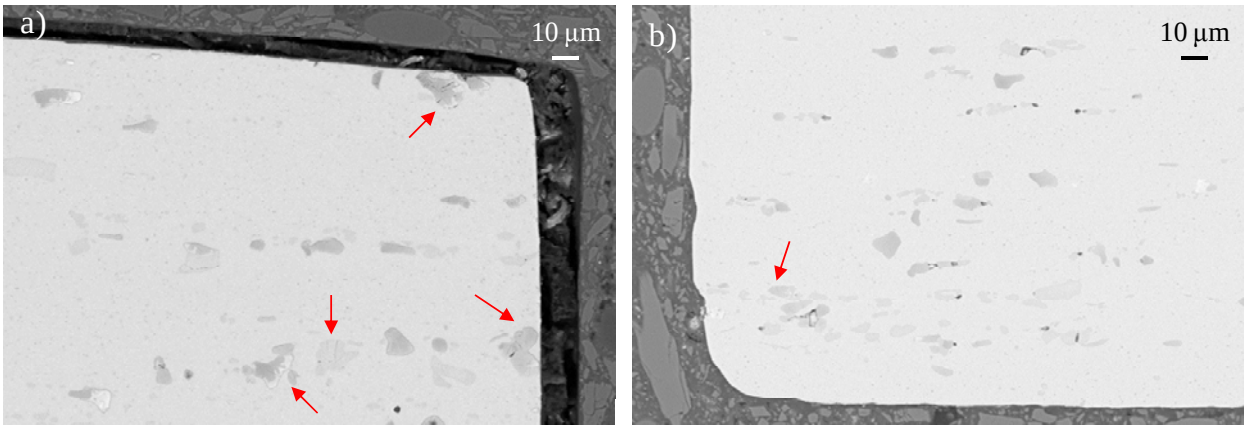

Figure 3.3.77 Microstructural inspection of the cross section of UNIVERSAL slitting tools: a) lower tool at 15000 strokes and b) upper tool at 15000 strokes

In case of HWS, only a lower tool was tested since no upper tool could be built. As shown in Figures 3.3.78 a) throughout c), the rake face of the lower tool is practically undamaged up to the 10000 strokes (compare Figures 3.3.78 a) at 0 strokes with Figure 3.3.78 b) at 10000). At 15000 strokes two rather big fractures are observed, one next to the other, as shown in Figure 3.3.78 c). However no other fractures are observed at the rest of the tool. The rake face of this tool presents wear at 10000 strokes (Figure 3.3.79 a)). In Figure 3.3.79 b) these two fractures shown in Figure 3.3.78 c) are shown at 15000 strokes. Notice that the geometry of these fractures is very different with respect to the rake and flank faces.

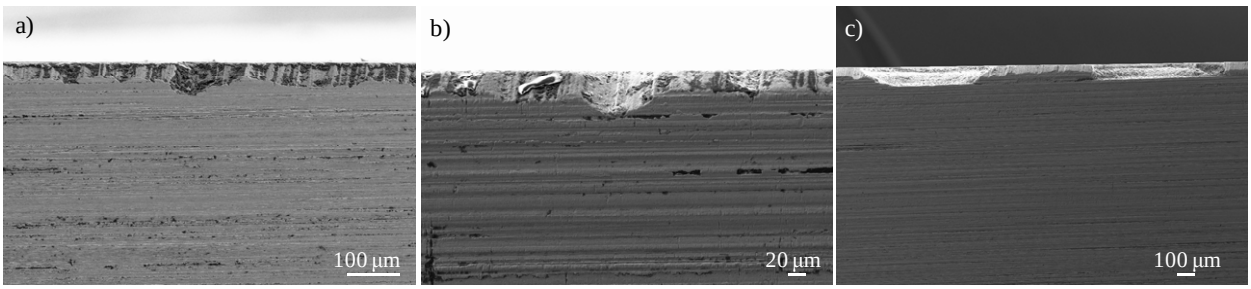

Figure 3.3.78 Images of the flank face of the lower HWS tool at: a) 0 strokes; b) 10000 strokes and c) 15000 strokes

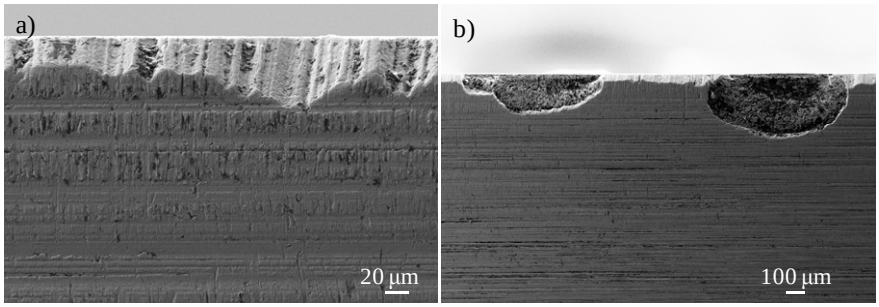

Figure 3.3.79 Images of the rake face of the lower HWS tool at: a) 10000 strokes and b) 15000 strokes

When paying attention to the state of the flank face of the HWS lower tool, some microcracks are detected, as show images of Figure 3.3.80, at 10000 strokes. The coalescence of these cracks may explain the existence of the fractures shown in Figure 3.3.78 c) and Figure 3.3.79 b). Notice that the high surface roughness of this tool can have a detrimental influence on its behaviour. The high peaks and valleys can act as notches and accelerate the nucleation of cracks from them.

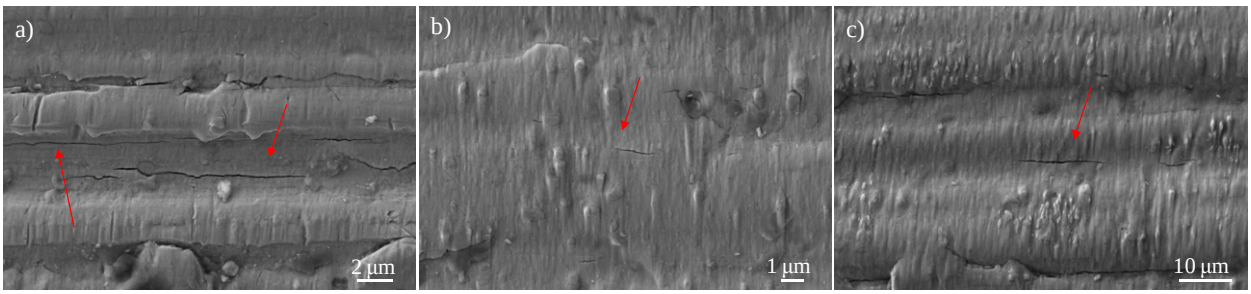

Figure 3.3.80 Microcracks at the flank face of the lower HWS tool at 10000 strokes

The cross sectional inspection of this tool at 15000 strokes reveals that some cracks nucleated at the flank face propagate perpendicular to the stroke direction (see Figure 3.3.81). However, none of the small primary carbides of HWS are broken instead.

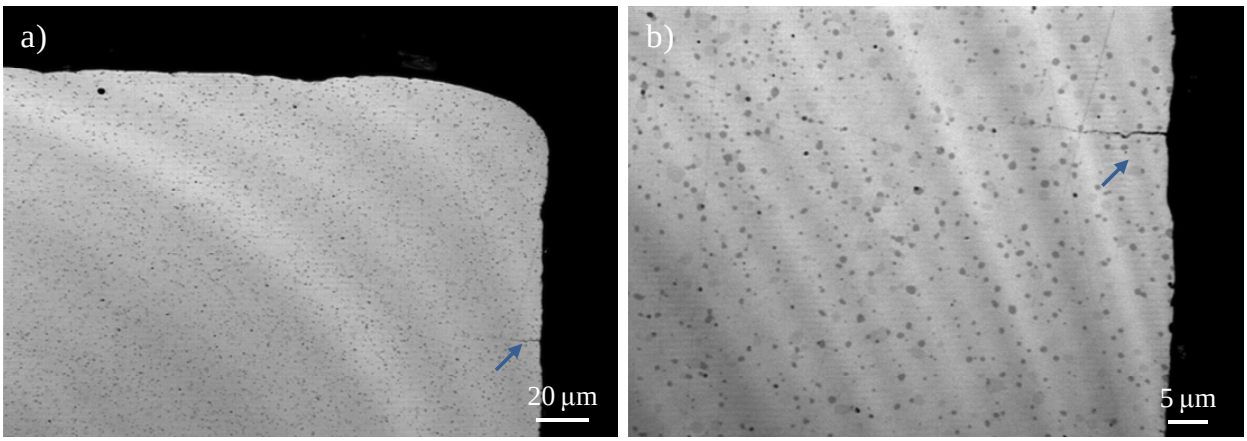

Figure 3.3.81 Microstructural inspection of the cross section of HWS lower tools at 15000 strokes

As follows from the results presented above these lines, both the direction of carbides bands with respect to the stroke movement and the surface quality of tools influence their mechanical response, as well as crack nucleation and propagation mechanisms. Thus, in this part of the investigation the effects of different carbide orientations and surface roughness on the performance of tools are analysed.

Slitting tests with a UNIVERSAL lower tool in which carbides bands are aligned parallel to the stroke direction show that damage at the rake face is very scarce, as shown in Figure 3.3.82. The surface is only grabbed with some lines due to the high frictional forces but no fractures can be detected even after 15000 strokes (Figure 3.3.82 c)). However, as shown in Figure 3.3.83, some microcracks are nucleated at the flank face of this tool after 10000 strokes (Figure 3.3.83 a)) and 15000 strokes (Figures 3.3.83 b) and c)). These microcracks are also originated because of the presence of defects generated by wear at the surface of the tool (like scratches, holes, etc.).

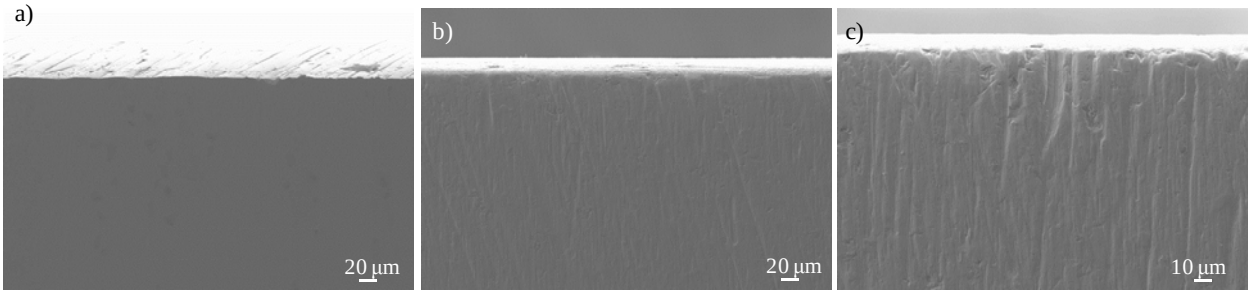

Figure 3.3.82 Images of the rake face of the UNIVERSAL lower tool with carbides aligned following the stroke direction at: a) 0 strokes; b) 5000 strokes and c) 15000 strokes

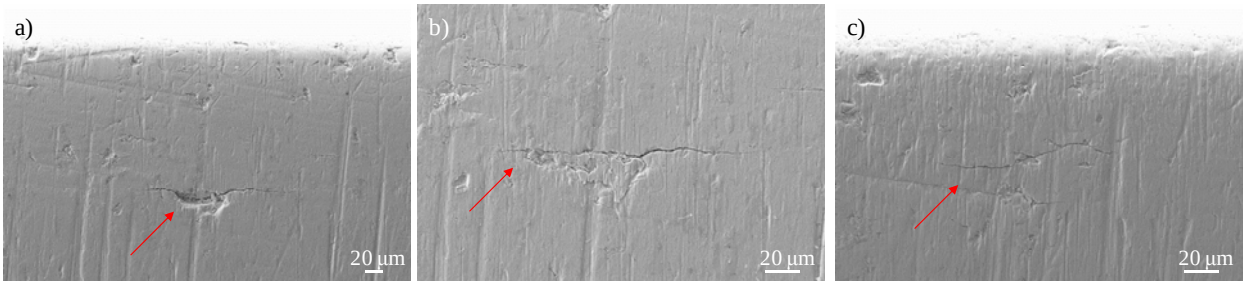

Figure 3.3.83 Microcracks at the flank face of the UNIVERSAL lower tool with carbides aligned following the stroke direction at: a) 10000 strokes and b) and c) 15000 strokes

Some of these microcracks do not propagate at the surface (even though they could have done it towards the interior of the tool). Figures 3.3.84 a) and b) show a crack identified at 10000 strokes and then at 15000 strokes respectively.

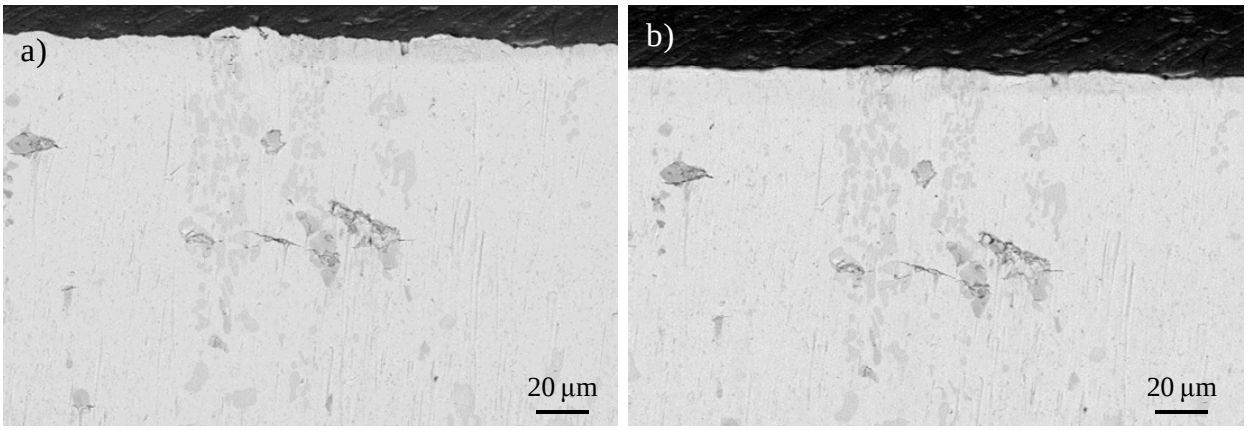

Figure 3.3.84 Microcrack at the flank face of the UNIVERSAL lower tool with carbides aligned following the stroke direction at: a) 10000 strokes and b) 15000 strokes

Figure 3.3.85 shows some examples of the cross sectional images at 15000 strokes of this UNIVERSAL tool with carbides aligned following the direction of the stroke. In this case, a few horizontal cracks are identified but they are very small compared to those observed in 1.2379 tools. Apart from these, no other cracks are observed in the microstructure, and opposite to the tools with the carbides aligned perpendicular to the stroke, carbides are not broken.

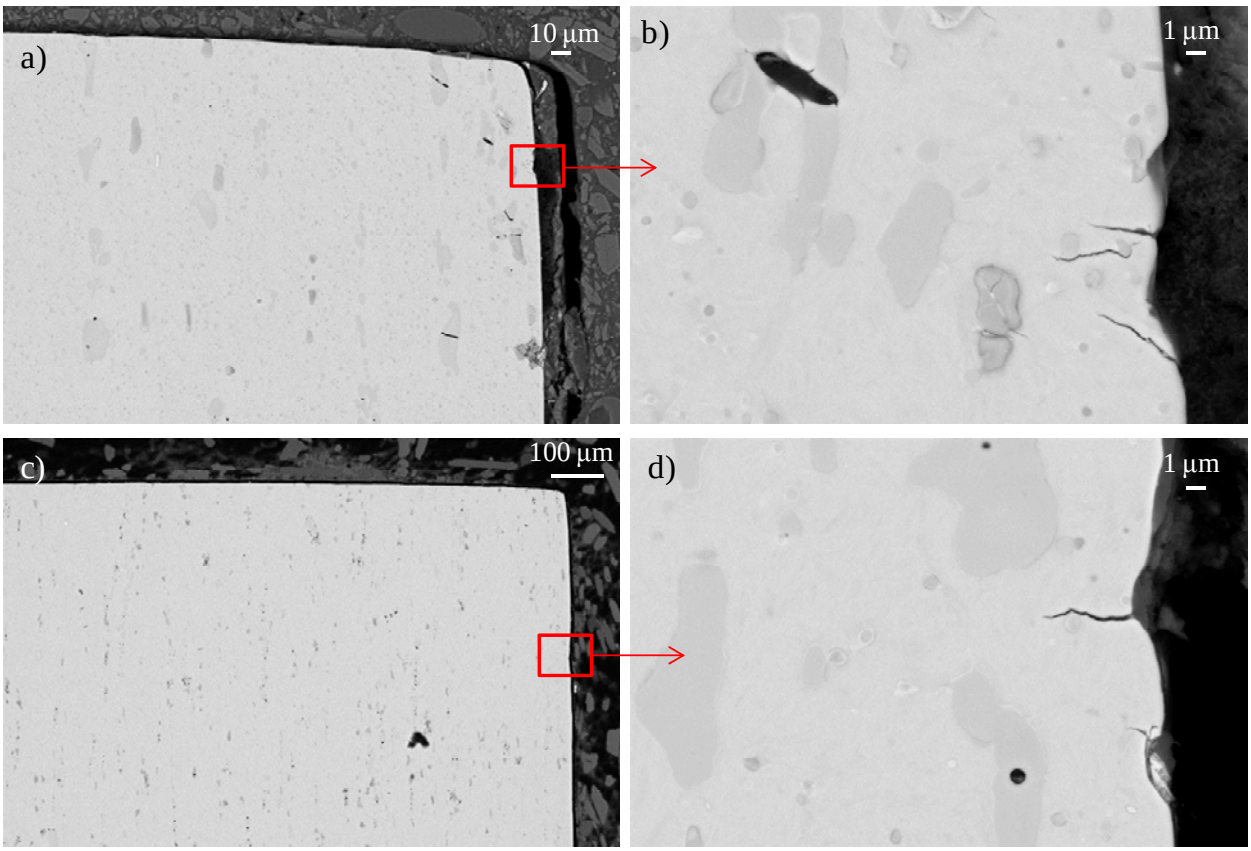

Figure 3.3.85 Microstructural inspection of the cross section of UNIVERSAL lower tool with carbides aligned following the stroke direction at 15000 strokes

The effect of the surface quality on the nucleation of cracks in slitting tools is assessed using a UNIVERSAL tool in which a half part has been polished after grinding. Polishing was manually performed on the rake and flank faces, paying special attention that the cutting edge radius was unmodified. However, this new UNIVERSAL tool was machined in a different company and they used different grinding parameters than those employed to machine the previous tools. As a result, the as-grinded part of this tool did not present the same surface conditions and roughness, R_a, as the tools analysed before (compare Figures 3.3.86 a) and b) to Figure 3.3.86 d)). The polished part had a considerable lower R_a compared to the other three, as shows Figure 3.3.86 c).

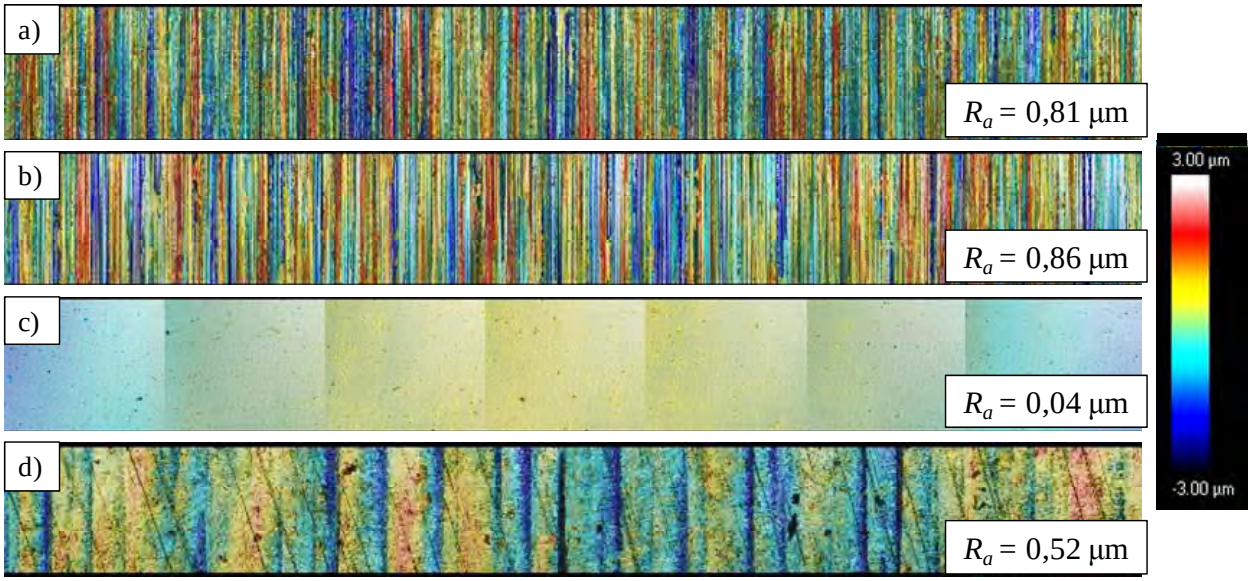

Figure 3.3.86 Topographic images obtained in CM of the flank face and R_a values of: a) 1.2379 tool; b) HWS tool; c) polished part of the new UNIVERSAL tool and d) as-grinded part of the new UNIVERSAL tool

In Figure 3.3.87 it can be observed that after 5000 strokes, the cutting edge of the as-grinded part of the new UNIVERSAL tool is undamaged, while the polished part shows some small chippings. The reason for these chippings is grooves near the cutting edge. As said before, polishing was performed trying to not affect the cutting edge radius (otherwise the results obtained would have not been comparable to the rest of studied tools). But as a consequence, near the cutting edge the surface quality was not as good as a little further from it. Nevertheless, 1.2379 tools after 8000 strokes showed a much worse damage at the cutting edge compared to both the polished and as-grinded parts of the new UNIVERSAL tool. In 1.2379 tools most of the cutting edge was fractured by cracks which grew following the machining lines (see Figures 3.3.87 c) and f)).

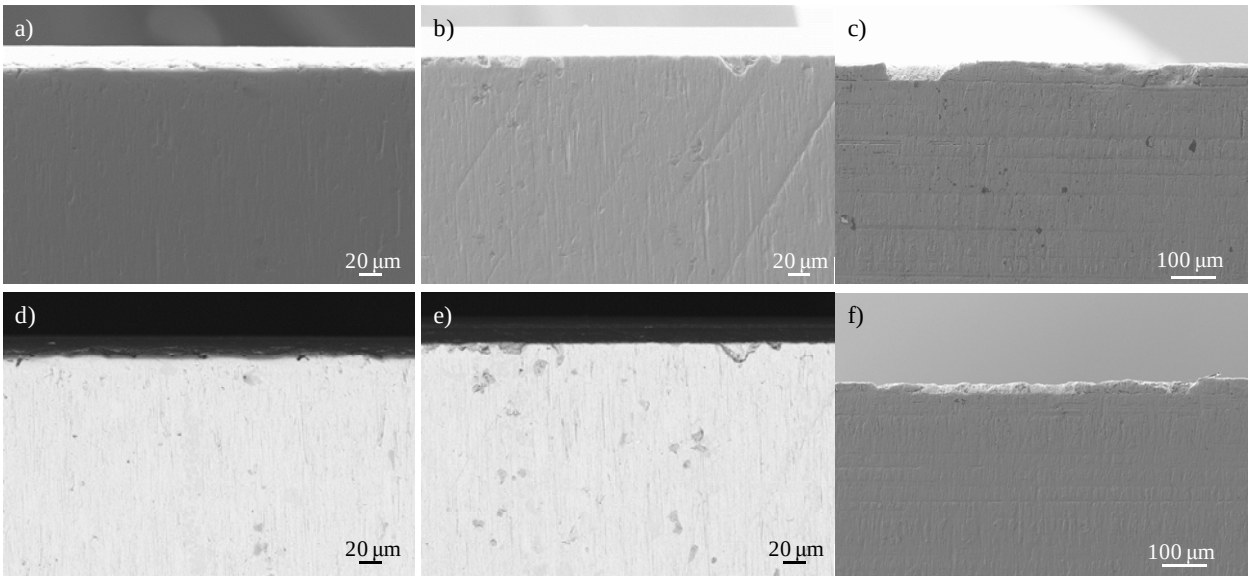

Figure 3.3.87 SEM micrographies of the tools surface: a) and d) new UNIVERSAL as-grinded, after 5000 strokes; b) and e) new UNIVERSAL polished, after 5000 strokes and c) and f) 1.2379, after 8000 strokes

The presence of deep grooves (as a result of grinding or polishing) has a direct impact on the nucleation and propagation of cracks and these are at the origin of fractures at the cutting edge. However, in Figure 3.3.88 it can be observed that with the increase of the number of strokes to 15000, and as the surface is progressively affected by wear, both the as-grinded and the polished parts of the new UNIVERSAL tool evolve to show a similar aspect. When wear starts to affect the surface, initial grooves smoothen progressively but new ones produced by wear damage appear. However, if initial grooves are very deep, this smoothening process is slower and typically, cracks start nucleating from these before they are smoothened (see Figures 3.3.88 c) and f)).

Therefore, an R_a of about 0,5 µm in an as-grinded tool surface has been proved to delay the fracture process compared to tools with R_a around 0,8 µm. This means that if the grinding parameters are the optimal for the tool material, hardness and geometry, no polish should be required (what is kind of good news since polishing is somewhat difficult to be carried out in industrial tools since it is a time and cost consuming operation).

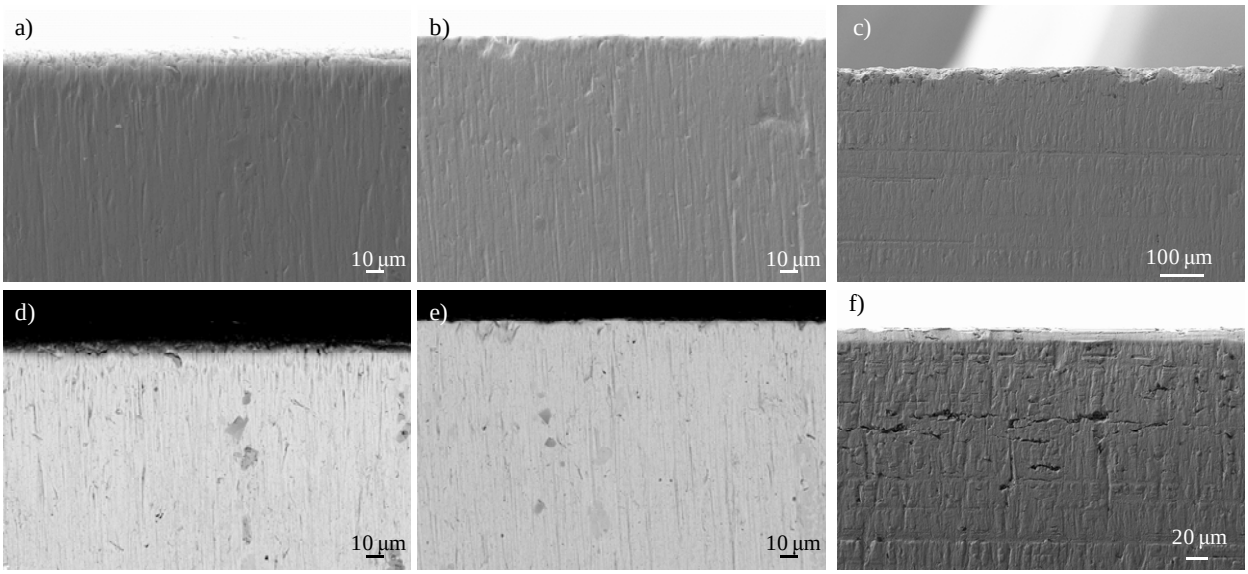

Figure 3.3.88 SEM micrographies of the tools surface: a) and d) new UNIVERSAL as-grinded, after 15000 strokes; b) and e) new UNIVERSAL polished, after 15000 strokes and c) and f) 1.2379, after 16000 strokes

3.3.4 Effect of the shearing process parameters on the quality of the cut edges, the performance of tools and the registered load - displacement curves

The effect of the shearing process parameters, such as the clearance and the tool edge radius, on the morphology of the sheet cut edge and the performance of tools is investigated and the results are presented in this section. One single stroke tests were carried out in the MTEC-p and MTEC-s (for punching and slitting processes respectively) using DP1000 2 mm thick, MS-W1200 2 mm thick and BORON-02 1,8 mm thick, as described in section 2.5.4. Continuous tests were performed in the HPC, using DP1000 2 mm thick as sheet material.

In order to assess the influence of the shearing parameters, i.e. cutting clearance and cutting angle, on the load – displacement curves registered in tools, an instrumented die aimed at slitting press hardened 22MnB5 was used. These tests were carried out within the frame of the exchange programme at the Technische Universität München (TUM) in the Lehrstuhl für Umformtechnik und Gießereiwesen (UTG) and the derived results are also summarized in this section.

3.3.4.1 Influence of the process parameters on maximum loads registered in tools and the quality of the sheared edges

-Punching process

Different clearances were assessed in the punching operation of the MTEC-p die from 2,5 % to 27,7 % (radial clearance expressed in terms of the percentage of the sheet thickness). Figures 3.3.89 a) to c) plot the obtained punching load – displacement curves using these clearances in case of DP1000 (Figure 3.3.89 a)), MS-W1200 (Figure 3.3.89 b)) and BORON-02 (Figure 3.3.89 c)). Figure 3.3.89 d) in turn, shows the evolution of maximum punching loads with respect to the clearance. The higher the punching clearance, the higher the required displacement of the punch to produce sheet fracture but the lower the maximum load. This can be understood by pre-bending effects of the sheet when the clearance increases.

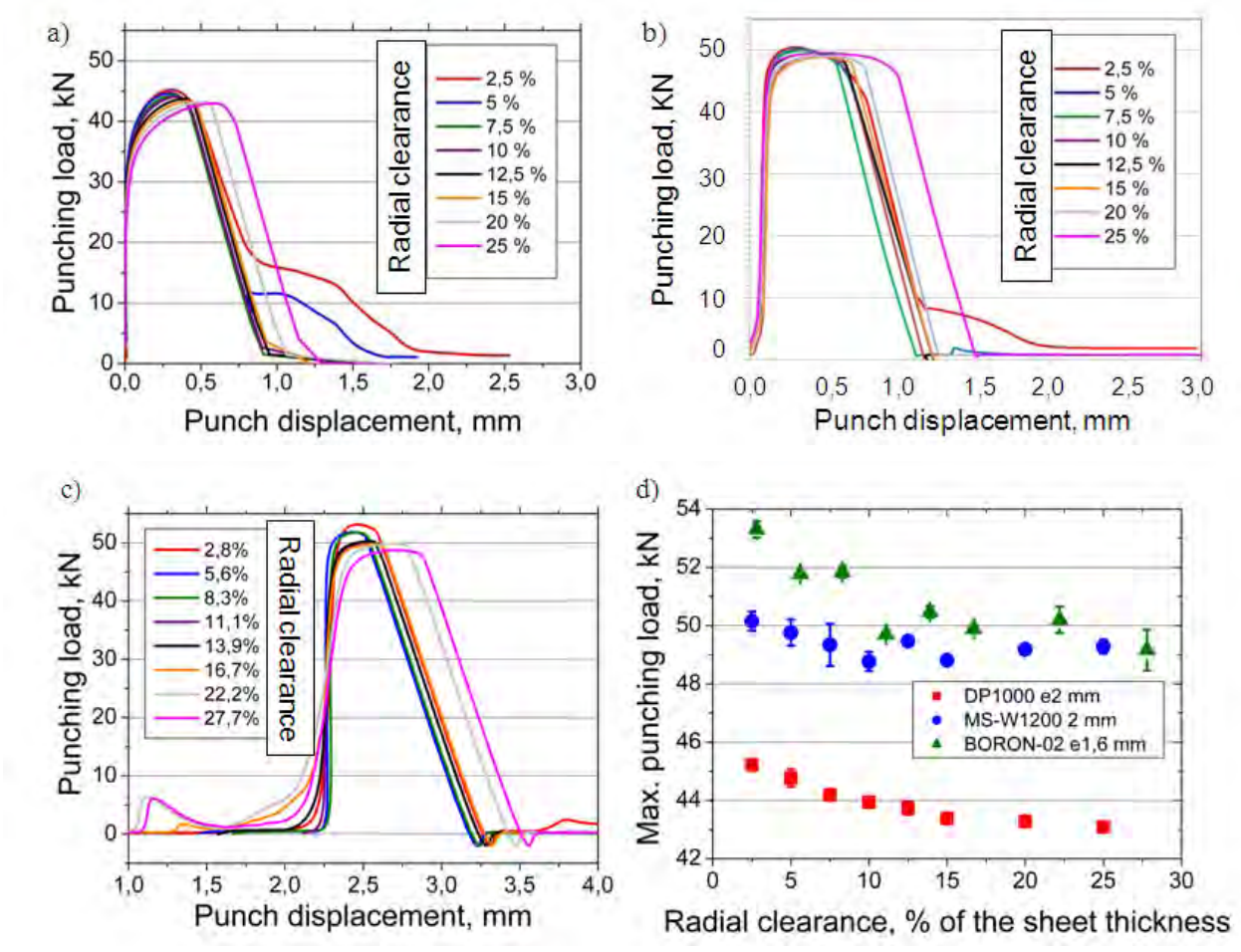

Figure 3.3.89 Load – displacement curves of the punching processes using different clearances ranging between 2,5 % and 27,7 % of a) DP1000 2 mm thick; b) MS-W1200 2 mm thick and c) BORON-02 1,8 mm thick; d) maximum punching load plotted in function of the clearance for each of the studied steels

Figure 3.3.90 shows schematically the resulting punched edges of DP1000 (Figure 3.3.90 a)), MS-W1200 (Figure 3.3.90 b)) and BORON-02 (Figure 3.3.90 c)) for the clearances between 2,5 and 27,7 %. In case of DP1000, burr formation is only observed at the clearances 2,5 % and 25 % (burr height of 0,15 and 0,17 mm respectively), being the clearances from 5 % to 20 % free of such defect. However, significant rollover and fracture angles are observed from clearance 15 % and higher. In case of MS-W1200, small burrs are identified at 2,5 and 5% clearances (burr height 0,05 and 0,04 mm respectively), but a large burr is measured at 25 % (0,36 mm height). Intermediate clearances show burr free edges, even though high fracture angles are observed at clearances higher than 10 %. BORON-02 shows small burr at the lowest clearance of 2,8 %, but it appears with burr heights of 0,1 mm and 0,3 mm at 22,2 % and 27,7 % respectively. The free burr clearances are comprised between 5,6 % and 16,7 %, despite the fracture angle is rather large at clearances higher than 13,9 %. Then, increasing the strength of the sheet the range of clearances for burr free edges reduces.

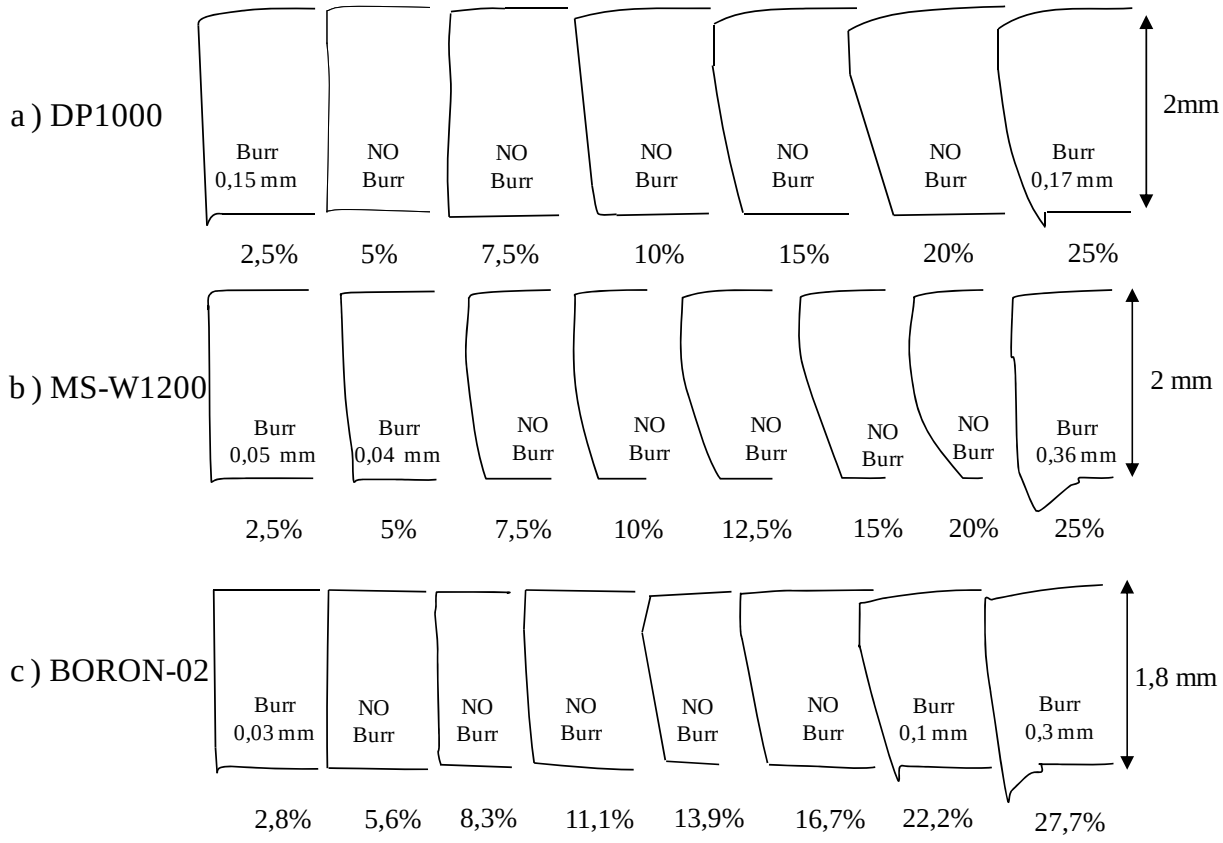

Figure 3.3.90 Schema of the punched sheet edge morphology of: a) DP1000 2 mm thick; b) MS-W1200 2 mm thick and c) BORON-02 1,8 mm thick for clearances between 2,5 % and 27,7 %

The influence of the punch edge radius on the punching load – displacement curves is shown in Figures 3.3.91 from a) throughout h) for increasing clearance values from 2,5 % throughout 25 %. Punches of 10 and 100 μm edge radii are compared in this study. It can be observed that sheet fracture occurs at higher punch displacements for 100 μm edge radius than 10 μm. The maximum load, in turn, is higher in case of the punch with 100 μm edge radius for clearances between 2,5 and 12,5 %, but it turns to be the lowest for clearances 15 %, 20 % and 25 %.

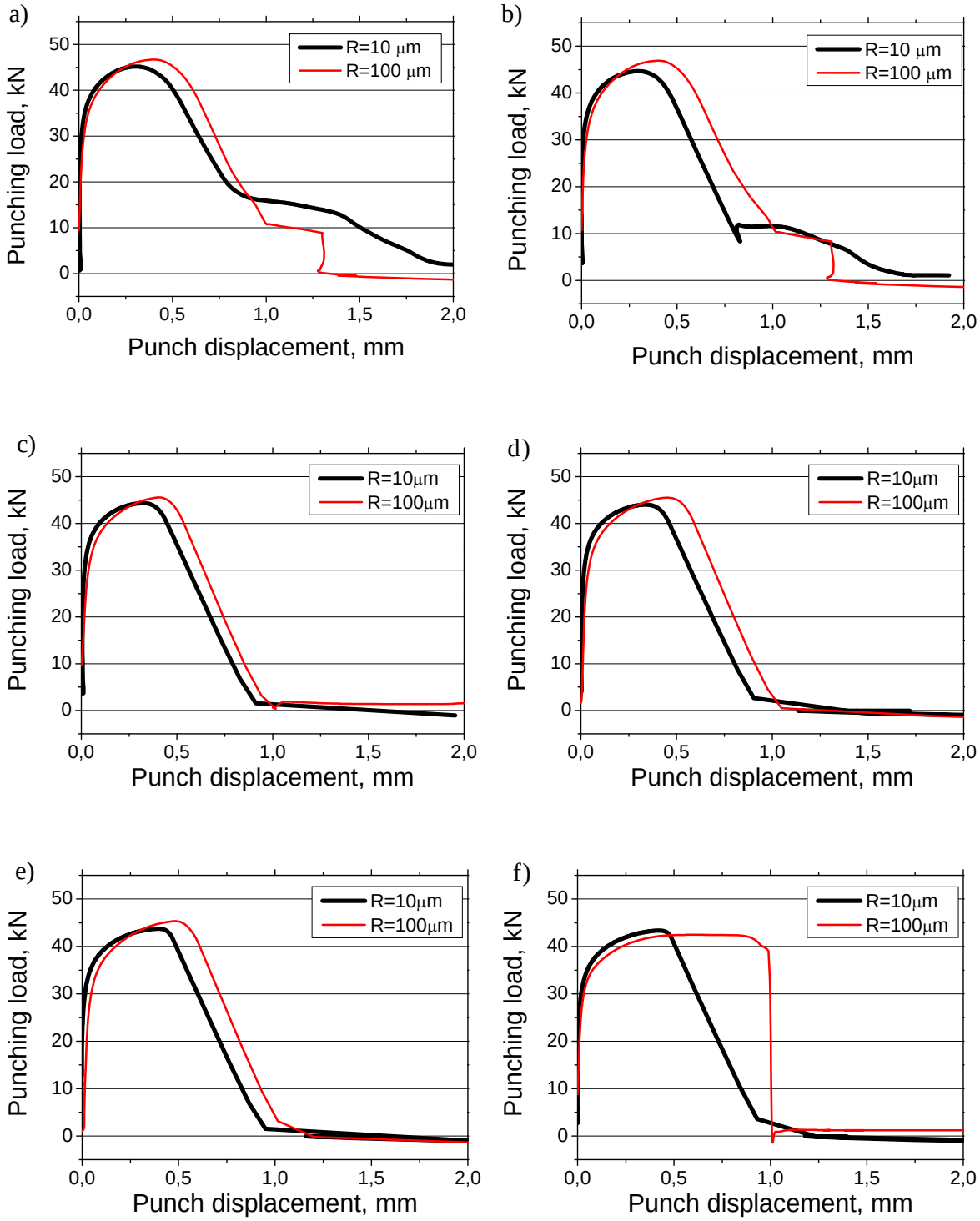

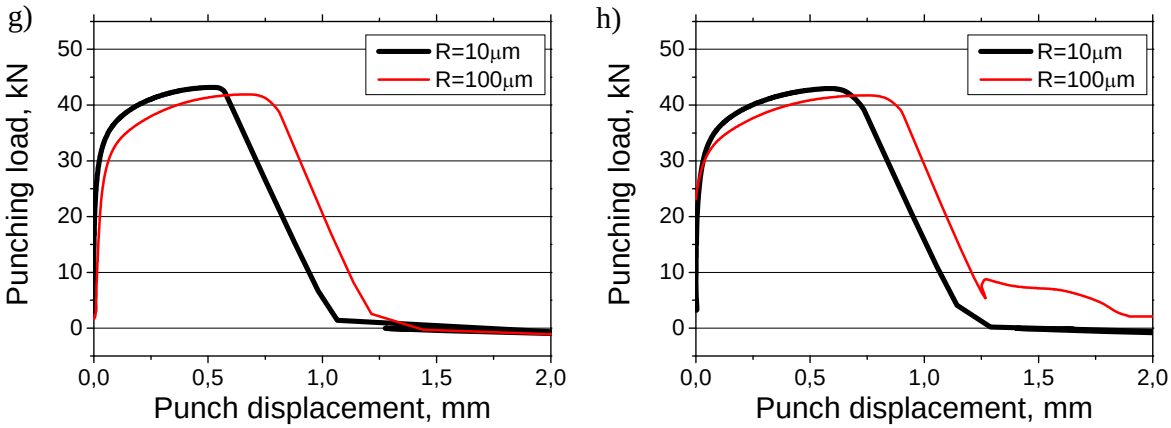

Figure 3.3.91 Load – displacement curves of the punching process of DP1000 2 mm thick with punch radii 10 and 100 µm and clearances: a) 2 %; b) 5%; c) 7,5 %; d) 10 %; e) 12,5 %; f) 15 %; g) 20 % and h) 25 %

The influence of the cutting parameters on the maximum stress registered in punches is estimated by FE-simulation. As shown in Figure 3.3.92, the effect of the clearance is less significant than the effect of the tool edge radius. Reducing the clearance from 20 to 10 %, von Mises stresses decrease between 50 to 100 MPa. In the meanwhile, increasing the edge radius from 10 to 100 µm, the stresses decrease between 300 and 500 MPa.

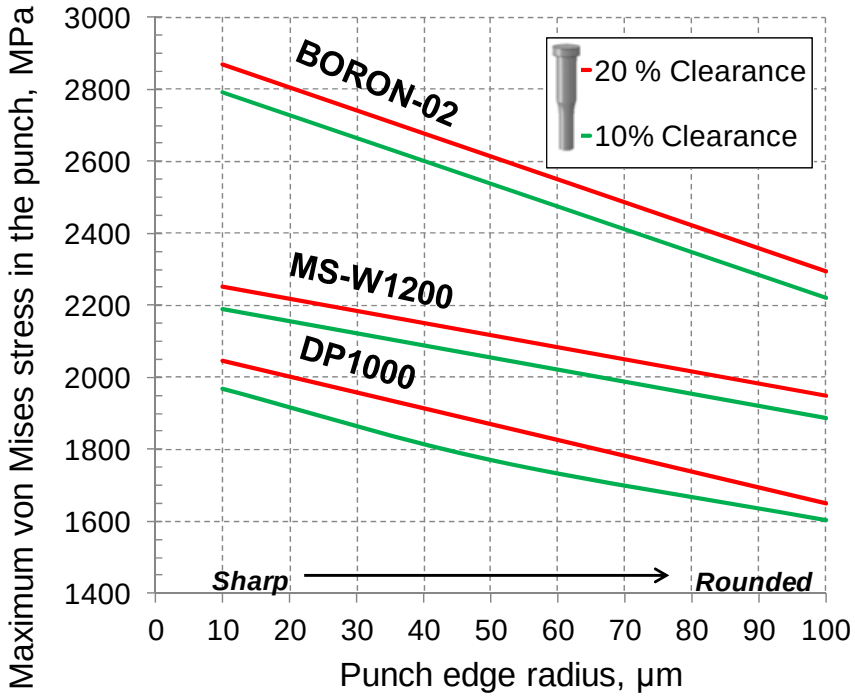

Figure 3.3.92 Maximum von Mises stresses estimated by means of FE-simulation for 10 and 20 % clearance values, punch edge radii from 10 to 100 µm and considering BORON-02 1,8 mm thick, MS-W1200 and DP1000 2 mm thick

As follows from results of Figures 3.3.89 d) and 3.3.92, stresses show an inverse tendency than loads with the increase of clearance and punch edge radius. Higher clearances and sharp tool edges lead to symptomatic reduction of maximum load and increase of maximum stress, and vice-versa. An explanation for this observation can be the difference in contact areas between the punch and the sheet when changing clearances and radii. At high clearances or tool radii the contact area is larger than at low clearances or radii. Thus, even if maximum loads are higher, maximum stresses in tools are lower since loads are distributed in a larger area.

In an attempt to give truthfulness to this theory, Nothhaft [NOT10] paid special attention to the contact area between the tool and the sheet during the slitting process of press hardened 22MnB5 1,75 mm thick. In Figure 3.3.93 it can be observed that the contact length is 0,07 mm (or 8,7 %) higher with a clearance of 5 % (contact length 0,798 mm) with respect to a clearance of 15 % (contact length 0,729 mm). These results show that the higher maximum stress at high clearances is due to the smaller contact area compared to lower clearances. The reduction in contact area is due, in turn, to the fact that sheet bending before fracture is more important as clearances increase.

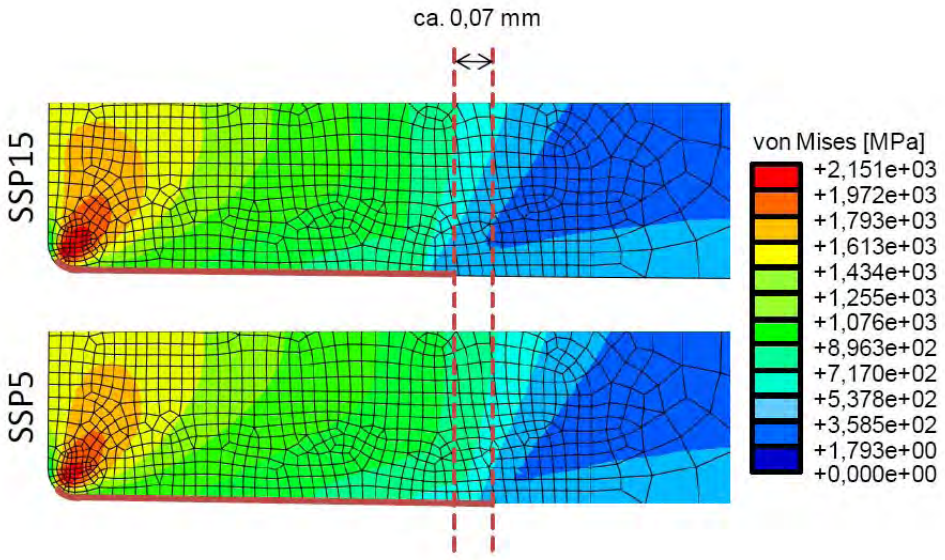

Figure 3.3.93 Comparison between the contact lengths at 15 % (SSP15) and 5 % (SSP5) clearance values and the effect on maximum von Mises stresses [NOT10]

The influence of the punch edge on the quality of the sheet sheared edges is also evaluated in this study. Figure 3.3.94 a) compares the morphology of the resulting edges when punching was performed using sharp, rounded and damaged tools. In each case, three clearance values were tested: 10, 15 and 20 % of the sheet thickness. BORON-02 1,8 mm thick, MS-W1200 and DP1000 2mm thick are used as sheet materials. The radii of the sharp and rounded edges are 10 μm and 100 μm respectively. The third punch is damaged by fracture, as shown in Figure 3.3.94 b).

No burrs are observed in case of the punch with sharp edge, except for BORON-02 at clearance 20 %. Using a rounded punch, burrs are generated in both BORON-02 and MS-W1200 with a clearance of 20 %, and a rather high fracture angle and rollover zones are obtained in DP1000 at 20% and BORON at 15 %. Finally, punching with a fractured tool produces large burrs in BORON-02 at 20 % and 15 %, as well as high rollover zones and rough fracture zone in MS-W1200 20 %. In case of DP1000, even though no burrs are observed, rollover and fracture angles are high at 20 % clearance and a rather discontinuous bright to fracture zone transition is revealed at 15 %.

After these results the influence of the punch edge on the sheared sheet quality is clear: the sharper the punch edge, the better the sheared sheet edge quality for a wider range of clearances. Then if tools must be removed from production in industrial conditions is because sheared parts start to reduce their quality. That is to say that up to a certain extent, punches can still work even if they present some fracture at the cutting edge, but as defects at sheet sheared edges are inadmissible for the industry, they must be replaced.

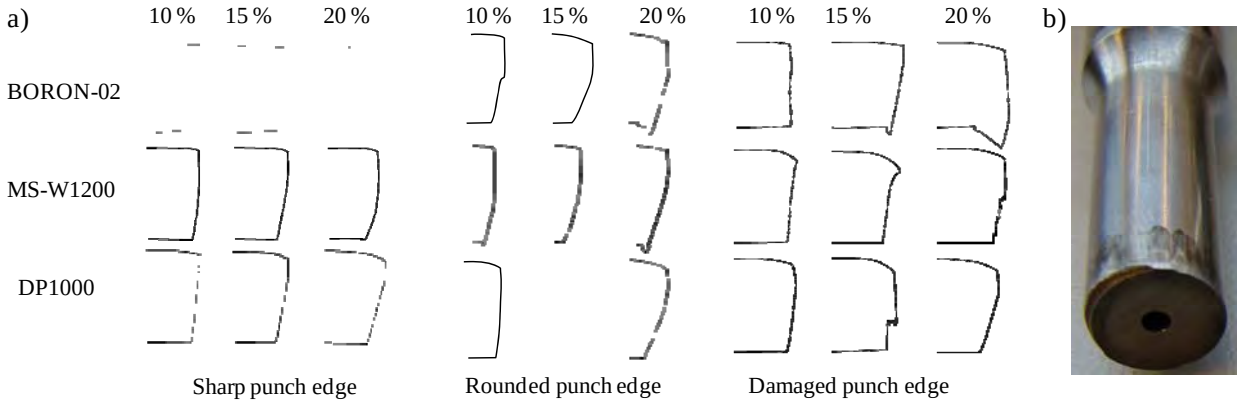

Figure 3.3.94 a) Comparison of sheet sheared edges obtained in punching BORON-02 1,8 mm thick, MS-W1200 and DP1000 2 mm thick, at clearances of 10, 15 and 20 % using sharp, rounded and damaged punch edges; b) damaged punch

-Slitting process

For the slitting process, only the effect of clearances and tool edge radii was investigated using the MTEC-s and DP1000 2 mm thick, as well as BORON-02 1,8 mm thick as sheet material. An in-depth analysis of the cutting parameters in slitting processes was performed at UTG, and results are presented in section 3.3.4.3.

Figure 3.3.95 shows that slitting is more critical with regard to the quality of sheared edges than punching. Burrs and other imperfections are already observed at 15 % clearances with DP1000 and 10 % with BORON-02. At a clearance of 20 % the quality of the sheared edges is not acceptable at all.

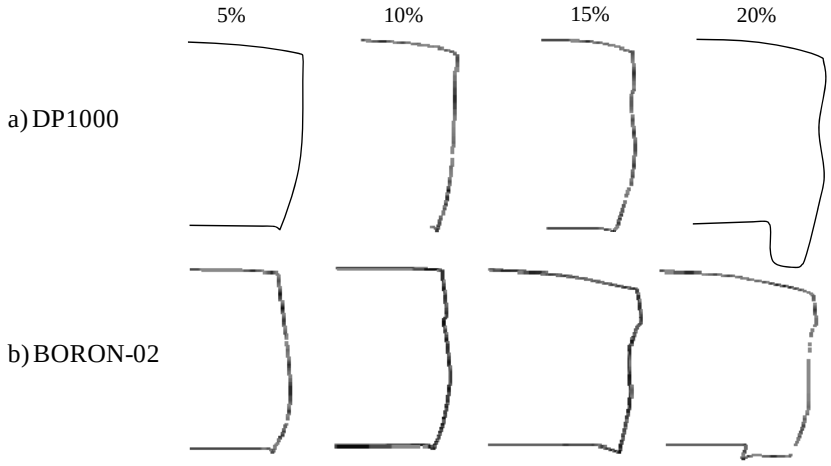

Figure 3.3.95 Schema of the sheet edge after slitting: a) DP1000 2 mm thick; b) BORON-02 1,8 mm thick for ranging clearances between 5 and 20 %

3.3.4.2 Influence of the shearing clearance and tool edge radius on the performance of tools

-Punching process

The fractographic analysis of 1.2379A punches with 10 and 100 μm edge radii reveals that after 3000 strokes at 10 % clearance, the punch with the sharpest edge is fractured (Figure 3.3.96 a) and b)), while the punch with rounded radius shows no signs of damage (Figure 3.3.96 c) and d)).

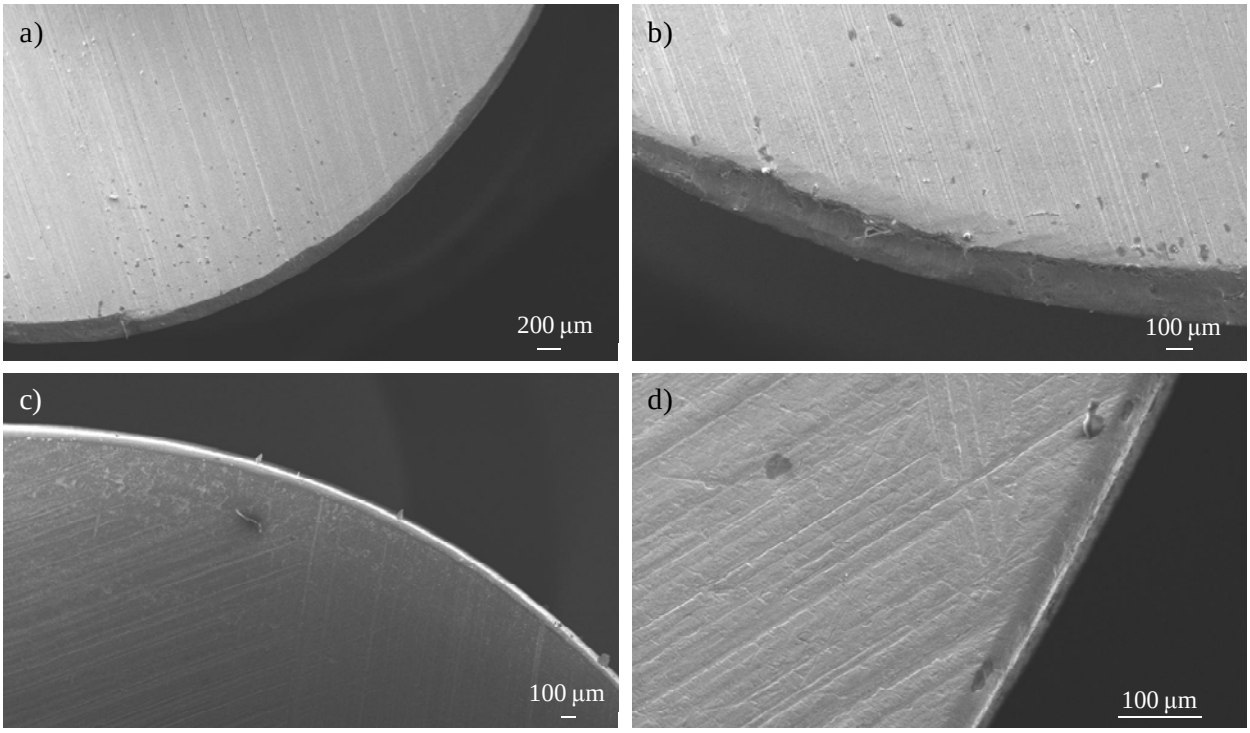

Figure 3.3.96 Fractography of the 1.2379A punches after 3000 strokes: a) and b) sharp edge (radius 10 μm); c) and d) rounded edge (radius 100 μm)

After 17000 strokes the punch with rounded edge starts to show indices of damage by chipping and wear, as shown in Figure 3.3.97 a) and b) respectively. After 26000 strokes the punch edge is rather worn out and new chippings are observed, as it can be seen in Figure 3.3.97 c) and d). Chipping occurs, once again, under the influence of defects such as grinding grooves.

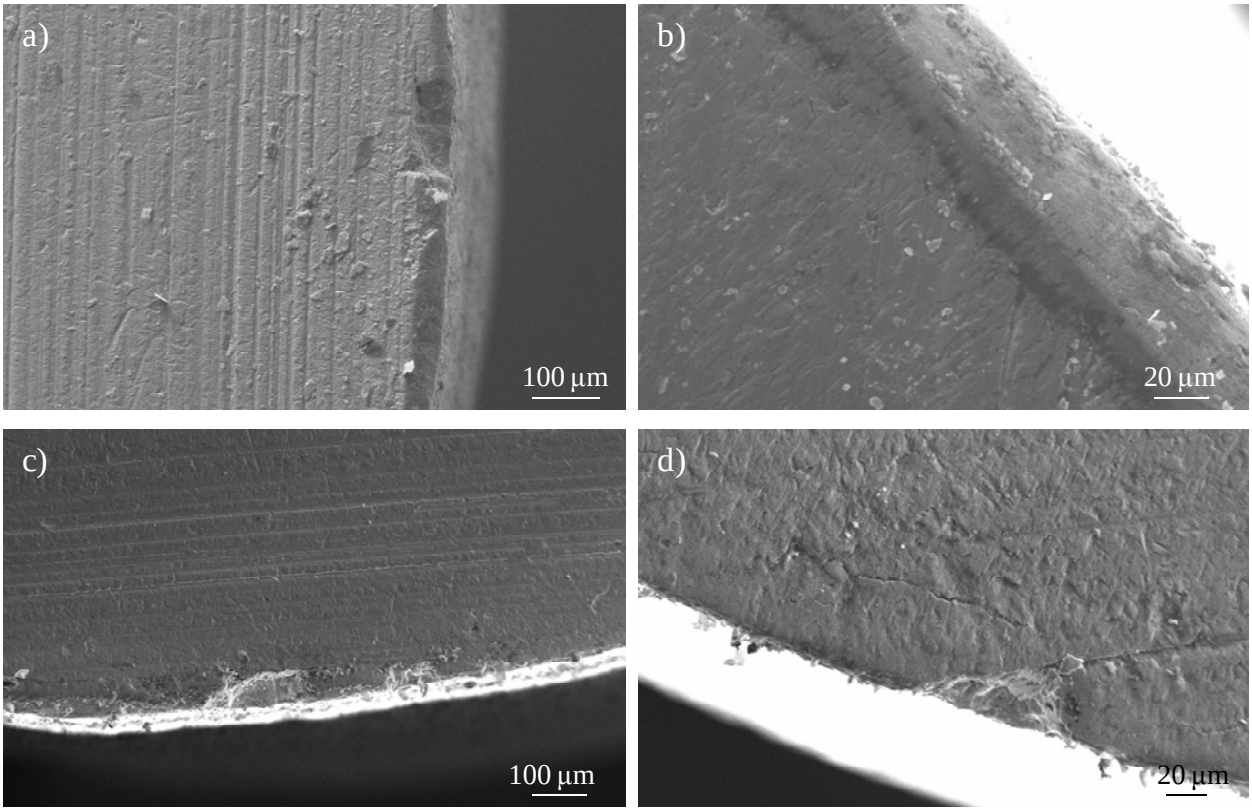

Figure 3.3.97 Fractography of the 1.2379A punches with 100 µm radius: a) and b) after 17000 strokes; c) and d) after 26000 strokes

In order to rationalize these experimental findings, the stress distribution and stress level acting in the punch with rounded edges are estimated by means of FE-simulation (Figure 3.3.98), and they are compared to those determined for the sharp punch (see Figure 3.3.38). Maximum estimated von Mises stresses inside the punch with rounded edge are lower than in the sharp one (maximum peaks at 1600 and 2000 MPa respectively). Therefore it is plausible to attribute the better performance of the rounded tool compared to the sharp one to its reduced stress level. Fracture is delayed several thousands of strokes using a rounded edge punch with radius 100 µm.

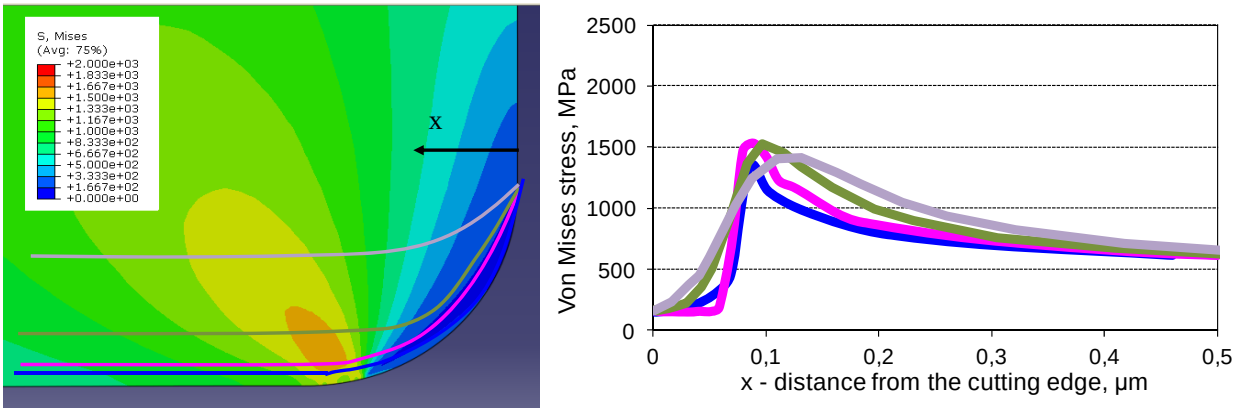

Figure 3.3.98 Von Mises stress distribution and level near the cutting edge in the punch with 100 μm edge radius

A similar study is carried out to determine the effect of the punching clearance on the tool performance. For that a 1.2379A punch with 100 μm radius was tested using 10 and 20 % clearances. No remarkable influence of the clearance on the fracture occurrence has been observed. But it must be said that at punch of round edge, damage is hardly observed no matter what the clearance is, since as shown in Figure 3.3.92, the effect of the tool edge radius on maximum stresses is more important than the effect of the clearance.

-Slitting process

The fractographic analysis of the 1.2379 lower tools with edge radius 10 and 500 μm reveals that in the rounded tools, no fracture takes place after 22000 strokes (Figures 3.3.99 a) and d)). On the contrary, in the tool with sharp edge several cracks and fractures are identified after 8000 strokes (Figures 3.3.99 b) and e)). After 22000 strokes wear at the rake face is more pronounced (Figure 3.3.99 f)) and some cracks, as well as fractures at the cutting edge, are also observed (Figure 3.3.99 c)).

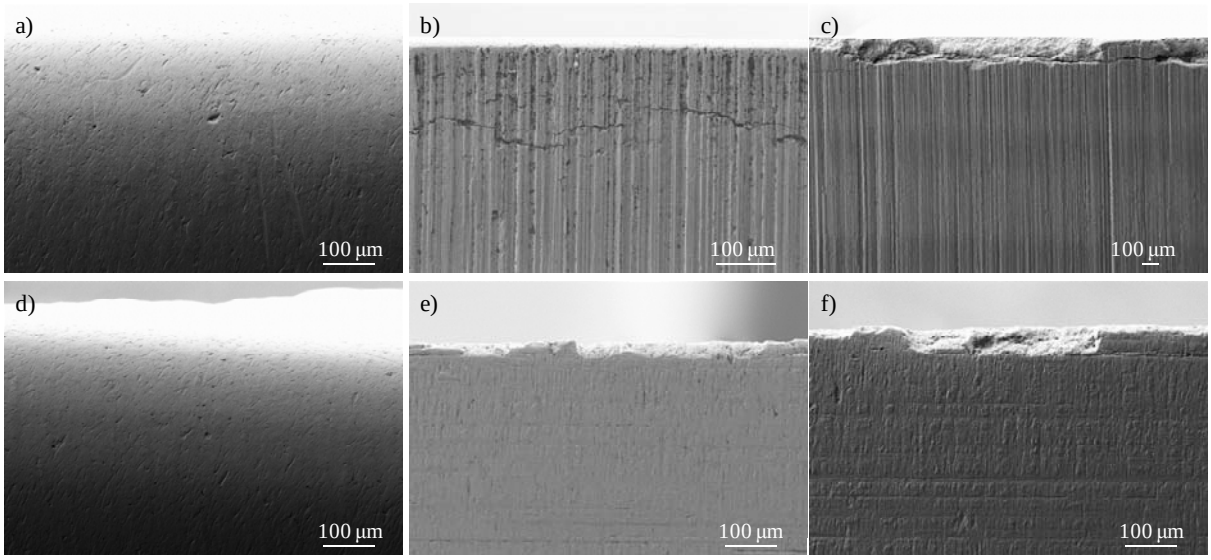

Figure 3.3.99 Fractography of the lower 1.2379 tools: a) flank face of the tool with radius 500 µm after 22000 strokes; b) flank face of the tool with radius 10 µm after 8000 strokes; c) flank face of the tool with radius 10 µm after 22000 strokes; d) rake face of the tool with radius 500 µm after 22000 strokes; e) rake face of the tool with radius 10 µm after 8000 strokes and f) rake face of the tool with radius 10 µm after 22000 strokes

The upper tools with radius 500 µm show significant damage by wear after 22000 strokes, as can be observed in Figures 3.3.100 a) and d). In tools with 10 µm radius, wear is not as severe as in the rounded ones neither after 8000 strokes (Figures 3.3.100 b) and e)) nor 22000 strokes (Figures 3.3.100 c) and f)). Some fractures are also observed at the cutting edge of the sharpest tools (Figures 3.3.100 c) and f)). Definitely, a tool edge as rounded as 500 µm is detrimental for the performance of the tool, as well as for the sheet edge quality (large, and completely inadmissible, burrs were obtained in these tests). Thus, optimal tool edges should be 100 – 200 µm.

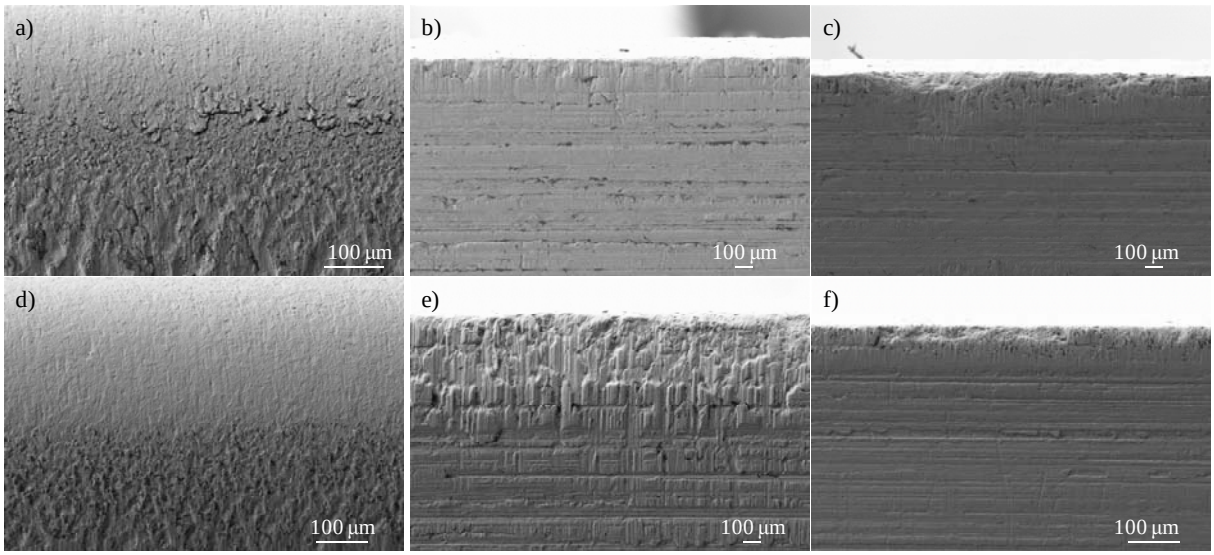

Figure 3.3.100 Fractography of the upper 1.2379 tools: a) and d) flank face of the tool with radius 500 µm after 22000 strokes; b) and e) flank face of the tool with radius 10 µm after 8000 strokes and c) and f) flank face of the tool with radius 10 µm after 22000 strokes

3.3.4.3 Influence of the slitting process parameters on the registered load and displacement of tools

Slitting tests were performed in an instrumented die in UTG, as detailed in section 2.5.4 using hardened 22MnB5 steel 1,5 mm thick, and the results were published by Nothhaft and Koebler in [NOT11]. Different clearances and cutting angles were chosen in order to assess their influence on the registered load – displacement curves. Loads both in X and Z directions were determined by means of sensors integrated within the cutting elements.

In Figure 3.3.101 the load – displacement curves in X and Z directions are respectively plotted for cutting angles of 0º, 2º, 7º and 20º and clearance 5 % (Figure 3.3.101 a)), 10 % (Figure 3.3.101 b)) and 15 % (Figure 3.3.101 c)). Loads are normalised with respect to the sheet width (50 mm). Maximum loads in Z direction increase with the cutting angle from 0º to 2º at both 5 and 15% clearances, but they rather coincide in case of 10 %. At cutting angles of 2º and 7º, maximum loads in Z direction are very similar in all three clearances. The most important reduction in Z- maximum loads is achieved using the tool with cutting angle 20º; the load is approximately 200 MPa lower than with the 0º, 2º or 7º angles.

Maximum loads in X direction are about 3,5 times lower than those registered in Z direction and they increase less than 100 MPa from 0º to 20º angles. The X- maximum load for the tool with 2º angle is lower than the other three, but no reasonable explanation other than an experimental error can be found to understand this finding. An increase of the cutting angle implies a higher tool displacement before sheet fracture (from 0,5 mm at 0º to approximately 2,1 mm at 20º). The higher the displacement of the slitting

tool at which fracture occurs accounts for the higher bending effect of the sheet when the cutting angle increases.

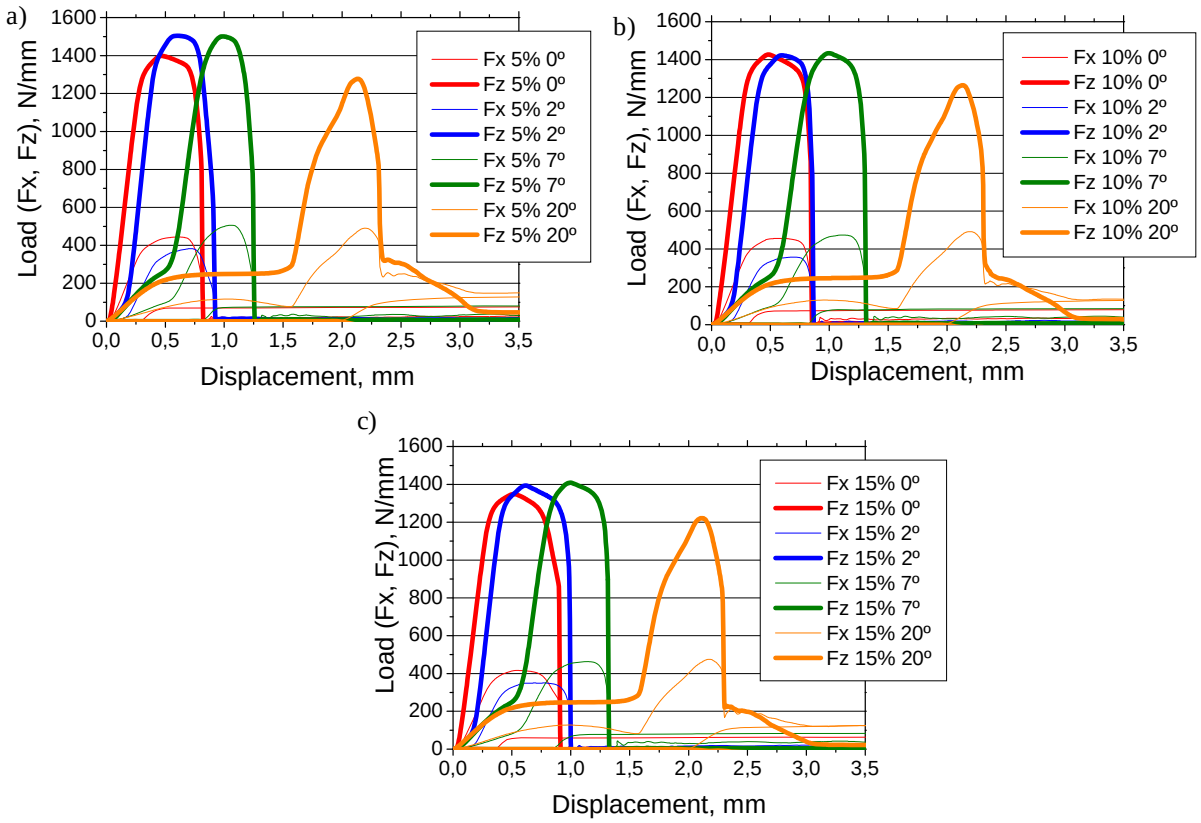

Figure 3.3.101 Load – displacement curves registered during tests in the instrumented slitting die using hardened 22MnB5 steel 1,5 mm thick. Loads in X and Z directions are plotted for cutting angles of 0º (red), 2º (blue), 7º (green) and 20º (orange) and cutting clearances of: a) 5% of the sheet thickness; b) 10 % and c) 15 %. Loads are normalised taking the sheet width into account (50 mm) [NOT11]

By re-plotting the experimental load – displacement curves (this time reassembled depending on the cutting angle, as shown in Figure 3.3.102 a) 0º, b) 2º, c) 7º and d) 20º), it can be observed that the clearance has not as much influence as the cutting angle in the maximum loads either in Z or X direction. Only a slight decrease in Z maximum loads is reported when increasing the clearance from 5 to 15 % (less than 100 MPa), while X maximum loads are still more similar from ones to each others. The displacement at which sheet fracture takes place is also driven towards higher values when the clearance increases. However, the influence of clearance on the displacement at which fracture takes place is much less important than the influence of the cutting angle.

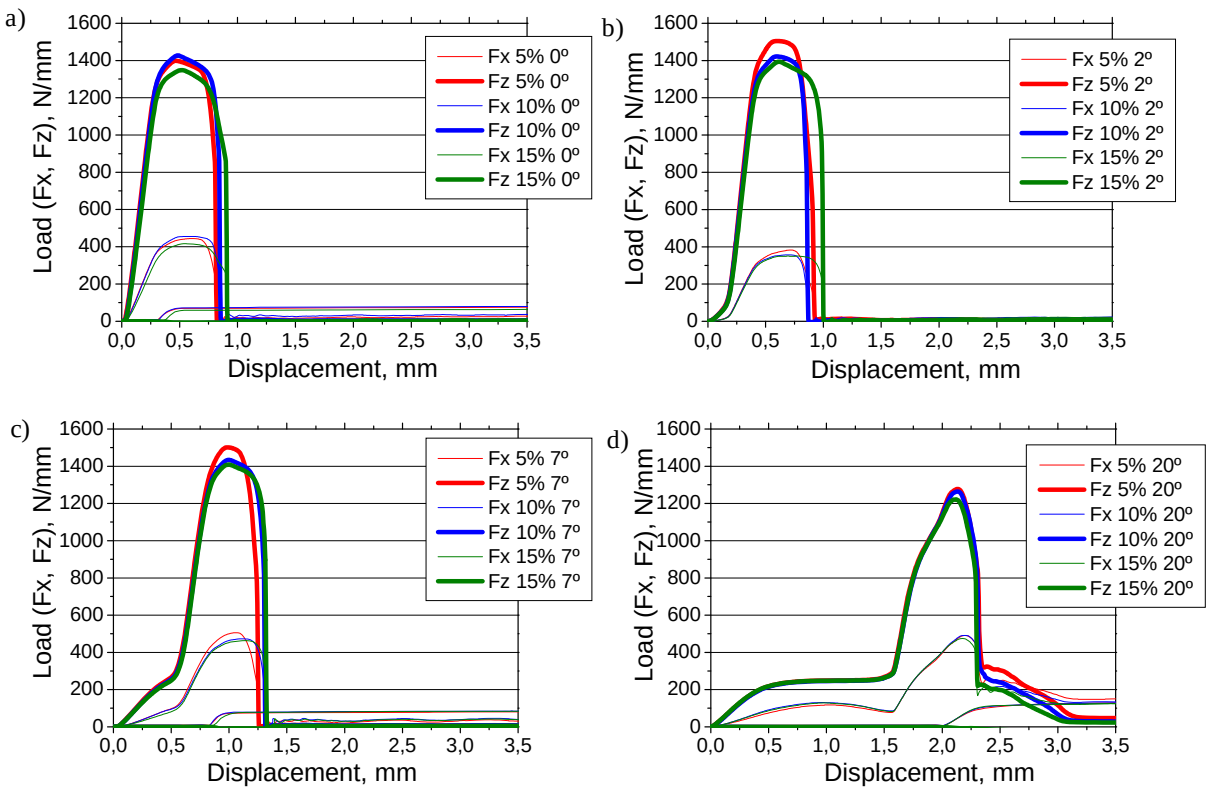

Figure 3.3.102 Load – displacement curves registered during tests in the instrumented slitting die using hardened 22MnB5 steel 1,5 mm thick. Loads in X and Z directions are plotted for cutting angles of 0º (red), 2º (blue), 7º (green) and 20º (orange) and cutting clearances of: a) 5% of the sheet thickness; b) 10 % and c) 15 %. Loads are normalised taking the sheet width into account (50 mm) [NOT11]

3.4 Tool life prediction models based on LEFM

As discussed in chapter 1.3, the integration of the Paris law is a well known approximation to estimate lives of engineering components subject to cyclic loads, provided that cracks are already present in the material, i.e. it is assumed that the time needed for crack nucleation is negligible. The number of cycles to failure, N, is related to the crack initial and final size, a_0 and a_f respectively, the applied stress, $\Delta\sigma$, the correction factor Y, and the Paris law's parameters, m and A, as shown in Equation 1.5.3.

In an attempt to assess the validity of Equation 1.5.3 in the materials of this study, it was applied in case of some of the specimens of 1.2379 D2, UNIVERSAL D2, K360 D2 and HWS D2 tested in fatigue. To proceed, a_0 was considered as the size of the initiating crack particle (carbides or inclusions for ingot cast or PM tool steels respectively), and the a_f was the size of the measured halo at the fracture surface (see Table 3.4.1). m and A values were those reported in Table 3.2.3 for the same materials and configuration and Y values were determined using the equations of Newman and Raju [NEW84].

Table 3.4.1 Applied stress, $\Delta\sigma$, and initial, a_0, and final, a_f, crack sizes measured at the fracture surfaces of some of the samples tested in fatigue ($\Delta\sigma$ in MPa, a_0 and a_f in μm)

	1.2379-1	1.2379-2	1.2379-3	UNI-1	UNI-2	K360-1	HWS-1	HWS-2	HWS-3	HWS-4	HWS-5
$\Delta\sigma$	810	720	630	990	990	765	1306	1347	1128	1260	1260
a_0	55	50	30	16	14	32	27	10	10	11	24
a_f	719	1216	957	435	382	483	155	120	134	172	175

In Figure 3.4.1 a) it can be observed that the model predicts with increased accuracy the *N* of ingot steels with respect to PM steels. The results of 1.2379, UNIVERSAL and K360 present a good coincidence between the modelled and the experimental number of cycles (as shown more in detail in Figure 3.4.1 b)). In contrast, the *N* values predicted for HWS are considerably lower than the experimental ones. The reason for such discrepancy is that the assumption of negligible time for nucleation is not valid in this steel, but contrarily and as discussed previously in section 3.2.5, the nucleation of cracks at inclusion particles requires very long incubation periods which are not taken into account in the present model. In fact, the number of cycles required to nucleate cracks in the microstructure of HWS can be significantly higher than the number of cycles required to propagate them to failure. According to the *m* and *A* values determined for this steel (which are the highest amongst the studied materials) the predicted *N* using the Paris law (which contemplates hence, only the *N* in the Paris regime of crack propagation) is completely different to the experimental *N*, e.g. 256 vs 753433 cycles, 4227 vs 640617 cycles or 402 vs 19550 cycles.

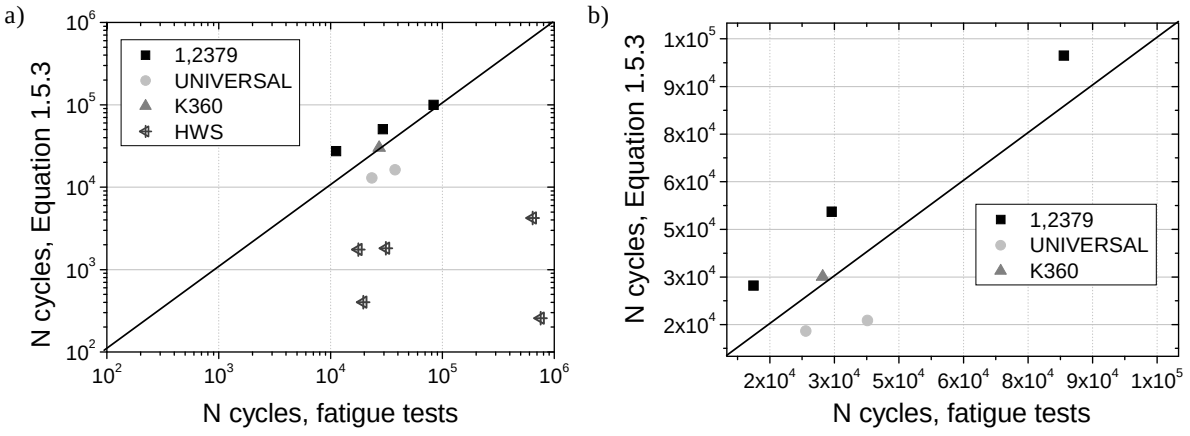

Figure 3.4.1 Comparison between the number of cycles, *N*, estimated through Equation 1.5.3 and the *N* determined experimentally for the fatigue samples: a) 1.2379, UNIVERSAL, K360 and HWS, all in D2; b) zoom in a) with 1.2379, UNIVERSAL and K360 results

Even though this model seems to give rather good estimations of N in case of 1.2379, UNIVERSAL and K360, the results presented in Figure 3.4.1 were aimed at being improved by means of the following consideration. As shown in section 3.2.5, nucleated cracks do not start to propagate stably until they attain a certain size. In particular, stable propagation in the Paris regime is not observed until the initial crack exceeds the limits of the carbide cluster. Thus, if the sizes of carbide clusters in fracture origins are considered as a_0 values instead of the initial carbide sizes (as shown in Figure 3.4.2, solid and dashed lines respectively) the accuracy of the results is expected to be improved.

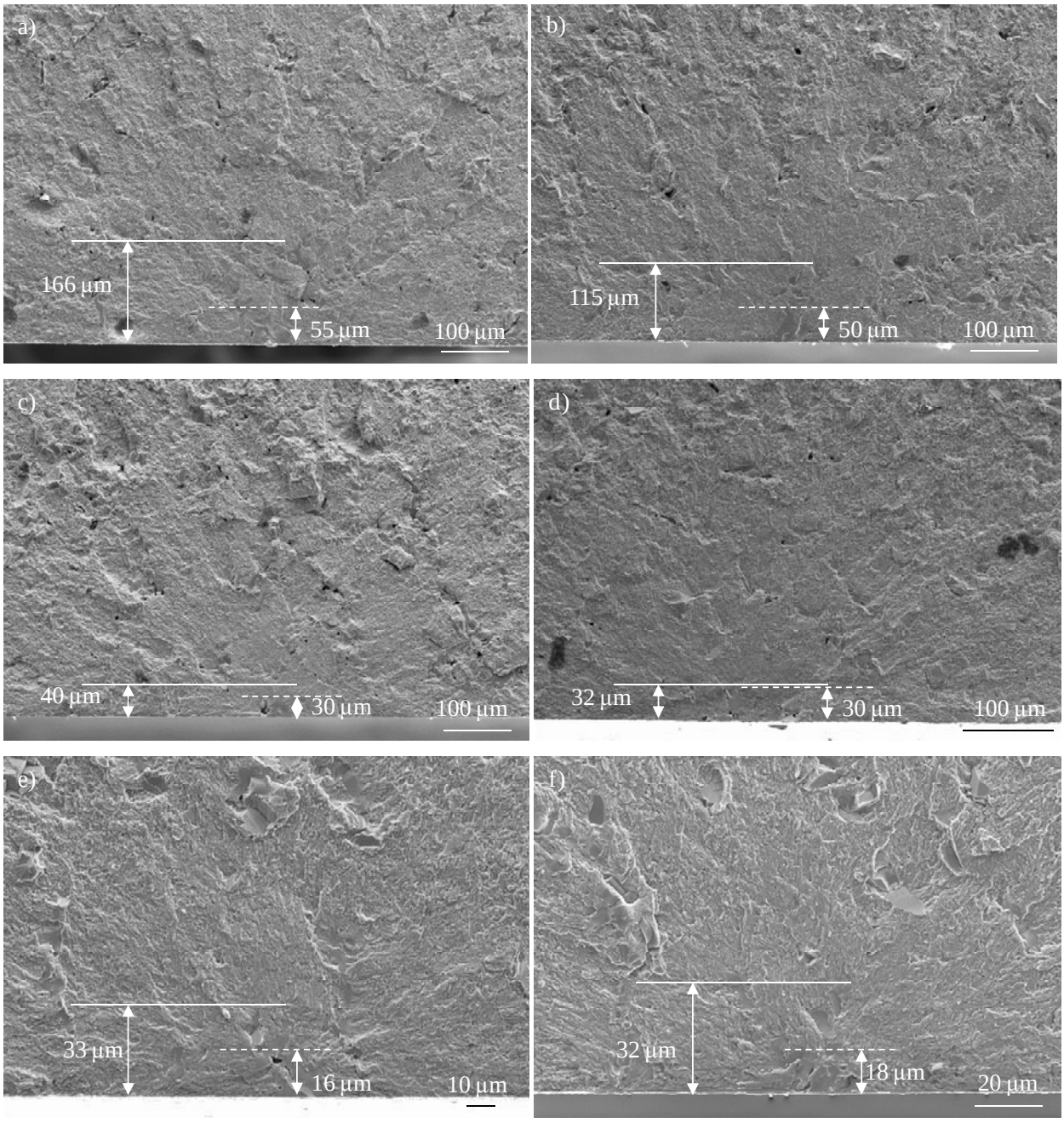

Figure 3.4.2 Fracture initiating sites of the samples considered for this study, and in which the sizes of the initial carbide particles (dashed lines) are compared to the sizes of the clusters in which they are embedded (solid lines): a) to c) 1.2379; d) K360 and e) and f) UNIVERSAL

As it can be observed in Figures 3.4.3 a) and b), the estimated *N* values considering the size of the initial clusters are much more in accordance to the experimental *N* of 1.2379 and K360, but in case of UNIVERSAL the results show still higher deviations. The improvement in case of 1.2379 and K360 is understood taking into consideration that as follows from section 3.2.5, carbides in these steels can break at the first cycles under the applied fatigue stress amplitudes (since $\sigma^{max} \geq \sigma^{RC}$). Therefore, the assumption of negligible time for nucleation is reasonably valid for these steels. As the propagation of initial cracks within clusters is rather unstable and it cannot be described by the same parameters regulating the Paris regime (since it applies for cracks propagating stably), the *N* values obtained using the size of clusters instead of that of carbides as the initial crack sizes are closer to the experimental results. In all cases of 1.2379 and K360, the re-estimated *N* values are closer but lower than the experimental ones (e.g. 11084 vs 11195 cycles, 28515 vs 29375 cycles, 83076 vs 83329 cycles, etc., respectively) and these differences are attributed to the time required for the crack to propagate within the cluster and until it attain the regime for stable propagation.

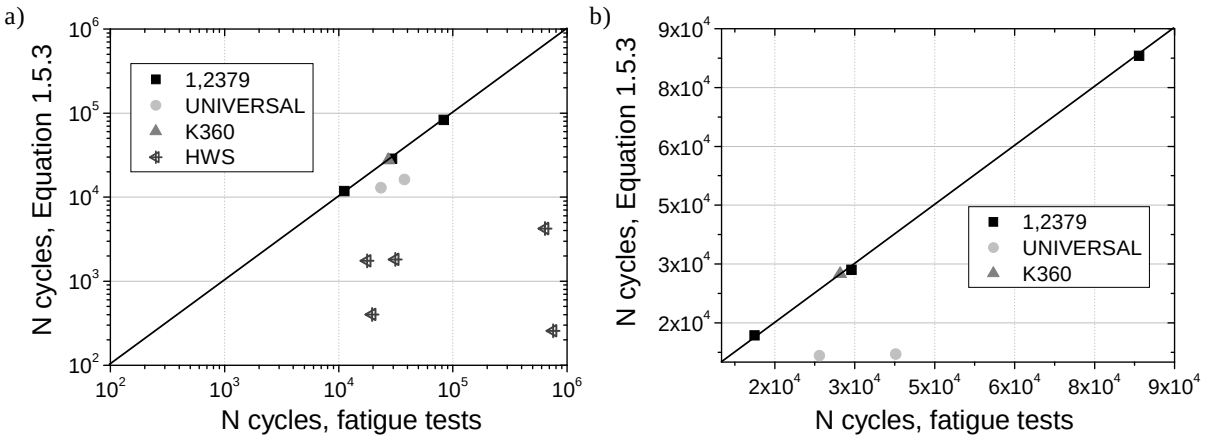

Figure 3.4.3 Comparison between the number of cycles, *N*, estimated through Equation 1.5.3 and the *N* determined experimentally for the fatigue samples: a) 1.2379, UNIVERSAL, K360 and HWS, all in D2; b) zoom of the squared region in a) with 1.2379, UNIVERSAL and K360

In UNIVERSAL, however, the aforementioned statements do not apply since as discussed in section 3.2.5, fracture of carbides and nucleation of cracks at the first cycle is not probable at the level of applied stress amplitudes, but an incubation time is required. In this sense, and taking advantage that in one of the UNIVERSAL samples the crack leading to failure was followed with the increasing number of cycles (see Figure 3.2.37), the *m* and *A* parameters for that crack were calculated. Using these values instead of those determined for long cracks, an *N* value of 14845 cycles is estimated instead of 7021 (as it is plotted in Figure 3.4.3).

Figure 3.4.4 shows that using the *m* and *A* parameters determined for this crack (they are shown in Table 3.2.12, see the medium crack), the number of cycles required for nucleation is in agreement with the experimental observations in the sense that it is comprised between 10000 and 15000, as it is shown in section 3.2.5.2 (see the left column of Figure 3.4.4). In contrast, a nucleation period of more than 20000 cycles was estimated after the results using the parameters for long cracks (as shown in the right column of Figure 3.4.4). It is also noteworthy that at 15000 cycles, this crack is observed to have already exceeded the limits of the cluster in which it is initially embedded; that is, it has started propagating in the regime described by Equation 1.5.3. This is also in agreement with the results obtained since at 15000 cycles the crack was estimated to propagate stably (15000 cycles lie in the pink rectangle in Figure 3.4.4 left).

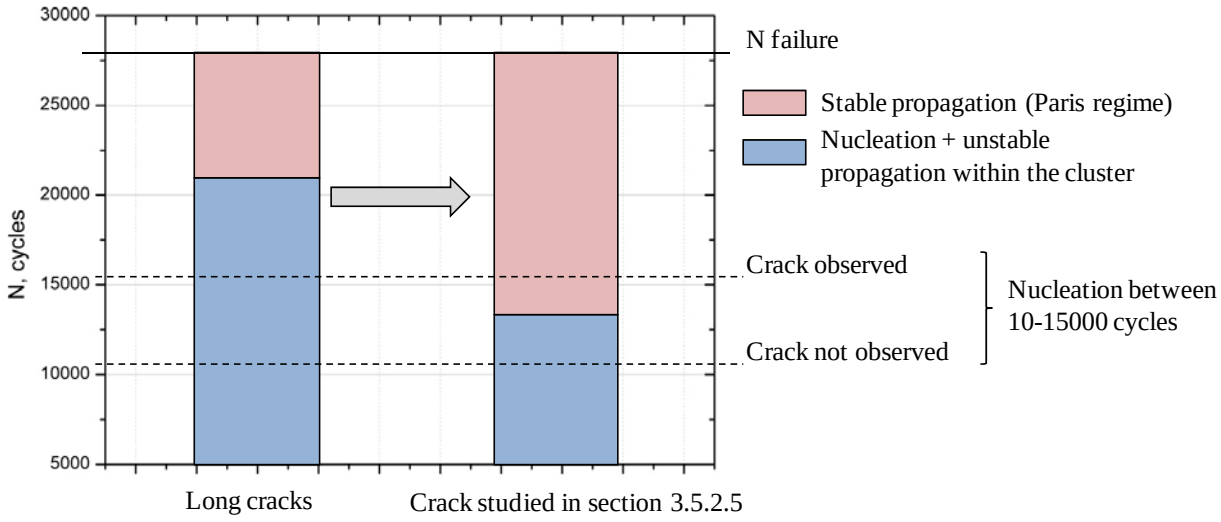

Figure 3.4.4 Comparison between the number of estimated cycles, *N*, both for nucleation and propagation of the crack observed in the UNIVERSAL sample analysed in section 3.2.5.2, considering the parameters of the Paris law determined for long cracks, and the parameters determined for this crack and shown in Table 3.2.12

Figure 3.4.5 shows the estimated number of cycles (in a logarithmic scale) after the Paris law, for the propagation of cracks in 1.2379, UNIVERSAL, K360 and HWS samples (light pink rectangles). In blue rectangles the number of cycles required for nucleation (or for nucleation plus unstable propagation within the initial carbide cluster, in case of ingot steels) is estimated through the difference between the modelled *N* and the experimental *N*. Note that for UNIVERSAL and as follows from the previous paragraph, *N* is calculated assuming the parameters of the Paris law determined for the sample analysed in section 3.2.5.2 instead of those determined for long cracks.

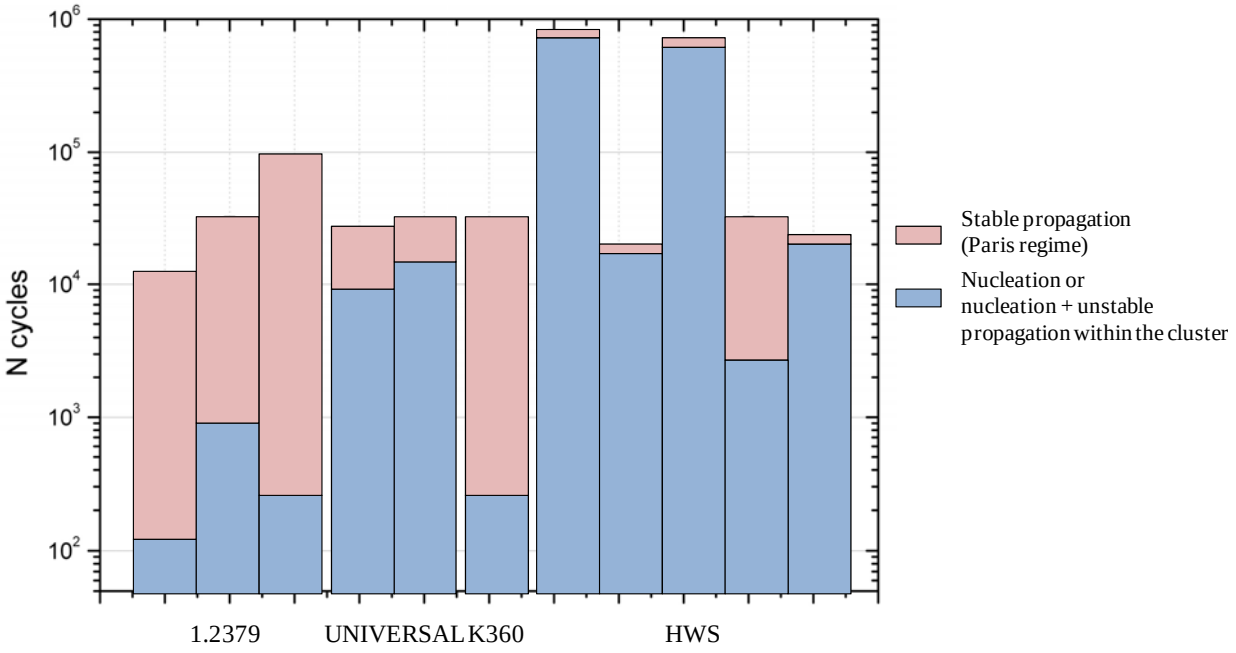

Figure 3.4.5 Comparison between the number of estimated cycles, *N*, both for nucleation and propagation of the samples studied

In the figure above it can be observed that the estimated time for nucleation (or nucleation plus propagation of the crack within the carbide cluster, in case of ingot tool steels) is rather short for 1.2379 and K360, much longer for UNIVERSAL, and extremely long for HWS. Then, a model for fatigue life prediction based on crack propagation data by means of the integration of the Paris law can satisfactorily be applied only in case of ingot cast steels with large carbides embedded, such as 1.2379 and K360, and provided that the size of the cluster instead of the size of the initial carbide is considered as the initial crack size. In these steels, cracks are nucleated at the first number of cycles and therefore, almost the entire fatigue life is spent in the propagation of these cracks. However, this model fails at estimating the fatigue lives of steels like UNIVERSAL and HWS, with smaller carbide sizes and in which the nucleation of cracks requires a certain number of cycles that cannot be predicted using the present model.

Meurling et al. [MEU01] and Melander et al. [MEL02] developed a model which in basis of LEFM, studied crack propagation in tool steels from a probabilistic approach. The novelty of the model proposed by these authors is that it permits to take into account the distribution of primary carbides or inclusions as initial crack sizes. As described in section 1.5, this model was implemented in this Thesis using data of 1.2379, UNIVERSAL, K360 and HWS, all in D2.

As performed by Meurling et al. and Melander et al. in their respective works, the estimated fatigue limit is compared to the experimental $\Delta\sigma^{fat}$ at $2{\cdot}10^6$ cycles. The exponential function $N_A(D)$ (Equation 1.5.7) is used to describe the cumulative size distribution of primary carbides (in terms of *ECD*, see Figure 3.1.2 "*ECD*") and determine the *f* and *k* constants, as scheduled in Table 3.4.2. (Note: for tool steels with two or more carbide types, their respective size distributions are summed together in order to find a unique $N_A(D)$ function for each material (for K360 only M_7C_3 and MC carbides are considered)). The resulting cumulative carbide size distribution of steels and the regression to the $N_A(D)$ equation can be observed in Figure 3.4.6.

Table 3.4.2 $N_A(D)$ fitting constants (Equation 1.5.7) of the cumulative carbide size distribution

Tool Steel	f (10^3 mm^{-2})	k (μm^{-1})
1.2379	2,16 ± 0,02	0,18 ± 0,00
UNIVERSAL	2,77 ± 1,22	0,25 ± 0,01
K360	1,52 ± 1,42	0,19 ± 0,00
HWS	304,02 ± 4,79	2,30 ± 0,04

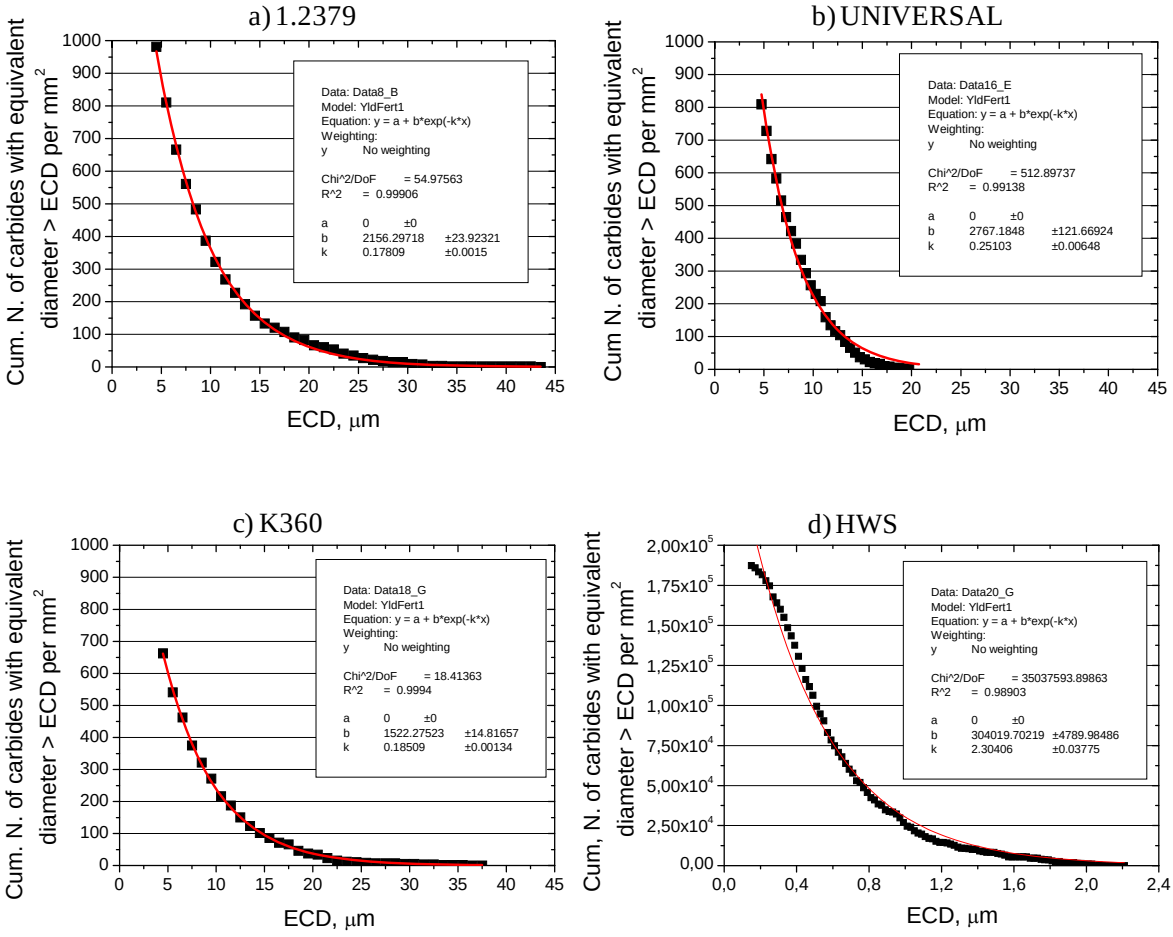

Figure 3.4.6 Cumulative carbide size distribution and regression to $N_A(D)$ equation of the considered steels

The fracture probability, P_f, is calculated following the method described by Meurling et al., and the resulting curves for each material are plotted in function of the applied stress range, $\Delta\sigma$ (see Figure 3.4.7 a)). Meurling et al. observed that the sensitivity of the method with respect to ΔK_{TH} is very low. In this study as follows from the work of the aforementioned authors, ΔK_{TH} is supposed to be equal to 4 MPa·m$^{1/2}$ for all materials since, according to Figure 3.2.11, ΔK_{TH} values of 1.2379, UNIVERSAL, K360 and HWS D2 show small differences (between 3,2 and 4,9 MPa·m$^{1/2}$).

Merurling et al. considered the stress corresponding to the calculated fracture probability of 50 %, P_f^{50}, as the fatigue limit of materials. 50 % of non-failure is the reliability rate obtained when determining the fatigue limit using the staircase method [DIE61]. Therefore, a direct comparison between $\Delta\sigma$ at P_f^{50} and $\Delta\sigma^{fat}$ at 2·10^6 cycles is completely reasonable and the results obtained are shown in Figure 3.4.7 b).

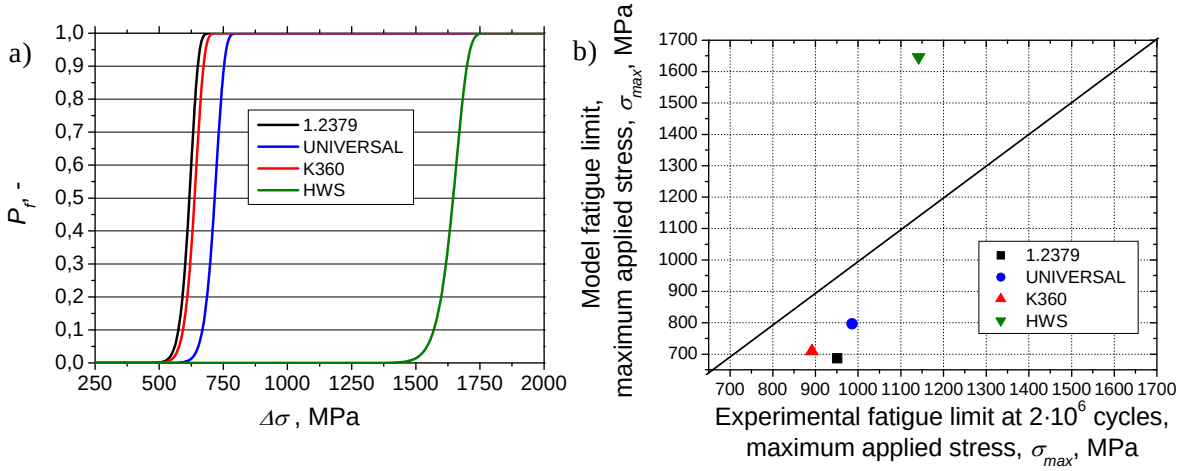

Figure 3.4.7 a) Fracture probability, P_f, in function of the applied stress range, $\Delta\sigma$, estimated using the method developed by Meurling et al. and applied to 1.2379, UNIVERSAL, K360 and HWS; b) model fatigue limit vs experimental fatigue limit at 2·10^6 cycles

Fracture probability results show good agreement with regard to the tendencies that could be expected after the carbide size distribution of the studied steels. 1.2379 and K360, which present similar cumulative size distribution of primary carbides, show very close P_f curves while UNIVERSAL, after its finer carbide distribution, shows slightly higher $\Delta\sigma$ values for fracture. In HWS in turn, fracture probability is markedly increased compared to the ingot cast steels owing to the much smaller size of carbides in the microstructure.

Results of 1.2379, UNIVERSAL and K360 are quite conservative, the modelled fatigue limit is lower than the experimental at 2·10^6. Meurling et al. already observed that the model underestimates the fatigue limit of ingot cast steels and these authors attributed such differences to the fact that the initiating carbide particles are often clusters of non-spherical carbides, which are not taken into account in the model.

Another observation by these authors was that the fatigue limit is considered as the fatigue strength at infinite life, but the fatigue strength at $2 \cdot 10^6$ cycles is likely higher than this value. Other reasons by which these authors attributed the differences between the modelled and the experimental fatigue limits are the accuracy of the measurements of the carbide distributions, and of the fitting exponential curves to these distributions.

Opposite to the aforementioned results, HWS shows that the model overestimates the experimental fatigue limit. That is due to the fact that in HWS, inclusions are the cause of experimental fatigue fracture instead of carbides. Then, in order to take into account the effect of inclusion particles on the fatigue limit predicted by the model, the cumulative size distribution of inclusions is determined following the same procedure as carbides, i.e. using image analysis in a total number of 15 images of the microstructure. In Figure 3.4.8, the regression of the cumulative inclusion size distribution to the $N_A(D)$ equation can be observed and the fitting parameters determined are f = 39,81 ± 2,14 mm^{-2} and k = 0,37 ± 0,04.

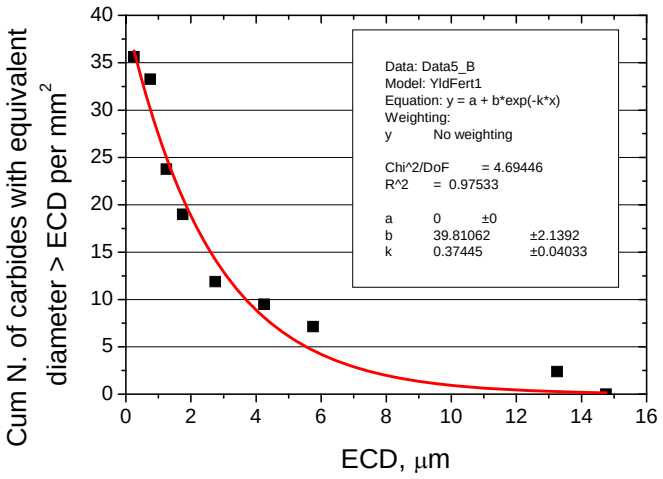

Figure 3.4.8 Cumulative inclusion size distribution and regression to $N_A(D)$ equation of inclusions in HWS

The fracture probability for HWS considering that inclusions are the controlling factor of the experimental fatigue life is plotted in Figure 3.4.9 a). In comparison to the previous results, $\Delta\sigma$ in which P_f takes values comprised between 0 and 1 is reduced by more than 500 MPa (orange curve with respect to the green one). As a consequence, the modelled and the experimental fatigue lives show good agreement, as shown in Figure 3.3.9 b). Such satisfactory results are explained because of the close to spherical shape of inclusions in HWS, and the fact that they are not distributed in clusters, in agreement to the assumptions of this model.

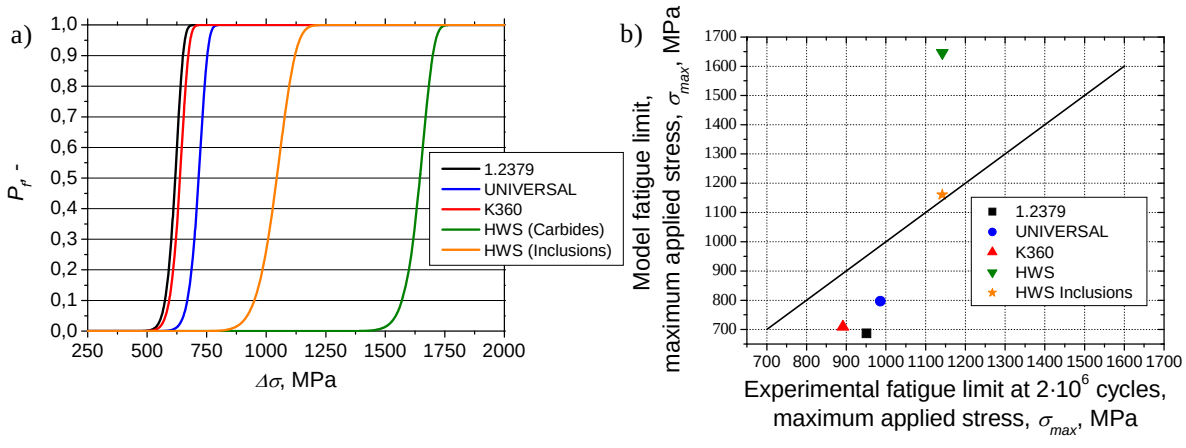

Figure 3.4.9 a) Fracture probability, P_f, in function of the applied stress range, $\Delta\sigma$, estimated using the method developed by Meurling et al. and applied to 1.2379, UNIVERSAL, K360 and HWS (green and orange curves considering carbides and inclusions as initiating particles in fatigue fracture); b) model fatigue limit vs experimental fatigue strength at $2 \cdot 10^6$ cycles (green triangle and orange star considering respectively carbides and inclusions as initiating particles in fatigue fracture)

From this standpoint it can be said that the method developed by Meurling et al., which integrates the statistic distribution of carbides or inclusion particles (as initial crack sizes) in a LEFM based approach, estimates with quite good accuracy the fatigue limit of tool steels (especially in case of PMs where no carbide clusters are present). As follows from these results, the equations of the method and the respective $N_A(D)$ curve fitting parameters of the studied steels were introduced, in form of algorithms, in the FE-simulation model of the DP1000 punching process at the HPC. The required script was written by Albert Llobet, and Ricardo Hernández implemented it into the FE-model. P_f values could be obtained directly as interface from FE-simulations, taking into account the von Mises stresses acting in tools during one stroke (as shown in Figure 3.4.10).

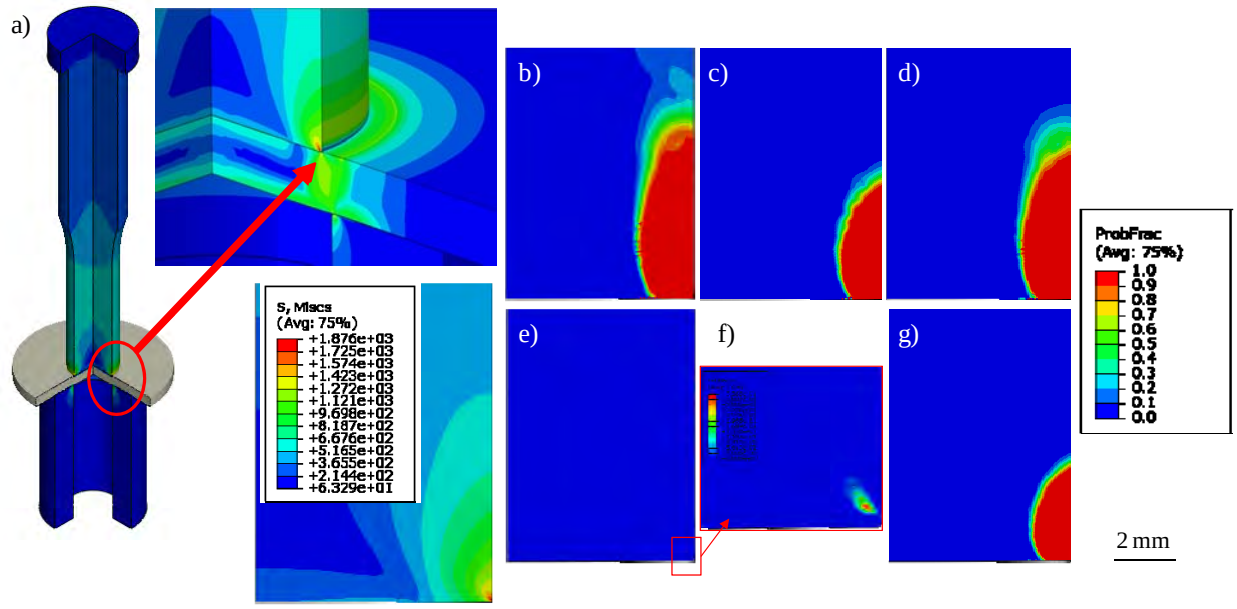

Figure 3.4.10 FE-simulation model for the punching process of the HPC in case of DP1000 2 mm thick: a) schema of the half cross sectional view of the punch in which the von Mises stresses at the moment when they are maximal are shown. Probability of failure determined at the same area and moment for a punch of b) 1.2379; c) UNIVERSAL; d) K360; e) HWS considering the particle distribution of carbides; f) zoom in image e); g) HWS considering the particle distribution of inclusions

The results of Figure 3.4.10 show that when the same stresses act in a punch (Figure 3.4.10 a)), 1.2379 presents the maximum area at the cutting edge with P_f equal to 1 (Figure 3.4.10 b). K360 presents a very similar P_f distribution than 1.2379, but it is slightly smaller (Figure 3.4.10 d)). In UNIVERSAL the area affected by P_f equal to 1 is reduced compared to 1.2379 and K360 (Figure 3.4.10 c)). HWS shows practically P_f equal to 0 in all the punch (Figures 3.4.10 e) and f)) but if inclusions are considered, then the area where P_f is higher than zero increases.

Although these results can be indicative of what may have been the behaviour of these punches made from different materials, in the sense that in experimental tests UNIVERSAL and HWS punches show less damage by fractures than 1.2379 and K360, damage observed in punches is substantially different than what is predicted in Figure 3.4.10 (see section 3.3.3.1). These differences however, can be understood taking into account that the method gives only information about the probability that a crack starts to propagate from a broken particle in the microstructure, according to the stress applied, the size and the distribution of these particles in the material.

In terms of fatigue limit, the model has been shown to work with quite good accuracy in the studied steels, and it also shows agreement predicting the materials which are more damaged in experimental punching tests. However, as the time for nucleation is neglected for the model, if the results would be expressed in terms of probability to fail after N number of cycles instead of probability to start propagating at a given stress value (what is much more interesting to give as a result of the model if it is to be applied in tools), it would show large inconsistencies compared to the experimental results.

As an approach to improve the consistency of the model on account of an application for predicting tool lives, the following considerations should be taken into account:

-For ingot cast steels, a statistical distribution of carbide band sizes should be determined instead of single carbides, since carbide bands dictate the onset for stable crack propagation.

-Data on N cycles to failure should be obtained from the model instead of a probability of a crack to start propagating. In this case, Equation 1.5.3 should be computed assuming a_0 as the N_A function of carbide bands, and a_f would depend on the material's K_{IC}. However, if acting stresses are high and in case of ingot cast steels, the R-curve behaviour should be considered if small cracks are involved in the fracture process (as the toughness of such small cracks will be lower than the K_{IC}).

Assuming that these two considerations help in estimating the time for crack propagation with increased accuracy, the predicted life of tools would still lack the information regarding the number of cycles for crack nucleation. Crack nucleation is however, something difficult to be considered in the model since besides the microstructural aspects, it is influenced by parameters such as wear, surface roughness, local overloads, clearances, tool radii, etc., which additionally, vary as the number of strokes increases. As follows from the images of Figure 3.4.10, it is clear that the geometries of the fractured zones observed in punches do not coincide with the geometries in which P_f is higher than 0 and that is because cracks are supposed to be nucleated in zones in which they are really not, and also because other phenomena than fracture of carbides can originate crack nucleation in tools.